UTS UNIVERSITY OF TECHNOLOGY SYDNEY

Investigation of Metal-Organic Frameworks in Gunshot Residue

Analisa Chiaravalle

Thesis submitted in fulfilment of the requirements for the degree of:

Doctor of Philosophy

Under the supervision of:

A/Prof Scott Chadwick

A/Prof Alison Beavis

Dist. Prof. Claude Roux

University of Technology Sydney
Faculty of Science

March 2024

Certificate of Original Authorship

I, Analisa Chiaravalle, declare that this thesis is submitted in fulfilment of the requirements for the award of Doctor of Philosophy, in the Faculty of Science at the University of Technology Sydney.

This thesis is wholly my own work unless otherwise referenced or acknowledged. In addition, I certify that all information sources and literature used are indicated in the thesis.

This document has not been submitted for qualifications at any other academic institution.

This research is supported by the Australian Government Research Training Program.

Signature:

Production Note:
Signature removed prior to publication.

Date: 08/03/2024

This page was left intentionally blank

Acknowledgements

Any PhD is filled with challenges, ups and downs, lefts and rights, and this one was no different. But it's what you learn from every step you take that shapes you into the researcher you become at the end of the journey. While it would be funny to be like Snoop Dogg and thank myself for getting through this thesis, it wouldn't be accurate or fair to everyone who has been by my side. I don't think the completion of this project or thesis would have been possible if it weren't for all my friends and family who stood beside me, offering me unconditional support and encouragement.

Firstly, I would like to thank my supervisors, Scott Chadwick, Alison Beavis and Claude Roux. Thank you for sticking with me over the last seven years (through the good, the bad and the spicy cough) and never giving up on me. Your guidance has helped shape the scientist I have become by allowing me the opportunity to make mistakes, learn from them and improve myself professionally (and sometimes personally). I hope I can take everything you have taught me and apply it to whatever comes next. Scott, thank you for all the advice you have given me, helping unjumble the chaos within my brain (and work desk) to create cohesive sentences. Whenever I doubted myself, you were always there reminding me how far I have come (and I will keep your encouraging words jotted onto a sticky note forever – it's just the hoarder in me). You remained a constant pillar throughout my candidature, and I have valued everything you have said and taught me over the past few years. You are the reason that 'The Bang and The Boom©' lives rent-free in my mind now. Alison, thank you for taking the chance on the quiet child who wanted to complete Honours with you. That opportunity changed my life for the better. Your calming presence complimented my always-stressed state, and you were always prepped with caffeine and biscuits for any on-campus meetings. Claude, thank you for jumping aboard my supervisory panel. Even with your busy schedule, you always made time for our meetings and provided me with feedback. Your words of encouragement that the finishing line was near (even if I didn't see it) helped me continue along.

A special acknowledgment to both Matt Bolton and Joel Waszczuk for all the time and energy you both put into this project. Thank you for helping me gain approval for access to a firing range, acquiring ammunition and firearms, and conducting all the shooting. Before you came along for the project, it was becoming increasingly difficult to progress. Your advice and expertise in this

field have been invaluable, and I hope to take everything you have taught me in my future endeavours.

To every single PhD student who has been by my side throughout this journey, what a massive vibe! Archie, Ayusha, Beth, Bridget, Ciara, Daz, Eathan, Harrison, Harry, Layal, Laura, Kathy, Macey, Matt, Mikki, Sam, Sandy, Teneil, Tom, Rach, Rin and Vicky, I am so grateful to have gotten to know every single one of you. Our scheduled lunch and 2 o'clock coffee (which transitioned into a more inclusive 2 o'clock beverage, for you tea drinkers), or the mischief of desk decorating and end-of-year movie days, were highlights of the days. Laura and Sam, you were like my older sisters, guiding me in the beginning and caffeinating me through the middle and end of my PhD. Thank you for always giving me advice (even if it took me a while to action it), for our breakfast adventures on the weekend and for letting me rant. Thank you for watching endless hours of Friends. Harry and Teneil, thank you for letting me distract you whenever I needed to have a break. The constant sticky notes of encouragement (or slight bullying) and knowing that I could roll to your desk and ask for your opinion, will not be forgotten. Ciara, you have been by my side since we started our undergraduate studies. Thank you for taking the chance and sitting next to this 'normal looking' girl in that first Physics lecture. You always manage to turn a bad day into a not-so-sucky day. I don't know how, but you had a Spidey sense for those days and were always at my door with food, wine, paint and Gilmore Girls. You always made sure I was doing okay, and your messages of empowerment were always appreciated. To everyone, thank you all for taking the time to listen to my utterly brilliant (or absolutely foolish) ramblings and ideas, it made the lab work and thesis writing all the more fun.

To my furthest and dearest friends, thank you for showing me endless support over the past few years. Jazz and Liz, your understanding that I couldn't always show up to gatherings, but never holding it against me, makes me so blessed to have you guys as my friend. Your constant encouragement that I was killing it and your spontaneous trips to Sydney to catch up will never be forgotten. Stace, thank you for being my other half and choosing to spend the past few years as my house sister, especially during the hard times. Our daily gossip sessions and TV show watching (or dissecting – if it was trashy) made home a safe space where I could unwind from long days in the lab.

To my Mum and Dad, I don't think there are enough words for me to say thank you. I appreciate all your support during every phone call, every weekend home, and every holiday season, which was spent listening to me ramble on about the ins and outs of my project, even if it was complete gibberish to you. Whenever I was stressed, you would take the time to visit, forcing me to take a

well-needed day off to recoup and refresh before starting again. Thank you for always pushing me to be the best version I can be, and I can see this reflected in my work. You gave me the strength and endurance that has allowed me to get to this point. My brother, Rich, you provided me with a ton of entertainment throughout these years. But you being there for me at the pointy end, always checking in on me and ready to go on a Macca's run, will not be forgotten.

And lastly, Jake, thank you for standing beside me throughout this whole journey, you always believed that I would get here. You have supported me during long nights in the lab and WFH during lockdowns and provided me with advice when an experiment didn't go to plan. Thank you for knowing when I was tired and planning adventures, reintroducing me to gaming and taking me out for late-night snack runs to get my mind off university. I appreciate you for always taking my mental load, even when you were at capacity.

I look back at what I have just written, and I honestly don't think I could think of a better support system to have gotten me through this PhD journey. Thank you, everyone, for being there for me, physically or virtually. You have all taught me and helped mold different aspects of myself, that has made me a better scientist, a better researcher and a semi well-adjusted adult.

COVID-19 Statement

This PhD project required access to an external police-operated firing range to conduct the incorporation of the ammunition, firearm discharge and sample collection. Due to COVID-19 restrictions, face-to-face contact and access to the firing range was unavailable to the public between March 2020 and January 2022. This impacted a substantial portion of the experimental component of this project, which could not be conducted until access to the public was granted to the firing range. Due to this disruption to the project, the direction of the project was re-evaluated to mitigate the loss of time. The reduced time to complete this project limited the number of specimens that were able to be discharged and collected.

Table of Contents

Certificate of Original Authorship ii
Acknowledgements iv
COVID-19 Statement vii
Table of Contents viii
List of Figures xi
List of Tables xiv
Research Communications xvi
Abbreviations xvii
Abstract xxii
Chapter 1. Introduction 1
1.1 Introduction 2
1.2 Gunshot Residue 3
1.2.1 Composition of GSR 3
1.2.2 Distribution 8
1.2.3 GSR Analysis 10
1.2.4 Interpretation 17
1.2.5 Challenges 22
1.3 Metal-Organic Frameworks 24
1.3.1 Synthesis Routes 24
1.3.2 Luminescent MOFs 24
1.3.3 Applications in Forensic Science 27
1.4 Application of MOFs in GSR Visualisation 33
1.4.1 Novel MOFs 34
1.4.2 Ammunition Encoding 41
1.4.3 Performance as LGSR 44
1.5 Project Aims 50
Chapter 2. Synthesis, Characterisation and Stability of Metal-Organic Frameworks 53
2.1 Introduction 54
2.2 Materials and Methods 59
SECTION I: Synthesis 59
2.2.1 Chemicals 59
2.2.2 Synthesis 59
SECTION II: Characterisation 63

2.2.3 Structural Elucidation 63
2.2.4 Structural Suitability 63
2.2.5 UV Photoluminescence Visualisation 64
2.2.6 Evaluation Criteria 64
SECTION III: Stability 67
2.2.7 Chemicals, synthesis and storage 67
2.2.8 Chemical Stability 67
2.2.9 UV Photoluminescent Stability 67
2.3 Results and Discussion 68
SECTION I: Synthesis 68
2.3.1 Synthesis Optimisation 68
SECTION II: Characterisation 70
2.3.2 General Observation 70
2.3.3 Structural Elucidation 71
2.3.4 Structural Suitability 83
2.3.5 UV Photoluminescence Visualisation 94
2.3.6 Characterisation Overview 97
SECTION III: Stability 100
2.3.7 Chemical Stability 100
2.3.8 UV Photoluminescent Stability 105
2.4 Conclusion 110
Chapter 3. Evaluation of Metal-Organic Frameworks in the Production of Luminescent Gunshot Residue 113
3.1 Introduction 114
3.2 Materials and Munitions 122
3.2.1 Chemicals and Synthesis 122
3.2.2 Firearm and Ammunition 122
3.2.3 Cleaning Process 123
3.3 PART I: Visualisation 124
3.3.1 Methods 124
3.3.2 Results and Discussion 126
3.3.3 Visualisation Overview 138
3.4 PART II: GSR Stub Evaluation 139
3.4.1 Methods 139
3.4.2 Results and Discussion 140
3.5 PART III: Projectile Performance 146

3.5.2 Results and Discussion 148
3.5.3 Projectile Performance Overview 154
3.6 Conclusion 156
Chapter 4. General Discussion and Future Direction 159
4.1 General Discussion 160
4.2 Future Work 162
4.2.1 MOF Synthesis 162
4.2.2 Shelf-life of incorporated ammunition 163
4.2.3 Incorporation process 163
4.2.4 Performance 164
Chapter 5. Conclusion 165
Appendices 169
Appendix 1: Ethics and Consent Forms 170
Appendix 2: Chapter 2 173
5.1.1 Characterisation Excitation Wavelengths 173
5.1.2 XRD 174
5.1.3 FTIR 177
5.1.4 SEM-EDS 185
5.1.5 TGA 188
5.1.6 UV Photoluminescence 191
5.1.7 FTIR Stability 198
5.1.8 Spectrophotometer Wavelength Optimisation 202
5.1.9 Fluorescence Stability 206
5.1.10 VSC Stability 212
Appendix 3: Chapter 3 218
5.1.11 Firearm 218
5.1.12 FCC 220
5.1.13 GSR Stub 223
References 226

List of Figures

Figure 1-1: Diagram of FEDERAL® .40 S&W ammunition. 4

Figure 1-2: Chemical group classification of ligands used in the synthesis of MOFs that are applied in the visualisation of LGSR. 37

Figure 1-3: Frequency of techniques used to characterise MOFs (n = 23). CHNS-O = elemental analysis, MS = Mass Spectrometry, PL = photoluminescence and VSC = Video Spectral Comparator. 38

Figure 2-1: Flowchart of the evaluation criteria applied to the synthesised MOFs. Contains instrumentation used for criteria (blue), the reason for the characterisation technique (grey), and thresholds (black) of individual factors considered before continuation (green) or discontinuation (red). 66

Figure 2-2: XRD pattern of as-prepared SH2-Er (top) and SH2-Ho (bottom). Stars indicate peaks most similar to literature. The insert represents the expected structure of the MOF as indicated by literature. 72

Figure 2-3: XRD pattern of as-prepared SH2-Tb. Stars indicate peaks most similar to literature. The insert represents the expected structure of the MOF as indicated by literature. 74

Figure 2-4: XRD pattern of as-prepared SH2-Gd (top) and SH2-Y (bottom). The insert represents the expected structure of the MOF as indicated by literature. 75

Figure 2-5: XRD pattern of as-prepared SH3-Gd. Stars indicate peaks most similar to literature. The insert represents the expected structure of the MOF as indicated by literature. 76

Figure 2-6: XRD pattern of as-prepared MW1-Tb. Stars indicate peaks most similar to literature. The insert represents the expected structure of the MOF as indicated by literature. 77

Figure 2-7: XRD pattern of as-prepared MW2-Tb (top) and MW3-Tb (bottom). The insert represents the expected structure of the MOF as indicated by the literature. 78

Figure 2-8: Comparison of metal core (grey line) and ligand (black line) precursors and the synthesised MOF (red line). Spectra are representative MOFs containing a) H_3BTC ligand; b) Htta ligand and c) H_2DPA ligand. Grey shading represents peaks associated with the starting material (metal core and ligand) that should not be present in the final product. 80

Figure 2-9: SEM images of a) SH2-Tb; b) SH2-Er; c) SH2-Ho; d) SH2-Gd; e) SH2-Y; f) SH3-Gd; g) MW1-Tb; h) MW2-Tb; i) MW3-Tb collected at 15.00 kV, mag = 1.5 K and WD = 10 mm. 86

Figure 2-10: TGA curves (black solid line) and DTA plots (red dotted line) of synthesised MOFs: a) SH2-Tb; b) SH2-Er; c) SH2-Ho; d) SH2-Gd; e) SH2-Y; f) SH3-Gd; g) MW1-Tb; h) MW2-Tb; i) MW3-Tb 92

Figure 2-11: Photoluminescence emission spectra of a) SH2-Er and b) SH2-Ho captured from the spectrophotometer. The inserts represent the pure MOF samples in the VSC (λ_{ex} = 365 nm; ISO = 100; integration time = 500 ms; iris = 100% and mag = 60x). 95

Figure 2-12: Photoluminescence emission spectra of a) SH2-Gd; b) SH2-Y and c) SH3-Gd captured from the spectrophotometer. The inserts represent the pure MOF samples in the VSC (λex = 365 nm; ISO = 100; integration time = 500 ms; iris = 100% and mag = 60x). 96

Figure 2-13: Photoluminescence emission spectra of a) SH2-Tb; b) MW1-Tb; c) MW2-Tb and d) MW3-Tb captured from the spectrophotometer. The inserts represent the pure MOF samples in the VSC (λ_{ex} = 365 nm; ISO = 100; integration time = 500 ms; iris = 100% and mag = 60x). 97

Figure 2-14: Stacked FTIR spectra of SH2-Tb at month 0 (black), month 6 (blue), month 12 (orange), month 18 (yellow) and month 24 (green). 102

Figure 2-15: Stacked FTIR spectra of MW3-Tb at month 0 (black), month 6 (blue), month 12 (orange), month 18 (yellow) and month 24 (green). 102

Figure 2-16: Stacked FTIR spectra of MW1-Tb at month 0 (black), month 6 (blue), month 12 (red), month 18 (yellow) and month 24 (green). 103

Figure 2-17: Stacked FTIR spectra of MW2-Tb at month 0 (black), month 6 (blue), month 12 (orange), month 18 (yellow) and month 24 (green). 104

Figure 2-18: Stacked spectrophotometer emission spectra of SH2-Tb at month 0 (black), month 6 (blue), month 12 (orange), month 18 (yellow) and month 24 (green) (λ_{ex} = 380 nm). Insert: Luminescence of SH2-Tb observed in the VSC8000 (λ_{ex} = 365 nm) for corresponding months.. 106

Figure 2-19: Stacked spectrophotometer emission spectra of MW1-Tb at month 0 (black), month 6 (blue), month 12 (orange), month 18 (yellow) and month 24 (green) (λ_{ex} = 380 nm). Insert: Luminescence of MW1-Tb observed in the VSC8000 (λ_{ex} = 365 nm) for corresponding months. 107

Figure 2-20: Stacked spectrophotometer emission spectra of MW2-Tb at month 0 (black), month 6 (blue), month 12 (orange), month 18 (yellow) and month 24 (green) (λ_{ex} = 380 nm). Insert: Luminescence of MW2-Tb observed in the VSC8000 (λ_{ex} = 365 nm) for corresponding months. 107

Figure 2-21: Stacked spectrophotometer emission spectra of MW3-Tb at month 0 (black), month 6 (blue), month 12 (orange), month 18 (yellow) and month 24 (green) (λ_{ex} = 380 nm). Insert: Luminescence of MW3-Tb observed in the VSC8000 (λ_{ex} = 365 nm) for corresponding months. 108

Figure 3-1: Flowchart of experimental design for evaluating the suitability of MOFs as LGSR particles. * indicates that shooting failure was evaluated for all firearm discharge in both Part I (n = 300 + n = 15) and Part III (n = 60 + n = 20). 122

Figure 3-2: UV light source and camera set up to visualise and photograph shooter's hand and firearm post discharge. 125

Figure 3-3: Count of visible LGSR particles observed on the shooter's hands (n=5). 127

Figure 3-4: Example of maximum distribution patterns observed by the LGSR particles visible under UV light following discharge of ammunition containing 4 wt% of MW1-Tb. Inserts are close up images of the area containing LGSR particles to enhance visibility. 128

Figure 3-5: Comparison of total count of LGSR particles visible on and within the firearm. Error bars are represented by the interquartile range error (n=5). 131

Figure 3-6: Image of SH2-Tb during incorporation with propellant at a) 2 wt%, b) 6 wt% and c) 10 wt%. 132

Figure 3-7: Image of MW1-Tb during incorporation with propellant at a) 2 wt%, b) 6 wt% and c) 10 wt%. 132

Figure 3-8: Image of MW2-Tb during incorporation with propellant at a) 2 wt%, b) 6 wt% and c) 10 wt%. 133

Figure 3-9: Image of MW3-Tb during incorporation with propellant at a) 2 wt%, b) 6 wt% and c) 10 wt%. 133

Figure 3-10: Median representation of LGSR particle count within different locations on the firearm at an incorporation ratio of 10 wt%. Error bars are represented by the interquartile range error (n=5). 135

Figure 3-11: Distribution of MW1-Tb LGSR particles at different incorporation ratios on the FCC. Images of the side, mouth and base of MW1-Tb FCC illuminated using white light (left) and the Labino® flood lamp (λ_{ex} = 365 nm, right) using a Canon EOS 700D (ISO = 1600; f-stop = f/2.8; exposure = 1/30 sec.). 137

Figure 3-12: Encountered particle morphologies (a-d) and associated elemental composition (e-h) on the control stub. Morphology of particles consist of a) atypical particle, b) irregular particle, c) irregular particle, and d) irregular shape. Abundance of particles decrease further down the list. 142

Figure 3-13: Abundance of discharged Tb-MOF on GSR stub. a) SH2-Tb-2 wt%; b) SH2-Tb-6 wt%; c) SH2-Tb-10 wt%; d) MW1-Tb-2 wt%; e) MW1-Tb-6 wt%; f) MW1-Tb-10 wt%; g) MW2-Tb-2 wt%; h) MW2-Tb-6 wt%; i) MW2-Tb-10 wt%; j) MW3-Tb-2 wt%; k) MW3-Tb-6 wt%; l) MW3-Tb-10 wt%. 144

Figure 3-14: Chronograph and firearm set up aimed perpendicularly at the target (10 m distance between muzzle and target), in an indoor firing range. 147

Figure 3-15: Ratio effect on the velocity comparison of MOF-incorporated ammunition and the unmodified ammunition (control). Error is represented by the standard error of mean (n=5). 150

Figure 3-16: Normalised projectile perforation location for each MOF and incorporation ratio in relation to the unmodified ammunition projectile. Colour represents incorporation ratio and shape represents MOF. Error is represented by the standard error of mean (n=5). 153

Figure 3-17: Hypothesised flight paths of the control and incorporated projectiles. 154

List of Tables

Table 1-1: Composition of propellant types [25, 34]. 6

Table 1-2: Common additives and their purpose [25, 34]. 6

Table 1-3: GSR categories according to ASTM International guidelines [8]. 8

Table 1-4: Different wavelengths evaluated on dark fabric to visualise GSR. * highlights that no precise wavelength was provided. 13

Table 1-5: Factors for consideration during interpretation for Bayesian hierarchy of propositions specific for GSR [141]. 18

Table 1-6: Possible sources for GSR-like particles in the environment for IGSR and OGSR. 19

Table 1-7: Ligand-based luminescence charge transfer processes [225, 226, 240]. 26

Table 1-8: Metal core and ligand combinations for MOF synthesis in GSR visualisation literature. 35

Table 1-9: Characteristic emission peaks for Eu-MOF [173, 186], Tb-MOF [179, 183], Dy-MOF [175], Gd-MOF [180] and Er-MOF [188]. ^ excited with UV wavelength. # excited at 980 nm. * represents the emission peak most responsible for luminescent colour. 39

Table 1-10: Wavelengths applied to literature focusing on the synthesis of novel LGSR on different objects in the literature. 41

Table 1-11: Current research evaluation of LGSR. 45

Table 2-1: MOFs previously synthesised for incorporation into ammunition. Listed in order of synthesis time. 55

Table 2-2: Advantages and limitations of SH and MW-assisted synthesis methods. * dependent on MW system. 56

Table 2-3: Luminescent stability of LGSR. Ln = Eu^{3+} and Tb^{3+}. 57

Table 2-4: Overview of MOFs synthesised for this study. 62

Table 2-5: SEM-EDS Parameters. 63

Table 2-6: Comparison of temperature and percentage yield for MW3-Tb synthesis. 69

Table 2-7: Comparison of synthesised MOFs in this study. n = 2. ^cost calculated per round (at 10 wt% incorporation of synthesised MOF). 70

Table 2-8: Peak position and relative peak intensity of SH2-Er and SH2-Ho comparison with literature XRD pattern [206]. 73

Table 2-9: Peak position and relative peak intensity of MW1-Tb comparison with literature XRD pattern [176]. 77

Table 2-10: FTIR assignments of the primary vibrations associated with the synthesised MOFs containing a BTC ligand. ✕ = No peak expected. 81

Table 2-11: FTIR assignments of the primary vibrations associated with the synthesised MOFs containing a tta ligand. 82

Table 2-12: FTIR assignments of the primary vibrations associated with the synthesised MOFs containing a DPA ligand. 83

Table 2-13: Theoretical mass loss associated with the synthesised MOFs containing a BTC ligand. 88

Table 2-14: Comparison of actual mass remaining from TGA curve and theoretical percent mass remaining for the synthesised MOFs, and product remaining. 91

Table 2-15: TGA comparison of published MOFs [78, 176, 180, 183, 186]. 93

Table 2-16: Photoluminescence transition assignments of the peaks associated with the synthesis of Tb-MOFs. 97

Table 2-17: Summary of MOFs discontinued from initial general observations. 98

Table 3-1: Overview of the variables associated with MOF incorporation into ammunition. 116

Table 3-2: SEM-EDS Parameters applied during GSR analysis. 139

Table 3-3: List of elements analysed during manual SEM-EDS analysis of traditional GSR, NTA GSR and LGSR stubs according to the E1588-17 Standard. * = characteristic, ^ = consistent, # = commonly associated with and + = additional elements. 140

Research Communications

Conferences

Oral Presentation: **Development of Luminescent Metal-Organic Frameworks for In-Field Detection of GSR.** 25th International Symposium of the Australian and New Zealand Forensic Science Society. 2022.

Oral Presentation: **The Effect of Different Ratios of Metal-Organic Frameworks Incorporated Into Ammunition.** 25th International Symposium of the Australian and New Zealand Forensic Science Society. 2022.

Oral Presentation: **Evaluation of Metal-Organic Frameworks in the Production of Luminescent Gunshot Residue and their Effect on Projectile Velocity.** 23rd Triennial Meeting of the International Association of Forensic Sciences held in conjunction with the 26th Symposium of the Australian and New Zealand Forensic Science Society. November 2023.

Abbreviations

1D	1 Dimensional
2,6-DNT	2,6-Dinitrotoluene
2D	2 Dimensional
2-nDPA	2-Nitrosodiphenylamine
2-tta/Htta	2-Thenoyltrifluoroacetone
3D	3 Dimensional
4-nDPA	4-Nitrosodiphenylamine
8-qu	8-Hydroxyquinoline
AFP	Australian Federal Police
AK-II	Akardite II
Al	Aluminium
ALS	Alternative Light Source
AMP	4-Aminomethyl Pyridine
ASTM	American Society for Testing and Material
ATR	Attenuated Total Reflectance
Ba	Barium
bipy	2,2'-Bipyridine
bpm	2,2'-Bbipyrimidine
BZP	Benzodiazepines
Ca	Calcium
CA	Cyanoacrylate
CBA	1,1-Cyclobutanedicarboxylic acid
CBC	Companhia Brasileira de Cartuchos
CH_3COONa	Sodium Acetate
CHNS-O	Elemental Analysis
Cl	Chlorine
cm	Centimeters
CP	Conjugated Polymer
Cu	Copper
dafone	4,5-Diazafluoren-9-one
dbm	Dibenzoylmethane
DDNP	Diazodinitrophenol
DEP	Diethyl Phthalate
DMF	N,n-Dimethylformamide
DMNB	2,3-Dimethyl-2,3-Dinitrobutane
DMP	Dimethyl Phthalate
DNB	Dinitrobenzene
DNP	2,4-Dinitrophenol
DNT	2,4-dinitrotoluene
DNT	2,4-Dinitrotoluene
DPA	Diphenylamine
DTA	Differential Thermal Analysis

Dy	Dysprosium
EC	Ethyl Centralite
ENFSI	European Network of Forensic Science Institutes
Er	Erbium
$Er(NO_3)_3.5H_2O$	Erbium (III) Nitrate Pentahydrate
ESI	Electron Spray Ionisation
EtOH	Ethanol
Eu	Europium
FCC	Fired Cartridge Case
Fe	Iron
FT-ICR-MS	Fourier-Transform Ion Cyclotron Resonance-Mass Spectrometry
FTIR	Fourier Transform Infrared
Ga	Gallium
GC	Gas Chromatography
Gd	Gadolinium
$Gd(NO_3)_3.6H_2O$	Gadolinium (III) Nitrate Pentahydrate
Gr	Grain
GSR	Gunshot Residue
H2BDC/BDC	Terephthalic Acid
H2DPA/HDPA/DPA/dipic	Dipicolinic Acid
H_2O	Water
H_3BTC/BTC/TMA	Trimesic Acid
H_4btec/Hbtec	1,2,4,5-Benzenetetracarboxylic Acid
Hbtfa/btfa	4,4,4-Trifluoro-1-Phenyl-1,3-Butanedione
hfth	4,4,5,5,6,6,6-Heptafluoro-1-(2-Thienyl)Hexane-1,3-Dione
HIS	Hyperspectral Imaging
HMX	Octogen
Ho	Holmium
$Ho(NO_3)_3.5H_2O$	Holmium (III) Nitrate Pentahydrate
HOMO	Highest Occupied Molecular Orbital
HPLC	High-Pressure Liquid Chromatography
ICP-MS	Inductively Coupled Plasma Mass Spectrometry
IGSR	Inorganic Gunshot Residue
IMS	Ion Mobility Spectrometer
K	Potassium
KeV	Kiloelectronvolt
kV	Kilovolt
LC	Liquid Chromatography
LDI(±)MS	Laser Desorption Ionisation-Mass Spectrometry
LGSR	Luminescent Gunshot Residue
LIBS	Laser-Induced Breakdown Spectroscopy
LLCT	Linker-to-Linker Charge
LMCT	Linker-to-Metal Charge
LMOFs	Luminescent Metal-Organic Frameworks
Ln	Lanthanide
LnMOFs	Lanthanide Metal-Organic Framework

LUMO	Lowest Unoccupied Molecular Orbital
m	Meters
MC	Methyl Centralite
MGT	Modified Griess Test
MIR	Mid-Infrared
MLCT	Metal-to-Linker Charge
mmol	Millimole
MOFs	Metal-Organic Frameworks
MS	Mass Spectrometry
MS	Mass Spectrometry
MS/MS	Tandem Mass Spectrometry
MW	Microwave-Assisted Synthesis
MW1	Microwave-Assisted Synthesis Route 1
MW2	Microwave-Assisted Synthesis Route 2
MW3	Microwave-Assisted Synthesis Route 3
MW-MOF	Microwave Synthesised MOFs
nA	Nanoampere
NaBDC	Terephthalic Acid Disodium Salt
NATO	North Atlantic Treaty Organisation
NC	Nitrocellulose
Nd	Neodymium
nd	2,4-Nonanedione
NDA	Naphthalene-2,6-Dicarboxylic Acid
NG	Nitroglycerin
$NH_2NH_2.H_2O$	Hydrazine Monohydrate
NH_3	Ammonia
NH_4OH	Ammonium Hydroxide
Ni	Nickel
NIR	Near Infrared
NIR-HSI	Near Infrared-Hyperspectral Imaging
Nm	nanometer
NM	Nitromethane
NMK	*n*-Methyl Caprolactam
N-nDPA	N-Nitrosodiphenylamine
NP	4-Nitrophenol
NQ	Nitroguanidine
NT	Nitrotoluene
NTA	Non-Toxic Ammunition
NX	2-Nitro-*m*-Xylene
OGSR	Organic Gunshot Residue
P	Phosphorus
pA	Picoampere
PA/PIC	Picric Acid
Pb	Lead
PCA	Principle Component Analysis

pfnd	4,4,5,5,6,6,7,7,8,8,9,9,10,10,10-Pentadecafluoro-1-(Naphthalen-2-yl)Decane-1,3-Dione
phen	1,10-Phenanthroline
PL	Photoluminescence
PLS-DA	Partial Least Squares Discriminant Analysis
POA	Point of Aim
POI	Person of Interest
Pr	Promethium
PSD	Passive Sampling Device
Pyr	2-(1H-,1,2,4-Triazole-3-yl) Pyridine
RDX	Trimethylenetrinitramine
REE	Rare Earth Element
ROI	Region of Interest
RT	Room Temperature
s	Second
S	Sulfur
S&W	Smith & Wesson
Sb	Antimony
SDD	Silicon Drift Detector
SEM-EDS	Scanning Electron Microscopy Energy Dispersive X-ray
SH	Solvothermal/Hydrothermal Synthesis
SH1	Solvothermal Synthesis Route 1
SH2	Solvothermal Synthesis Route 2
SH3	Solvothermal Synthesis Route 3
SH4	Solvothermal Synthesis Route 4
SH5	Solvothermal Synthesis Route 5
Si	Silicon
Sm	Samarium
Sn	Tin
SPL	Special
SPR	Small Particle Reagent
SRT	Sodium Rhodizonate Test
Sr	Strontium
SWIR	Short-Wave-Infrared
T0	Directly after Discharge
Tb	Terbium
$Tb(NO_3)_3.5H_2O$	Terbium (III) Nitrate Pentahydrate
TBZ	Thiabendazole
TGA	Thermalgravimetric Analysis
Ti	Titanium
Tm	Thulium
TNP	2,4,6-Trinitrophenol
TNR	Trinitroresorcinol
TNT	2,4,6-Trinitrotoluene
TPPO	Triphenyl Phosphate Oxide
UHPLC-MS/MS	Ultra High-Pressure Liquid Chromatography-Tandem Mass Spectrometry

µm	Micrometer
US	Ultrasound Synthesis
UV	Ultraviolet
UVA	Ultraviolet-A
UVC	Ultraviolet-C
VSC	Video Spectral Comparator
W	Watts
wt%	Incorporation Weight Percent
XRD	X-ray Diffraction
$Y(NO_3)_3.6H_2O$	Yttrium (III) nitrate pentahydrate
Yb	Ytterbium
Zn	Zinc
Zr	Zirconium
ε-cap	ε-caprolactam
λ	Wavelength

Abstract

The investigation of firearm-related events has typically relied on the presence of an entrance hole, fired cartridge cases (FCCs) or firearm at the scene to indicate firearm discharge. The ability to link a person of interest (POI) to the act of discharging a specific firearm relies on the detection of gunshot residue (GSR), mostly inorganic GSR which contains characteristic elemental composition associated with ammunition. These GSR particles are generated during the discharge process from the ignition of primer and combustion of the propellant and have been documented to deposit on nearby surfaces, including a POIs hand. However, due to the minute size of GSR particles, investigators cannot easily visualise where these particles deposit, instead rely on research and experience to indicate which locations contain the highest levels of these particles. This leads to investigators blindly collecting specimens that are potentially absent of GSR particles contributing to the backlogs often encountered by law enforcement during laboratory analysis. Current procedural standards do involve the use of colourimetric tests to locate lead (sodium rhodizonate test) and nitrate (modified Griess test) particles at the crime scene; however, both are limited by the possibility of detecting common environmental contaminants.

It has been reported that the incorporation of luminescent metal-organic frameworks (MOFs) into ammunition can simplify the process of GSR visualisation and collection and support the investigator by creating a visible link between the crime scene, firearm and POI. The addition of MOFs in ammunition appears advantageous as they are chemically and thermally stable, highly luminescent and can contain rare-earth elements (REE), which are not typical in the environment. This low-cost, quick, in-field visualisation technique requires an ultraviolet (UV) light source to highlight the presence of GSR at the crime scene. The application of incorporating MOFs into ammunition has been demonstrated to be a viable preliminary technique to visualise luminescent GSR (LGSR), specifically on a shooter's hand. Research has also indicated that, once collected, LGSR specimens can undergo traditional inorganic GSR (IGSR) or organic GSR (OGSR) analysis procedures in the laboratory and provide additional 'characteristic' information. Current research has focused on building a list of potential luminescent MOFs for incorporation; however, there has been less effort in identifying whether the addition of MOFs impacts the discharge process.

This project aimed to identify the suitability of introducing luminescent particles into ammunition by not only evaluating the ability to visualise LGSR but also evaluating the performance of the projectile post-discharge. A range of novel MOFs were synthesised during the project, containing

a variety of metal cores and ligands, to indicate whether there were cost-effective MOFs with alternative luminescent properties. Each MOF was characterised via a range of instrumentation including X-ray diffraction, Fourier-transform infrared, scanning electron microscope-energy dispersion spectroscopy, thermogravimetric analysis and fluorescence spectrophotometer. The characteristics of the pure MOFs provided insight into the chemical and luminescent properties of the frameworks. The ability for these MOFs to emit a strong visible luminescence when exposed to ultraviolet A (UVA) wavelengths (320 nm – 400 nm) was also evaluated. The strong luminescence observed from the pure MOF suggested that once incorporated into ammunition and discharged, the deposited LGSR will be visible to an investigator. All luminescent MOFs were further assessed to determine whether their chemical and luminescent properties would be durable over a long-term period. The stability of these MOFs highlighted that they would be able to withstand long periods (up to two years) of incorporation without degradation or loss of luminescence.

The luminescent MOFs were then incorporated into the propellant powder at a range of ratios (2 wt% – 10 wt%) to identify whether the amount of MOF to propellant powder affected the behaviour of the LGSR dispersion. Visualising the shooter's hand, firearm, and FCC highlighted a trend that was influenced by the distance from the point of ignition between the firearm and ammunition. The effect of MOF particles on the discharge process was further evaluated by assessing the performance of the projectile via projectile velocity, accuracy and precision. Understanding the effect of MOF addition on the ammunition and projectile behaviour expands the knowledge about LGSR and suggests its suitability in a real-world environment. A comparison between the control ammunition (unmodified) and incorporated ammunition identified that the evaluated MOFs impacted both the velocity and accuracy of the projectile. The variation on velocity highlighted that the addition of the MOFs into the cartridge case was impacting the discharge process of the propellant, which further influenced the LGSR plume and dispersion.

The results of this research have shown that the incorporation of the tested MOFs compromises the functionality of the firearm and projectile, at this stage, they are not viable for incorporation into ammunition. To become a viable option, research should focus on identifying MOFs that can be detected using materials and processes that are already apart of the forensic investigation process (e.g. appropriate light sources and visualisation parameters). While this was attempted in this research, there is still scope to expand on the pool of MOFs through different metal cores and ligand combinations. Additionally, the method of how MOFs are incorporated into the ammunition warrant further investigation as this could attribute to the difference in performance

of the MOFs that were evaluated in this study compared to previous literature. Overall MOFs have the potential to be a valuable tool in the investigation of firearm-related incidences, however further development and refinement is required in order to progress this research endeavour.

Chapter 1. Introduction

1.1 Introduction

In the past two decades, Australia has become recognised as a country with strict firearm acts and regulations. Following the Port Arthur massacre (1996), Australia's government introduced policies to protect the safety of its citizens. These policies have been observed a positive effect on firearm violence in Australia [1]. The Bureau of Crime Statistics and Research (BOCSAR) has followed the trends for offences (robberies, non-domestic assault, and domestic assault) involving the use firearms over a 20-year span (2003 – 2023) in New South Wales (NSW), Australia [2]. Overall, the 20-year trend illustrated a 74% decline in the number of firearm-related scene. However, between October 2022 and September 2023, NSW Police Force recorded 110 robberies, 59 non-domestic assault and 21 domestic assault crimes involving a firearm. These number of incidents show that even with the strict laws governed in Australia and decline in reported offences, firearm-related scenes are still reported to law enforcement, with 40.8% occurring in the Greater Sydney region [2].

The traces obtained from firearm-related crimes are crucial in providing information for the reconstruction of events and creates links between persons of interest (POI), victims, a firearm and/or crime scenes [3]. Firearm investigations are split into two areas of examination: ballistics and gunshot residue (GSR) examination. Within ballistics, there are three areas that can be evaluated; internal (motions within the barrel, typically interactions within the cartridge and between the firearm and projectile), external (projectile in motion), and terminal (projectile contact with an object) [4]. Typically, an investigation will predominantly involve the examination of microscopic marks etched onto the cartridge case and projectile, as well as the performance of the projectile after it exits the muzzle. This area of analysis can link the recovered bullet or fired cartridge case to the firearm [5]. GSR analysis concentrates on the inorganic (IGSR) and organic (OGSR) particles produced during the discharge of a firearm, which settle on surrounding surfaces [6]. The detection of GSR traces on a POI or at a crime scene can establish a link with the recent discharge of a firearm [7]. The examination of GSR has been an area of interest since the early 1900s [6], with instrumental analysis in the laboratory being the standardised process for detecting these traces. During the 1990s, the American Society for Testing Materials (ASTM-E1588-20) established a standardised procedure for the analysis of IGSR [8]. Whereas, research into the analysis of OGSR via analytical instrumentation is still ongoing, with a proposed standard for this analysis recently being considered (OSAC 2022-S-0003) [9, 10].

While the laboratory analysis of IGSR is established and routine, a challenge associated with GSR is the ability of the investigator to detect and recognise this trace type at the crime scene, due to its minute size (1 – 5 μm). This indicates that the investigator collects specimens from the POI from areas known to have a high probability of GSR deposition [11]. To overcome this challenge, research has been conducted into incorporating luminescent particles into ammunition. Following the discharge of the firearm these luminescent particles have behaved similarly to GSR, and through using an alternative light source, the investigator is able to visualise them with the naked eye. Metal-organic frameworks (MOFs) have been confirmed to provide the greatest results for the visualisation of GSR since the first investigation in 2011 [12]. This concept has the potential to be a low-cost, fast, in-field method for visualising GSR, but can also aid with introducing new characteristic components (specific to GSR) and can reduce the number of specimens sent for testing in the laboratory.

1.2 Gunshot Residue

The generation of GSR particles occurs during discharge, when burnt and unburnt GSR particles are produced in a concentrated gaseous plume [13]. Once GSR exits the firearm, through the muzzle, ejection port and gaps in the frame, it solidifies and deposits onto the shooter, target and other surrounding surfaces [14, 15]. At firearm-related scenes, investigators routinely collect specimens from the POI's hands [16]. Research has indicated many factors affect the variability in GSR composition and distribution [17], including ammunition and firearm type, the distance between the shooter and the target, and the time since and activity of the shooter following firearm discharge [18, 19].

1.2.1 Composition of GSR

The type of GSR detected during analysis is primarily affected by the chemical composition of the ammunition [20-22]. To date, several reviews and studies have compiled lists outlining the inorganic [16, 21, 23] and organic components [16, 23, 24] that are present within ammunition. A recent review by Feeney et al. [16] has indicated that as modifications are made to the chemical composition of ammunition, comprehensive lists outlining the composition of GSR must be updated [16].

Ammunition, also known as a 'round', is a term used to describe a single self-contained unit, which comprises of four core components: (i) a projectile, (ii) cartridge case, (iii) propellant and (iv)

primer (*Figure 1-1*). However, depending on the manufacturer, firearm type and purpose for shooting, ammunition can be manufactured in all different calibres, shapes and materials [6].

Figure 1-1: Diagram of FEDERAL® .40 S&W ammunition.

The projectile, more commonly known as the bullet, of handgun and rifle ammunition, is a single component that exits the muzzle to penetrate the target [25]. There are considerable differences in projectile designs available, including the type of material used and physical characteristics (nose type, core/jacket and base of projectiles). Handgun and rifle projectiles consist entirely of soft metals, primarily lead or copper, and are designed with a lead core surrounded by a hard metal [3]. The projectile design depends on the ammunition application and affects the projectile's overall velocity and trajectory in flight [6]. The projectile in unjacketed ammunition is primarily composed of lead, with a thin copper coating to avoid lead fouling, which is discharged from firearms that contain low power and velocity, such as revolvers, pistols and rifles. Ammunition required for high-velocity firearms requires the addition of a jacket (semi– or full– jacketed) around the soft metal of the projectile to avoid deformation and metal stripping [6].

The cartridge case is the outer casing of either handgun or rifle ammunition and is commonly made of brass; however, steel, copper and nickel can also be used [3, 6, 26]. Regardless of the material used, the manufacturing process for each cartridge case undergoes meticulous quality control to ensure the cartridge case is strong, pliable and a reasonable weight [6]. These factors influence the GSR particles elemental composition.

1.2.1.1 *Propellant*

The propellant is located within the cartridge case and is added to ammunition to ensure the expected energy and overall velocity of the projectile is achieved [26]. It is composed of a range of organic compounds situated above the primer and below the projectile in ammunition and generates the OGSR particles (*Figure 1-1*). Although often termed 'propellant powder', the propellant is rarely observed as a powder in the cartridge case and instead is manufactured in a range of shapes (balls, discs, flakes and cylinders) and grain size [6].

As the propellant burns, the cartridge case acts as a pressure vessel [25]. Once sufficient pressure and temperatures are achieved, the casing will expand, causing the edges to press against the chamber walls [27, 28]. This action creates friction between the chamber and cartridge case allowing the projectile to dislodge from the cartridge case and travel down the barrel. The friction distributes the energy generated by the push-out forces, which is absorbed between the weapon's bolt and the barrel chamber [29, 30]. The rate at which propellant grains burn influences the pressure and energy generated and affects the distance the projectile travels, as well as the GSR distribution [14]. The burning rate of propellant is influenced by the propellant surface [6] and shape [31] and can be classified as degressive (slow), neutral (control) or progressive (fast) [32, 33].

In modern ammunition, smokeless powders contribute to the explosive fraction of propellant. Ammunition can be manufactured with three propellant types; single-, double- and triple-based propellant (*Table 1-1)* [34]. Additional additives, including stabilisers, plasticisers, flash inhibitors and lubricants, are also added to the propellant of ammunition to improve overall performance (*Table 1-2)* [25]. Depending on the ammunition, the propellant can consist of varying proportions of smokeless powders, explosives, stabilisers, plasticisers, sensitisers, flash inhibitors [35-37].

Table 1-1: Composition of propellant types [25, 34].

Propellant type	Common Ingredient	Purpose
Single-based	Nitrocellulose (NC)	Common energetic ingredient
Double-based	NC and Nitroglycerin (NG)	Flash-inhibitor Reduces flame temperature Maintains required chamber pressure
Triple-based	NC, NG and Nitroguanidine (NQ)	Removes flash Low flame temperature Low barrel erosion Longer shelf life

Table 1-2: Common additives and their purpose [25, 34].

Additive	Compound	Purpose
Stabilisers	Diphenylamine (DPA) Ethyl Centralite (EC) Methyl Centralite (MC) Resorcinol	Improve shelf-life Prohibit spontaneous decomposition
Plasticisers	Dimethyl Phthalate (DMP) Diethyl Phthalate (DEP)	Strengthens flexibility of the grains
Flash Inhibitors	2,4-dinitrotoluene (DNT)	Dilute muzzle gasses

Currently the analysis of OGSR particles does not follow published standards [9, 10]; which depending on the ammunition manufacturer and calibre, can lead to different compounds of interest being researched. An example of this is seen with compounds DPA, DNT and EC being identified as 'characteristic' OGSR [38, 39]. However, since 2018, DPA and EC were the most commonly analysed compounds, followed by a mixture of N-nitrosodiphenylamine (N-nDPA), MC, 2-nitrodiphenylamine (2-nDPA), akardite II (AK-II), 4-nitrodiphenylamine (4-nDPA) and NG [31, 33, 40-51].

1.2.1.2 Primer

The base of ammunition is loaded with a mixture of inorganic and organic chemicals, known as the primer mixture. During the act of firearm discharge, the trigger is pulled, causing the firing pin to impact with the primer cup (which contains the primer mixture), resulting in ignition [52].

Energy is transferred from the ignited primer to the propellant causing the propellant to combust. Pressure begins to build up within the cartridge, which eventually forces the projectile out of the barrel of the firearm [53]. These chemicals are released in a vaporous phase during ignition before condensing into spherical particles. The composition of the IGSR particles is mostly dependent on the type of primer used [54].

The primer mixture is placed in either a rimfire or centrefire primer cup system [25]. For rimfire ammunition, the primer mixture is built into the rim of the cartridge case base. Due to the construction of the base, this ammunition is cheaper to manufacture than centrefire ammunition [25]. Centrefire ammunition contains a separate anvil that is filled with the primer mixture and placed in the centre of the cartridge case base. Once discharged, centrefire ammunition can be reused if the cartridge case is undamaged by replacing the used anvil with a new reloaded primer cup. This is not possible in rimfire ammunition [25].

Conventional primer mixture primarily consists of explosives, oxidisers, fuels, and additives [34]. The composition of the primer mixture can vary between ammunition depending on the manufacturer, calibre of ammunition and ammunition type (rimfire vs centrefire) [6, 55]. The primary explosives in conventional primers include lead styphnate, azides and fulminates. Barium nitrate and lead dioxide are added as oxidisers, while antimony sulfide is the fuel to assist in the ignition of the primer. Primer mixture can also be found to include other additives (potassium chlorate and aluminium powder), sensitisers (tetrazene and 2,4,6-trinitrotoluene (TNT)), frictionators (ground glass and calcium silicide) and binders (gum) [34, 40, 55].

While conventional ammunition is still widely used [56], the link between lead poisoning and ammunition has been established since the 1980s [57]. Both the projectile and priming mixture may contain lead components [58]. To reduce exposure to lead and the health risks associated with conventional ammunition, the primary explosive in the primer, lead styphnate, has been replaced with diazodinitrophenol (DDNP) [40, 59]. Non-toxic ammunition (NTA) primer mixture may also contain additional elemental components including aluminium (Al), calcium (Ca), copper (Cu), gallium (Ga), silicon (Si), strontium (Sr), tin (Sn), titanium (Ti) or zinc (Zn) [54, 60]. Gadolinium (Gd) has also been added to European police-issued NTA as a taggant to eliminate some of the challenges associated with NTA GSR particles [54, 61, 62].

For the inorganic composition, ASTM International periodically updates the standard practice and highlights the data analysis and expected composition and morphology of IGSR [8]. The detection of lead (Pb), antimony (Sb) and barium (Ba) within a single particle is classified as ‘characteristic’.

Characteristic GSR particles contain a spheroid morphology with a diameter range of 0.5 – 5.0 µm, while particles 'consistent with' GSR contain irregular morphology and a diameter range of 100 µm. Each particle is categorised based on the elemental compositions detected (*Table 1-3*) [54].

Table 1-3: GSR categories according to ASTM International guidelines [8].

Ammunition Type	Characteristic GSR	Consistent with GSR	Associated with GSR
Conventional	Pb–Sb–Ba	Pb–Ba–Ca–Si Ba–Ca–Si Ba–Sb Pb–Sb Ba–Al Pb–Ba	Pb Sb Ba
NTA	Gd–Ti–Zn Ga–Cu–Sn	Ti–Zn Sr	–

1.2.2 Distribution

As most GSR particles are not visible to the naked eye, it is difficult for investigators to know the exact deposition location of residues until the specimens are analysed in the laboratory to confirm or deny the particles presence. Investigators rely on research that outlines the deposition and distribution behaviours of GSR [16], which establishes the relationship between the type of firearm used and the GSR plume distribution [63]. Depending on the firearm used, the shooter's hands, clothes, face and hair are common areas to detect GSR [64]. A study by Blakey et al. [18] focussed on investigating the spatial distribution of GSR generated from a pistol by mapping GSR quantities in 14 areas of the shooter's body, including the hands, arms, face, hair, torso and legs [18]. The highest GSR levels were detected closer to the point of ignition (shooter's hands), followed by the shooter's face, inner arms and shoulders [18].

Each firearm type is designed with identifiable features in the frame and internal mechanisms, which affect the behaviour of the GSR particles and the projectile characteristics [6]. One factor that is known to influence GSR distribution on the shooter's hands is the barrel length of the firearm [26]. Handguns (pistols and revolvers) are smaller-sized firearms with short barrels, while shoulder firearms (rifles, shotguns and machine guns) contain longer barrels [65]. Ditrich [53] evaluated the differences in GSR plumes resulting from all firearm types [53]. This study determined that the barrel length, construction of the firearm and ejection port of the firearm

affected the amount of GSR distributed onto the shooter's hands. This study highlighted that the smaller the firearm barrel length, the higher the GSR proportion settles onto the shooter's hands. An increased amount of GSR was also observed on the shooter's hands from firearms that contain gaps in the frame (revolvers). Upon generation, most GSR particles pass through the barrel and forward with the projectile, while a smaller amount of particles escape through gaps in the firearm frame [53, 66]. A study by Lucas et al. [52] also provided a statement indicating this trend was observed between different firearm types used in suicides cases; however, this observation was not supported with additional research [52]. Schwoeble and Exline [63] conducted a study observing plume patterns from several firearm types. A widespread plume was produced in handguns containing an ejection port, whereas shoulder firearms formed a compact plume [63].

The size and shape of individual GSR particles was also found to influence the distribution pattern of GSR at a crime scene. An extensive review by Blakey et al. [14] highlighted that the size of GSR particles and the environment play a significant role in the time taken for airborne particles to deposit onto a surface [14]. The deposition behaviour of GSR onto a surface was found to result from either impact or fallout deposition. Impact deposition occurs at discharge, whereas fallout deposition occurs from airborne GSR particles that settle sometime after discharge [14]. A study by Fojtášek and Kmječ [67] highlighted that the firearm type and ammunition calibre influenced the time required for GSR particles to deposit onto a surface in a still room. Airborne particles from pistols were observed to settle up to 2.5 minutes (9 mm calibre) or five minutes (7.65 mm calibre) after discharge, while particles from revolvers were found to remain airborne for up to eight minutes [67]. However, a later study by Luten et al. [68] observed airborne GSR particles in the air for up to three hours after discharge [68]. Both studies identified smaller particles took longer to deposit than larger particles [67, 68]. A study by Kara [27] developed a Boltzmann distribution principle model to determine GSR distribution based on the particle size and shape [27]. Initial studies believed that GSR particles' spherical shape depended on the solidification process of the particle post-discharge [69]. This study determined that the dimensional distribution was not random, and instead, the gaseous GSR particles move at different velocities depending on their size and direction. This distance, a GSR particle travels, is dependent on the particle velocity. Smaller GSR particles travel at faster velocities in their gaseous phases, indicating that they will travel a further distance; however, they reach equilibrium and solidify at a faster rate [27]. The distance GSR particles travel has been investigated thoroughly. As the distance travelled increases, the number of GSR particles decreases [70]; however, the number of particles observed is inconsistent [14, 71]. The chemical composition of the propellant has also been observed to affect the distance GSR particles travel. Carreras and Palma [72] were the first to

highlighted that the propellant burn rate also influences the maximum distance travelled by GSR [72]. The slower the propellant burns, the further GSR particles travel [14, 73]. Environmental factors were also observed to impact the overall distance in which particles can be detected. In an enclosed room, there is very little force causing GSR to deviate from the projectile trajectory. However, it was identified that the climatic conditions of open environments influence the amount of GSR particles observed. A comparison by Fojtášek et al. [71] of open and closed environments highlighted that GSR particles were detected at a maximum of ten and six metres, respectively [71].

Although there are several studies highlighting the deposition behaviour of traditional GSR, the general limitation of these studies is that the investigator cannot visualise the traces at the crime scene. The addition of luminescent particles to the primer or propellant would provide investigators with a greater chance of GSR recovery at the crime scene by visualising the precise location of the GSR traces.

1.2.3 GSR Analysis

The detection, collection and analysis of GSR traces are all key stages in a firearm-related investigation. GSR is a valuable trace that can provide information in the shooting scene reconstruction; however, this trace can easily be lost if not detected, preserved or collected correctly [74].

1.2.3.1 Detection of GSR

The detection of GSR at the crime scene can assist the investigator in the reconstruction of events, with the distribution pattern of the GSR predominantly inferring information regarding the direction and distance of shooting from the target [75]. To determine this, colourimetric tests are a preliminary technique applied for rapid detection of GSR at the scene [21]. In Australia, the modified Griess test (MGT) and sodium rhodizonate test (SRT) are conducted to estimate firing distance and presumptively confirm the presence of GSR. For the MGT, desensitised photographic paper is placed on the area of interest before being steam ironed. The nitrites, resulting from the burnt powder, are collected onto the photographic paper which is then sprayed with the MGT mixture (sulfanilic acid/H_2O and α-naphthol/methanol solutions) producing an orange colour change when present [3, 65, 76]. The application of SRT can be conducted through a direct approach (directly onto the item of interest) or by placing a sheet, usually filter paper, saturated in the reagent (sodium rhodizonate/ H_2O), onto the area of interest. In both applications of SRT, a colour change in the presence of divalent Pb (blue-violet to scarlet) and Ba (red-brown) particles

occurs [77]. Traditionally, both tests are conducted at the crime scene; however, MGT provides investigators the option to collect specimen at the crime scene for analysis in the laboratory. There has been a study by Werner et al. [77] who applied the SRT method to specimen post collection onto three different sampling devices. This allowed the GSR to be collected from the shooter's hand and visualised on the sampling device in the lab without interfering with Scanning Electron Microscopy Energy Dispersive X-Ray Spectroscopy (SEM-EDS) analysis [77]. Although these colourimetric tests (MGT and SRT) are still used in some countries [78], they present some disadvantages as presumptive tools. Both require the use of an extensive amount of chemicals to obtain presumptive results, and can lead to trace destruction [21, 34, 76]. The occurrence of nitrites, Pb and Ba particles in the environment (not from firearm discharge) reduces the specificity of these colourimetric tests, which has shifted their main use to distance from target estimation instead of GSR preliminary detection [19]. SRT is limited through its design of Pb detection, which is becoming less commonly encountered due to the increasing manufacture of NTA ammunition, while the challenge encountered with MGT is that it is predominantly conducted within the laboratory.

There has been movement to improve the current SRT [75, 79] and MGT [80-82] methods through adjustments or substitution of reagents made to the chemicals required. As well as additional colour tests (4-nitrosophenol, nitrous acid test and sodium borohydride test) are being evaluated for other OGSR targets (DPA, resorcinol, MC, and EC) [83]. However, the specificity of these tests for detecting GSR particles only and not GSR-like contaminants is a challenge.

The ability to visualise GSR at the crime scene through non-destructive means and without the addition of chemicals is a research area that has been gaining traction. Limited research has applied spectral imaging to GSR analysis, despite previous studies indicating its ability to detect smokeless powders [84]. Infrared hyperspectral imaging (HSI) is a non-destructive and quick tool that can capture reliable chemical information and a visual image of the GSR pattern [85]. This method allows investigators to capture the spatial and spectral representation of the GSR around an entrance hole using either a near-infrared (NIR), short-wave-infrared (SWIR) or mid-infrared (MIR) spectral camera [86]. Using HSI to distinguish between GSR specimen and background was observed to be accurate, providing target material-specific calibration was conducted [87]. With spectral imaging using IR wavelengths, a drawback to this technique is that there is no efficient processing framework to analyse the spectral data collected [87]. There have been instances in which garments will absorb IR and obscure GSR particles visualisation [88]. In each study, near infrared-hyperspectral imaging (NIR-HSI) was applied to control targets containing entrance holes.

At crime scenes where there is no obvious indication of a firearm discharge, the application of NIR-HSI can become difficult. The investigator will need to apply spectral imaging to the whole crime scene, adding a substantial amount of time to the investigation.

The combined use of alternative light sources (ALS), IR lights and filters is a concept that has also received little investigation as a screening method for GSR present at a scene [89]. Comparing a range of different wavelengths on dark fabric, it was identified that GSR particles were able to be illuminated using specific UV wavelengths and filter combinations (*Table 1-4*). Optimal fluorescence was observed using a wavelength of 440 – 450 nm combined with an "orange-coloured filter" [90] or a Tiffen Orange #21 filter [76, 91, 92]. It has been suggested that the unburnt propellant GSR particles respond to the excitation wavelength by absorbing the light [76, 90, 91]. Illuminating the GSR particles with NIR wavelengths presented varied results. Barrera et al. [90] identified contrast between the GSR and dark fabric provided mixed results ranging from good (38.4%) to poor (30.8%) to no (30.8%) visible GSR [90]. Whereas Vecellio [92] indicated the use of IR light, in conjunction with an IR camera and filter combination (695 nm or 830 nm), was an efficient tool in identifying burning, scorching and bullet wipe marks on dark fabrics [92]. Overall, Vecellio [92] identified that the use of a 450 nm ALS (identified scattered GSR particles) and IR to visualise GSR particles should be used in conjunction with each other [92]. The variation between the IR results on dark fabrics has been suggested to contribute from the interaction between the fabric type and GSR [90].

Table 1-4: Different wavelengths evaluated on dark fabric to visualise GSR. * highlights that no precise wavelength was provided.

Excitation Wavelength	Result	Reference
< 415 nm	Illuminated lint and background particles.	[76]
440 and 450 nm	Most efficient contrast.	[76, 90-92]
455 – 495 nm	Good contrast.	[76, 90]
575 nm	Camera settings were unable to capture luminescence.	[76]
> 600 nm	Low contrast between GSR and background fluorescence.	[76]
> 830 nm	Varied contrast.	[90]
IR*	Efficient contrast.	[91, 92]

Two studies decided to focus on the ability to visualise GSR particles on dark fabrics, and it was identified that the observations did not correlate between substrates. Vecellio [91] evaluated the effect of visualising GSR distribution on painted drywall using 450 nm wavelength and IR light; however, GSR particles were not able to be visualised on the drywall samples [91]. Although only one type of paint was analysed in this study, it does suggest that paint type may impact the ability to visualise GSR [91]. Husak [93] adapted the ALS and IR methods to analyse GSR particles on the skin, specifically the shooter's hand, and evaluated three ALS wavelengths [93]. At 475 nm and 480 nm, regardless of filter colour (yellow or orange), no fluorescent particles were observed. However, at 520 nm combined with an orange filter, the GRS particles (confirmed through SEM-EDS analysis) were observed as small fluorescent specks. Under the IR (850 nm) lights, black and white particles were observed on the shooter's hands. Unfortunately, the camera was unable to capture the contrast, indicating additional processing steps were required to enhance and develop the images [93]. While visualising GSR with ALS or IR lighting is not harmful to the POI, is non-destructive and does not require hazardous chemicals there are factors that require further evaluation before it is suitable for real-world application. The variability in optimal ALS or IR lighting conditions between the studies has indicated that substrate type plays a large role in the ability to visualise GSR particles. The combination of weak fluorescence of GSR particles [76] and interferences caused by different fabrics limit the functionality of this visualisation technique [90]. The angle of incidence between the light, particle and camera was also identified to impact the ability to see the particles on the shooter's hands. It has been suggested that further analytical analysis be conducted on the fluorescent, black and white particles to confirm whether they are indicative of IGSR or OGSR as a result of contamination [76, 93].

The introduction of luminescent particles to ammunition would be beneficial in removing the need for investigators to carry or apply a range of hazardous chemicals to an object or victim at the crime scene [94]. The ability to visualise the GSR presents as an alternative screening test that relies solely on the additional use of ALS for detection also eliminates the requirement of modified IR cameras at a crime scene.

1.2.3.2 Collection of GSR at the Crime Scene

Specimen collection at a crime scene is a crucial aspect of GSR analysis [21], which is continuously progressing, particularly in specimen collection methods, as highlighted in a recent Interpol review [95]. Current standardised protocols (ASTM-E1588-20) indicate that the use of carbon adhesive stubs are the most appropriate method to collect IGSR at a crime scene or on a POI [8]. However, a proposed standard for the collection and preservation of OGSR has suggested swabbing and vacuuming as two additional methods that are acceptable for use [9].

Research has compared the collection efficiency of different substrates for the collection of OGSR, including stubs, swabs, vacuum lifts and passive sampling devices (PSDs) to highlight the optimal collection technique [16, 36, 96]. Comparative studies by Reid et al. [97], Taudte et al. [37], and Gassner et al. [36] compared the efficiency between swabs and stubs, which highlighted that stubs collected a higher amount of OGSR particles [36, 37, 97]. Swabs, usually cotton or cloth, were moistened with an organic solvent before being wiped along the area of interest [37, 98]. The traces on the swab are extracted and analysed to focus on the OGSR particles present [16]. The use of stubs for GSR collection is advantageous over the other techniques, as minimal preparation is required, and sequential analysis (IGSR and OGSR) is possible with minimal specimen loss [46, 51]. A proof-of-concept study by Zuy et al. [99] hypothesised that the use of PSDs, particularly silicon wristbands, would improve specimen recovery in comparison to current sampling techniques [99]. Instead of evaluating the use of PSDs when discharging a firearm, this study placed the silicon wristband into a closed chamber along with 1.0 g pellets of 2-nDPA, DPA and EC [99]. Following mechanical detonation, the particles were extracted from the wristband for analysis via high–pressure liquid chromatography (HPLC). While DPA and EC were detected, the issue with this technique is that it can only be applied to OGSR, and the shooter must be wearing the silicon wristband at the time of shooting [99]. Reyes et al. [64] designed a nasal stub as a collection device that could perform the same way as the traditional stub and be inserted into a shooter's nose [64]. Reducing the size to 9 mm diameter, adding a stainless-steel handle for the investigator and adhering to a graphite adhesive effectively collected GSR particles [64].

Although research suggests new and alternative collection methods for different GSR types, the general challenge with GSR collection techniques has not been addressed. The research proposed still requires the investigator to sample an area blindly [98, 100]. Due to the minute size of GSR, it is usually not possible to visualise the deposition location of GSR, leaving the investigator to collect from known sample areas; hands, arms and face, hair and clothing [16]. The collection and detection of GSR traces in a controlled environment are easier to achieve than casework, where there are unknown variables, which affect the potential to detect GSR. The ability for an investigator to visualise and 'see' GSR particles would simplify the collection process, remove the possibility for collecting specimen void of GSR particles and reduces causing backlogs in the laboratory.

1.2.3.3 Instrumental Analysis

A bibliometric review by Sobreira et al. [101] indicated that GSR analysis has received extensive attention, particularly in the development of new analytical approaches to the detection these traces in the laboratory between 2006 and 2018 [101]. A large portion of the research output in the GSR area has focused on the implementation of analytical or spectroscopic techniques [95]. The preferred confirmatory route for the analysis of GSR involves the use of analytical techniques due to the improved separation and sensitivity of results.

The currently accepted procedure for GSR analysis focuses on detecting IGSR particles through SEM-EDS [49, 102, 103]. While this procedure is employed worldwide and is non-destructive, many limitations are encountered through IGSR analysis. The standard laboratory-based SEM-EDS procedure is time–consuming, taking anywhere between 4 – 10 hours, and there is no quick, field-deployable analysis [16]. For a case, depending on the number of POIs, the number of specimens analysed can be substantial, causing a bottleneck for the instrument. The other main issue encountered is NTA ammunition, which lacks the characteristic Pb, Sb and Ba particles [101]. A range of alternative analytical techniques have been assessed for NTA-specific IGSR analysis, including inductively coupled plasma mass spectrometry (ICP-MS) [98, 104-107] and laser-induced breakdown spectroscopy (LIBS) [102, 108-111]. While ICP-MS is a cost-efficient, sensitive and multi-elemental technique that provides a rapid response, it is destructive to the specimen [112, 113]. The ASTM guidelines highlight that specimen preparation required results in the loss of size, shape and particle identification information [8]. On the other hand, LIBS is receiving increasing attention for GSR analysis [111, 114, 115], as it is a non-destructive, field-deployable and rapid screening technique [116]. There are still limitations to this technique compared to SEM-EDS, including the cost of the instrument [102] and its inability to identify single GSR particles based on

characteristic morphology and elemental composition [117]. With the well-established analysis of IGSR highlighted in the ASTM-E1588 procedure [8], current research focuses on advancing OGSR analysis due to the increasing use of NTA in some countries. The use of analytical techniques, such as liquid chromatography coupled to either mass spectroscopy (LC-MS) [50] or tandem mass spectroscopy (LC-MS/MS) [44, 45, 49, 51] and gas chromatography coupled to mass spectroscopy (GC-MS) [31, 43, 108] allows for OGSR compounds to be successfully separated and identified. However, the disadvantage of these techniques is that specimen preparation often requires the specimen to be dissolved in an organic solvent and, as a result, destroyed [50]. For the detection of OGSR components, LC-MS techniques provide the most promising results; however, as research attempts to improve LC-MS sensitivity, there is an increase in background signal causing problems with interpretation of the results [50]. The use of voltammetric analyses has undergone preliminary investigation for the detection of NC components to determine shooting distance [118]. It was suggested that this method could replace the SRT method when NTA are discharged; however, further research is required to ensure analysis of all organic components in ammunition is possible [118]. There has been one study by Minzière et al. [119] that has evaluated the order of operations for analysis of IGSR (SEM-EDS) and OGSR (LC-MS/MS) in the laboratory to identify how protocols can efficiently obtain the maximum recovery of both GSR types [119]. Control tests (IGSR and OGSR analyses only) were conducted to determine a threshold for recovery before evaluating the order of operations. Both proposed protocols had their own advantages and disadvantages. The OGSR-first procedure required a modified cation extraction, which could potentially disturb the IGSR particle location on the stub, whereas the IGSR-first procedure resulted in a slight reduction of two compounds (EC and MC) [119].

Spectroscopic techniques, such as Raman [120-124] and FTIR [125-128], have successfully differentiated the spectral identification of different ammunition types. Many proposed methods are non-destructive and do not require tedious specimen preparation. The challenges associated with spectroscopic analysis are that discrimination between ammunition relies on the investigator interpretation, and visual discrimination is sometimes difficult when the presence or absence of bands is unclear [33]. Implementing a chemometric analysis to the spectral data obtained from the spectroscopic analysis could become a powerful screening tool for the classification for OGSR deriving from different ammunition [33, 124]. The disadvantage of using spectroscopic techniques is that only a small range of GSR components can be analysed, the instrument sensitivity is limited and there is no formal compound identification method [86]. X-ray fluorescence (XRF) is another non-destructive spectroscopic technique used for elemental mapping of GSR, particularly for special distribution of GSR particles on an item [129] or shooting distance determination by

detecting GSR around the entrance hole [130]. Compared to traditional techniques, XRF can screen large surface areas (such as t-shirts) to reveal elemental information regarding GSR composition from different entrance holes [131, 132]. A study by Gong et al. [133] has suggested the use of XRF to analyse the total GSR from a target to determine the ammunition type by identifying the elemental quantities detected [133].

The greatest challenge encountered with all instrumental techniques for detecting GSR is that there is no identifiable aspect that indicates that the specimen collected contained traces of GSR. This information would not be known until the analyst conducts the analysis and interprets the data. For outcomes void of GSR particles, time and chemicals are wasted. The visualisation of GSR at the crime scene would aid the investigator in collecting a positive GSR trace that could be analysed at the laboratory for further information regarding composition.

1.2.4 Interpretation

In casework, the interpretation of GSR results from a firearm-related scene provides the investigator and later court personnel with valuable information that will aid in the confirmation or rejection of a hypothesis [134, 135]. To assist the interpretation of GSR results, statistical models [136, 137] and probabilistic evaluations [138, 139] are utilised to ensure the value of the findings are captured. The evaluative reporting of GSR results has shown to be challenging, which has led to the European Network of Forensic Science Institutes (ENFSI) proposing a set of guidelines to standardise how scientists report GSR results [140].

A review on 42 closed court cases involving GSR expert testimonies between 2014 and 2017 was conducted to identify how the interpretation of GSR findings was portrayed in these proceedings [135]. It was identified that for the majority of cases the experts discussed the GSR findings correctly. However, for the cases where there was a potential for a miscarriage of justice (e.g. prosecutor's fallacy or misuse of results) it was observed that the GSR findings were incorrectly explained by the court. This study highlighted that although GSR is a marginal piece of an investigation, in some instances it was identified as the resounding findings for the case [135]. This illustrates that the investigator needs to consider factors that can challenge the interpretation of findings (e.g. contamination from GSR-like particles and transfer and persistence) [138, 141]. The ASTM guidelines developed a classification system for the characteristic IGSR elements to reduce misinterpretation (*Table 1-3*) [8]; however, false-positive errors were still observed. Romolo et al. [142] introduced a probabilistic approach using the Bayesian theorem to evaluate the detected GSR traces [142]. A critical review by Maitre et al. [141] analysed current research concerning GSR

interpretation via the Bayesian perspective. This review highlighted how the interpretation of both the source level (I) and activity level (II) [141] of GSR could provide the investigator and judicial personnel with a holistic view of the data (*Table 1-5*).

Table 1-5: Factors for consideration during interpretation for Bayesian hierarchy of propositions specific for GSR [141].

Proposition Level	Proposition questions	Important considerations
Source Level (I)	Is the trace detected on the POI GSR?	**a)** Background occurrence of GSR and GSR-like substances **b)** Link GSR to specific ammunition
Activity Level (II)	Did the POI discharge a firearm?	**a)** Transfer and persistence **b)** Activity of the person before, during and after the event
Offence Level (III)	Did the POI shoot the victim?	N/A

Another challenge encountered during the interpretation of specimen data from crime scene is that the interpretation of the proposition levels (source and activity) has previously been targeted to IGSR components. Studies by Feeney et al. [143] and Menking-Hoggatt et al. [144] focused on evaluating the source level propositions from leaded, lead-free or mixed ammunition to expand IGSR and OGSR population sets [143, 144]. Machine learning algorithms trained with the observed IGSR and OGSR particles were implemented to distinguish and classify between non-shooters (low-risk and high-risk occupational populations – GSR-like particles) and shooters (GSR particles). An observation that was identified was that the non-shooter populations contained lower detection of OGSR-like compounds than IGSR-like analytes [143]. These new interpretation systems provided updated frequencies of identifying GSR-like particles on the hands of non-shooters, which improves the ability for differentiation with GSR particles and strengthens the weight of evidence in court proceedings [143, 144]. Maitre et al. [145] approached the evaluation of activity level propositions through the use of a likelihood ratio approach using published OGSR-specific data sets [145]. The data sets [40, 44] applied to this study supported a potential cross-contamination scenario where OGSR was detected on a POI following arrest by a police officer. As a proof-of-concept investigation, Maitre et al. [145] highlighted the importance of interpreting OGSR, in conjunction with IGSR, in activity level propositions [145].

By incorporating luminescent particles into ammunition, the forensic evaluation of GSR could be strengthened, only if there is a low probability that these traces could be detected in the same specimen. For this to be possible, the luminescent particle chosen for incorporation would need to be a compound that is not naturally sourced or commonly encountered in the environment. It would also have to contain characteristic luminescent and chemical properties that distinguish it from traditional GSR and any potential environmental contamination.

1.2.4.1 Contamination

At a crime scene, investigators will only collect GSR specimens if there is an indication of a firearm discharge, which can include the presence of an entrance hole, fired cartridge case (FCC) or firearm. The evidential value of GSR as a trace is impacted by the environmental and occupational sources of 'GSR-like' particles [146]. During interpretation, contaminating sources, such as location and events before shooting and the occupation of the POIs must be considered [147, 148]. Research has suggested that the natural occurrence of GSR-like particles' in the environment has the potential to contribute to false-positive results and challenges the overall interpretation process (*Table 1-6*) [147].

Table 1-6: Possible sources for GSR-like particles in the environment for IGSR and OGSR.

IGSR			**OGSR**		
IGSR particle	**Contamination Source**	**Reference**	**OGSR particle**	**Contamination Source**	**Reference**
Pb–Sb–Ba	Airbags	[149-152]	NC	Paint, varnish and lacquers	[38]
	Brake pads	[148]			
	Fireworks	[146, 153]	NG	Pharmaceutical preparation	[141]
Pb–Ba, Ba–Ca–Si, Pb and Ba	Nail Guns	[146]	DPA	Onions, tea leaves and citrus fruit peel	[154]
Al–Ti (NTA)	Welding	[155]		Insecticides, plastic and perfume	[141]
			4–nDPA	Rubber products	[38]

Although many environmental sources can lead to false-positive GSR detection, investigators evaluate the elemental composition, frequency and morphology of the particles being detected

as a whole [148]. Three recent studies conducted in Australia [156], Europe [157] and the United Kingdom (UK) [158] have evaluated the distribution of GSR particles or GSR-like particles in the random population. In the Australian survey by Lucas et al. [156], positive detection of characteristic or consistent with IGSR particles was observed on 0.3% and 9% of the population, respectively. This study highlighted that although IGSR particles were detected, the limited number of characteristic particles indicates that they are not common in the general population [156]. A later study by Stamouli et al. [157] compiled data collected from 32 forensic laboratories in Europe, Asia and North America, of which only six positively detected characteristic IGSR. It should be noted that this study only presented data for the positive detection of characteristic IGSR particles [157]. Blakey et al. [158] evaluated the occurrence of IGSR particles on public transport (e.g. trains, taxis, hire cars, and buses) in the UK. It was identified that no characteristic IGSR particles were observed on any public transport; however, particles consistent with IGSR were detected at low levels [158].

From these studies, it can be inferred that there is a very low possibility that characteristic IGSR particles are present in the environment [156, 157]. However, the limitation of these studies is that the collected specimen's analysis focused only on the IGSR components. Conducting a similar analysis on OGSR components would have provided additional knowledge on the potential sources of contamination in random metropolitan populations. Even though it is uncommon to detect 'characteristic' or 'consistent with' GSR-like particles in the environment, the investigator needs to be cautious when interpreting GSR data to avoid false-positive results [156]. Unfortunately, there are only two compounds, MC and EC, from the OGSR components, that are manufactured solely for ammunition and are not encountered in the environment [38]. Because of this factor, the detection of centralites in a specimen reduces the possibility of environmental contamination and strengthens the probability that the GSR specimen resulted from a firearm discharge. However, without the detection of characteristic GSR particles, the likelihood of firearm discharge is low [159].

The detection of IGSR-like and OGSR-like particles in the environment is a challenge that is not easily overcome. One approach to alleviate this issue has been to include 'taggant' chemicals into the propellant composition, that are not commonly encountered in the environment. The first successful addition to manufactured ammunition, to date, is Gd particles in NTA ammunition. Since then, there has been some research in introducing alternative taggants by spiking the primer or propellant with ytterbium(III) nitrate pentahydrate ($Yb(NO_3)_3.5H_2O$) [160], samarium oxide (Sm_2O_3) and titanium oxide (TiO_2) [161], or molybdenum disulfide grease (MoS_2) [162]. If the incorporation of luminescent particles was solely applied to ammunition it could be a viable

alternative as the chemical composition would not be readily encountered in the environment. This approach to improving ammunition would also indicate that the detection of the luminescent components could not be misinterpreted as a false negative GSR finding and provide additional support to the presence of GSR.

1.2.4.2 Transfer and Persistence

Transfer and persistence are two fundamental aspects of GSR analysis that must also be considered when interpreting GSR [21]. Although there are a number of studies focusing on this area of GSR analysis, a review by Séguin et al. [163] indicated that research in this area is still necessary.

When GSR is detected on a POI, investigators must establish whether they were present during discharge or came into contact with the shooter after the fact [164]. French et al. [165] highlighted that the primary transfer of GSR occurs during discharge when GSR particles directly settle onto the shooter's hand, bystander or surface [165]. A secondary and tertiary transfer occurs when the shooter contacts another object or person. A common trend observed by investigators highlights that as the chain of transfer increased (primary > secondary > tertiary), the amount of GSR particles observed on an area decreases [42, 44, 66]. Research has determined GSR transfer three different scenarios including, shaking hands [164] or conducting an arrest [44]. However, there is an inconsistency in the reported GSR amounts detected on the secondary person post-handshake between the studies. Arndt et al. [166] observed typical OGSR peaks on the shooter's hands; however, the secondary person showed no peaks associated with discharge [166]. This secondary transferability was determined to be affected by OGSR compounds undergoing absorption into the shooter's skin and evaporation. This study also highlighted that the analytical instrument is chosen, an ion mobility spectrometer (IMS), was not sensitive enough to detect the low limits of GSR traces [166]. Gassner et al. [42] later conducted a similar transfer scenario using an LC-MS to analyse a combination of firearm and ammunition types to observe a secondary transfer rate of 9.2–20.9% [42]. Lucas et al. [167] later confirmed that the contact activity's type and length affected the transfer level. An 'arrest' scenario highlighted a transfer rate of 27% between a police officer and a POI [167]. Gassner et al. [42] and Maitre et al. [44] conducted a 'firearm handling' scenario and an 'arrest' scenario [42, 44]. Post-discharge firearm handling resulted in a higher degree of GSR transfer than arrest (40% compared to 23%) [44]. The transfer (primary or secondary) percentages were variable between shots in each study [42, 44, 166, 167]. These varied results observed among the studies highlight challenges that can arise with interpretation. If transferred, GSR particles can be observed on a bystander, leading to a false-positive error [167].

A recent study evaluated the secondary transfer of GSR particles from a shooter onto a towel after having a shower [168]. It has always been assumed that following a shower, GSR traces would be completely lost; however, Rosengarten et al. [168] highlighted that while the act of having a shower reduced the chances, it was still possible to detect a small amount of GSR traces on the POI towel [168].

Although most GSR deposits onto the shooter's hands, these traces are lost through contact with other surfaces or washing of hands over time [18, 169, 170]. The persistence of GSR on a surface depends on a range of factors, including environmental factors, skin conditions and actions of the shooter, and collection and analysis methods, which add to the literature's inconsistencies [14]. Using an ultra-high pressure-liquid chromatography-mass spectrometry (UHPLC-MS/MS) procedure, Maitre et al. [40] detected OGSR up to 4 hours post-discharge, observing the greatest decrease of particles from the hands after 2 hours [40]. Similarly, Arndt et al. [166] detected traces of OGSR up to 4 hours later [166]. A later study by Romanò et al. [54] detected IGSR compounds 6 hours later [54]. The disparity between these studies could be due to the maximum length of time evaluated, differences in ammunition type and GSR type being analysed [40, 54]. With POI's not often remaining at the scene after the crime, understanding the persistence of GSR is essential for an investigator when trying to determine the reconstruction of events [41]. The ability to visualise the transfer and persistence behaviour of GSR could provide additional information to investigators when linking a POI to a firearm or crime scene.

1.2.5 Challenges

The field of GSR detection is continually evolving, with new analysis procedures focusing on OGSR analysis development. With the known health issues associated with conventional ammunition, once NTA becomes more mainstream in manufacturing and selling, the detection of characteristic IGSR traces (specifically Pb particles) will become obsolete. While many new avenues for OGSR analysis have successfully detected the propellant's discharged components in the laboratory, some limitations are still present at a crime scene.

Regardless of ammunition types and interpretation issues, the challenge for investigators to easily visualise GSR at the crime scene indicates a need to develop a non-destructive and quick visualisation procedure. Current procedures rely on collecting potential GSR traces from either a shooter, bystander or victim; however, sometimes, these people are not known at the time. Investigators collect GSR from a surface that may or may not contain these traces, resulting in a laboratory specimen backlog [101]. The introduction of a quick visualisation technique will assist

investigators by highlighting the presence of GSR at the scene, determining the shooter and victim, and shooting location and distance. The visualisation of GSR will also aid in the accuracy of the current collection process, leading to fewer false-negative specimen collected. Visualising GSR will also add value to the interpretation at a source level and potentially at the activity level for the interpretation.

Research has incorporated luminescent complexes in the past decade by using small luminescent molecules [171] or MOFs [12, 78, 172-192]. Following discharge, the investigator can directly visualise luminescent GSR at the crime scene using an ultraviolet light source to enable practical and comfortable collection. Research has also highlighted that they do not interfere in current IGSR or OGSR analysis procedures and provide additional peak information. The addition of MOFs into GSR is advantageous as they are chemically and thermally stable, highly luminescent and can contain rare-earth elements (REE), which are not characteristic in the environment [95, 193].

1.3 Metal-Organic Frameworks

MOFs are an inorganic-organic hybrid complex composed of aggregated networks of metal cores (inorganic) coordinated to the ligands (organic). MOFs are unique complexes that are customisable, depending on the metal core and ligand components, solvents and synthetic route [194]. The coordination sites of the metal core determine whether the final MOF arrangement will be one-dimensional (1D), two-dimensional (2D) or three-dimensional (3D) [195]. A variety of MOF classes can be formed based on the hybrid nature of the complex. Luminescent MOFs can generate a visible luminescence following excitation by an external light source [196]. To date, there is an extensive amount of thorough reviews readily available, covering the different aspects of MOFs [197-203]. This literature review is not intended to be a comprehensive review and instead will focus on luminescent MOFs and their potential application to GSR.

1.3.1 Synthesis Routes

The final structural environment of a MOF is affected by the chosen synthetic route and parameters such as molar ratios, solvents, pH, reaction time, temperature and pressure [204, 205]. There are a number of synthetic routes available for the synthesis of MOFs, each with its own advantages and disadvantages. Solvothermal/hydrothermal (SH) synthesis [206-211] is the conventional synthesis route applied to generate structurally stable frameworks [204, 212, 213]. The chosen metal cores and ligands are immersed into a polar solvent in a sealed pressure reaction vessel at high temperatures above the boiling point of the solvent [214]. Microwave (MW)-assisted [215, 216] and ultrasound (US) [217, 218] synthesis are two other main synthesis routes undertaken to produce MOFs. Various other synthetic approaches have been recognised over the years, including electrochemical [219], mechanochemical [220], and ionothermal flow chemistry [221, 222] for the synthesis of MOFs. To date, the majority of research conducted on MOFs has conducted small-scale synthesis, with a critical focus on generating high-quality and stable frameworks [223].

1.3.2 Luminescent MOFs

The ability to observe the luminescence of a MOF is dependent on the components incorporated into the structural environment during synthesis. The structure must contain strong coordination bonds between the metal core and chelating ligand molecules to enhance steric hindrance and cause permanent porosity and strong luminescent emissions [196]. The environment must also exclude guest molecules from attaching to the frame [224]. The luminescence observed from

MOFs can be attributed to the electron transitions between light-emissive metal ions and organic ligands [196]. The two main electron transitions observed in MOFs are metal-based and ligand-based luminescence [225, 226], which depends on the spacing and structure of the MOF [227].

1.3.2.1 Lanthanide Metal Cores

The optimal light-emissive metal ions incorporated into LMOFs are lanthanide (Ln) ions. Ln ions are REE, consisting of 15 elements ranging from lanthanum to lutetium (^{57}Ln to ^{71}Lu). Incorporating Ln ions into high-technology industrial applications has occurred for quite some time and has since become standard practice [228, 229]. Ln ions contain variable coordination geometries and many coordination sites in the complex form, where ligands with multidentate oxygen or nitrogen components can form highly stable bonds [196]. Lanthanide MOFs are the preferred sub-class of MOFs due to their characteristically high quantum yields, ligand-induced Stokes shifts and long and sharp emission [230-232]. Lanthanide MOFs are unique luminescent complexes with a range of topological structures and optical properties that vary depending on the chosen Ln ion's coordination sphere location. Europium (Eu^{3+}) and terbium (Tb^{3+}) are the most attractive Ln metal cores for MOFs due to their distinctive intense red and green visible emissions, respectively [233, 234]. While samarium (Sm^{3+}), dysprosium (Dy^{3+}) and thulium (Tm^{3+}) do not contain a strong luminescence, it is possible to observe them in the visible range emitting orange, yellow and blue emission properties, respectively. Other Ln ions can be visualised in the ultraviolet (Gd^{3+}) or NIR (neodymium (Nd^{3+}), promethium (Pr^{3+}), holmium (Ho^{3+}) and erbium (Er^{3+}) and ytterbium (Yb^{3+})) ranges [194, 195]. The challenge with Ln ions is their forbidden *f-f* transition can cause weak light absorption.

However, when an Ln ion and a strong absorbing ligand are paired together, the metal centre luminescence is enhanced. The Ln^{3+} ion prefers large electrostatic components, such as oxygen or nitrogen-containing ligands, to generate a 3D network with a wide range of properties, including porosity, magnetism, and luminescence [235]. The advantage of using lanthanides as the metal core for MOF synthesis is that it is not encountered in the environment as an ion or within the MOF structure.

1.3.2.2 Metal-Based Luminescence

Metal-based luminescence is observed predominantly in MOFs containing lanthanide metal ions. Individually, lanthanide ions are weak light absorbers due to the Laporte forbidden 4*f*–4*f* transition [232]. The metal core luminescence is enhanced when paired with a strong absorbing ligand (antenna) [195, 230]. This process is known as the “antenna effect” and occurs when a highly π-

conjugated system absorbs the light from the metal before transferring the energy back [194, 236]. Heffern et al. [237] illustrate this antenna effect process for Lanthanide complexes and the luminescent 4*f*−4*f* transitions of Eu^{3+} and Tb^{3+} complexes [237]. The strength of the luminescence observed in lanthanide MOFs is also dependent on the lanthanide ion's vicinity and the ligand. A closed-form lanthanide MOF results in a fast energy transfer and greater luminescence due to the lanthanide ion and ligand's proximity. However, an open-form lanthanide MOF has a more considerable distance between the lanthanide ion and ligand, resulting in slower energy transfer and weaker luminescence [238].

1.3.2.3 Ligand-Based Luminescence

Alternatively, ligand-based luminescence is observed mainly in *d*-block transmission metals. The organic ligand is integral to luminescence, as aromatic or π-conjugated ligands contain the greatest ability to absorb light during excitation [239]. In MOFs that rely on ligand-based luminescence, a variety of charge transfer processes are possible, including metal–to–ligand charge transfer (MLCT), ligand–to–metal charge transfer (LMCT) and ligand–to–ligand charge transfer (LLCT) (*Table 1-7*) [196, 225].

Table 1-7: Ligand-based luminescence charge transfer processes [225, 226, 240].

Charge Transfer	Metal Core Requirements	Ligand Requirements
MLCT	Second- or third-row transition metals d^6, d^8 and d^{10} electron configurations low oxidation states	π-acceptor ligands Low-filled orbitals
LMCT	Empty or low-lying d-orbitals d^{10} electron configurations	Full molecular orbitals
LLCT	d^{10} electron configurations	Energy transfer from the excited states of one ligand to another

There have been some instances where LMCT was observed in some lanthanide MOFs when the lanthanide ion contains high electron affinity, and the ligand comprises low oxidation potential [234]. Synthesis of these MOFs is less common as it can result in non-luminescent complexes [195].

1.3.2.4 Advantages

A review by Cui et al. [230] highlighted that the isostructural performance of lanthanide MOFs is advantageous over traditional MOF structures [230]. The lanthanide ion choice controls the luminescent properties, often resulting in an intense visible luminescence, specifically for Eu^{3+} and Tb^{3+}. The number of coordinated bonds to the lanthanide ion generates long-lived narrow and characteristic emissions that improve the visible emission's colour purity [230]. Lanthanide MOFs are materials with the isostructural ability to host more than one Ln ion in the complex (mixed-metal MOFs). The additional lanthanide adds to the MOFs' unique optical features by providing a multi-emission spectrum [241]. Depending on the structural configuration, lanthanide MOFs contain a combination of porous architectures, active sites, strong water stability and high surface area within the complex. These features can lead to increased selectivity and can sense low trace detection levels [242]. Overall, lanthanide MOFs contain unique structural and optical properties, making it unusual to locate these complexes in the environment due to natural occurrence [228, 243].

1.3.3 Applications in Forensic Science

A great deal of attention has been given to MOFs in chemical (sensing, gas storage and delivery) [244-249] and medical (bioimaging) [250-254] fields. Recently the application of these complexes is being applied in various forensic research areas, including fingermark detection, explosives analysis, illicit drug detection, anticounterfeiting and gunshot residue analysis. This highlights the potential opportunity for MOF application; however, this could also lead to an issue of overuse and contamination if MOFs are found to be suitable for each forensic space.

1.3.3.1 Fingermark Detection

Fingermark detection is continually evolving, with research aiming to improve current development techniques [255-257]. Investigators must consider various factors, including fingermark composition, age, donor type, and substrate properties [258]. To date, only five research groups have focused on the potential for using MOFs as a detection method for fingermarks. These groups assessed the same MOF structure, focusing on using the same ligand (terephthalic acid, H_2BDC) and two metal cores (Ln = Eu^{3+} and Tb^{3+}) [259-262].

Liang et al. [259] was the first to investigate the potential application of thin-film luminescent MOFs on latent fingermarks [259]. This study deposited a ‘fingermark’ (commercial stamp pressed against aqueous bovine serum albumin solution) onto various surfaces, prior to immersion in a

MOF solution for 30 seconds before being washed off with deionised water. This study was able to visualise fingermarks using a 254 nm light source and indicated that the luminescent MOFs could adhere to fingermarks aged for up to two months [259]. Although the success of thin-film luminescent MOFs on latent fingermarks was highlighted, subsequent studies evaluated the method and identified issues. Moret et al. [260] observed the immersion of sebaceous-rich fingermarks for 60 seconds resulted in good luminescence; however, natural or charged fingermarks resulted in either poor-quality marks or overdevelopment, respectively [260]. The results highlighted several issues, including a lack of sensitivity and high background noise, and concerns involving the solution's inappropriate application method and stability [260]. de Jong et al. [261] observed high background noise on the aluminium foil substrates due to the MOF preference of adhering to the metal surface. Whereas it was not possible to develop fingermarks on the glass substrates due to the water-based solution washing off the hydrophilic fingermark components [261]. A comparison between the MOF methods and traditional methods (cyanoacrylate fuming, small particle reagent, basic yellow 40 and gentian violet) highlighted that the use of MOFs to develop fingermarks provided worse luminescence, reproducibility and homogenous ridge detail. Overall, it was concluded that while the application of MOFs to fingermark detection could become a viable alternative process following optimisation, the current research did not provide satisfactory results [260, 261]. Hafner et al. [262] decided to investigate which component of the fingermark the MOF was targeting specifically [262]. Ten representative compounds of sebaceous and eccrine secretion were cast onto a glass slide and immersed in a MOF solution. Palmitic acid (fatty acid substitute) was the only compound to result in a homogenous luminescent spot, highlighting that fatty acids trigger the crystallisation of MOFs on fingermarks via a biomimetic replication, and biomolecules with high solubility are crucial for the MOF growth on a fingermark [262].

Instead of using a solution-based MOF, Kumar et al. [263] evaluated the use of Zn(NDA)(AMP) (NDA = naphthalene-2,6-dicarboxylic acid and AMP = 4-aminomethyl pyridine) as a fingerprint powder substitute [263]. Under UV visualisation, a blue fluorescence identified that the MOF powder interacted with the fingermark ridges to provide great contrast. Kumar et al. [263] was the only research group to conclude that the application of MOF powder is more efficient and less time-consuming than traditional methods [263]. A mutual comment made by the other research groups and recent reviews is that MOF application as a technique for fingermark detection could benefit this discipline. However, the traditional techniques typically produce equal or better results, indicating that further research is required before this is deemed suitable [256, 264, 265].

1.3.3.2 Explosives Analysis

The detection of explosives in the air, soil, and waterways, is an essential aspect of anti-terrorism operations [266, 267]. However, the detection of the post-blast residue can be challenging as it often depends on the physical properties of the collected substrate (particulate, solution or vaporous material), as well as, the sampling and extraction technique applied to the substrate type [268]. While many methods are developed to detect explosives [269-273], explosive sensing via fluorescence quenching using water-stable MOFs is a cheaper and simpler alternative [274-278]. MOFs containing a high luminescent behaviour result in an easy-to-visualise fluorescence quench, while MOFs containing high surface areas improve the sensitivity of the technique by increasing the number of interactions with different explosive compounds [279].

Fluorescence quenching using thin-film luminescent MOFs was first introduced by Lan et al. [280], where exposure to 2,3-dimethyl-2,3-dinitrobutane (DMNB) and 2,6-dinitrotoluene (2,6-DNT) vapours resulted in fluorescence quenching of the MOF solution [280]. An advantage observed using MOFs for fluorescence quenching was that the luminescence could be returned following exposure to the vapours [280]. Since then a range of nitroaromatic and aliphatic nitro-organic compounds including, dinitrobenzene (DNB) [276, 281], 2,4-dinitrophenol (DNP) [282], 2,4-dinitrotoluene (DNT) [276, 283-287], 2,6-DNT [283], octogen (HMX) [281], nitrobenzene (NB) [276, 281, 285-289], nitromethane (NM) [289], 4-nitrophenol (NP) [281, 289, 290], nitrotoluene (NT) [276, 281, 283, 285, 287, 288, 290], 2-nitro-m-xylene (NX) [286], trimethylenetrinitramine (RDX) [281, 283], trinitroresorcinol (TNR) [284], and TNT [276, 281-285, 287, 291] have been assessed. Within the literature, 2,4,6-trinitrophenol (TNP) [274-276, 282, 284, 285, 290, 292, 293] has consistently resulted in the greatest fluorescence quench of MOFs, which can be attributed to its higher acidity and low space between the highest occupied molecular orbital and lowest unoccupied molecular orbital (HOMO-LUMO) gaps [282, 294]. Only two studies have applied this detection method to natural water environments and targeted the quenching of picric acid (PA), due to its emergence as an explosive precursor [276, 295]. Jiang et al. [276] and Majeed et al. [295] evaluated water samples from rivers and taps or rivers and lakes, respectively, to determine whether this approach could detect PA specifically. In both studies, fluorescence quenching was observed [276, 295]; however, these studies limitations are that PA can come from a range of sources [275], and there is no approach to determine its origin was from explosives.

Research suggests that MOFs could be suitable as a preliminary technique for detecting explosives due to being highly sensitive and selective; however, there are limitations in the literature associated with this detection method. There has been no research that has explored the effect

of a MOF when exposed to explosive compounds in a mixed standard. Research has focused on evaluating explosive compounds as single analyte standards. It is unknown how the fluorescence quenching mechanisms of the MOF will react and whether it will be challenging to identify what is causing the MOF to quench when multiple explosive compounds are present in a sample [266]. Additionally, the quenching of the respective MOFs can occur from a range of compounds. Traditional methods of using trained canines and modern analytical techniques remain the benchmark for explosives detection, as they are selective and accurate. However, applying MOFs for explosive detection is becoming a popular research area as it is a cheaper alternative that has the potential for in-field, pre-screening applications [268].

1.3.3.3 Illicit Drug Detection

Detection of illicit substances focuses on the use of chemosensors [296-298] and colourimetric detection kits [299, 300]. Research into the application of using MOFs to detect illicit substances in different spiked matrices (urine and saliva) via chemical sensing has increased in recent years [301]. The detection of illicit drugs in a urine matrix is more commonly researched in literature than in saliva matrices. The urine samples were spiked with varying concentrations of either benzodiazepine [302], morphine [303], or methcathinone [304]. Similarly, the saliva matrix was spiked with an amphetamine-type substance [305]. The MOF was then immersed into the sample mixture before analysis with ultraviolet (UV) radiation to measure the luminescence spectra at room temperature based on the visible quenching. In each study, the application of MOFs as a sensor for the illicit drug of interest revealed that the high adsorption affinity of the MOF resulted in an acceptable degree of luminescence sensitivity. The luminescent sensing was compared to traditional analyses and was found to have better detection of the drug at trace levels. The process was deemed to be simple and fast producing highly sensitive and accurate results [302-304].

There has also been research into the use of a surface-enhanced Raman scattering (SERS) platform [306] or electrochemical sensing of illicit drugs using MOF-based materials [307, 308]. A range of MOFs have been synthesised for the detection of cocaine [309], fentanyl [310], ketamine [311], opioids [312] and synthetic cannabinoid (RCS-4) [313]. These studies show that illicit drug detection is possible by applying MOFs for chemical adsorption, fluorescence quenching or electrochemical sensing. However, in order to identify the true potential of these method types, further assessment of real samples is required.

1.3.3.4 Anticounterfeiting

The application of MOF research has recently been applied to anticounterfeiting in a range of encoding areas, via optical tags, barcodes and banknote identification [314-316].

The use of MOFs as an optical tag has been evaluated due to their unique and complex properties. For this encoding process, the MOF is synthesised prior to suspension in either a synthetic polymer (usually polyvinyl alcohol) [317], aqueous solutions [318], incorporated into a resin solution [319] or hydrogel [320]which is then printed as an image onto a surface and allowed to cure. The MOF-embedded image is then easily visualised with a UV light source (λ_{ex} = 254 nm or 302 nm) in all suspension mediums. The advantage of using MOFs as optical tags is that different visual properties are available depending on the MOF type (single-metal, mixed-metal, multiple MOFs or MOFs containing different molar ratios). However, a limitation of these studies is that there is no indication of whether additional analysis (other than visualisation) of the ink composition would be possible, which limits the unique characteristics associated with MOFs.

Tuneable Ln-MOFs that can be developed in an epitaxial heterostructure have also been evaluated as spatially responsive multicolour photonic 'barcodes' [321]. The MOF undergoes a step-by-step assembly process that requires a thin layer of one MOF crystal seed to be deposited onto a substrate (usually glass) and allowed to grow before the addition of another MOF crystal seed [321]. The barcode can be developed as either rod-shaped or block-shaped and includes MOFs containing different metal cores [322]. For example, the rod-shaped heterostructure can be designed with a Tb-MOF centre and an Eu-MOF at either end of the rod, whereas the block-shaped heterostructure contained an inner Tb-MOF square with an Eu-MOF border [322-324]. The possibility of integrating a spectrum-based evaluation, in addition to the photoluminescent evaluation, when using MOFs as photonic barcodes was also highlighted.

A recent study by Macrino et al. [325] introduced the concept of using powdered MOFs to deal with the falsification of counterfeit banknotes [325]. The powdered MOF was deposited onto the paper-based Brazilian banknotes by outlining the respective monetary value on the surface of the note using a swab and then visualised under UV (λ_{ex} = 254nm, 312 nm and 365 nm) light. Following the successful visualisation of the MOFs, the banknote was further analysed using laser desorption ionization – mass spectrometry in positive and negative mode (LDI (±) MS) to determine the chemical profile of the banknote surface [325]. While this study highlighted the ability to use MOFs as a new security feature, it also lacked foresight into the real-world application of the proposed method. As banknotes are constantly moving, the placement of the MOF would not be suitable for long-term use. Further experimentation is required looking into how the MOF can be

incorporated into the banknote as a powder at a manufacturer level and whether the manufacturing process will affect the characteristics of the MOF presented above. It should also be noted that Brazilian currency already contains fluorescent ink located at the value of the note and in the serial number.

While the use of MOFs in the anticounterfeiting space has grown in interest and proven to be a possible alternative, there are challenges that require investigation before MOFs are a viable substitution. A review by Kumar et al. [326] highlighted a list of these challenges ranging from improving synthesis methods, developing appropriate MOFs and identifying appropriate mediums for MOF suspension [326]. Ultimately, the question remains as to whether the addition or replacement of the current security inks is required or beneficial.

1.4 Application of MOFs in GSR Visualisation

The minute size of traditional GSR has remained a challenge for investigators when locating potential GSR particles quickly at the crime scene. The concept of incorporating luminescent particles into ammunition was initially presented as a low-cost and fast method that would simplify GSR sampling at the crime scene [12]. The incorporation of luminescent particles in ammunition was considered for visualising GSR due to previous research that focused on using photoluminescence (PL) spectroscopy to detect traditional GSR [327, 328]. To determine the most appropriate marker for the visualisation of GSR, a range of luminescent particles were assessed. Lanthanide MOFs were selected as the optimal marker due to their thermal and chemical stability, high luminescent properties and unique composition [12]. Post-discharge, it was observed that MOF particles exited the muzzle with the traditional GSR, depositing on areas of interest [174]. The particles observed were coined 'luminescent GSR' (LGSR) to indicate that the collected or visual GSR contained luminescent traces [174].

In most of the research, MOFs have been the chosen luminescent particle to be incorporated into ammunition, with only one study by Parmar et al. [171] focusing on non-lanthanide small luminescent molecules. Three compounds, pyrene (Py), fluorescein (Fl) and a Pt-CNN complex (Pt = platinate), were evaluated via incorporation into the propellant powder as a solution and allowed to dry prior to reassembly and discharge. While Parmar et al. [171] was able to visualise these luminescent particles on the shooter's hands and the firearm (λ_{ex} = 375 nm), there are a few limitations with using these types of particles, specifically with commercial Py and Fl. The first limitation is that these particles are predominantly composed of purely organic components indicating that they will not be detected in the standard IGSR analysis. These commercially available particles can also be encountered in the environment at a higher likelihood than MOFs [329]. As the only synthesised particles from this study, Pt-CNN contained its own set of limitations. It consists of platinum components, which while detectable via SEM-EDS analysis, are commonly associated with metal products and known to cause environmental problems. The unique structure and inability to encounter lanthanide MOFs in the environment indicate these particles are superior to non-lanthanide small molecules. As only one study suggests an alternative to MOFs, it can be assumed that there has not been a better cost-effective or visual compound.

Since the initial evaluation, there has been a range of research on the incorporation of MOFs in ammunition, with literature focussing on three key areas of interest; novel MOF synthesis (64%), performance as LGSR (18%) and ammunition encoding (18%).

1.4.1 Novel MOFs

Most LGSR research has focused on synthesising diverse novel MOFs for incorporation into ammunition [78, 172, 173, 175, 179, 180, 183, 186]. The purpose of this research area is to synthesise better MOFS that contain improved luminescence, shorter synthesis time, reduced chemical precursors and are more cost-efficient.

The unique composition of the MOFs indicates that it is rare to detect these complexes from environmental or occupational contamination [12, 182]. Due to the endless combinations possible for MOF formation, there has been little consistency within the literature regarding which synthesised MOFs are appropriate for incorporation into ammunition. Over 20 different MOFs have been synthesised and evaluated for GSR visualisation. Three essential characteristic requirements must be considered when developing an LMOF for GSR visualisation; (i) strong luminescence, (ii) thermal stability, and (iii) chemical stability [12, 173, 175, 181, 182]. Compared to its pure form in a laboratory, literature has highlighted that the LGSR particles are not observed in clumps, so they must contain an intense luminescence to ensure observation [186]. The MOF will be exposed to high temperatures, so it must be thermally and chemically stable to ensure that it does not disintegrate during discharge and does not react with the GSR or metallic components of the firearm [12, 173]. There has been extensive research on the incorporation of MOFs with Eu^{3+} or Tb^{3+} metal cores and dipicolinic acid (H_2DPA) or trimesic acid (H_3BTC) ligands (*Table 1-8*).

Table 1-8: Metal core and ligand combinations for MOF synthesis in GSR visualisation literature.

Ln^{3+} Ion	Ligand *	Reference
Eu^{3+}	H_2BDC	[181][a]
	H_2DPA	[12, 174, 177, 181, 185][a]
	H_3BTC	[187][a] [176, 177, 181, 182, 184, 185][b] [190, 192][c]
	H_4btec	[186][c]
	Hbtfa	[191][c]
	Htta	[191][c]
	Na_2BDC	[177, 179][a] [187][b]
	$NH_2NH_2.H_2O$	[173, 174][a]
	PIC	[78][b]
	TBZ	[180][a]
Tb^{3+}	H_2DPA	[12, 174][a]
	H_4btec	[183][c]
	Na_2BDC	[179][a]
	$NH_2NH_2.H_2O$	[173, 174][a]
	TBZ	[180][a]
Dy^{3+}	H_2DPA	[175][a]
Gd^{3+}	TBZ	[180][a]
Er^{3+}, Yttrium (Y^{3+}) and Yb	NH_4VO_3	[188][a, b, c]
Eu^{3+} and Tb^{3+}	H_4btec	[189][c]
Eu^{3+} and Y^{3+}	H_3BTC	[178, 182][b]
Eu^{3+}, Sm^{3+} and Y^{3+}	H_3BTC	[182][b]
Tb^{3+} and Yb^{3+}	H_2DPA	[172][a]
	H_3BTC	[182][b, c]
Tb^{3+}, Yb^{3+} and Y^{3+}	H_3BTC	[182][b, c]

* In alphabetical order. Htta = 2-thenoyltrifluoroacetone; H_2BDC = terephthalic acid; H_4btec = 1,2,4,5-benxenetetracarboxylic acid; Hbtfa = 4,4,4-trifluoro-1-phenyl-1,3-butanedione; Na_2BDC = terephthalic acid disodium salt; $NH_2NH_2.H_2O$ = hydrazine monohydrate; NH_4VO_3 = ammonium metavanadate; PIC = picric acid; TBZ = thiabendazole. Total Metal Core. a = $Ln(NO_3)_3.xH_2O$; b = Ln_2O_3; c = $LnCl_3.xH_2O$.

1.4.1.1 MOF Composition

The synthesis and application of both single-metal MOFs and mixed-metal MOFs containing lanthanide metal cores have been encountered in LGSR literature. Single-metal MOFs containing Eu^{3+} or Tb^{3+} metal ions are preferred for incorporation into ammunition due to the large energy gap between the ground and excited states [173, 330]. An intense red colour was observed for all Eu-MOFs upon illumination with an alternative UV light source [78, 173, 186], while Tb-MOFs provided a green colour [179, 183]. For both Eu-MOFs and Tb-MOFs, the main excitation mechanism occurs through the antenna effect [225]. As an alternative MOF for incorporation into ammunition, Lucena et al. [175] synthesised a novel Dy(DPA)(HDPA) [175]. The intense yellow emission observed when excited at 395 nm results from the direct excitation of the Dy^{3+} ion (*f-f* transition) [175]. Although this MOF could contribute to ammunition encoding, the luminescence observed from this MOF does not appear as intense as Tb(DPA)(HDPA) or Eu(DPA)(HDPA). A comparative study between the three MOFs should be conducted post-discharge to determine whether LGSR detection or ammunition encoding could benefit from the incorporation of Dy-MOFs [175]. Filho et al. [180] synthesised another novel single-metal MOF containing a Gd^{3+} metal core. A comparison was conducted between the GdTBZ, TbTBZ and EuTBZ particles [180]. This study identified that the luminescence emission spectrum observed for GdTBZ resulted from the triplet state energy of the ligand (TBZ). When compared to TbTBZ and EuTBZ, which accept energy transfer from the ligand, GdTBZ did not provide any advantage as a marker and therefore was not evaluated as LGSR in this study [180]. Mixed-metal MOFs have been highlighted to offer better performance than single-metal MOFs due to containing multiple metal cores within the structure [331]. Weber et al. [172] evaluated the emission of mixed-metal MOFs containing both a Tb^{3+} and Yb^{3+} metal core. The addition of Y^{3+} and Yb^{3+} ions to accompanying metal cores (Eu^{3+}, Tb^{3+} and Sm^{3+}) is conducted because they are known to act as sensitisers and strengthen luminescence [172]. The main limitation encountered in mixed-metal MOFs is the lack of reproducibility and control of the final metal distribution in the framework, regardless of the synthesis route [332]. It is unknown how the metal cores distribute within the framework, which can affect the emission states energy transfer and cause the MOF visual luminescence to be quenched [331, 333].

In LGSR literature, the most common ligands used to synthesise MOFs contained carboxylic acids [172, 175, 179, 183, 186]. Carboxylate ions are excellent electron-withdrawing groups that readily deprotonate to coordinate metal cores [334, 335]. High-affinity ligand binding occurs with the metal core [183], which results in a complex containing a rigid structure that enhances the lanthanide luminescence through the antenna effect [336]. Ligands containing imidazolates [180], amines [173], and nitroarenes [78] were also used to synthesise MOFs (*Figure 1-2*). In the MOF

complex, these groups allow the ligand's easy binding to form multiple coordination modes with the metal core creating a rigid and stable structure [183]. Regardless of the ligand, it is challenging for an investigator to distinguish between the visible luminescence of different MOFs. Differentiation between ligands can only be conducted at the spectroscopic level (see Section 1.4.2).

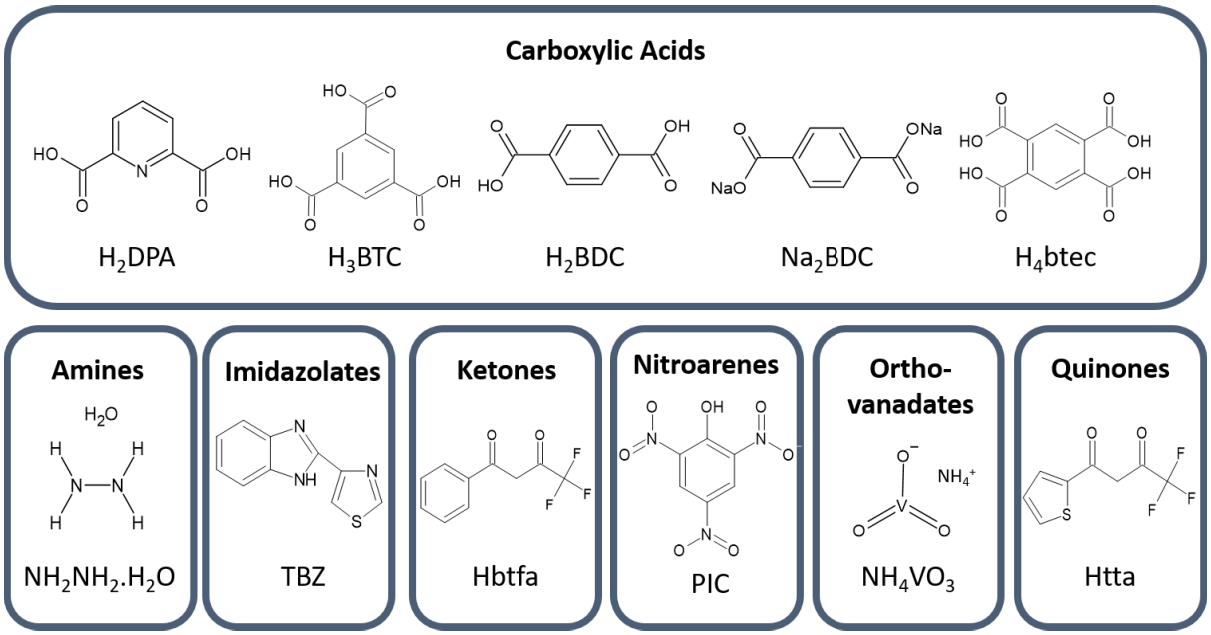

Figure 1-2: Chemical group classification of ligands used in the synthesis of MOFs that are applied in the visualisation of LGSR.

1.4.1.2 MOF Characterisation

Post-synthesis characterisation of these MOFs (*Table 1-8*) was conducted to confirm the structural and chemical properties. For this, a range of spectroscopic, elemental, physical and analytical techniques were applied to the MOF. It is interesting to highlight that among the literature, there was not one consistent characterisation technique used across the various studies conducted. The two most common characterisation methods for MOFs included photoluminescence spectroscopy and X-ray diffraction (XRD), followed closely by Fourier-transform infrared (FTIR), SEM-EDS, thermogravimetric analysis (TGA) and Raman spectroscopy (*Figure 1-3*).

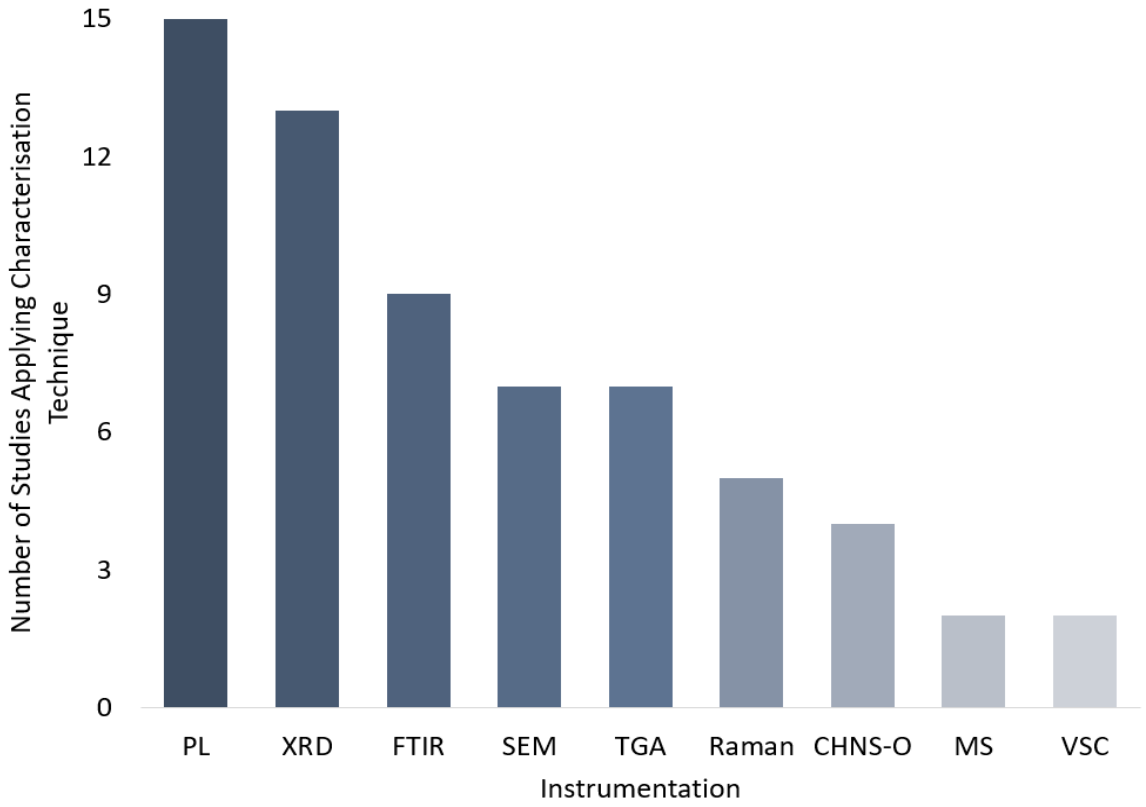

Figure 1-3: Frequency of techniques used to characterise MOFs (n = 23). CHNS-O = elemental analysis, MS = Mass Spectrometry, PL = photoluminescence and VSC = Video Spectral Comparator.

It is not surprising that photoluminescence analysis was the most common technique used for MOF characterisation as the luminescent properties of MOFs make these particles interesting for incorporation into ammunition. Using spectroscopic and visualisation techniques for characterisation is required to ensure the synthesised compound will be suitable for GSR visualisation. Photoluminescence spectroscopy can measure both the MOF excitation and emission spectrum, highlighting the characteristic peaks associated with the chosen metal core (*Table 1-9*). Eu-MOFs have been excited between a range of UV wavelengths (λ_{ex} = 291 nm and 430 nm) [12, 78] resulting in five characteristic Eu^{3+} emission peaks, regardless of ligand [179]. The most intense emission transition, $^5D_0 \rightarrow {}^7F_2$, emphasised that the MOF displays an intense red emission colour [181]. Excitation of Tb-MOFs occurred between 294 nm [12] and 355 nm [172] resulting in each emission spectrum containing four characteristic Tb^{3+} peaks [180]. Tb-MOFs associate with an intense green emission resulting from the main transition of $^5D_4 \rightarrow {}^7F_5$ [179]. Three other REE metal cores evaluated as MOFs under UV excitation conditions were Dy(DPA)(HDPA) [175], GdTBZ [180] and $Y_{0.98-x}Er_{0.02}Yb_xVO4$ [188]. Like Eu- and Tb-MOFs, the observed yellow or green luminescence from the Dy-MOF or Er-MOF, respectively, resulted from the direct excitation of the ion and correlated to all characteristic peaks [175, 188]. Unlike the

other MOFs, it was identified that the Gd-MOF luminescence was attributed to the ligand-centred transitions. This indicated that the two emission peaks observed were both related to the TBZ ligand fluorescence and phosphorescence. In both studies, these novel metal-cored MOFs were compared to Eu-MOFs and Tb-MOFs [180]. Although photoluminescence spectroscopy is a sensitive technique, the main challenge associated with this technique is instrument availability in forensic laboratories [187]. The use of a VSC was suggested as an alternative as it would achieve similar emission data and is widely used in police laboratories. The VSC could identify and characterise peaks; however, it was found to have a lower resolution than the traditional photoluminescence spectroscopy. The one advantage of using the VSC over photoluminescence spectroscopy for characterisation was that it can simultaneously capture an image of the MOF luminescence [187].

Table 1-9: Characteristic emission peaks for Eu-MOF [173, 186], Tb-MOF [179, 183], Dy-MOF [175], Gd-MOF [180] and Er-MOF [188]. ^ excited with UV wavelength. # excited at 980 nm. * represents the emission peak most responsible for luminescent colour.

^ Eu^{3+}		**^ Tb^{3+}**		**^ Dy^{3+}**		**^ Gd^{3+}**		**# Er^{3+}**	
580 nm	$^5D_0 \rightarrow {}^7F_0$	489 nm	$^5D_4 \rightarrow {}^7F_6$	483 nm*	$^6F_{9/2} \rightarrow {}^4H_{15/2}$	365 nm	$S_1 \rightarrow S_0$	526 nm*	$^2H_{11/2} \rightarrow {}^4I_{15/2}$
592 nm	$^5D_0 \rightarrow {}^7F_1$	546 nm*	$^5D_4 \rightarrow {}^7F_5$	572 nm*	$^6F_{9/2} \rightarrow {}^4H_{13/2}$	467 nm	$T_1 \rightarrow S_0$	554 nm*	$^4S_{3/2} \rightarrow {}^4I_{15/2}$
613 nm*	$^5D_0 \rightarrow {}^7F_2$	586 nm	$^5D_4 \rightarrow {}^7F_4$	659 nm*	$^6F_{9/2} \rightarrow {}^4H_{11/2}$			660 nm	$^4F_{9/2} \rightarrow {}^4I_{15/2}$
651 nm	$^5D_0 \rightarrow {}^7F_3$	622 nm	$^5D_4 \rightarrow {}^7F_3$						
694 nm	$^5D_0 \rightarrow {}^7F_4$								

Microstructural analysis of MOFs can be conducted using an array of techniques, depending on the aim of characterisation. XRD analysis focused on the size, spatial arrangement of crystal patterns and distances between crystal planes [175, 337]. FTIR and Raman spectroscopy are complementary techniques used to identify the chemical composition through the bonding arrangement of a chemical structure and vibrations [338, 339]. These techniques are highly dependent on the organic component and capture the coordination of ligand bonds [180]. SEM-EDS is a technique able to image and determine the elemental components of the MOFs. While many studies stated that SEM-EDS was applied to the pure MOF, only Lucena et al. [173] presented the results obtained from this analysis. SEM showed that the MOF ($ZnAl_{1.95}Eu_{0.05}O_4$) contained large aggregates and granulometry and was 15 μm in size, which is substantially larger than the usual size of 'characteristic' GSR particles [173]. This difference in shape and size between the

pure MOF and traditional GSR particles indicated it was adequate for addition to ammunition. The complimentary EDS data confirmed the presence of the metal core element within each particle [173]. In comparison, the LGSR was observed to retain the traditional spheroidal shape of GSR and confirm the presence of traditional elements (Pb, Sb, Ba and Tb) [12], while also observing particles and elements consistent with the MOF [179]. CHNS-O elemental analysis calculates the quantity of carbon (C), hydrogen (H), nitrogen (N), sulfur (S) and oxygen (O) elements within the structure [180]. Applying this technique, in conjunction with XRD analysis, can aid the analyst in quality control and determine the overall structure.

The implementation of a highly specific analytical instrument, a Fourier-transform ion cyclotron resonance-mass spectrometer (FT-ICR-MS), introduced a fast and powerful analytical method for LGSR analysis. Two studies characterised different MOFs to evaluate the complex MOF molecule by measuring the fragment masses and assigning molecular formulas [78, 180]. Destefani et al. [78] evaluated negative and positive electrospray ionisation (ESI) sources on an Eu-MOF. Evaluating the MOF in ESI(-)FT-ICR-MS, two observations were made [78]. This method could detect the MOF characteristic fragments in the 200 – 1200 mass-to-charge (m/z) range and free-form ligand anions at an m/z range of 200 – 250. This study did not indicate which OGSR compounds were detected or whether the pure MOF fragments were detected in the LGSR specimen [78]. Filho et al. [180] evaluated and compared an Eu-MOF and Tb-MOF in ESI(+)FT-ICR-MS mode [180]. The same three characteristic peaks were observed for both MOF complexes and differed in m/z ratio depending on the lanthanide mass. This indicated that the nitrogen from the ligand stabilised the MOF complex. The presence of the metal core generated characteristic signal identification, specific for Tb^{3+} and Eu^{3+} metal ions [180].

The majority of research on incorporating luminescent particles into ammunition has revolved around developing a novel, low-cost, fast-synthesis and highly luminescent MOF. The characterisation methods applied to the vast range of novel MOFs, while inconsistent, do indicate that a range of analysis techniques can be applied to characterisation before incorporation into ammunition.

1.4.1.3 LGSR Visualisation and Analysis

Following the synthesis and characterisation of each novel MOF, a proof-of-concept study was conducted to ensure that the corresponding LGSR is visible on the shooter's hands and firearm post-discharge. The visualisation of LGSR has been successfully shown in the literature using a UV light source (*Table 1-10*).

Table 1-10: Wavelengths applied to literature focusing on the synthesis of novel LGSR on different objects in the literature.

Visualisation Wavelength (nm)	Category	LGSR Deposition Areas Visualised	Reference
254	UVC	Firearm; FCC; Floor (≤ 12.5 m); Shooter's hands, Clothes and face; Target (≤ 120 cm)	[172, 173, 175, 176, 179, 180, 186, 188, 190, 340]
380 – 395	UVA	Firearm; FCC; Floor (≤ 60 cm); Shooter's hands; Target (≤ 60 cm	[78, 189, 191]
980	IR	GSR Stub	[188]
Not defined	-	Firearm; Shooter's hands; Target	[12]

A large portion of research has focused on visualising LGSR via shortwave UVC radiation (254 nm). The limitation of this wavelength is that GSR primarily deposits on the shooter's hands, and UVC radiation is not ideal as it can damage or degrade DNA, even in small doses [341, 342]. There has been a growing interest in the use of UVA wavelengths for evaluating LGSR particles [78, 189, 191]. The application of a light source fitted with a UVA lamp would be beneficial for investigators to visualise LGSR at crime scenes and will minimise the potential risk of adverse health effects to a POI's hands during exposure. In a non-forensic context, UVA radiation (365 nm) is encountered by a subpopulation predominantly through the use of commercial nail lamps [343]. A comparison can be made between these commercial nail lamps and an ALS system due to the similar wavelength and power of the light source and the primary location of UV illumination of the skin. Studies have assessed multiple UV nail lamps fitted with a range of wavelengths (365 – 405 nm) and power (2 – 50W) [344, 345], highlighting the risk for carcinogenesis mutation of the DNA is minor if the exposure time is limited. Although the application of UVC radiation provides sufficient illumination of current MOFs and LGSR particles, future studies should consider using UVA radiation to reduce the possibility of causing unnecessary health effects to POIs and the investigator during the investigation.

1.4.2 Ammunition Encoding

Following the successful application and visualisation of LGSR, the research perspective shifted to synthesising novel MOFs with different chemical compositions. As the generation of novel MOFs

grew, encoding different ammunition types based on ammunition manufacturer, calibre or target user (e.g. law enforcement, civilian and military) was proposed [12, 187]. The combination of non-destructive spectroscopic and chemical data can infer the chemical composition of the LGSR particles. 'Ammunition encoding' would allow investigators to track the ammunition origin when multiple shooters were involved, based on the chemical composition of the LGSR [173]. With a predominant quantity of studies evaluating Eu- or Tb-MOF incorporation into ammunition, chemometric analysis has been investigated to determine whether ammunition encoding would be possible for MOFs with the same metal core but different ligands. Initial studies indicated it was possible to observe a difference in luminescent intensity between MOF visibly [174]. However, it became clear that the visual distinction of the LGSR is complicated and dependent on several factors, including synthetic route, the concentration of metal core to the ligand, and is subjective to the investigator [177].

Three studies have since evaluated the ability to differentiate between Eu-MOFs with either an H_3BTC, H_2BDC or H_2DPA ligand using NIR-HSI [181], fluorescence and Raman spectroscopy [185] or VSC [187]. Preliminary observations from the studies indicated that each complex had the same luminescent colour and similar emission spectra, regardless of the ligand. Albino de Carvalho et al. [181] applied NIR-HSI analysis on Eu(BTC), Eu(DPA) and Eu(BDC) to determine the ability of differentiation between the three ligand types [181]. NIR-HSI was chosen as the analysis technique as it can visualise the chemical components in a specimen; however, the cost of the instrument and the complexity of the spectral data discourage the use of this technique [346]. Of the specimen tested, 16% were either misidentified or not detected. The study encountered misidentification between Eu(BDC) and Eu(BTC) due to the overlapping band peaks in the 2000-2500 cm^{-1} range, leading to the suggestion that H_3BTC not be used as an encoding ligand [181]. This overlap should be expected because both H_2BDC and H_3BTC contain similar structures composed of a benzene ring with carboxylic acids (two and three, respectively), leading to the generation of similar peaks. Albino de Carvalho et al. [181] highlighted that the technique was efficient for the differentiation of MOFs; however, indicated that the incorrect identification of MOFs containing BTC ligands encountered would need to be addressed and optimised [181]. The collection device, presence of GSR and selection of regions of interest (ROI) each impacted the differentiation of the LGSR. Among the different collection devices, masking tape presented with the least amount of background disruption; however, it still caused spectral overlap with the LGSR, affecting the detection of peaks specific to the MOF. The additional presence of OGSR compounds caused a high NIR uptake, which further affected this technique's ability to detect and classify LGSR peaks [181]. Successful NIR-HSI highly depends on the size of the particle being analysed

[346]. From the images highlighting the ROI on the masking tape, there are instances where only small particles are present on the specimen. The smaller particles provided a low signal-to-noise ratio due to the NIR radiation penetrating more of the masking tape than the LGSR [181].

Two follow-up studies by Carneiro et al. [185, 187] stated that the above research presented a range of drawbacks, which could be addressed using other spectroscopic techniques, particularly luminescence and Raman spectroscopy [185] and VSC [187]. It was hypothesised that the chemical environment of the Eu^{3+} ion would provide distinguishable spectral profiles and relative intensities of the transition peaks. Manual examination of the data highlighted the difficulty in observing variation between the spectra due to similarity in peak profiles. Further analysis via principal component analysis (PCA) or partial least squares discriminant analysis (PLS-DA) resulted in misidentification of the specimen. A spectral variation in the Raman spectra caused misidentification of Eu(DPA), producing a false-negative result. It is unknown whether this variation occurred in some or all the Eu(DPA) specimen; however, further investigation into this MOF is required to ensure that it is thermally and structurally stable. Similar to NIR-HSI, during the normal Raman spectroscopy analysis, background interference peaks were observed from the carbon adhesive stubs and the OGSR components affecting the MOF peaks' detection. A midlevel data-fusion of the PCA and PLS-DA scores was applied to improve the ligands' differentiation. It was highlighted that because the misidentification problems encountered in the individual PCA and PLS-DA analyses resulted from different aspects of the spectra, the data fusion was able to combine the data to provide 100% correct classification for all specimens. Although these techniques would generate an arduous quantity of data for the investigator, the development of a multivariate analysis technique and LGSR reference library would reduce investigators' manual work. Carneiro et al. [185] stated that the advantage of using luminescence over NIR-HSI was that the substrate and OGSR components did not affect the spectra of the MOF [185]. The VSC provided luminescent spectra with low resolution and high spectral noise, suppressing two of the four characteristic bands. Regardless of this interference, the study indicated that the intensity ratio of $^5D_0 \rightarrow {}^7F_1$ and $^5D_0 \rightarrow {}^7F_2$ (for Eu-MOFs) could supply essential information about the metal core's chemical environment. The wide availability of VSC instrumentation in forensic laboratories makes the use of luminescence analysis useful for LGSR [187].

A different approach to ammunition encoding was encountered in Lucena et al. [182] presented mixed-metal MOFs as an ammunition encoding system [182]. This study decided to keep the same ligand among each synthesised MOF, and instead, introduced different molar ratios for different MOFs. By incorporating different concentrations of Eu^{3+}, Tb^{3+}, Sm^{3+}, Y^{3+} and Yb^{3+} ions into the MOF

structure, as chemical 'barcodes', investigators hypothesised that they would be able to distinguish between MOFs. This study highlighted that the combined use of a VSC and SEM-EDS was able to successfully differentiate 87.5% of the MOFs based on the unique lanthanide components [182]. The limitation with this study is the distribution of the different metals within the framework between different synthesis batches [331-333]. Further investigation into the differentiation of the mixed-metal MOFs containing varying concentrations of the Ln^{3+} ions would benefit this field.

While there was the occurrence of misidentification among the MOFs in each study, combining techniques in a data-fusion analysis could provide optimal differentiation between the ligands [185]. While the aim of incorporating MOFs into ammunition is to illuminate GSR traces, the ability for investigators to distinguish between ammunition present at a crime scene can strengthen the hypothesis regarding who discharged the firearm. To date, only three MOFs have been evaluated; however, all novel MOFs need to be exposed to this chemometric analysis for a more comprehensive evaluation.

1.4.3 Performance as LGSR

Most studies have highlighted the ability for their specific MOF to be visualised with UV wavelengths and applied for LGSR visualisation on the shooter's hand, firearm or FCC (*Table 1-11*). However, there have been minimal studies that further evaluate the effect these MOFs have on the behaviour of the GSR, ammunition or firearm. The introduction of LGSR in to the propellant may inhibit the reaction by reducing the gas and pressure production required to propel the projectile. The impact this mass difference will have on the ballistics and behaviour of GSR should be a priority for research. However, only five studies have evaluated the performance of LGSR beyond the ability for visualisation (*Table 1-11*) [174, 177, 178, 184, 192].

Table 1-11: Current research evaluation of LGSR.

Research Subject	MOF Ratio (wt%)	Forensic Relevance	Reference
Visualisation	2-10	Visualise deposition of LGSR	[12, 78, 172-192]
Dispersion	2 or 5	Shooter position and distance determination	[174, 177, 178]
	10	Pistol Type Identification	[177]
Transfer and Persistence	2, 5 or 10	Illustrate link between firearm, crime scene and POI	[174, 177, 184]
Other	2, 5 and 10	Bullet speed Shooting failure	[174]
	5	Blood Interference	[177]
	10	Fabric Colour Interference	[184]
	10	New GSR Analysis	[192]

1.4.3.1 Dispersion of LGSR

The dispersion of traditional GSR can reconstruct the scene. The shooting distance and position estimation are most straightforward when an FCC, projectile or entrance hole is present at the crime scene. Given the opportunity to visualise LGSR, shooter position and distance determination may become easier for investigators by observing a dispersive pattern on the floor or around the entrance hole.

Weber et al. [174] was the only study to assess the dispersion pattern of LGSR during a drive-by shooting scenario. Three situations were evaluated; (i) shooting from within the vehicle, (ii) shooting from outside the vehicle, and (iii) shooting a windscreen. When the shooter discharged the firearm from within the vehicle, LGSR particles were visualised within the vehicle, on the door, and on the front seats. Whereas discharging the firearm from outside the vehicle resulted in a reduced abundance of LGSR observed on the front seats. Overall, the visualisation of LGSR made it easier for investigators to locate the trace, determine if the hole resulted from firearm discharge and identify the shooter's position [174].

Arouca et al. [177] and Lucena et al. [178] evaluated the dispersion of LGSR at a muzzle to target distances of 0.06 – 1.2 m and 0.1 – 8 m, respectively, with both studies observing similar trends. The trigger point contained a concentrated abundance of LGSR particles on the floor, making it

easy for investigators to identify the shooter's position. However, as the distance increased away from the point of ignition, the reduction of LGSR on the floor caused difficulties in evaluating the distance. However, the associated bullet wipe was visible on all targets at each distance, indicating the possibility of determining shooting distance by visualising the projectile entrance holes at greater distances. The dispersion of the LGSR around the entrance hole indicated that the abundance of LGSR particles reduced as the distance from target increased. The visualisation of the bullet wipe pattern to determine the projectile's trajectory and shot angle [177, 178]. To verify the efficiency of using LGSR to determine the shooter position and distance, Arouca et al. [177] implemented a blind testing study. Post-discharge, an analyst investigated either the shooting room or a target using only a UV light source (λ = 254 nm). In 100% of the scenarios, the analyst was able to identify the shooter's distance and position, highlighting that visualising the LGSR dispersion pattern could aid investigators during event reconstruction at an indoor firearm-related crime scene. An investigation into the influence of six different pistol types on LGSR dispersion onto a shooter was also conducted. While LGSR visualisation on the shooter's hands was positive for all firearms, investigators could not distinguish between individual pistol types. In pistols with an exposed hammer, LGSR was visualised on the shooter's face and chest, while the Glock pistols confined the LGSR dispersion to the shooter's hands, ejection port and trigger gap [177].

Within the literature, the ability to visualise LGSR on the shooter's hands, regardless of firearm and ammunition combination has been demonstrated to be an easy process. However, two studies highlighted a lack of LGSR particles dispersing onto the shooter's hands [183, 186]. Silva et al. [183] and Júnior et al. [186] synthesised Tb(Hbtec) and Eu(Hbtec), respectively. The data collected from the MOFs, pre-discharge, indicated suitability for incorporation into ammunition due to the high luminescence and thermal stability. LGSR particles were only visualised on the muzzle of the firearm, FCC, and the range floor. The investigators hypothesised that the inability to visualise LGSR dispersion on the shooter's hands could be attributed to the pistol type. Both studies evaluated 0.40 pistols (Imbel, MD7) and CBC (Companhia Brasileira de Cartuchos) ammunition, which varied from the previously used Glock 19 and Luger ammunition combination. The slightly longer barrel length on the Imbel models could cause most LGSR particles to expel forward with the projectile and not deposit onto the shooter's hands [183, 186]. A limitation of these studies was that GSR specimens were not collected or analysed from these discharges to indicate whether traditional GSR was deposited onto the shooter's hands from this firearm type. This supplementary information for investigators would identify whether the lack of visualisation correlated to a lack of traditional GSR particles.

1.4.3.2 Transfer and Persistence

Due to the ease of GSR transfer and persistence, when recovered particles are characteristic and consistent with GSR from a POI, an investigator must consider whether that person was the shooter, a bystander present at the crime scene or someone present after the fact [14, 164].

Weber et al. [174] was the only study to evaluate the persistence of Eu-LGSR on a shooter's hands after washing [174]. The hands were examined directly after discharge and again hourly after washing their hands with soap and water. LGSR was observed to be quite resistant to the hand washing process and could be detected on the shooter's hand for up to 9 washes (9 hours). This data was compared to a shooter who did not wash their hands post-discharge, where it was discovered that particles could be seen up to 10 hours post-discharge, indicating that the LGSR exists for a reasonable period. A qualitative analysis on the ability for secondary transfer was also conducted between the shooter's hands and ordinary objects (e.g. folding knife, watch, badge and book cover), which saw a successful transfer of particles to each item [174]. The limitation of this study was that investigators focused on the visualisation capability of the LGSR particles and did not indicate any collection or analysis of the GSR from the shooter's hands. Comparing the GSR traces (conventional and incorporated) provides information regarding the quantitative dispersion and differences between the GSR type behaviours.

Arouca et al. [177] later conducted a quantitative analysis on the transfer of LGSR between individuals. Following discharge, the shooter shook hands with a secondary individual, who shook hands with a tertiary individual. Visualisation of LGSR particles was only possible with the shooter's hands. However, following collection with the carbon adhesive stubs, LGSR particles were found on all three individuals. As expected, the shooter contained the highest number of particles, with this number decreasing along the chain. While this study concluded that secondary and tertiary transfer is possible and can be used to distinguish between primary transfer and further transfer, caution should be taken with interpretation. The variations could be influenced by many factors, such as skin type and sweat. An additional evaluation was conducted to assess the adhesion strength of LGSR particles on cotton by shaking the target surface to simulate movement. This was the first study to indicate the considerable variation between replicates in (i) the total amount of LGSR particles (sum of particles in primary, secondary and tertiary transfer) and (ii) the number of transferred LGSR particles. A comparison was made with the targets before and after they were disturbed. The investigators indicated no difference in the dispersion pattern of LGSR post-shaking, indicating good quality adhesion to cotton [177].

In a later study, Arouca et al. [184] evaluated the effect of different fabrics on the persistence of LGSR, both visually (VSC) and qualitatively (SEM-EDS) [184]. Preliminary assessment of the materials observed that fabric with low sheddability (leather and polyester) contained a higher percentage of LGSR than cotton and denim. The number of LGSR particles visible on the different fabric types was not observed to be impacted by shaking action; however, the quantitative analysis highlighted high variability between the replicate shots. This inconsistency could result from either the fabric fibres saturating the carbon tapes, making detection on the SEM-EDS challenging, or from the target move to the VSC in which particles could be lost. During the comparison between post-discharge and post-shaking, there were several instances where particles were not lost but instead gained [184]. This was not addressed in the study; however, it establishes a potential for cross-contamination between samples and should be reassessed to ensure this is not a trend.

1.4.3.3 Other Factors Evaluated

To date, Weber et al. [174] has been the only study to address the effect MOFs have on the ballistics aspect of forensic firearm investigation [174]. Bullet speed and automatic cartridge case ejection were evaluated using ammunition incorporated with 2, 5 and 10 wt% of MOF. It was evident that as the ratio of MOF increased, the overall shooting efficiency decreased. At the maximum ratio (10 wt%), optimal visualisation was observed; however, bullet speed was recorded to be 25% slower, and cartridge cases were no longer ejecting automatically from the firearm (shooting failure). At 2 wt% incorporation, bullet speed was not affected, and the failure rate was classed as 'negligible'; however, fewer LGSR particles were visualised. This indicated that the addition of 10 wt% to the propellant would negatively affect the pressure build-up [174]; however, since this study, there have been numerous examples where 10 wt% have been evaluated without indication of shooting failure. Further assessment into the behaviour of the projectile to ensure the performance of the projectile is not affected is required.

There has been limited research highlighting the effects of possible interfering matrices on LGSR visualisation. Because it is common to observe biological specimens (particularly blood) at a firearm-related crime scene, Arouca et al. [177] evaluated whether the presence of blood would affect the visualisation of LGSR [177]. GSR patterns are often masked by the presence of blood [94]. Following VSC analysis, no noticeable changes could be observed in the luminescence of the LGSR, indicating that investigators could visualise this trace in blood. However, difficulties were encountered when investigators attempted to collect LGSR from dried blood for analytical analysis as the particles became 'glued' to the fabric [177]. A later study by Arouca et al. [184] investigated

the influence of fabric colour on visualising LGSR [184]. Red and white cotton fabrics were assessed due to the luminescent colour of the Eu metal core and the natural luminescence of the optical brighteners', respectively. The application of UV light (λ = 254 nm) found that the visualisation of the LGSR was easier on the red fabric, even though it was the same colour as the particles. Although visualisation of the particles was possible on the white fabric, the contrast between the red luminescence of the LGSR and the self-luminescence of the white background made visualisation challenging [184].

A recent study by Chedid et al. [192] approached the application of LGSR for GSR analysis differently from the previous literature. Instead of identifying how the addition of the MOF affected the LGSR behaviour, Chedid et al. [192] aimed to implement a new technique that could detect both IGSR and LGSR components concurrently. $(Eu_2Zr)(btc)_3(Hbtc)_{0.5}.6H_2O$ MOFs were incorporated into the ammunition so that the LGSR could be visualised with a UV light source prior to collection and subsequent GSR analysis through electrochemical detection [192]. Squarewave voltammetry (SWV) was chosen as the detection technique due to the ease of identifying trivalent (Eu^{3+}) complexes. To collect the LGSR specimens, a carbon paste working electrode was pressed against the shooter's hands and firearm before being voltammetric analysis was initiated using a KCl solution (supporting electrolytes). The voltogram results were able to detect traces of IGSR and OGSR particles and distinguish between these conventional GSR particles and LGSR particle peaks. Overall, Chedid et al. [192] suggested that SWV is a more cost-effective and sensitive method to traditional analysis and, when used in conjunction with SEM-EDS, can provide complementary results to aid interpretation [192]. While this technique indicates that LGSR analysis is possible, further validation and standardisation of the method and tools for this technique are required.

Considering each study took place in a controlled environment (indoors, dark surroundings, no environmental factors), the observation of variability in the number of LGSR particles is problematic and needs to be addressed. Successful visualisation of LGSR assists investigators in locating GSR particles for collection and instrumental analysis. However, the inconsistent variables (firearm and ammunition type, type of MOF, MOF ratio and camera parameters) between the available literature prohibits accumulating and comparing the performance of LGSR. A holistic, large-scale comparison would be beneficial to determine which complexes are most suitable for additional research focus. For this to occur, the visualisation wavelength, the ratio of MOF incorporation, the behaviour of GSR, cost of MOF manufacturing, safety and toxicity of MOF, and the effect of MOF on internal ballistics must be assessed for all novel MOFs.

1.5 Project Aims

The application of MOFs into ammunition for the visualisation of LGSR has been evaluated to be a viable preliminary technique in GSR analysis [12, 78, 172-192]. The application of MOFs in firearm-related cases can substantially improve the investigators' ability to visualise the particles for collection, can provide support for the interpretation of the results and subsequently assist the likelihood of one proposition over an alternative proposition. Although there is a wide range of current research available, this concept of incorporating ammunition with luminescent particles is still considered experimental [193]. The ability to visualise these LGSR particles has been well documented; however, a better understanding of MOF behaviour both prior to incorporation and post-discharge is required. With the aim that ammunition will eventually be manufactured with incorporated MOF, further research is required to highlight aspects that have not been considered for all MOFs [176, 347].

The overall aim of this project was to investigate the behaviour of MOFs and their ability to improve the overall effectiveness of the GSR examination. This will provide insight into the appropriateness of introducing additional chemical components into ammunition at a manufacturer level. In order to accomplish this overall aim, the project was split up into two chapters; Chapter 2 focused on the synthesis, characterisation and stability of the MOF (first and second objective) and Chapter 3 focused on the behaviour of the MOF during post-discharge (third and fourth objective).

The first objective was to synthesise and characterise a novel MOF that had not been considered previously in the application of visualising LGSR. The synthesis of novel MOFs has predominantly focused on evaluating different ligands, with minimal opportunities to explore a change to the chosen metal core from Eu^{3+} or Tb^{3+} ions. The need to identify whether alternative metal cores can be introduced as a novel MOF is important as it can assist with building a list of suitable options for ammunition encoding. It also provides additional information into whether there is a more cost-efficient, highly luminescent MOF that has not been considered yet.

The second objective was to identify the stability of the MOFs to ensure that they would be able to retain their chemical and luminescent properties over an extended time period. The longevity of these MOFs is a factor that has not been researched or considered within the literature. The stability of the MOF highlights whether it would be suitable in a long-term situation, especially considering the potential shelf-life of traditional ammunition.

The third objective was to identify the optimal ratio for incorporation into ammunition that would provide the best visual observation of the LGSR distribution. Literature has indicated that not all MOFs behave the same way and often require different incorporation ratios to work at optimum conditions. The considerations for the differences between incorporation ratios has not been addressed; however, could infer if differences in the chemical structure or morphology affect the ability to visualise LGSR.

The fourth objective focused on the performance of the projectile by evaluating the velocity, accuracy and precision. There has been little research into the impact the addition of MOFs has on the discharge process, which has the potential to affect the behaviour of the projectile. This area of research requires additional investigation to ensure that the MOF is not impacting the performance (e.g. safety of shooter and bystanders, as well as scene reconstruction). Understanding the effect that the additional MOF has on the ammunition and projectile behaviour expands the knowledge about LGSR and suggests its suitability in a real-world environment.

This page was left intentionally blank

Chapter 2. Synthesis, Characterisation and Stability of Metal-Organic Frameworks

2.1 Introduction

Research outlining the applicability of MOFs for GSR visualisation is a growing field, the increasing number of MOFs being synthesised for LGSR analysis provides the opportunity to incorporate different MOFs into different ammunition types or manufacturers. This can assist investigators in differentiating between the type of LGSR deposited on a POI, police officer or at a crime scene, through chemical, structural or luminescent properties [181, 182, 185, 187]. The limitation of LGSR studies is that they have predominantly synthesised MOFs with either Tb^{3+} or Eu^{3+} as the metal core [173, 179, 181], with only three studies evaluating MOFs with other metal cores; Dy^{3+} [175], Gd^{3+} [180] and Er^{3+} [188] (*Table 2-1*). This limits the potential to expand on the number of MOFs suitable for incorporation into ammunition, with few suggestions as to why other metal cores have yet to be explored for LGSR visualisation. Another aspect of MOF synthesis that has yet to be compared in LGSR literature is the effect of the chosen synthetic route on the production of LGSR. The synthetic route and reaction conditions are known to affect the size of the MOF [348], which could affect its behaviour during the firearm discharge process. To date, only SH and MW-assisted routes have been used to synthesise MOFs generated for the purpose of incorporation into ammunition (*Table 2-1*).

Table 2-1: MOFs previously synthesised for incorporation into ammunition. Listed in order of synthesis time.

Synthetic Route	MOF	Synthesis Parameters		Reference
		Time	Temperature	
SH	$ZnAl_2EuO_4$ $ZnAl_2TbO_4$	Unknown	100 – 480°C	[173, 174]
	$Eu_2(BDC)_3(H_2O)_4$ $Tb_2(BDC)_3(H_2O)_4$	30 minutes	RT	[179]
	$Eu(BTC)(H_2O)$	1 hour	RT	[181]
	Eu(TBZ) Tb(TBZ) Gd(TBZ)	2 hours	Unknown	[180]
	$YVO_4:Er^{3+},Yb^{3+}$	> 9 hours	80°C – 1100°C	[188]
	$Eu(btfa)_3(\varepsilon\text{-cap})(H_2O)$ $Eu(tta)_3(\varepsilon\text{-cap})(H_2O)$	12 hours	RT	[191]
	$Eu(BDC)(H_2O)_2$	12 hours	140°C	[181]
	$(Eu_2Zr)(btc)_3(Hbtc)_{0.5}.6H_2O$	24 hours	120°C	[192]
	$Eu_{0.1}Tb_{0.9}(Hbtec)$	24 hours	185°C	[189]
	$Eu(PIC)_3(NMK)_3$	~ 27 hours	100°C	[78]
	$(Eu_2Zr)(btc)_3(Hbtc)_{0.5}.6H_2O$	30 hours	120°C (24 hours) RT (6 hours)	[190]
	Tb(Hbtec)	72 hours	185°C	[183]
	Eu(Hbtec)	72 hours	185°C	[186]
	Dy(DPA)(HDPA)	120 hours	150°C	[175]
MW	Eu(DPA)(HDPA) Tb(DPA)(HDPA)	10 minutes	160°C	[12, 174, 181]
	TbYb(DPA)(HDPA)	10 minutes	160°C	[172]
	Eu(BTC)	10 minutes	160°C	[177]
		20 minutes	150°C	[176, 185, 187]
		20 minutes	160°C	[184]
	$Eu_2(BDC)_3(H_2O)_2$ Eu(DPA)(HDPA)	20 minutes	160°C	[177, 185, 187]
	YEu(BTC) YYbTb(BTC)	20 minutes	150°C	[178]
	YLn(BTC) Ln = Eu^{3+}, Sm^{3+}, Tb^{3+} and/or Yb^{3+}	20 minutes	150°C	[182]

Traditionally, MOF synthesis has been conducted through the application of SH synthetic routes and is still widely used today [349-351]. However, a movement in MOF synthesis highlights that

the MW-assisted synthesis route will eventually replace conventional SH synthesis as the preferred route [352]. This is evident through the growing limitations encountered in SH synthesis that can be avoided through the use of the MW-assisted synthetic route (*Table 2-2*). For SH reactions, synthesis occurs in a closed system and is held at a steady temperature and static conditions to allow for nucleation and formation of MOF crystals. The conductive heating involved in SH synthesis is slow due to the constant transfer of heat from the external source to an intermediate vessel and finally to the solvent. This results in non-uniform heating of the solvent as the solution is heated layer by layer [353]. MW-assisted synthesis is much faster as the radiation does not need to interact with the vessel and instead immediately reacts with the solution by causing dipole rotation of polar molecules. The energy passes through the PTFE and glass substrates of the reaction vessel to directly interact with the polar compounds. The energy is absorbed by the solvents and causes the molecules to constantly rotate and align to generate heat from multiple areas in the solution [354]. This rotation generates bulk heating, causing the temperature of the reaction to be reached faster [355].

Table 2-2: Advantages and limitations of SH and MW-assisted synthesis methods. * dependent on MW system.

	Advantages	**Reference**
SH Synthesis	Allows flexibility with solvents used	[203, 356]
	Well-known synthetic route	[203, 204, 221, 356]
	Limitations	
	Time-consuming process (hours/days/weeks)	[221, 352, 356, 357]
	Heavy energy consumption	[352, 357]
	High temperatures and pressure	[203, 356]
	Large volumes of solvent required	[221, 352]
MW-assisted Synthesis	**Advantages**	
	Rapid process (minutes/hours)	[203, 204, 221, 352, 357, 358]
	Obtain nanoscale MOFs with high-purity	[203, 204, 221, 352, 356, 357]
	Low energy consumption and high efficiency	[204, 221, 352]
	Low volume of chemical waste	[352]
	Simultaneous synthesis of up to 36 vessels*	[357]
	Limitations	
	Differences in irradiation power affect the reproducibility between different equipment	[204, 352]

The processes and definitions for determining whether a MOF is suitable for visualising LGSR has been established since the first LGSR study by Weber et al. [12]. The suitability of any synthesised MOF is determined during the post-discharge analysis and focuses on different aspects of stability. Traditionally, there are three essential criteria considered for each newly synthesised MOF; (i) strong luminescence, (ii) thermal stability and (iii) chemical stability [173, 175, 181, 182]. The (i) strong luminescence refers to the ease for the investigator to visualise the LGSR post-discharge either on the shooter, in the firearm or in the general area of discharge. The thermal stability of the MOF refers to the ability of the MOF to withstand high discharge temperatures (1500 – 3600 °C [359, 360]) and retain their chemical structure to allow them to be visualised post-discharge. The chemical stability of the MOF indicates that it is chemically inert and does not impact the chemical profile of the propellant powder or primer behaviour during discharge or the metallic components of the ammunition or firearm [12]. To confirm the luminescent, thermal and chemical stability of the MOF, the discharged LGSR particles must be visible on an area of interest and detected through traditional analysis techniques (SEM-EDS) [183, 186].

To a lesser extent, three studies have additionally analysed the 'LGSR stability'. This type of stability emphasises the ability to visualise the luminescence post-discharge from collected LGSR specimens after a set time period. Destefani et al. [78] and Weber et al. [12] evaluated the LGSR stability directly from items collected (FCCs and targets, respectively), whereas Serwy et al. [179] evaluated LGSR stability from GSR stubs. Regardless of how the LGSR specimens were incorporated, discharged, collected or stored, these studies indicated that the LGSR particles were able to retain their luminescence months later (*Table 2-3*). The differences in the time since discharge between the studies were sizable; however, none of the studies suggested the reason for this was related to a reduction or loss of luminescence in the LGSR specimens. Although, from an investigative point of view, identifying LGSR particles in a location months after the firearm-related scene had occurred is not ideal, it is still valuable information that the MOFs can be visualised up to a minimum of 4 months post-discharge.

Table 2-3: Luminescent stability of LGSR. Ln = Eu^{3+} and Tb^{3+}.

MOF	Time Since Discharge	Collection Device	Collection Area	Storage Conditions	Reference
$Eu(PIC)_3(NMK)_3$	4 months	N/A	FCC	Unknown	[78]
$Ln_2(BDC)_3(H_2O)$	18 months	SEM stubs	Shooter's hands	RT No humidity	[179]
Ln(DPA)(HDPA)	30 months	N/A	Target	Damp environment	[12]

There are no published studies related to the stability of MOF as a function of time since synthesis. This type of stability would determine the maximum shelf-life of the pure MOF by highlighting whether it retains the same structural framework and luminescence properties after a set time without evidence of degradation. Determining the possible shelf-life is important as it can advise whether the MOF will remain stable during the time that has lapsed between synthesis, incorporation, and discharge. This stability can impact the shelf-life of traditional ammunition, which is already dependent on the propellant type, along with the type of stabilisers and additives, encased within the cartridge [361-364]. The length of time in which ammunition is stockpiled by civilians, law enforcement or defence organisations varies and is often unknown. In Australia, it is recommended to destroy ammunition containing powders older than 10 years if no best-before date is supplied by the manufacturer [365]. Understanding the stability of the pure MOF provides insight into whether the MOF would be suitable in a long-term situation. If it was identified that the pure MOF framework began to degrade or their luminescence began to reduce substantially, it would suggest that the incorporated MOF would follow a similar trend. This observation would indicate that there would be no point in incorporating MOFs into ammunition if their prime identifying features degraded during the time between manufacture and discharge.

This chapter encapsulates the different aspects required to ensure a suitable MOF is chosen for incorporation into ammunition. Section I presents the synthetic routes applied to a range of 'novel' MOFs that have not yet been evaluated as LGSR. Considering the availability and cost of metal cores within Australia, Tb^{3+}, Er^{3+}, Ho^{3+}, Gd^{3+} and Y^{3+} were evaluated to determine whether any additional MOFs would provide greater luminescence than those published in the literature for LGSR visualisation [366]. All synthesised complexes were characterised based on their chemical and structural, thermal, and luminescent properties in Section II. Additionally, a comparison between the SH and the MW-assisted routes was conducted to identify whether the variation between the MOF features (ligand and morphology) could affect the distribution of GSR and the ability to visualise the luminescence. The aim of this chapter was to identify MOFs that would be able to withstand changes to their chemical structure and luminescence to ensure their functionality in a real-life situation following incorporation into ammunition. With no LGSR research delving into the stability of the pure MOFs pre-discharge, Section III aims to investigate the chemical and luminescent stability of four pure MOFs over the course of 24 months. Any indication of degradation was monitored to identify whether the MOFs would be suitable for incorporation into ammunition and subsequent evaluation as LGSR.

2.2 Materials and Methods

SECTION I: Synthesis

2.2.1 Chemicals

Terbium(III) nitrate pentahydrate ($Tb(NO_3)_3.5H_2O$, 99.9%), erbium(III) nitrate pentahydrate ($Er(NO_3)_3.5H_2O$, 99.9%), holmium(III) nitrate pentahydrate ($Ho(NO_3)_3.5H_2O$, 99.9%), gadolinium(III) nitrate hexahydrate, ($Gd(NO_3)_3.6H_2O$, 99.9%), yttrium(III) nitrate hexahydrate, ($Y(NO_3)_3.6H_2O$, 99.9%), trimesic acid (H_3BTC or TMA, 95%), Htta (99%), 8-hydroxyquinoline (8-qu, ACS reagent, 99%), 2-(1H-1,2,4-triazol-3-yl)pyridine (Pyr, 97%), 2,6-pyridinedicarboxylic acid (H_2DPA, 99%), ε-caprolactam (ε-cap, 99%), n,n-dimethylformamide (DMF, anhydrous, 99.8%), ethanol (EtOH, ≥99.5%), sodium acetate (CH_3COONa, ACS reagent, 99%), ammonium hydroxide (NH_4OH, ACS reagent, 28.0 – 30.0% NH_3 basis) and ace pressure tubes (38 mL, 20.3 cm (L) × 2.54 cm (O.D.)) were purchased from Sigma-Aldrich (Castle Hill, NSW, Australia). Ultrapure water (H_2O, 18.2 MΩ × cm) was collected from a Sartorius arium® pro UV ultrapure water system. Sirchie GREENCHARGE™ Fluoro-Magnetic Print Powder was purchased through Optimum Technology (Queensland, Australia) and used as supplied.

2.2.2 Synthesis

*2.2.2.1 Solvothermal Synthetic Route 1 (**SH1**)*

A round-bottom flask was filled with $Ln(NO_3)_3.xH_2O$ (Ln = Tb and Er) (0.1 mmol), H_3BTC (0.1 mmol), ε-cap (0.1 mmol) and a mixture of DMF (10 mL) and EtOH (2 mL). The reaction was left to stir at room temperature (21°C) for 2 hours under a steady nitrogen stream. The mixture was heated to 55°C for five days before being filtered and washed with EtOH (3 x 10 mL) to remove excess DMF [206].

*2.2.2.2 Solvothermal Synthetic Route 2 (**SH2**)*

In a covered beaker, $Ln(NO_3)_3.xH_2O$ (Ln = Tb, Er, Ho, Gd and Y) (0.2 mmol), H_3BTC (0.2 mmol) and ε-cap (0.2 mmol) were stirred in a mixed solvent of DMF (10 mL), EtOH (4 mL) and H_2O (2 mL) for 1 hour. The solution was transferred into a pressure tube and placed into a Dynapump oven at 75°C for 48 hours. The solution was removed from the oven and left to cool to room temperature (21°C) for 1 hour before the precipitate was filtered and washed with EtOH (3 x 10 mL).

*2.2.2.3 Solvothermal Synthetic Route 3 (**SH3**)*

Two solutions were prepared in separate beakers under constant stirring. An aqueous solution composed of $Gd(NO_3)_3.6H_2O$ (1.14 mmol), CH_3COONa (12.5 mmol) and H_2O (5 mL), and an ethanolic solution comprising of Htta (3.42 mmol) and EtOH (8 mL) was left to stir for 1 hour at 360 rpm. The aqueous solution was added dropwise to the ethanolic solution and mixed for 24 hours. The precipitate was filtered and washed with H_2O (3 x 10 mL) before drying for 1 hour [367].

*2.2.2.4 Solvothermal Synthetic Route 4 (**SH4**)*

A 1% alcoholic solution consisting of 8-qu (3.44 mmol) and EtOH (49.5 mL) was stirred until completely dissolved and stored in a shott bottle until use. A round bottom flask was filled with $Gd(NO_3)_3.6H_2O$ (0.25 mmol) and H_2O (25 mL) at 360 rpm until dissolved. Additional H_2O (100 mL) and a small excess of 1% alcohol solution were added to the RBF before heating at 60°C. To ensure the reaction occurred in slightly basic conditions, NH_4OH was added to the solution dropwise and monitored with a Thermo Scientific™ Eutech™ pH 700 meter until a pH of 8 was achieved. The reaction was left stirring for 24 hours before cooling for 1 hour. The precipitate was filtered, washed with H_20 (3 x 10 mL) and dried at 110°C [368].

*2.2.2.5 Solvothermal Synthetic Route 5 (**SH5**)*

A metal solution and ligand solution were prepared independently in separate beakers. The metal solution was prepared by mixing $Ln(NO_3)_3.xH_2O$ (Ln = Tb, Er, Ho, Gd and Y) (1 mmol) and H_2O (2 mL), while the ligand solution was prepared by dissolving Pyr (3 mmol) in H_2O (3 mL) and EtOH (1 mL). Both solutions were stirred for 10 minutes until dissolved before the metal solution was added dropwise to the ligand solution. The mixture was stirred at 45°C for 3 hours. The mixture was dried under ambient conditions until cool and then left under vacuum at room temperature (21°C) overnight to remove excess H_2O. The precipitate was filtered and washed with EtOH (3 x 10 mL) [369].

*2.2.2.6 Microwave-assisted Synthetic Route 1 (**MW1**)*

$Tb(NO_3)_3{\cdot}6H_2O$ (0.35 mmol), H_3BTC (0.35 mmol) and H_2O (5 mL) was placed in a 70 mL glass vial. The glass vial was inserted into a 100 mL PTFE-TFM vessel on top of a Weflon™ cap and placed into the Milestone ETHOS X microwave system. A ramp time of 10 minutes was applied to reach temperature before the reaction took place at 160°C for 10 minutes. The precipitate was washed with deionised H_2O and acetone and then dried at 110°C [182].

*2.2.2.7 Microwave-assisted Synthetic Route 2 (**MW2**)*

MW2 followed a similar procedure to MW1; however, H_3BTC (0.35 mmol) was replaced with H_2DPA (0.7 mmol) [12].

*2.2.2.8 Microwave-assisted Synthetic Route 3 (**MW3**)*

$Tb(NO_3)_36{\cdot}H_2O$ (0.2 mmol), H_3BTC (0.2 mmol) and ε-cap (0.2 mmol) were immersed in a mixed solvent of DMF (10 mL), EtOH (4 mL) and H_2O (2 mL) and placed in a 70 mL glass vial. The glass vial was inserted into a 100 mL PTFE-TFM vessel on top of a Weflon^{TM} cap and placed into the Milestone ETHOS X microwave system. A ramp time of 10 minutes was applied to reach temperature before the reaction took place at 150°C for 10 minutes. The precipitate was washed with acetone (3 x 10 mL) and then dried at 110°C.

2.2.2.9 MOF Synthesis Overview

To summarise the MOFs synthesised for this work, the synthesis parameters can be seen in *Table 2-4*.

Table 2-4: Overview of MOFs synthesised for this study.

Synthetic Route	MOF	Ligand	Solvents and catalysts	Synthesis Time	Synthesis Temperature
SH1	SH1-Tb SH1-Er	H_3BTC	DMF H_2O ε-cap	5 days	55°C
SH2	SH2-Tb SH2-Er SH2-Ho SH2-Gd SH2-Y	H_3BTC	DMF EtOH H_2O ε-ca	48 hours	75°C
SH3	SH3-Gd	Htta	EtOH H_2O CH_3COONa	24 hours	21°C
SH4	SH4-Gd	8-qu	EtOH H_2O NH_4OH	24 hours	60°C
SH5	SH5-Tb SH5-Er SH5-Ho SH5-Gd SH5-Y	Pyr	EtOH H_2O	24 hours	45°C
MW1	MW1-Tb	H_3BTC	H_2O	20 minutes	160°C
MW2	MW2-Tb	H_2DPA	H_2O	20 minutes	160°C
MW3	MW3-Tb	H_3BTC	DMF EtOH H_2O ε-cap	20 minutes	150°C

SECTION II: Characterisation

Each of the synthesised MOFs underwent structural and luminescent characterisation to confirm their chemical and luminescent properties. The pure MOFs did not require further sample preparation prior to the characterisation analyses.

2.2.3 Structural Elucidation

Powder X-ray diffraction (PXRD) measurements were performed using a Bruker D8 Discover diffractometer (Bruker, Germany) with Cu-Kα radiation source. The instrument was operated at 40 kV and 40 mA in the Bragg–Brentano geometry and completed a full scan with 2θ range of 5 – 70° and 0.02 step size to identify the crystallographic structure of the MOFs. Samples were ground, mounted and flattened in polymethyl methacrylate specimen holders (C79298A3244D82/D84; 8.5 mm height, sample reception: Ø 25 mm, 1 mm depth). All spectra were analysed using the associated DIFFRAC.EVA software.

The chemical structure was elucidated using a Nicolet Magna-IR 6700 Spectrometer (Thermo Scientific, USA) with the associated OMNIC software suite. The FTIR spectrum were recorded in attenuated total reflectance mode (ATR). Each spectrum was collected using 64 scans with a spectral resolution of 4 cm^{-1} and acquired over a range of 400–4000 cm^{-1}. Each MOF was analysed in triplicate.

2.2.4 Structural Suitability

The size, morphology and elemental analysis of the MOF were characterised using a Zeiss Evo LS15 SEM (Zeiss, Germany) with a silicon drift detector (SDD) XFlash 5030 detector (Bruker, Germany). The sample was fixed onto a carbon-coated stub (12.5 mm diameter), and a manual run was conducted under high vacuum pressure (*Table 2-5*).

Table 2-5: SEM-EDS Parameters.

Parameters	SEM	EDS
Magnification	1500 x	250 x
Accelerating voltage	15 kV	15 kV
Working Distance	10.5 mm	10.5 mm
iProbe	300 pA	15.0 nA
Aperture Size	30 µm (large)	30 µm (large)
Dead Time	N-A	20% – 30%

The thermal stability of the MOF was characterised using a TA Instruments SDT Q600 thermal analyser (Waters, Melbourne, Australia). Samples were placed into 90 µL alumina crucibles and all experiments were conducted under an atmosphere of air (100 mL min^{-1}) and a heating rate of 10 °C min^{-1} over a temperature range of 20 °C to 1500 °C.

2.2.5 UV Photoluminescence Visualisation

A Varian Cary Eclipse Fluorescence Spectrophotometer (Agilent Technologies, Victoria, Australia) was used to measure the spectral luminescence emitted by the MOFs when excited by UV radiation. The emission spectra were monitored in the visible range of 400–600 nm and were obtained using a 5 nm slit and integration time of 0.1 s. Each MOF was characterised in triplicate using the excitation wavelength indicated in the literature for the luminescence spectra (*Table A2 - 1* in Appendix 2). Sirchie GREENescent™ Fluorescent Latent Print Powder was used to align the spectrophotometer.

The visual and spectra luminescence analysis of each MOF was captured using the Foster+Freeman Video Spectral Comparator 8000 (VSC) under UV radiation (λ_{ex} = 365 nm). The ISO and iris were set to 100 and 100%, respectively, for all MOFs. The integration time for the MOFs remained at 500 ms. However, as the VSC is not a portable device, the Rofin Polilight® PL550XL (λ_{ex} = 350 nm) and Labino® TrAc Pack PRO (λ_{ex} = 365 nm) were also used to capture the visual luminescence of these MOFs. Images of the MOFs were captured using a Canon EOS 750D camera.

2.2.6 Evaluation Criteria

Previous research has described three essential characteristic requirements for MOFs incorporated into ammunition; (i) chemical stability, (ii) thermal stability and (iii) high luminescence [12, 173, 175, 181, 182]. This chapter reported on the characterisation of each synthesised MOF to ensure that it met the characteristic requirements and if it did not, the MOF was discontinued from further assessment. A summary of the techniques applied to the MOFs and the factors for MOF discontinuation can be observed in *Figure 2-1*.

The general observations of synthesis yield and cost were the first to identify whether any MOF would be unsuitable for incorporation. In Australia, ammunition is sold in boxes of 20 – 100 rounds, depending on the ammunition type, and the addition of MOFs would result in an inflation of ammunition prices. To ensure prices for ammunition would not increase substantially, both criteria were assessed simultaneously. XRD and FTIR analysis were conducted to identify the MOF crystalline phase and confirm the molecular structure of the framework obtained during synthesis,

respectively. SEM-EDS and TGA ensured that the synthesised MOFs would be suitable for traditional GSR detection methods. The photoluminescence analysis focused on the characteristic emission features presented by the metal core components. A combination of instruments was required for this analysis to a) compare the synthesised MOF to the literature and b) highlight the characteristic luminescence properties of the MOFs using UVA excitation conditions. If the MOF was observed to pass each criterion, it was deemed suitable for further evaluation as LGSR.

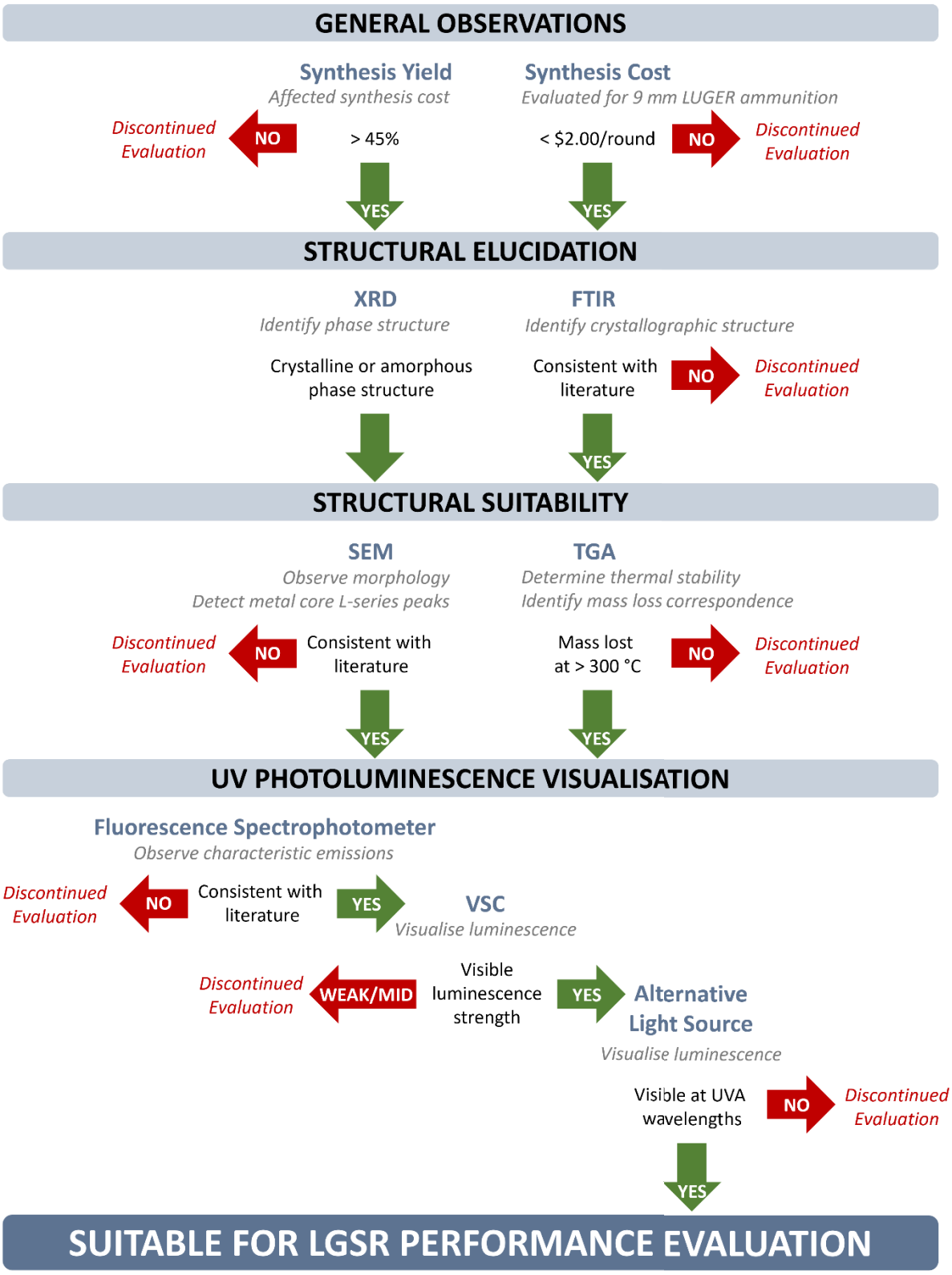

Figure 2-1: Flowchart of the evaluation criteria applied to the synthesised MOFs. Contains instrumentation used for criteria (blue), the reason for the characterisation technique (grey), and thresholds (black) of individual factors considered before continuation (green) or discontinuation (red).

SECTION III: Stability

2.2.7 Chemicals, synthesis and storage

Chemicals required for the synthesis of SH2-Tb, MW1-Tb, MW2-Tb and MW3-Tb were identical to those previously listed in Section 2.2.1. Synthesis of SH2-Tb, MW1-Tb, MW2-Tb and MW3-Tb followed the procedure outlined in Section 2.2.2.2, Section 2.2.2.6, Section 2.2.2.7 and Section 2.2.2.8, respectively. Following synthesis and characterisation, the pure MOFs were stored in glass scintillation vials, which were then placed in a closed drawer in an air-conditioned (20-22°C) laboratory. The MOFs were removed from these storage conditions once a month for data collection.

2.2.8 Chemical Stability

The FTIR data collection parameters remained consistent with those previously outlined in Section 2.2.3. Prior to analysis, the instrument was aligned to ensure the maximum detector signal documented an intensity value between 4.00 – 7.00 a.u. A small quantity of MOF from each synthesis batch was removed from the scintillation vial during analysis and was analysed in triplicate per month for 24 months. The monthly spectral data was analysed using Microsoft Excel.

2.2.9 UV Photoluminescent Stability

2.2.9.1 Varian Cary Eclipse Fluorescence Spectrophotometer Wavelength Optimisation

A *3-D Mode* scan was conducted using the Varian Cary Eclipse Fluorescence Spectrophotometer (Agilent Technologies, Victoria, Australia). The emission spectra were monitored in the visible range of 400–600 nm and were obtained using a 5 nm slit and integration time of 0.1 s. The *3-D Mode* scan applied a range of excitation wavelengths between 320 nm – 400 nm (UVA range) at increments of 10 nm.

2.2.9.2 Monthly Stability

The fluorescence spectrophotometer and VSC data collection parameters remained consistent with those previously outlined in Section 2.2.5. To outline any issues with inter-day variability of the spectrophotometer and VSC, Sirchie GREENescent™ Fluorescent Latent Print Powder was analysed prior to all MOF time point evaluations. This was chosen due to its strong and stable luminescence under similar conditions to the tested MOFS. Each MOF was assessed in triplicate per month for 24 months. The monthly spectral data was analysed using Microsoft Excel.

2.3 Results and Discussion

Although all synthesised MOFs underwent complete synthesis and characterisation, not all the data will be presented in this chapter. The data presented in this section covers the MOFs that were found suitable for incorporation following each characterisation technique. Data on MOFs discontinued from further evaluation can be found in Appendix 2. All MOFs synthesised via SH1 – SH5 and MW3 synthetic routes are termed 'novel MOFs' as they have not previously been applied as a tool to visualise LGSR. MOFs synthesised via MW1 [182], and MW2 [12] have previously been incorporated into ammunition and proven efficient for visualising GSR, and so will be termed as 'established MOFs'.

SECTION I: Synthesis

2.3.1 Synthesis Optimisation

The initial synthetic route, SH1, followed the procedure outlined in Li et al. [206], recommended by the Sigma-Aldrich *MOF Constructor* tool [370]. The resulting yields for SH1-Tb and SH1-Er (*Table 2-7*) were low when compared to the yields obtained by literature (50 – 63%) [206] and inhibited any characterisation analysis on the synthesised MOFs. The method was adapted, and a range of variables was explored, including the type of temperature-controlled environment, the temperature of the reaction (55°C, 65°C and 75°C), molar concentrations (0.1 mmol, 0.2 mmol and 0.3 mmol) and reaction times (1-day, 2-days, 3-days, 4-days and 5-days). Changing the temperature required for synthesis was the first parameter assessed for the SH2-MOFs. Increasing the temperature of the reaction accelerated the deprotonation of the H_3BTC carboxylate ions to allow additional coordination to the metal core [356]. The greatest increase in yield production occurred when setting the temperature to 75°C where an increase from 1% to 44% was observed. Amendments to the molar concentrations of the metal core, ligand and catalyst were next evaluated, while the solvents (DMF, EtOH and H_2O) remained consistent with the specified volumes outlined in Li et al. [206]. As the molar concentration of the metal core, ligand and catalyst increased, the yield and cost of the synthesis of the MOF also increased. While 0.3 mmol concentrations provided the best yields (82%), it was also calculated to be the most expensive synthetic route. At a concentration of 0.2 mmol, the yield obtained was above 77% and a cheaper alternative. The last aspect of the reaction that required optimisation was the length of the reaction and due to the change in reaction environment and temperature, a reduction in the reaction time was expected [356]. For reactions set for two to five days, there was not much variation in the yields obtained (71 – 77%), whereas the one-day reactions provided a

comparatively lower yield at 63%. Although the one-day reaction yield would allow for a more efficient output over time, the two-day reaction was chosen as it provided a suitable yield of 73.8%, which was above the threshold. The optimised process of the SH2-Tb core was then applied to the remaining metal cores (Er^{3+}, Ho^{3+}, Gd^{3+} and Y^{3+}), in which suitable yields were observed for all MOFs, indicating additional optimisation was not required.

To confirm whether the novel MOFs synthesised via SH1 – SH5 would be appropriate to incorporate into ammunition they were compared against two established MOFs. The MOFs discussed in Lucena et al. [182] (MW1-Tb) and Weber et al. [12] (MW2-Tb) were chosen as the comparison MOFs, as they were some of the most common MOFs evaluated as LGSR (*Table 1-8*) [174, 177, 184, 187]. With the introduction of MW-assisted synthesis, it was further decided that a novel MW-MOF should be synthesised via this synthetic route (MW3-Tb). The molar concentration of reagents and solvent volumes outlined in SH2-Tb were transferred to MW3-Tb to compare product yield and cost. Unfortunately, a limitation of MW-assisted synthesis is that synthetic route parameters are not easily transferred between different MW instruments, indicating that synthesis optimisation was required for the time and temperature of MW3-Tb [204, 352]. Two synthetic routes were assessed for the synthesis of MW3-Tb, varying in temperature and time of reaction [371, 372], due to the presence of DMF as the solvent (*Table 2-6*). Comparing the MW3-Tb MOFs synthesised via the two synthetic routes no discrepancies in the chemical, structural or luminescence characterisation were observed. The greatest variation between the two routes was observed from the synthesis yield, where the higher temperature of 150°C provided yields above the threshold (*Table 2-6*). This is consistent with literature that highlights higher temperatures present with higher yields and time efficiency [354], indicating that setting the temperature to 150°C would be favoured as the MW parameters.

Table 2-6: Comparison of temperature and percentage yield for MW3-Tb synthesis.

Temperature	Ramp Time	Steady Time	Percentage Yield (%)
105°C	10 minutes	20 minutes	46.5
150°C	10 minutes	10 minutes	67.4

SECTION II: Characterisation

2.3.2 General Observation

An initial comparison between the synthesised MOFs was conducted by observing the MOF powder colour and consistency, yield, and cost of production (*Table 2-7*). From the general observations of the synthesised MOFs, SH1-Tb, SH1-Er and SH5-Er provided yields below the 65% threshold, removing them from further evaluation. Whereas SH4-Gd and the remaining SH5-MOFs were removed due to high production costs.

Table 2-7: Comparison of synthesised MOFs in this study. n = 2. ^cost calculated per round (at 10 wt% incorporation of synthesised MOF).

Synthetic Route	MOF Number	Final Product		Percentage Yield (%)	Cost ($AUD)^	Met All General Observations
		Colour	Powder Consistency			
SH1	SH1-Tb	White	Flaky	0.407	$527.00	×
	SH1-Er	Light Pink	Flaky	6.00	$38.00	×
SH2	SH2-Tb	White	Fluffy	76.9	$1.60	✓
	SH2-Er	Light Pink	Fluffy	78.4	$0.95	✓
	SH2-Ho	Light Orange	Fluffy	75.1	$1.35	✓
	SH2-Gd	White	Fluffy	65.3	$1.10	✓
	SH2-Y	White	Fluffy	72.6	$1.10	✓
SH3	SH3-Gd	Cream	Chalky	75.3	$0.85	✓
SH4	SH4-Gd	Mustard Yellow	Putty	78.9	$3.10	×
SH5	SH5-Tb	White	Chalky	48.8	$3.55	×
	SH5-Er	White	Chalky	29.8	$9.05	×
	SH5-Ho	Light Orange	Chalky	53.6	$3.00	×
	SH5-Gd	White	Chalky	46.0	$2.90	×
	SH5-Y	White	Chalky	45.7	$3.45	×
MW1	MW1-Tb	White	Chalky	71.6	$1.80	✓
MW2	MW2-Tb	White	Fluffy	82.4	$0.95	✓
MW3	MW3-Tb	White	Fluffy	67.4	$1.80	✓

For SH1-Tb and SH1-Er, the inadequate yields (0.406% and 6.00%) were comparably different to the literature (63% and 50%, respectively) [206], which could be due to variations in equipment used for the reaction. The SH5-MOFs were also observed to contain yields lower than the threshold, which is likely to be a result of the reaction conditions. The low yields obtained from

SH1-Tb and SH1-Er caused the calculated synthesis cost to inflate, which is unacceptable for both small- and large-scale synthesis. The high cost of the SH5-MOF ligand, which was identified as being approximately 15 times more expensive than the other ligands, was another factor that resulted in the removal of the MOFs for further evaluation. Although a high yield was obtained for SH4-Gd, the synthesis cost was above the threshold. This cost correlates to the high molar concentration and volume requirements of the alcoholic solution portion of the reaction.

The general observations identified the synthesis yield and cost of nine MOFs (SH2-Tb, SH2-Er, SH2-Ho, SH2-Gd, SH2-Y, SH3-Gd, MW1-Tb, MW2-Tb and MW3-Tb) would be acceptable for incorporation into ammunition.

2.3.3 Structural Elucidation

Confirmation of the structural orientation of particle bonds was attempted; however, due to the limited number of MOFs available in the DIFFRAC.EVA software database packages automatic pattern matching was not possible. Instead, a manual comparison was conducted, which discovered that due to altering the synthetic routes, there were obvious geometric variations between the synthesised MOFs and the available published data. The slight variation in the synthesis parameters applied to the synthesised MOFs can affect the structural arrangement of the particle, leading to the geometric variations observed within the MOF [373]. Due to observing these variations in six of the nine remaining synthesised MOFs, it was decided that the XRD analysis would not be used as an exclusionary characterisation technique, shifting the focus of the XRD analysis to identifying the MOFs crystalline phase.

The only observation that could be identified across all synthesised MOFs was the presence of sharp peaks in the XRD patterns indicating that all MOFs were completely crystallised, indicating a crystallographic relationship between the lattice planes. Among the SH-MOFs, only two were observed to contain patterns consistent with the literature; SH2-Er and SH2-Ho. A comparison with literature, highlighted that the peaks marked with a star (*Figure 2-2*) have relative intensities that approximately correlate to the published pattern (*Table 2-8*) suggesting that the synthesised MOFs adopt the same crystal structure as the literature [206]. These starred peaks were observed to be shifted in position by 0.1° – 0.8°, which suggests that the 3D arrangement of the crystal lattice differs from literature. Additional peaks are also present in the XRD patterns which results from either the occurrence of a secondary phase and/or breaking of symmetry in the crystal lattice.

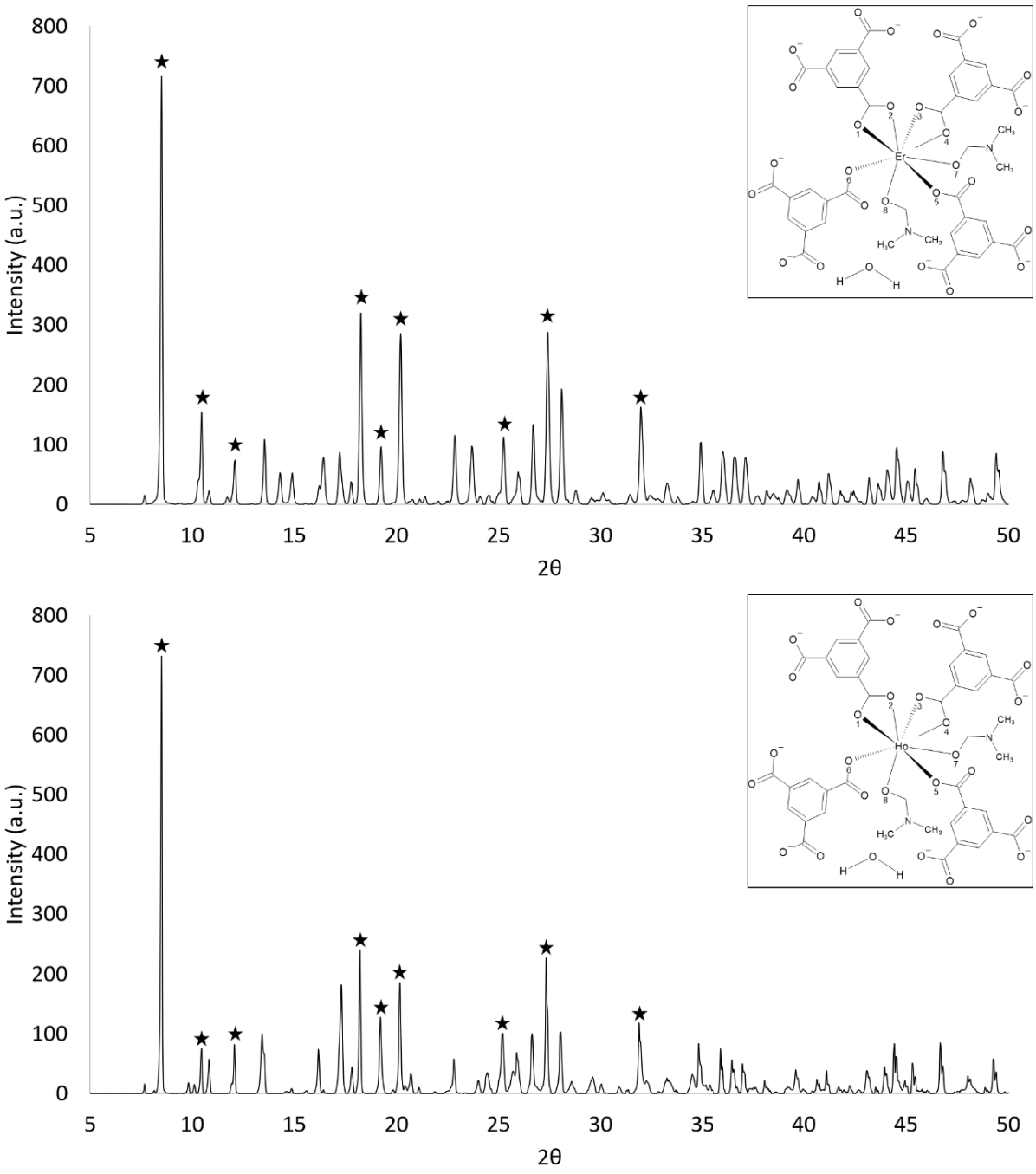

Figure 2-2: XRD pattern of as-prepared SH2-Er (top) and SH2-Ho (bottom). Stars indicate peaks most similar to literature. The insert represents the expected structure of the MOF as indicated by literature.

Table 2-8: Peak position and relative peak intensity of SH2-Er and SH2-Ho comparison with literature XRD pattern [206].

Literature		Experimental			
		SH2-Er		SH2-Ho	
Peak Position	**Relative Peak Intensity (%)**	**Peak Position**	**Relative Peak Intensity (%)**	**Peak Position**	**Relative Peak Intensity (%)**
9.19	100	8.51	100	8.51	100
10.1	22.3	10.5	21.5	10.5	8.90
12.0	13.5	12.1	9.72	12.1	11.3
18.0	28.4	18.3	45.1	18.2	33.5
19.2	15.5	19.3	13.5	19.2	15.4
19.7	58.1	20.2	40.2	20.2	25.7
24.7	23.0	25.2	13.3	25.2	13.9
27.7	29.7	27.4	40.6	27.3	31.4
31.1	18.9	31.9	22.8	31.8	16.4

The XRD pattern of SH2-Tb was observed to have one consistent peak with literature at 8.55° (*Figure 2-3*). This peak contained the maximum intensity, highlighting the large number of atoms detected in this location of the crystal lattice. The other peaks, while observed to be in similar 2θ° peak locations to the literature did not contain similar relative peak intensities. The remaining SH-MOFs (SH2-Gd, SH2-Y and SH3-Gd) are not consistent with their supporting literature XRD patterns, which suggests that these MOFs did not adopt the same crystal lattice (*Figure 2-4*). For these MOFs, it was only possible to determine the crystalline size (as calculated by the Scherrer equation) and the order of arrangement. The crystalline size of SH2-Y was calculated to be from 49.6 nm – 67.0 nm, suggesting some long-range order was present in the unidentified crystal structure. However, SH2-Gd and SH3-Gd were observed to have a wider crystalline size range extending from 16.5 nm – 66.1 nm. The presence of these smaller crystallites in the XRD pattern suggest there may be some short-range crystallinity, but the overall sample does not appear to have long range ordering. The SH3-Gd MOF does contain 5 peaks in similar locations to the literature; however, the low intensity of the XRD pattern makes it difficult to distinguish further peaks from the background noise (*Figure 2-5*). The variation observed in the peak intensities between the synthesised MOF and literature correlates to the crystalline phases coexisting in the structure [374]. The peak intensities are also affected by the particle morphology [375]. As the literature does not always provide morphological information of their MOFs, this cannot be confirmed for these MOFs.

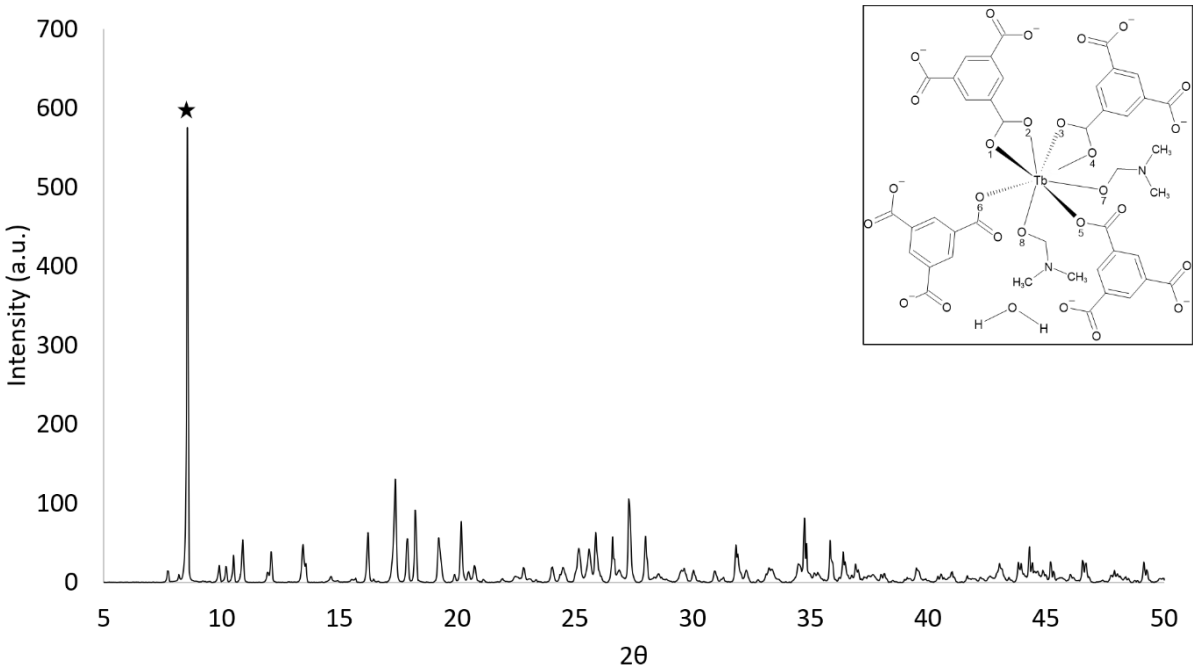

Figure 2-3: XRD pattern of as-prepared SH2-Tb. Stars indicate peaks most similar to literature. The insert represents the expected structure of the MOF as indicated by literature.

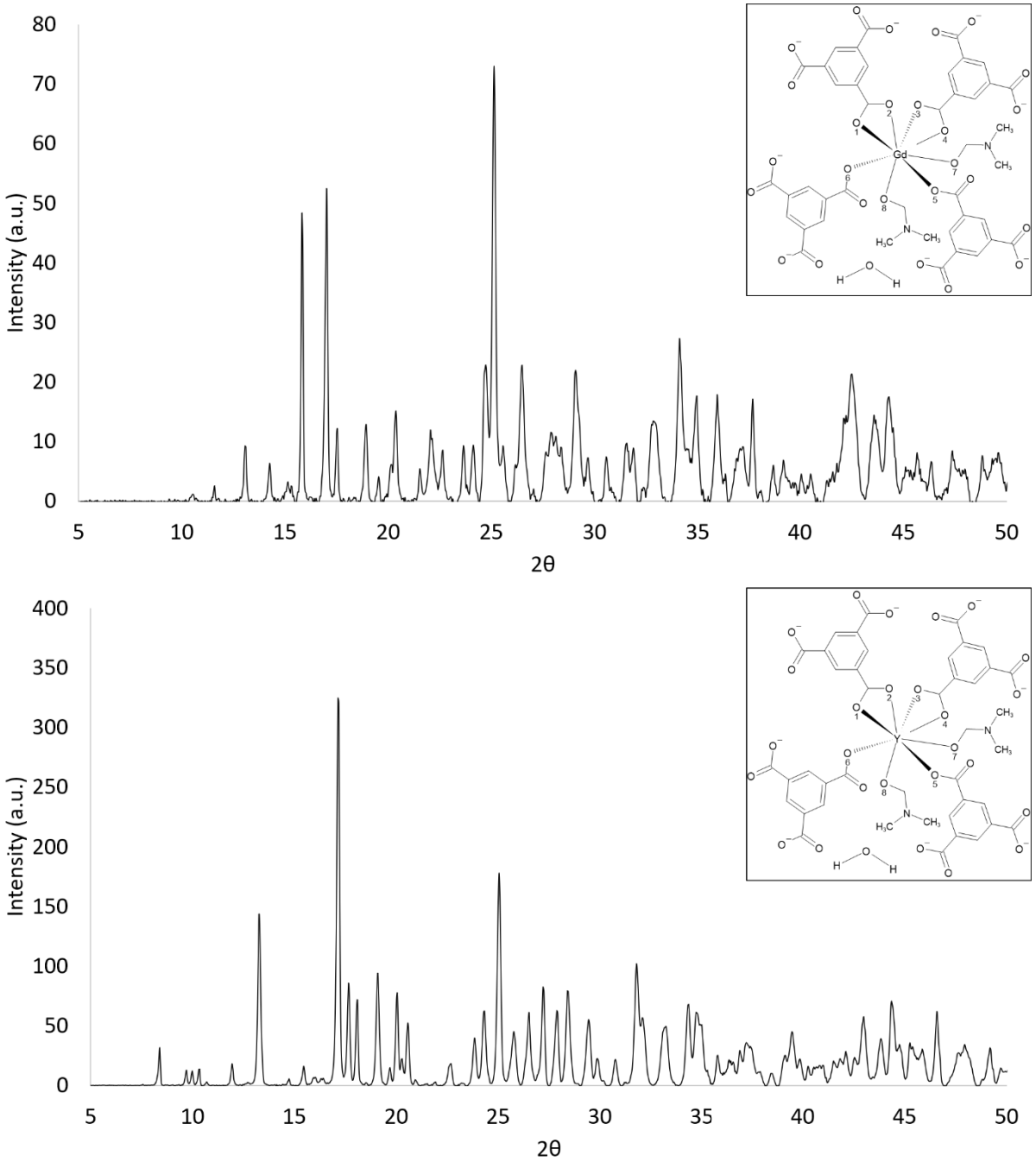

Figure 2-4: XRD pattern of as-prepared SH2-Gd (top) and SH2-Y (bottom). The insert represents the expected structure of the MOF as indicated by literature.

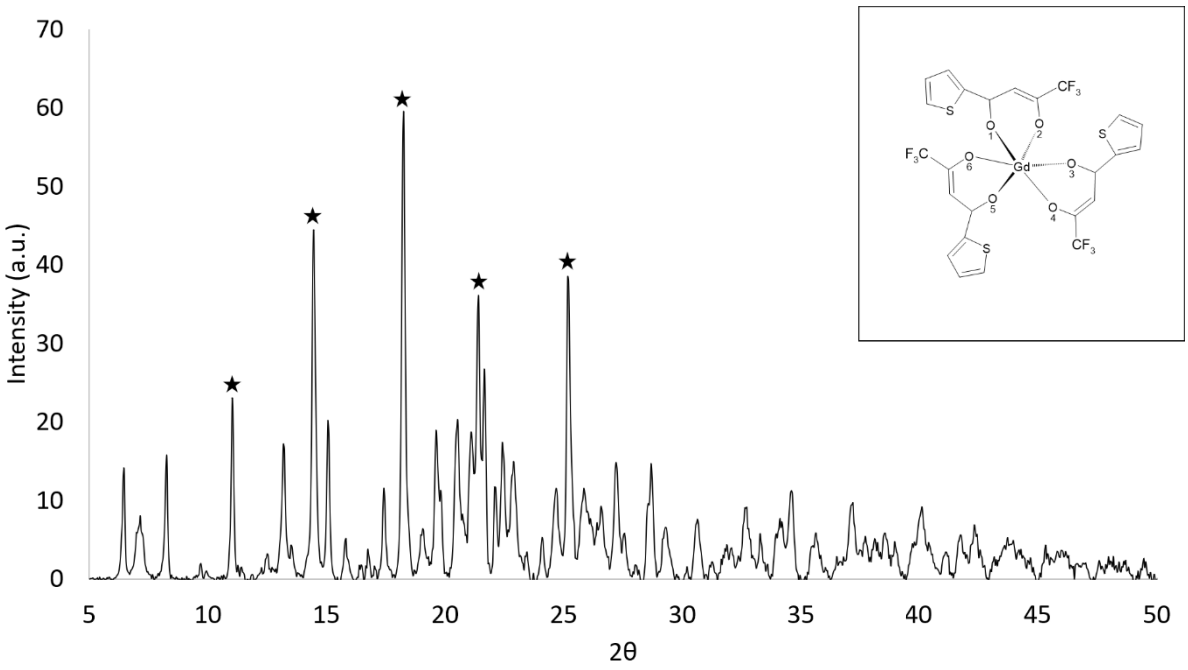

Figure 2-5: XRD pattern of as-prepared SH3-Gd. Stars indicate peaks most similar to literature. The insert represents the expected structure of the MOF as indicated by literature.

For the MW-MOFs, only MW1-Tb contained similar peak positions and relative peak intensities (*Table 2-9* and *Figure 2-6*) with the literature XRD patterns, suggesting that there is a slight difference in the 3D arrangement of the crystal lattice [176]. MW2-Tb and MW3-Tb did not contain peaks correlating to their supporting literature XRD patterns, suggesting the same crystal lattice was not adopted for these MOFs (*Figure 2-7*). The crystalline size and the order of arrangement were able to be determined. The crystalline size of MW2-Tb was calculated to be from 40.3 nm – 66.2 nm, suggesting some long-range order was present in the unidentified crystal structure. However, MW3-Tb was observed to have a wider crystalline size range extending from 12.5 nm – 40.0 nm, suggesting that there may be some short-range crystallinity, but the overall sample does not appear to have long-range ordering. The variations observed in the XRD patterns between the synthesised MOFs and the literature can be attributed to the slight differences in the synthetic routes (instrumentation parameters and temperature modification) [376]. The variations in 3D arrangement between the synthesised MOF XRD patterns and literature patterns could suggest potential differences in the MOF morphology and size of the particles, which could further impact the chemical properties of the MOFs [377].

Table 2-9: Peak position and relative peak intensity of MW1-Tb comparison with literature XRD pattern [176].

Literature		MW1-Tb	
Peak Position	**Relative Peak Intensity (%)**	**Peak Position**	**Relative Peak Intensity (%)**
10.0	100	10.7	100
12.1	16.7	11.7	3.10
14.7	5.56	14.5	1.66
15.6	3.22	15.4	0.57
16.3	62.3	16.0	39.7
20.9	5.26	20.4	3.16
25.6	23.4	25.4	13.9
27.1	11.7	26.7	10.0
28.5	7.31	28.2	4.76
34.9	4.68	34.3	8.63
38.3	4.39	38.0	3.31

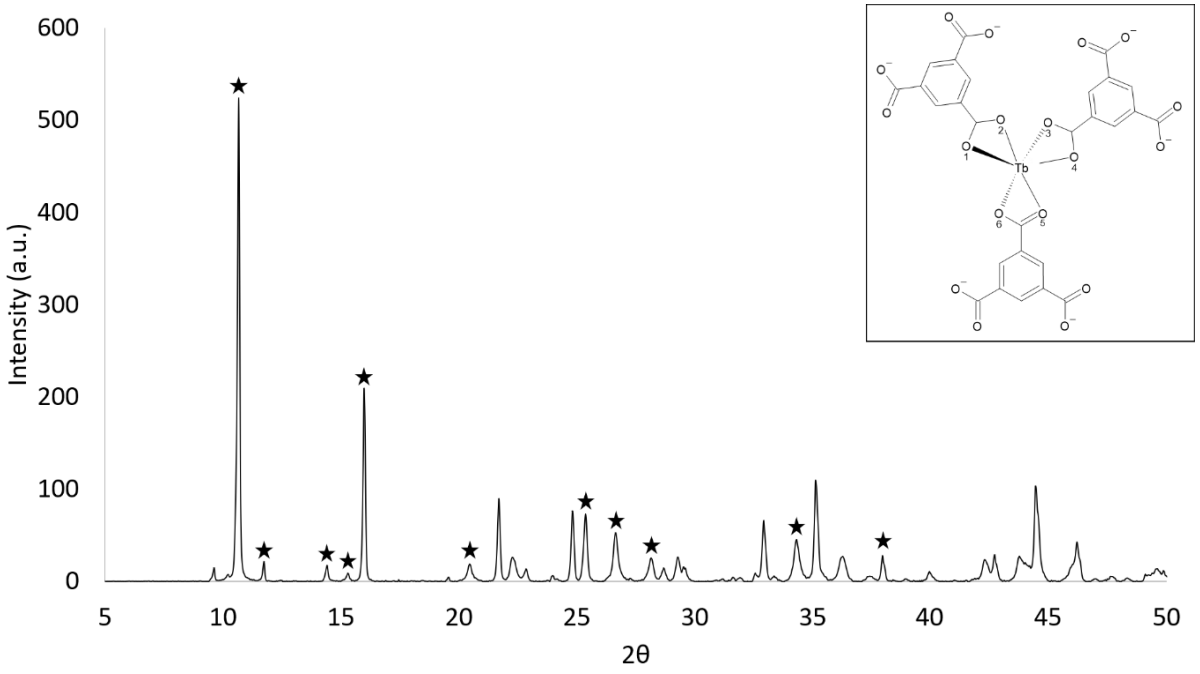

Figure 2-6: XRD pattern of as-prepared MW1-Tb. Stars indicate peaks most similar to literature. The insert represents the expected structure of the MOF as indicated by literature.

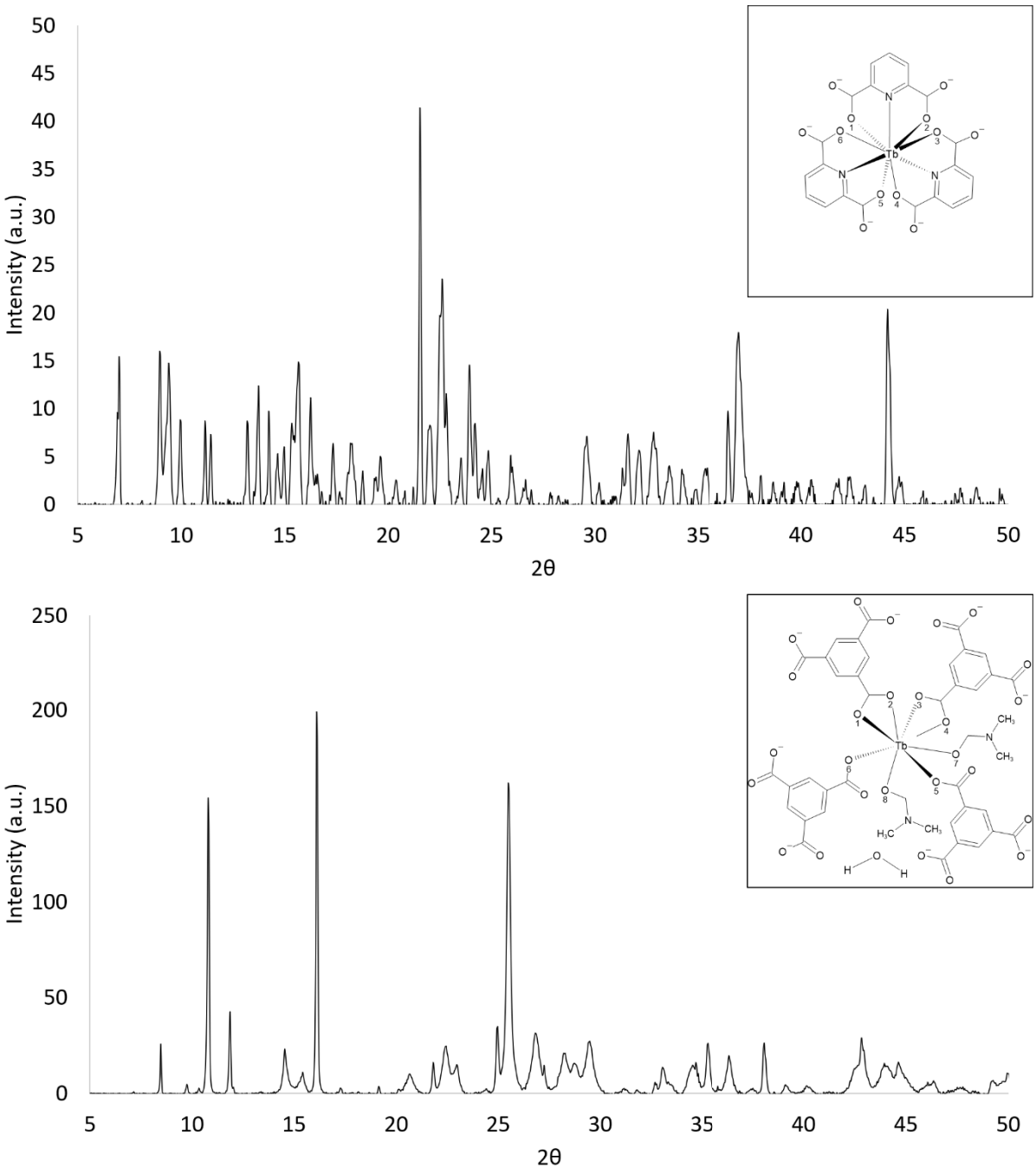

Figure 2-7: XRD pattern of as-prepared MW2-Tb (top) and MW3-Tb (bottom). The insert represents the expected structure of the MOF as indicated by the literature.

The FTIR spectrum collected for each synthesised MOF identified the critical functional groups present within the synthesised structures. *Figure 2-8* illustrates the differences between the metal core (grey line) and ligand precursors (black line) against a representative MOF structure (red line). All MOF spectra collected can be found in Appendix 2. Within all spectra, no nitrate-related peaks above 3400 cm^{-1} were observed, indicating that the nitrate ions from the precursor, $Ln(NO_3)_3.xH_2O$ (x = 5 or 6), detached from the metal core. There was evidence of slight spectral fluctuations

observed in the intensity and shape of the peaks, which is not uncommon and results from the bridging mode of the ligands [378, 379]. For MOFs containing the BTC ligand (SH2-MOFs, MW1-Tb and MW3-Tb), the lack of peaks corresponding to a C=O stretch at 1624 cm^{-1} indicates complete deprotonation of the H_3BTC and suggests that the starting material is fully consumed [183, 206] (*Figure 2-8a*). For SH3-Gd, a reduction in C=O bond strength is observed through peak shifting from 1655 cm^{-1} to 1605 cm^{-1} and peak weakening at 1528 cm^{-1} to allow the coordination of the metal ion and the oxygen [380, 381] (*Figure 2-8b*). In the MW2-Tb MOF spectra, complete deprotonation of the carbonyl groups is evident through the absence of characteristic C=O bands at 1694 cm^{-1} [382, 383] (*Figure 2-8c*).

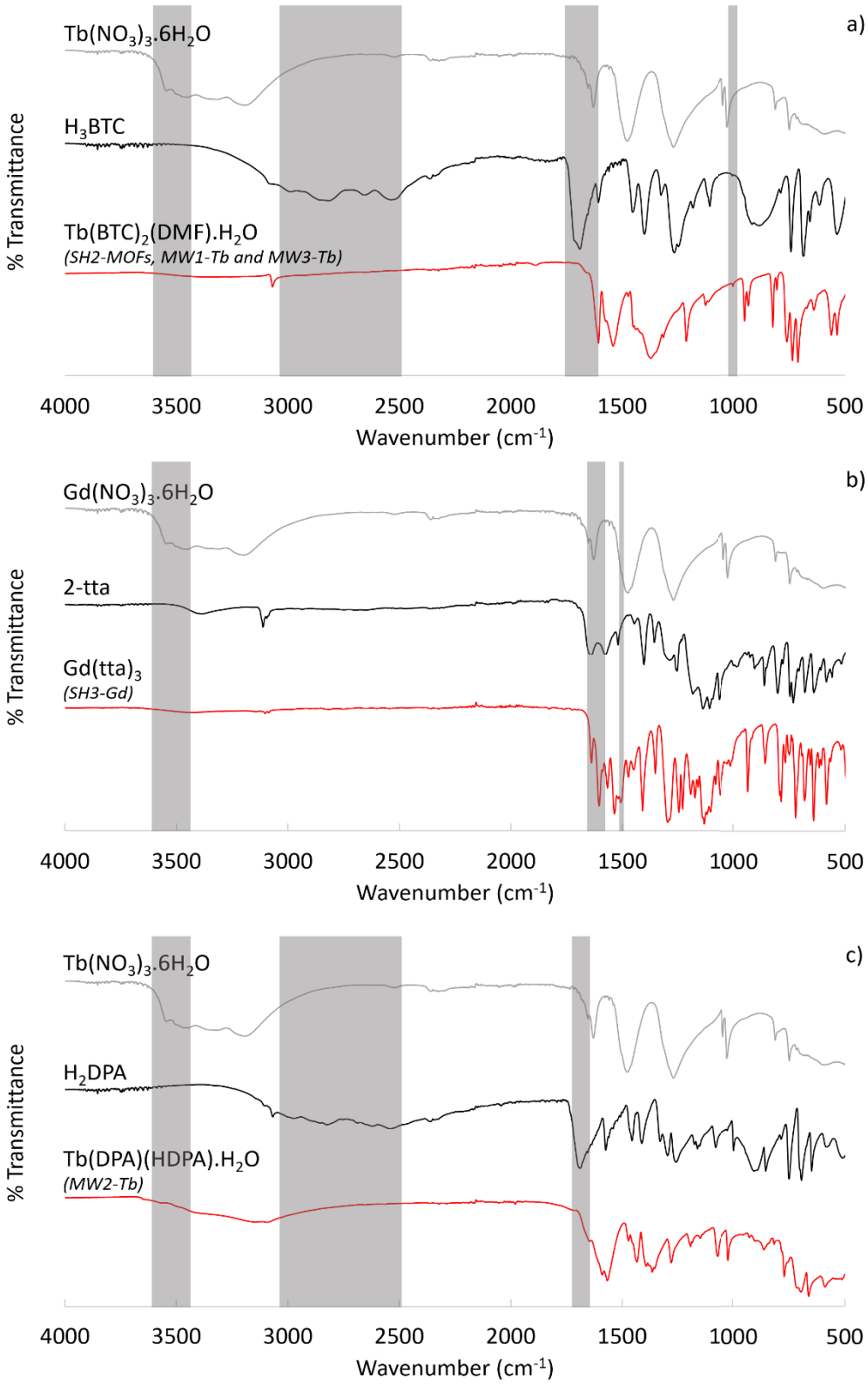

Figure 2-8: Comparison of metal core (grey line) and ligand (black line) precursors and the synthesised MOF (red line). Spectra are representative MOFs containing a) H_3BTC ligand; b) Htta ligand and c) H_2DPA ligand. Grey shading represents peaks associated with the starting material (metal core and ligand) that should not be present in the final product.

The data obtained from the FTIR analysis of MOFs synthesised from SH2 and MW3 outlined functional groups resulting from the BTC and DMF molecules in the synthesised MOFs, which were consistent with the literature [372, 378]. Regardless of the metal core incorporated into the framework or the synthetic route, the spectra from these MOFs contained similar peak positions and shapes (*Table 2-10*). Focusing on SH2-Tb, a broad band ranging from 3600–3100 cm^{-1} is visible, which illustrates an O–H stretching vibration indicating the presence of H_2O molecules in the structure [384]. The asymmetric and symmetric carboxylate peaks at 1540 and 1371 cm^{-1}, respectively, are evident of the BTC constituent [206]. Investigating the ionic values (Δν = 160–174 cm^{-1}) between the metal core and the ligand oxygen atoms indicates bidentate bridge coordination [385, 386]. A C=C stretch was observed at 1576 cm^{-1}, indicative of the BTC benzene ring [387]. This weak – medium C=C stretch was not observed in SH2-Gd, due to being eclipsed by the strong peak at 1541 cm^{-1}. The peaks at 1606, 860, 757 and 637 cm^{-1} are assigned to the 1,3,5 trisubstituted BTC ring [372]. For the coordinated DMF molecule, the bands at 3068 and 1212 cm^{-1} can be attributed to the C–H stretch and C–N stretch, respectively [372]. MW1-Tb contained all functional group peaks consistent with the coordination to the BTC ligand and was consistent with the literature [340, 386, 387].

Table 2-10: FTIR assignments of the primary vibrations associated with the synthesised MOFs containing a BTC ligand. ✕ = No peak expected.

Literature (cm^{-1})	Experimental (cm^{-1})							Assignment	Reference
	SH2-Tb	SH2-Er	SH2-Ho	SH2-Gd	SH2-Y	MW1-Tb	MW3-Tb		
3155 – 3400	3100 – 3600	3100 – 3600	3100 – 3600	3100 – 3600	3100 – 3600	✕	✕	O–H stretching	[384, 387]
3077	3068 (m)	3103 (w)	3083 (w)	3069 (m)	3102 (w)	3069 (m)	3068 (m)	C–H stretching	[372]
1615	1605 (s)	1613 (s)	1612 (s)	1605 (s)	1613 (s)	1605 (s)	1607 (s)	1,3,5 tri-substituted ring	[372]
1574	1576 (w)	1571 (m)	1571 (m)		1574 (m)	1575 (m)	1574 (w)	C=C stretching	[387]
1555	1540 (s)	1535 (m)	1535 (m)	1541 (s)	1538 (m)	1560 (m)	1539 (s)	$O–C–O_{as}$ stretching	[206, 386]
1383	1371 (s)	1375 (s)	1375 (s)	1367 (s)	1375 (s)	1388 (s)	1374 (s)	$O–C–O_s$ stretching	[206, 386]
860	820 (m)	828 (w)	822 (w)	819 (m)	825 (w)	823 (s)	820 (s)	C–H bending	[372]

In comparison with the literature, SH3-Gd contained bands consistent with functional groups associated with a thiophene ring and chain (*Table 2-11*) [388]. Two weak C–H stretch peaks at

3102 and 3090 cm^{-1} are attributed to the thiophene ring [389]. The C=C peak at 1536 cm^{-1} results from the thiophene ring [390]. The C–S stretch relating to the thiophene ring can be observed at the 1230 cm^{-1} and 1246 cm^{-1} peaks [389], followed closely by the asymmetrical and symmetrical C – F stretch of the trifluoromethyl group at 1193 and 1132 cm^{-1}, respectively [381, 388].

Table 2-11: FTIR assignments of the primary vibrations associated with the synthesised MOFs containing a tta ligand.

Literature (cm^{-1})	Experimental (cm^{-1})	Assignment	Reference
	SH3-Gd		
3118, 3109	3102, 3090	C–H stretching	[389]
1602	1604 (s)	$C=O_{thio}$	[381]
1535-1539	1536 (m)	C=C stretching	[390]
1524	1528 (w)	$C=O_{trifluoromethyl}$	[381]
1244, 1222	1246 (s), 1230 (s)	C–S stretching	[389]
1202, 1142	1193 (m), 1132 (m)	$C\text{-}CF_3$	[388]
722	727 (s)	C–H bending	[388]

The spectra observed for MW2-Tb contained peaks consistent with pyridine and carboxylate functional groups and were in accordance with the literature (*Table 2-12*) [383]. The peak between 3460 and 2820 cm^{-1} can be attributed to a mixture of O–H and N–H stretches resulting from adsorbed H_2O molecules and the uncoordinated pyridinium ion protonation, respectively [382, 391]. The peaks at 1589 and 1432 represent the C=N and C=C vibration of the pyridine ring, respectively [383]. Observing peaks at 1632 and 1364 cm^{-1} highlights the asymmetric and symmetric carboxylate stretch [336, 392]. The pyridine ring C–N peak is observed at 1279 cm^{-1} [393], followed closely by C–C stretch peaks at 1193 cm^{-1} and 1149cm^{-1} [383] and C–H in-plane bend at 1071 cm^{-1} and 1021 cm^{-1} [391, 393].

Table 2-12: FTIR assignments of the primary vibrations associated with the synthesised MOFs containing a DPA ligand.

Literature (cm^{-1})	Experimental (cm^{-1})	Assignment	Reference
	MW2-Tb		
3375	3460 – 2820 (m)	O–H stretching	[391]
3100	3460 – 2820 (m)	N–H stretching	[391]
1623	1632 (w)	$O–C–O_{as}$ stretching	[392]
1591	1589 (m)	C=N stretching	[383]
1435	1432 (s)	C=C stretching	[383]
1383	1364 (m)	$O–C–O_s$ stretching	[392]
1275	1279 (s)	C–N stretching	[393]
1193, 1155	1193 (m), 1149 (w)	C–C stretching	[383]
1069	1071 (s)	C–H bending	[393]

The structural elucidation identified that the remaining nine MOFs (SH2-Tb, SH2-Er, SH2-Ho, SH2-Gd, SH2-Y, SH3-Gd, MW1-Tb, MW2-Tb and MW3-Tb) contained differences in the 3D arrangement the components; however, the chemical composition was consistent with available literature. The variation in the 3D arrangement was not identified as being influential to the MOF structure and resulted in no removal of the nine MOFs.

2.3.4 Structural Suitability

As no MOFs were removed during the chemical validation, the remaining nine MOFs underwent structural characterisation via SEM-EDS and TGA analyses to ensure they would be suitable for incorporation into ammunition.

The morphology and size of each synthesised MOF were analysed under SEM (*Figure 2-9*). The shape of all MOFs synthesised via the SH2 route were consistent with rectangular rod-like crystallites; however, ranged in length between 13 – 51 µm. The synthesis of SH3-Gd resulted in small spherical particles ranging between 1 – 3 µm in size. Within the MW-MOFs various morphology and sizes were observed; MW1-Tb presented with long rod morphology ranging between 13 – 18 µm, MW2-Tb was observed as an agglomerate of cuboid particles between 22 – 32 µm, whereas MW3-Tb particles showed the smallest oval morphology ranging from 4 – 7 µm (*Figure 2-9*). One advantage related with MOF synthesis is their structural tuneability through manipulating the compositional and process parameters, which affect the stages associated with MOF formation [394, 395]. The self-assembly and morphology of the MOF particle is primarily influenced by the reaction energy contributed from the synthetic route [204]. The assembly of the

SH-MOFs and MW-MOFs are approached via two different crystallisation processes due to their reaction mechanisms. The SH synthesis relies on external heat to generate a pressurised, static environment conducive to self-assembly [352]. Whereas the MW synthesis emits radiation energy which forces polar molecules into a constant state of stimulation in order to align the dipoles [357]. This indicates that the MOFs synthesised via different synthetic routes will present with different morphology and size, even if the same precursors are present in the reactions [396]. The morphology of MOFs can be affected by changes in the compositional parameters, such as molar concentration of the reactants, variation of ligands, solvation effects, and pH [397, 398]. The morphology of all SH2-MOFs contains a consistent rod shape indicating that the metal core does not influence the surface morphology of the MOF. This is supported by a study conducted by Laurinkenas et al. [378], where a total of 14 $Ln(BTC)(DMF)_2(H_2O)$ MOFs (Ln = La, Ce, Pr, Nd, Sm, Eu, Tb, Dy, Ho, Er, Tm, Yb and Lu) illustrated that most of the MOFs formed rectangular plate-like crystallites [378]. The obvious morphological distinction between the SH2-MOFs and SH3-MOFs correlates to the variation in ligands used, as a result of their structural shape and further coordination to the metal core [399]. The ligand effect is also observed between the MW-MOFs. Although MW1-Tb and MW3-Tb both contain the same ligand, BTC, the change in the reactants molar concentrations, solvation effects and the additional DMF molecules present in the framework influence the shape of the MW3-Tb [396]. The disparity in size observed between the MOFs is directly linked to differences in process parameters, specifically the length and temperature of the reaction [397, 398]. It was evident that the reactions exposed to longer reaction lengths and higher temperatures produced larger particles. The additional time allows extra bonds to form between the metal core and ligands increasing the nucleation and formation of MOF crystals [203, 205]. The aggregation observed in SH3-Gd and MW3-Tb results from the small size of the individual spherical particles [400]. For MOFs containing the same compositional parameters (SH2-Tb and MW3-Tb), but variation in synthesis routes can also be observed to contain differences in the morphology and size of their particles. Jung et al. [401] and Ahnfeldt et al. [402] evaluated the particle size of MOF-177 and CAU-1-$(OH)_2$, respectively. For MOF-177, three different synthesis routes were evaluated (SH, MW and US). It was found that the SH particles were 30 times larger than both the MW [401]. A similar trend was observed with CAU-1-$(OH)_2$, across different synthesis temperatures (120°C, 125°C and 130°C), where it was reported that MW heating produced MOF particles 2-3 times smaller than conventional SH heating [402]. In both studies the molar concentration of the reactants were kept the same, identifying that as the reaction time decreased the MW synthetic route can produce a higher population of small crystals due to the heating process [396]. It is possible that the variation observed between the

novel MOFs in morphology and size can influence the MOFs properties and ability to act as LGSR [204]. A comparison with literature to identify whether there were any similarities with the synthesised MOFs and published MOFs would have confirmed this. However, this comparison was not possible as the literature provides information on the SEM-EDS analysis of discharged LGSR and not the pure MOF. One study by Lucena et al. [173] briefly presents the morphology of the pure MOF, $ZnAl_2O_3:Eu^{3+}$ and stated that while this MOF presents in large aggregates, it was still able to generate LGSR on the shooter's hands, firearm and firing range [173]. Through comparison with the $ZnAl_2O_3:Eu^{3+}$ particle a prediction into whether the synthesised MOFs will be suitable for LGSR visualisation cannot be determined, due to the variation in reactants and synthetic routes.

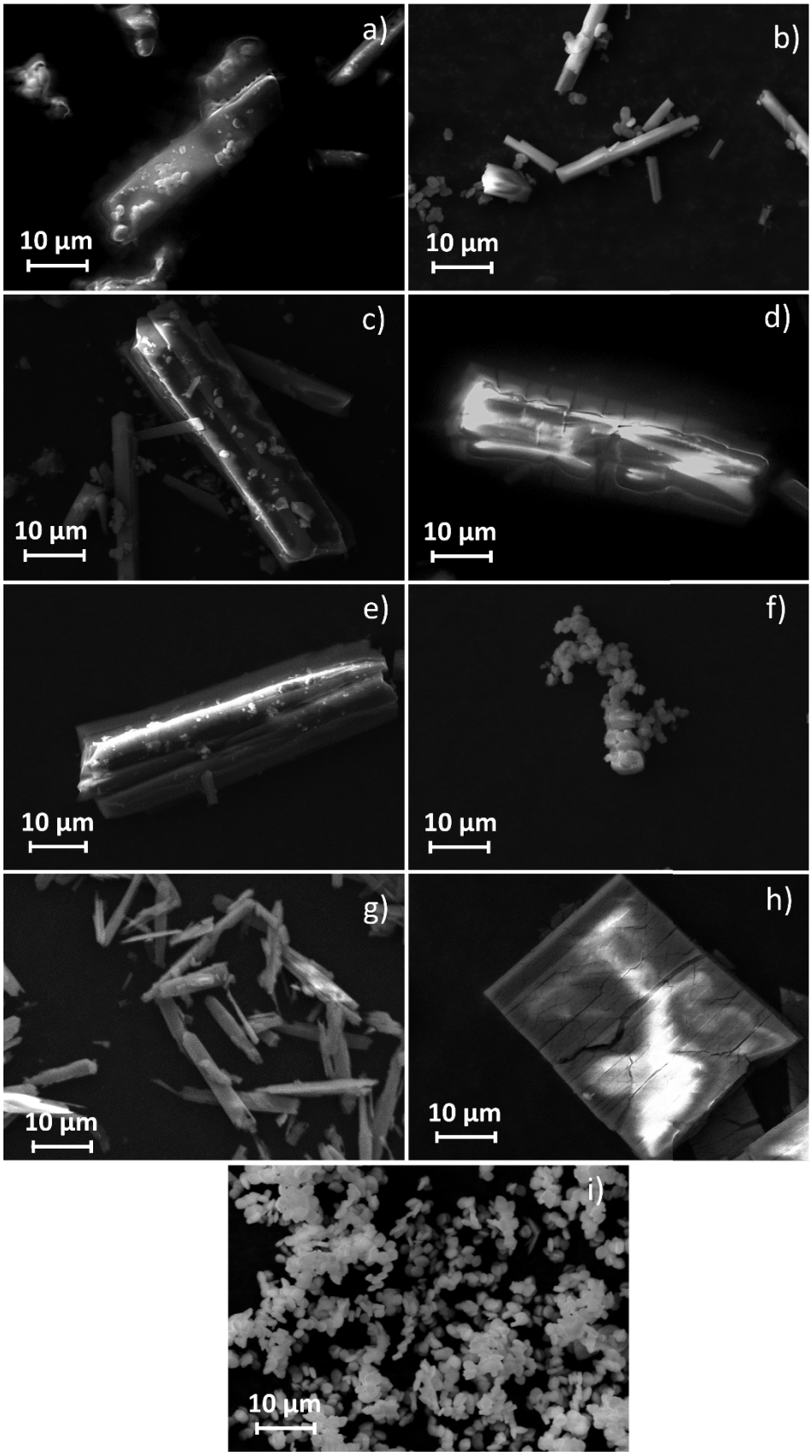

Figure 2-9: SEM images of a) SH2-Tb; b) SH2-Er; c) SH2-Ho; d) SH2-Gd; e) SH2-Y; f) SH3-Gd; g) MW1-Tb; h) MW2-Tb; i) MW3-Tb collected at 15.00 kV, mag = 1.5 K and WD = 10 mm.

The EDS spectrum automatic peak identification for each MOF detected the respective characteristic peaks of the critical elements confirming the presence of the metal core, as well as carbon, nitrogen and oxygen (from the ligand) (Appendix 2). All MOFs containing the same metal core presented similar spectrum, regardless of synthetic route. The EDS spectrum of all Tb-MOFs (SH2-Tb, MW1-Tb, MW2-Tb and MW3-Tb) detected characteristic Lα and Mα transition peaks at 6.27 keV and 1.24 keV, respectively. The EDS analysis detected characteristic Lα and Mα transition peaks at 6.95 KeV and 1.39 KeV for SH2-Er and 6.73 KeV and 1.36 KeV for SH2-Ho. For both Gd-MOFs (SH2-Gd and SH3-Gd) the peaks detected at 6.05 keV and 1.19 keV were indicative of the characteristic Lα and Mα transition peaks, respectively, for Gd^{3+} elements. Detection of only the Mα transition peak was observed for SH2-Y at 1.91. A Lα transition peak should have been observed at 14.93 KeV; however, was not detected in the MOF or in the precursor, $Y(NO_3)_3.6H_2O$, spectrum. This could be attributed to the accelerating voltage of the instrument (15 kV), for characterisation, was not sufficient enough for excitation of the Y^{3+} Lα transition peak. The detection of only the Mα transition peak has been reported when analysing Ti-17Al-27Nb-0.85Y alloys [403] and Eu:Y_2O_3 nanoparticles [404]. Because the Lα transition peak is substantially smaller than the Mα transition peak, it could also be lost in the baseline. With the automatic peak detection, the EDS analysis can differentiate the metal elements from each other, as well as from traditional GSR, indicating it would be suitable to use as a chemical identifier in the detection of the incorporated MOF in LGSR. The determination of the MOF thermal stability highlighted its capability to withstand firearm discharge temperatures. The TGA curves of the synthesised MOFs displayed multistage degradation of the frameworks when exposed to extreme temperature in an oxidative environment. During the degradation of MOFs, two factors are considered; ligand-centred and metal core-centred degradation. Ligand-centred degradation plays a large role in the curve shape observed in the main mass loss event [405], while meal-centred degradation affects bond strength and temperature for degradation.

All MOFs showed exothermic events consistent with the degradation of the solvent and ligand components of the framework (*Figure 2-10*). The differential thermal analysis (DTA) plot highlights the first exothermic events occurring prior to 200°C was observed in SH2-MOFs and MW2-Tb, and is consistent with the loss of H_2O molecules [406]. In the region of 20°C – 100°C, a decrease in the TGA curve corresponds to the loss of free H_2O molecules, which have been absorbed into the MOF from the moisture in the air, due to their hygroscopic nature. The losses recorded between 100°C – 200 °C result from the loss of guest H_2O molecules, which are coordinated into the MOF framework [407]. The carboxylate ions from the ligand molecule bond to the metal core via either a monodentate or bidentate coordination mode. The Ln–O–C bond from the bidentate

coordination mode eliminates room for guest molecules (such as H_2O) to enter the framework [408]. However, a monodentate coordination mode introduces the option for guest molecules (such as H_2O) to enter and become encapsulated within the framework and can impact the framework and extent of distortion [405]. There was no mass loss observed in this temperature range for SH3-Gd, MW1-Tb and MW3-Tb, indicating an absence of H_2O molecules, which correlates to the FTIR results in Section 2.2.3.

Two common mass loss events are observed in each of the SH-MOFs (*Table 2-13* and *Figure 2-10a-e*). The first mass loss event is observed as a two-step mass loss, which occurs at ranges of 84°C – 106°C and 278°C – 293°C. SH2-Gd is the only MOF that contains a one-step mass loss in this temperature range. The mass loss at this temperature range indicates a loss of H_2O and two DMF solvent molecules, respectively. The main event loss occurred at a range of 430°C – 590°C and was attributed to the loss of the BTC ligands (and one DMF molecule for SH2-Gd) bonded to the framework. Again, the actual mass loss results agree with the theoretical mass loss for each synthesised MOF. For MW1–Tb (*Figure 2-10g*) and MW3–Tb (*Figure 2-10i*), the DTA plots highlight only one exothermic event occurring at 450°C – 540°C and 430°C – 520°C, respectively (*Table 2-13*). In MW1-Tb, the mass loss is attributed to the degradation of the three BTC ligands coordinated to the metal core. While the mass loss in MW3-Tb results from a loss combination of two DMF solvent molecules and one BTC molecule. Focusing on the MOFs with a BTC ligand, although the TGA curves appear similar, there are some differences in the temperature of the main mass loss events, as well as the number of degradation steps observed.

Table 2-13: Theoretical mass loss associated with the synthesised MOFs containing a BTC ligand.

Mass Loss Event	MOF	Actual Mass (%)	Theoretical Mass (%)
84°C – 293°C	SH2-Tb	18.2	24.6
	SH2-Er	21.3	24.3
	SH2-Ho	20.4	24.4
	SH2-Gd	10.0	14.1
	SH2-Y	26.0	28.4
430°C – 590°C	SH2-Tb	38.6	39.2
	SH2-Er	38.9	32.6
	SH2-Ho	39.4	32.7
	SH2-Gd	43.9	43.3
	SH2-Y	45.7	38.2
	MW1	60.5	57.4
	MW3	50.8	56.3

Between the SH2-MOFs there is a 40°C temperature difference at the main mass loss event occurs. The five metal cores were chosen due to their similar chemical and physical behaviour, with four belonging to the lanthanide group and one a d-block metal. The slight difference in their properties; however, has the ability to affect how the framework distorts during the desolvation process [405]. This observation is supported by a study by Jiang et al. [409], who compared five $Ln(BTC)(H_2O).(DMF)_{1.1}$ (Ln = Y^{3+}, Tb^{3+}, Dy^{3+}, Er^{3+} and Yb^{3+}) MOFs and highlighted a temperature difference of 80°C in the main event loss for [409]. A comparison between the synthesised MOFs and Jiang et al. [409] can be conducted for the Tb-MOF, Er-MOF and Y-MOF. In both studies, the Tb-MOF had the lowest degradation temperature, followed by the Er-MOF and Y-MOFs. This variation in the degradation curve can be explained by the metal core-centred degradation mechanism, where some metal cores require higher temperatures to begin the degradation of the framework [405]. The reason for this can be linked to the carboxylic bond between the metal core and ligand. Depending on the metal core, the strength of the bonds within the framework backbone to prevent easy pyrolysis can vary [409]. Another main difference was the number of degradation steps involved in the TGA curve between 25°C – 356°C. The curve patterns ranged from containing 1-step to 4-step mass loss events, which has been observed in the literature. Li et al. [206] evaluated six $Ln(BTC)(DMF)_2.H_2O$ MOFs and observed a 2-step mass loss. The two mass loss events occurred in the ranges of 35°C – 250°C (H_2O and DMF) and above 375°C was attributed to the 'remaining' framework (one DMF solvent molecule and one BTC ligand) [206]. Another 2-step mass loss curve was observed in Dang et al. [372] during the evaluation of $Eu(BTC)(H_2O).DMF$. A mass loss measuring at 19.88% and 40.42% in the temperature range from 100°C – 500°C [372] was recorded. The first mass loss agreed with the loss of a coordinated H_2O molecule and one guest DMF molecule, while the second mass loss was consistent with the loss of the organic ligand [372]. Alternatively, Fonseca et al. [410] observed three weigh loss events occurring between 30°C – 350°C [410]. The mass loss was calculated to be 23.46% and indicated that 1.5 H_2O and one DMF were lost during this gradual degradation. Above 400°C, the main mass loss event of 39.9% was indicative of the BTC ligand degradation [410]. Comparing the literature and the SH2-MOFs it is evident that the number of steps involved in a TGA curve can vary even if the same constituents are present in the MOF and do not affect the final product present after the main mass loss event. Looking at MW1-Tb, the 1-step degradation, where all three BTC ligands are lost at 450°C – 540°C, is consistent with the Tb(TMA) TGA curve outlined in Souza et al. [385]. It was suggested that because Tb^{3+} ions contain a small ionic radius, the spatial conformation is likely to form an anhydrous framework due to the robust coordination of the BTC ligands [385]. It has also been suggested that differences in sample weight within the crucible, morphology and size of the MOF

framework and filling conditions can affect the shape of the curve, without affecting the temperature of mass loss events [411]. The same reasoning can be applied to MW3, which follows a similar TGA curve, despite having two DMF solvent molecules in the framework. Although there are slight differences in the TGA curves, it is evident that the synthesised MOFs are degrading at a similar rate and pattern to published literature.

The DTA plot of the SH3-Gd MOF highlights two exothermic events occurring at 260°C – 560 (*Figure 2-10f*). The main mass loss of 51.3% (theoretical: 46.2%) is consistent with the loss of two tta ligand molecules, while the second mass loss of 19.0% (theoretical: 23.1%) can be attributed to the final tta ligand. When comparing SH3-Gd to the synthesis literature for $Eu(TTA)_3 \cdot 3H_2O$ it is evident that the TGA curves follow a similar trend [54]. Lui et al. [54] indicated that there were three exothermic phenomena; the first at 178°C, a second at approximately 300°C and the final at 477°C. The first peak, indicative of a loss in H_2O is not observed in SH3-Gd. This difference in curve could be attributed to the hygroscopic nature of the MOF and how it was dried after synthesis. The second and third mass loss events are present in both SH3-Gd and $Eu(TTA)_3 \cdot 3H_2O$ and indicate that this framework undergoes a gradual degradation process [54]. The major difference between SH3-Gd and $Eu(TTA)_3 \cdot 3H_2O$ is the visual appearance of the TGA curve; SH3-Gd contains steep and distinctive mass loss events, while $Eu(TTA)_3 \cdot 3H_2O$ is less defined. It is possible that these visual differences can be attributed to the atmospheric conditions of the TGA. Lui et al. [54] does not specify whether an N_2 or O_2 atmosphere was applied to the system, which could affect the TGA degradation curve [412, 413].

A 3-step degradation process was observed in the MW2-Tb TGA curve (*Figure 2-10h*). Following the loss of H_2O event between 85°C – 163°C, the second and third mass loss event occurred at 290°C – 330°C and 410°C – 510°C, respectively. The second and third mass loss events collectively result in a 57.9% mass loss (theoretical: 61.4%) and can be attributed to a gradual degradation of the coordination bonds between the ligand and the metal core. Four studies evaluating the thermal degradation of MOFs containing DPA ligands present spectra following a similar 3-step degradation pattern. Gao et al. [57], Zhou et al. [56], Tan et al. [78] and Lopez-Ruiz et al. [414] evaluated $Nd(DPA)(H_2O)_{1.5}$, $Na_3Tb(DPA)_3\ 8H_2O$, $Eu(DPA)_3$ and Eu_2DPA_3, respectively. All studies found that the first mass loss event was consistent with the loss of H_2O. The second and third mass loss events were explained to be a result of the gradual degradation of the DPA ligand from the metal core (actual: 67.0%/ theoretical: 69.6%). Differences could be noticed between the curves within the studies; however, the completion of the final mass loss event indicated a total loss of approximately 60% [414], 70% [57] and 75% [78]. Zhou et al. [56] had the lowest mass loss of approximately 50%, and this can be factored into the mixed-metal core containing both Na^+ and

Tb^{3+} ions within the framework [409, 411]. Following the distinctive exothermic events in all MOFs, no major exothermic reactions between 600 – 1500°C occur. The remaining components following the mass loss events was consistent with a single metal core and the coordinated oxygen molecules from the ligand (*Table 2-14*).

Table 2-14: Comparison of actual mass remaining from TGA curve and theoretical percent mass remaining for the synthesised MOFs, and product remaining.

MOF	Actual mass remaining (%)	Theoretical mass remaining (%)	Final Product
SH2-Tb	42.6	42.6	Tb_2O_3
SH2-Er	39.8	43.0	Er_2O_3
SH2-Ho	40.2	42.9	Ho_2O_3
SH2-Gd	46.1	42.0	Gd_2O_3
SH2-Y	28.3	33.4	Y_2O_3
SH3-Gd	29.7	30.7	Gd_2O_3
MW1-Tb	39.5	42.6	Tb_2O_3
MW2-Tb	33.0	30.5	Tb_2O_3
MW3-Tb	49.2	43.7	Tb_2O_3

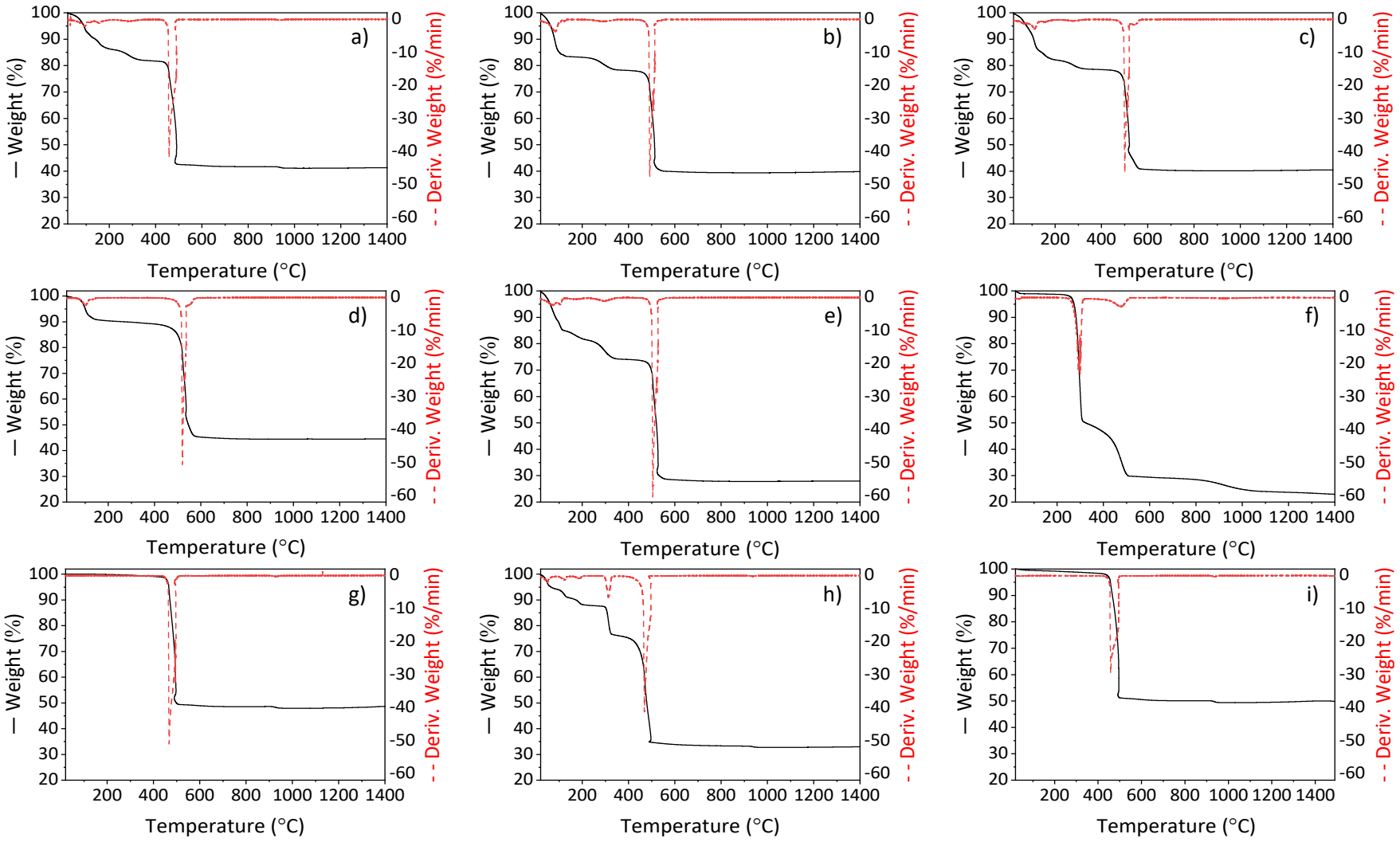

Figure 2-10: TGA curves (black solid line) and DTA plots (red dotted line) of synthesised MOFs: a) SH2-Tb; b) SH2-Er; c) SH2-Ho; d) SH2-Gd; e) SH2-Y; f) SH3-Gd; g) MW1-Tb; h) MW2-Tb; i) MW3-Tb

When comparing the novel MOFs to the published MOFs, there are a number of variations ranging from differences in the metal core, ligand, solvents, molar concentrations and synthetic route. Among the published MOFs [78, 176, 180, 183, 186], it is evident that ligands containing carboxylates (Hbtec and BTC) begin degradation later than N-donating ligands (PIC and TBZ) (*Table 2-15*). This is attributed to the strength of the Ln-O-C bond requiring higher temperatures to cleave the ligand from the lanthanide. The degradation temperature in SH2-Tb, MW1-Tb and MW3-Tb resembles the degradation of the Eu(BTC) MOF by Lucena et al. [176], an observation attributed to the use of the same ligand. This comparison suggests that the novel MOFs synthesised in this study are comparable to the published MOFs and may be able to withstand the discharge process in order to generate LGSR.

Table 2-15: TGA comparison of published MOFs [78, 176, 180, 183, 186].

MOF	Main Mass Loss Event				Reference
	Temperature Range (°C)	Percent Loss	Degradation Reason	Final Product	
$Eu(Hbtec)_3$	489 – 1100	51.5%	$Hbtec_3$ ligand	Eu_2O_3 and $Eu_2(CO_3)_3$	[186]
$Tb(Hbtec)_3$	476 – 822	51.1%	$Hbtec_3$ ligand	Tb_4O_7	[183]
Eu(BTC)	430 – 600	51%	BTC ligand	Eu_2O_3	[176]
$Eu(PIC)_3(NMK)_3$	300 – 500	84.5%	NMK ligand, PIC ligand	Eu_2O_3	[78]
EuTBZ	250 – 350	78.2%	NO_3 solvent, TBZ ligand	Eu_2O_3	[180]
TbTBZ		73.5%		Tb_4O_7	

While TGA is a good tool to understand at what temperature these MOFs are thermally stable until, it is not comparable to the temperature profile of a firearm discharge (1500 – 3600 °C in 1 – 2 ms) [359, 360]. The TGA method is set to increase 10°C per minute, which exposes the MOFs to a slow and steady heat for 150 minutes, when in comparison, the firearm discharge process would exceed this temperature for a brief moment before re-equilibrating to room temperature. The time in which the MOF is exposed to the temperature would play a role in how the MOF degrades and whether the luminescence can be seen after being heated.

The structural characterisation of the synthesised MOF indicated that all nine MOFs would be able to introduce additional characteristic identifiers in traditional GSR analysis, and are able to withstand thermal temperatures up to 350°C.

2.3.5 UV Photoluminescence Visualisation

The UV photoluminescence visualisation characterisation was the most insightful criterion as it showed whether the MOFs luminescence was suitable for the application of LGSR visualisation. Currently, literature evaluating the application of MOFs for LGSR visualisation has focused on implementing 254 nm UV light sources (*Table 1-10*). Shorter UVC wavelengths have been linked to damaging or degrading DNA [341, 342], making it problematic for investigators to use. The application of longer wavelengths, specifically 365 nm, to visualise LGSR at a crime scene would be beneficial as it minimises additional risk to the potential shooter and investigators.

The spectrophotometer analysis was used to confirm that the observed characteristic emissions from the synthesised MOFs were consistent with the available literature. However, because the spectrophotometer only provides a photoluminescent spectrum, and is not a common instrument within forensic laboratories [187], it is limited in its potential use in real-world applications. The additional application of the VSC, Polilight® and Labino® lamp provided the visual indicator of the MOFs luminescence under UVA excitation conditions, which was a vital requirement of this study (Appendix 2). It was seen that the visual identity of the MOFs was uniform between the VSC, Polilight® and Labino® lamp, so only the VSC images are included in this chapter as representative images of the MOF visualisation. From the photoluminescence analysis, it was evident that the MOFs were able to be grouped into three different luminescent phenomena; (i) SH2-Er and SH2-Ho (*Figure 2-11*), (ii) SH2-Gd, SH2-Y and SH3-Gd (*Figure 2-12*), and (iii) SH2-Tb, MW1-Tb, MW2-Tb, MW3-Tb (*Figure 2-13)*.

Research has indicated that Er-MOFs and Ho-MOFs contain unique photoluminescence that extends between the visible and NIR regions [415-418]. This is due to the paramagnetic properties of these metal cores affecting the LMCT. The ligand fluorescence is weakened and causes the f-f emission bands from the Er^{3+} and Ho^{3+} to be visible when using longer NIR wavelengths [419]. Synthesis literature by Li et al. [206] excites the $Ln(BTC)(DMF)_2.H_2O$ with a UV wavelength (λ_{ex} = 235 nm) and reports a photoluminescence in an emission range of 320 – 440 nm [206]. Focusing on the UV-visible range, both SH2-Er and SH2-Ho present a max peak at 425 nm consistent with the literature (*Figure 2-11*). These observed spectra can be attributed to the $\pi^* \rightarrow$ n intraligand emission; however, the f-f transitions associated with the Er^{3+} and Ho^{3+} metal cores emit in the NIR region during UV excitation. The inserts associated with SH2-Er and SH2-Ho in *Figure 2-11* highlight that under excitation at 365 nm it is not possible to visualise the pure MOF powder in the VSC. This is evident in Zhao et al. [420], and Martin-Ramos et al. [416], where three Er-MOFs; $ErAg_3(L)_3(H_2O)$, $ErAg_3(HO - L)_3(H_2O)$ and $Er_2(nd)_6(\mu\text{-bpm})$, were excited with UV wavelengths (λ_{ex} = 305 nm – 375 nm) and in each instance reported a single broad peak at 1550 nm [416, 420]. Two studies by Dang et al. [421] evaluated the

luminescent properties of a total of five different MOFs; $Ho(dbm)_3phen$, $Ho(dbm)_3bipy$ and $Ho(dbm)_3TPPO$ [418], and $Ho(hfth)_3dafone$ and $Ho(pfnd)_3dafone$ [421]. In each instance, regardless of ligand or excitation wavelength (λ_{ex} = 392 nm – 425 nm), three peaks were observed in the NIR range at 985 nm, 1195 nm and 1495 nm [418, 421]. The inability to visualise NIR emission without additional equipment indicates that SH2-Er and SH2-Ho would not be suitable for the visualisation of LGSR.

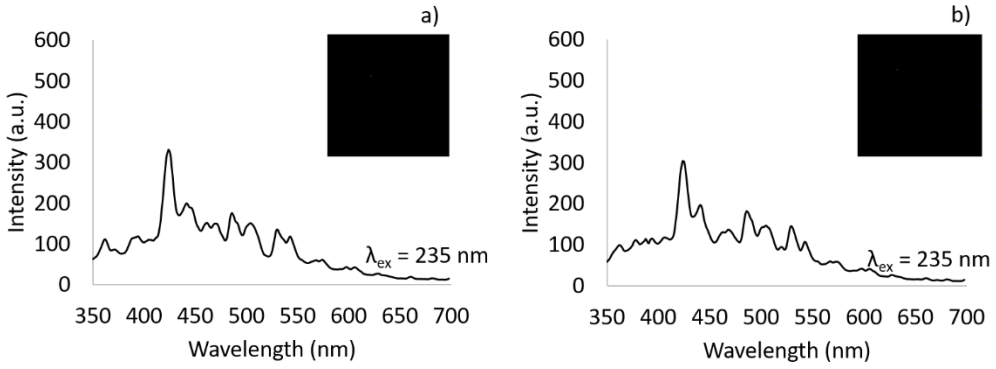

Figure 2-11: Photoluminescence emission spectra of a) SH2-Er and b) SH2-Ho captured from the spectrophotometer. The inserts represent the pure MOF samples in the VSC (λ_{ex} = 365 nm; ISO = 100; integration time = 500 ms; iris = 100% and mag = 60x).

Three peaks are observed in the photoluminescence spectra of SH2-Gd and SH2-Y, while SH3-Gd contains a single broad peak (*Figure 2-12*). The max peaks in SH2-Gd and SH2-Y are located at 489 nm (λ_{ex} = 290 nm) and 511 nm (λ_{ex} = 315 nm), respectively, which is consistent with the literature [385]. While not observed in the literature spectra, the additional peaks at 530 nm – 550 nm are attributed to the intraligand $\pi \rightarrow \pi^*$ transitions. This variation in spectra could be due to the temperature difference applied during analysis between the literature (-196°C) and synthesised MOFs (room temperature, 21°C). As the temperature applied in Souza et al. [385] is lower, the peak intensity increases allowing small peaks to be observed [422, 423]. SH3-Gd presented a max peak at 521 nm (λ_{ex} = 380 nm), which was similar to the literature [367]. The observed luminescence of the Gd-MOFs and Y-MOF can be attributed to the intraligand $\pi \rightarrow \pi^*$ transitions due to the T1 state energy of the ligand being lower than the first excited state of the ion [424, 425]. The intensity observed in the spectrum of SH2-Gd, SH2-Y and SH3-Gd suggests it would be difficult to observe the MOF.

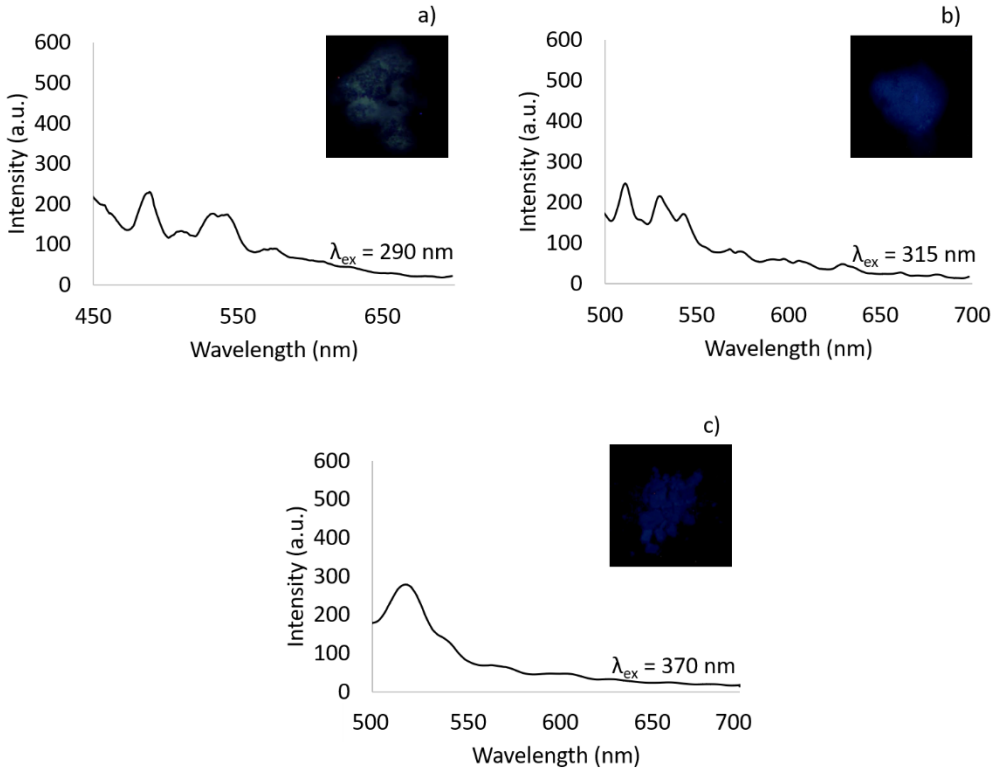

Figure 2-12: Photoluminescence emission spectra of a) SH2-Gd; b) SH2-Y and c) SH3-Gd captured from the spectrophotometer. The inserts represent the pure MOF samples in the VSC (λex = 365 nm; ISO = 100; integration time = 500 ms; iris = 100% and mag = 60x).

The observed visual luminescence of the MOFs from the VSC, Polilight® and Labino® lamp was as predicted from the emission spectra. No visual luminescence was observed for SH2-Er and SH2-Ho during visualisation with the VSC. While MOFs with Gd^{3+} metal cores were initially predicted to provide an acceptable visual luminescence, a weak blue visual luminescence was observed for in SH2-Gd and SH3-Gd when exposed to 350 – 365 nm wavelengths (VSC, Polilight® and Labino® lamp). Similarly, while it was possible to visualise SH2-Y, only a weak blue visual luminescence was captured from this MOF. While it was possible to visualise, the pure MOFs containing Gd^{3+} or Y^{3+} metal cores, the visualisation of LGSR would be challenging to observe at a crime scene, indicating that these MOFs are not suitable for further evaluation.

Regardless of ligand or excitation parameters, each of the Tb-MOFs; SH2-Tb, MW1-Tb, MW2-Tb and MW3-Tb, contained the four characteristic green emission peaks assigned to the Tb^{3+} transitions ($^5D_4$ → ^7F_J, J = 6, 5, 4, 3) (*Figure 2-13*, *Table 2-16*) [230]. The presence of all four characteristic green emission peaks at the various excitation wavelengths supports that the luminescence is dependent on the metal core; however, the coordinated ligand may affect the intensity observed in the spectrum. In the MOF complex, the Tb^{3+} metal core undergoes an antenna effect energy transfer

process with the ligand to generate the luminescence observed [230]. All MOFs containing Tb^{3+} metal cores displayed an intense green visual luminescence during VSC analysis, further supporting why they are constantly considered for LGSR visualisation in literature.

Table 2-16: Photoluminescence transition assignments of the peaks associated with the synthesis of Tb-MOFs.

λ_{ex}	Literature (nm)		Experimental (nm)				Reference
	λ_{em}	Transition Assignment	SH2-Tb λ_{em}	MW1 -Tb λ_{em}	MW2 -Tb λ_{em}	MW3 -Tb λ_{em}	
254 nm or 302 nm	491	$^5D_4 \rightarrow {}^7F_6$	492	491	491	490	[172, 182, 206]
	548	$^5D_4 \rightarrow {}^7F_5$	547	548	546	546	
	585	$^5D_4 \rightarrow {}^7F_4$	585	585	584	585	
	622	$^5D_4 \rightarrow {}^7F_3$	622	622	621	622	

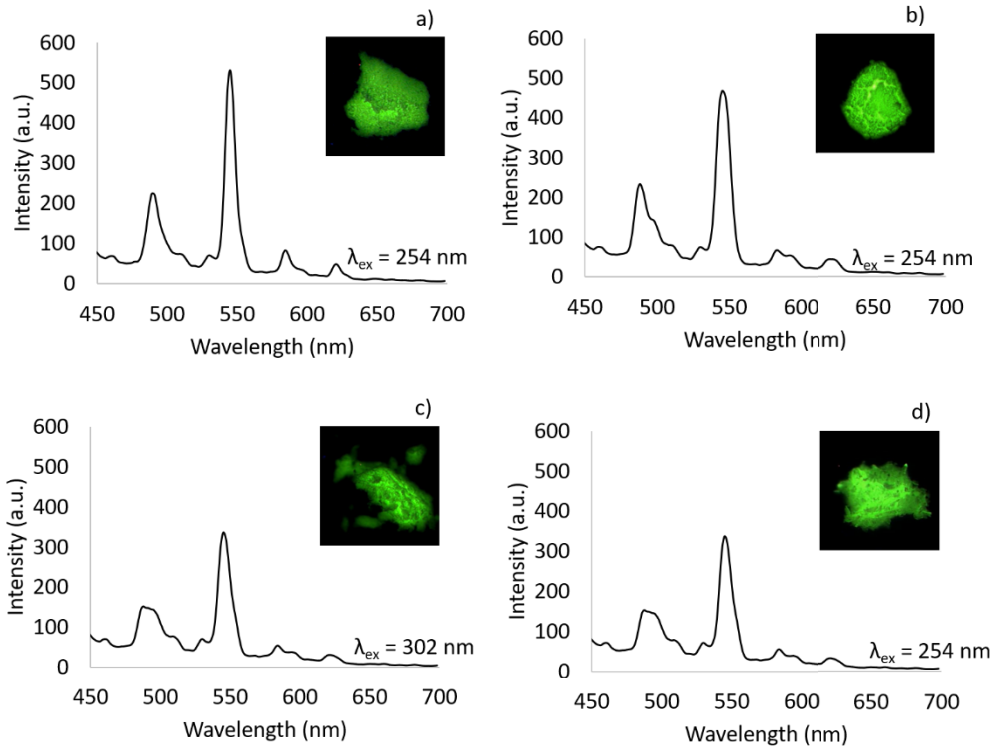

Figure 2-13: Photoluminescence emission spectra of a) SH2-Tb; b) MW1-Tb; c) MW2-Tb and d) MW3-Tb captured from the spectrophotometer. The inserts represent the pure MOF samples in the VSC (λ_{ex} = 365 nm; ISO = 100; integration time = 500 ms; iris = 100% and mag = 60x).

2.3.6 Characterisation Overview

Characterisation evaluated the chemical, structural and luminescent behaviour of 17 synthesised MOFs and was able to highlight four MOFs that would be suitable to undergo further evaluation

before incorporation into ammunition. The general characterisation focussed specifically on synthesis yield and cost, highlighting that eight novel MOFs would not be suitable for incorporation into ammunition from a production and sales perspective. The chemical (XRD and FTIR) and structural (SEM-EDS and TGA) did not remove any remaining MOF from further evaluation. The UV photoluminescence analysis identified five of the synthesised MOFs as unsuitable for visualising LGSR. This criteria characterisation was informative, in that it identified altering the metal cores (Er^{3+}, Ho^{3+}, Gd^{3+} and Y^{3+}) does not automatically produce suitable visualisation. The metal core must emit strong luminescence in the UV range before coordination with a ligand. This is evident with the Tb-MOFs containing a strong green luminescence as the precursor and coordinated within the MOF due to the characteristic *f-f* transitions. *Table 2-17* summarises the reason thirteen novel MOFs have been discontinued from additional evaluation.

Table 2-17: Summary of MOFs discontinued from initial general observations.

Criteria	**General Observations**		**Structural Elucidation**	**Structural Suitability**	**UV Photoluminescence Visualisation**	
Reason	Unsuitable Yield	Unsuitable production cost	None	None	No Visual Luminescence	Weak Visual Luminescence
MOFs Discontinued	SH1-Tb SH1-Er SH5-Tb SH5-Er SH5-Ho SH5-Gd SH5-Y	SH4-Gd	None	None	SH2-Er SH2-Ho	SH2-Gd SH2-Y SH3-Gd

Overall, the characterisation indicated that four MOFs; SH2-Tb, MW1-Tb, MW2-Tb and MW3-Tb, were most suitable according to the criteria applied. The greatest differences between these MOFs were observed in their synthesis yield and cost, along with their morphology. Both factors have the potential to affect the ability to incorporate these MOFs into ammunition or impact the performance of the LGSR, respectively.

The synthesis yield and cost of precursors are important considerations for the potential decision to formally incorporate MOFs into the production of either primer or propellant powders. MOFs containing fewer precursors and/or low molar concentrations, such as MW2-Tb, would be preferred for incorporation, as they contain a lower starting cost for synthesis. MW2-Tb was identified to cost approximately 60% less than SH2-Tb, MW1-Tb, and MW3-Tb; however, the synthesis yield and reaction time are other factors that can impact the production costs. Comparing the SH2-Tb MOF and

the MW-MOFs, it is obvious that the synthesis yield was not the largest contributor to impacting production costs (67% – 82%). While there was not a great difference between the yield obtained between the SH-MOFs and MW-MOFs, the reduced time required in the MW-assisted synthetic round highlights its efficiency and could be deemed as the favourable synthetic approach.

All MOFs were observed to contain distinctive morphological features. SH2-Tb and MW3-Tb, which contained identical chemical compositions, contained vastly different shaped and sized particles, which is expected due to the differences in synthetic routes [397, 426, 427]. SH2-Tb and MW1-Tb contained the most similar morphology, presenting with a rod-like shape but varied in their size. The impact of the particle morphology on the generation or dispersion of LGSR is a factor that has not yet been evaluated. Identifying whether these differences in the shape and size of particles will impact either the stability of the particle or how it interacts with GSR will provide further support into whether MOFs are suitable particles to incorporate into ammunition.

SECTION III: Stability

The FTIR and spectrophotometer spectra and visual luminescence pertaining to the chemical and luminescent stability of the pure MOFs were collected at monthly intervals; however, the data in this chapter has been presented in 6-month intervals (month 0, month 6, month 12, month 18 and month 24). This has been conducted to highlight the overall behaviour of the MOFs. Data pertaining to the full 24-month stability study can be found in Appendix 2.

2.3.7 Chemical Stability

The purpose of the FTIR stability analysis was to observe any changes in the critical functional groups present in the structures. To assess the stability of the structure two factors were analysed: the peak location and the peak intensity. It was hypothesised that if the peak location shifted or if the intensity of the peak reduced significantly, this would demonstrate the degradation of the MOF and would indicate its unsuitability for visualising GSR. Overall, the FTIR spectra for each MOF displayed no peak shifting or peak loss indicating that the structural formation of the particles did not degrade within the 24 months of assessment. The absence of a trend to indicate an overall decrease in peak intensity suggests that the functional groups making up the molecular bonds within the MOF structures were not reducing. Slight fluctuations were observed in the peak intensities for all MOFS, which were attributed to daily fluctuations in the IR beam signal intensity influencing the instrument inter-day variability. The structural stability of the MOF framework has been linked to the strength of the coordination between the metal ion and the ligand. Ligands with a highly rigid environment have been observed to produce robust frameworks that were less susceptible to degradation [428]. *Figure 2-14, Figure 2-15, Figure 2-16* and *Figure 2-17* highlight the structural behaviour of the Tb-MOFs at six-month intervals. The overall absence of peak shifting or loss of key functional group peaks indicated that the coordination arrangement of the chelating carboxylate groups from the BTC and DPA ligands have restricted bond movement [197, 428]. The level of restriction in the bond movements between the four MOFs is further impacted by the presence of guest molecules, such as DMF and H_2O (SH2-Tb and MW3-Tb), or the pyridine functional group within the DPA ligand (MW2-Tb).

The key spectral variations observed in the FTIR spectrum of the MOFs were located at 3600 – 3100 cm^{-1}, regardless of ligand, and could be attributed to the hygroscopic nature of the MOF [429]. Water instability has proven to be an issue with MOF frameworks as a result of guest H_2O molecules causing displacement of bound ligands, leading to the decomposition of the structure [429-431]. This was not observed in any of the synthesised MOFs, which suggested that the strong coordination bonds

between the metal core and ligands were causing the MOFs to be water-stable [242]. The isostructural MOFs SH2-Tb (*Figure 2-14*) and MW3-Tb (*Figure 2-15*) followed a similar trend in their structural stability over the 24 months. Both MOFs consisted of highly charged metal ions (Tb^{3+}) and carboxylate-based ligands (BTC) which enhanced the hydrophobicity of the compound [428]; however, the addition of the DMF into the framework increased the vulnerability against H_2O molecules entering the structure [432]. During month 0, SH2-Tb presented with a weak peak in the 3600 – 3100 cm^{-1} range which suggested that the initial complex was in a hydrate form, while MW3-Tb did not present with a peak in this region. This variation in the initial spectrum could be attributed to the synthetic route applied during the synthesis of the MOF (as discussed in Chapter 2). For both MOFs, by month 6, the repeated exposure to H_2O from the air during the stability analysis generated a broad O–H peak. The hygroscopic nature of these MOFs continued to absorb H_2O from the air until month 24 [378]. The level of H_2O absorption into the active sites of the framework can be attributed to the large pore size of the MOF [433]. Garg et al. [434] assessed MOF-76(Tb) as a humidity sensor and determined that while the MOF did absorb moisture from the air, the humidity sensing measurement displayed high or moderate impedance in low (11%) or high (98%) humidity conditions, respectively [434]. This indicated that while these types of MOFs were able to absorb moisture from air, contributing to the growing O–H peak, they were stable and retained their structure. Although there is a change in the intensity of these bonds, there is no evidence of shifting or loss of peaks, suggesting that the molecular structure of the MOFs, SH2-Tb and MW3-Tb, are not degrading over the course of the 24 months.

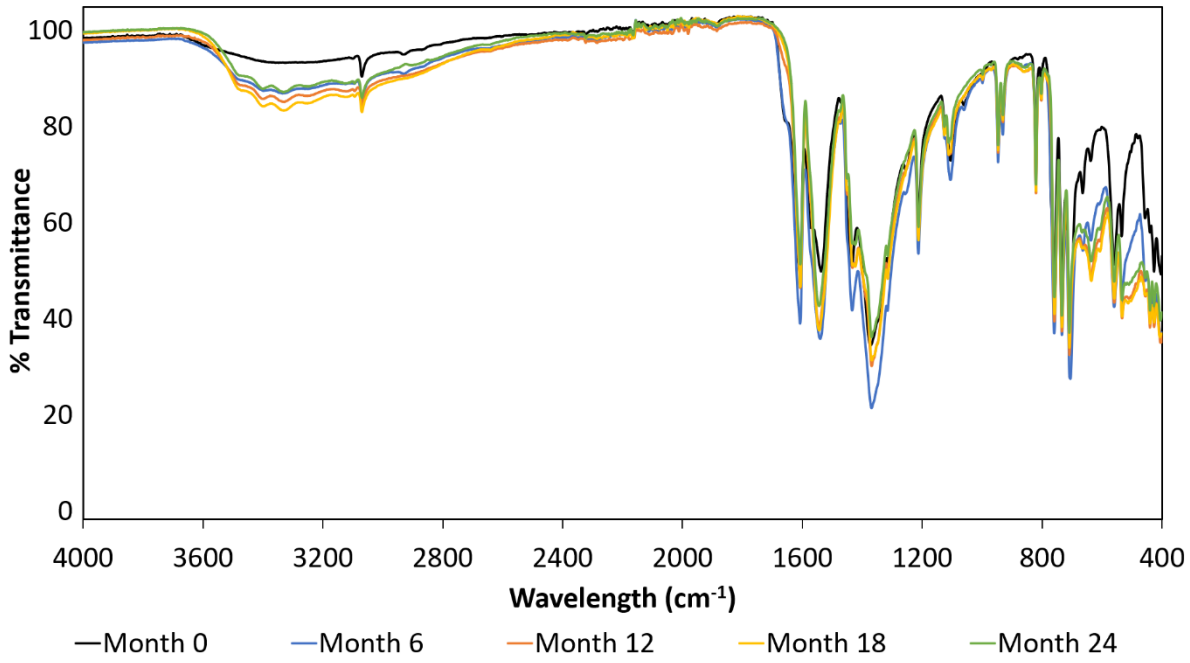

Figure 2-14: Stacked FTIR spectra of SH2-Tb at month 0 (black), month 6 (blue), month 12 (orange), month 18 (yellow) and month 24 (green).

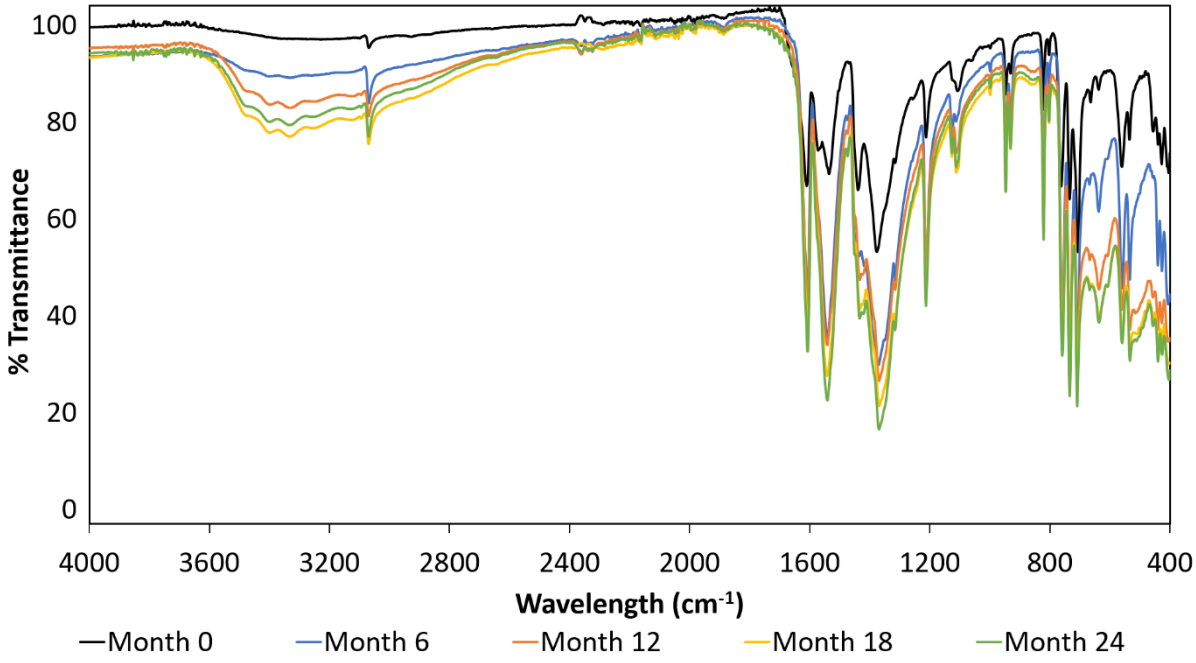

Figure 2-15: Stacked FTIR spectra of MW3-Tb at month 0 (black), month 6 (blue), month 12 (orange), month 18 (yellow) and month 24 (green).

While MW1-Tb (*Figure 2-16*) contained the same ligand as SH2-Tb and MW3-Tb, the absence of DMF guest molecules in the structure was seen to affect the bonding arrangement, as well as the hygroscopic nature of the MOF. The coordination of three bidentate BTC ligands to one Tb^{3+} metal

ion eliminates room for guest molecules to enter the framework [408]. This was evident in month 0, month 6 and month 12, where there was no variation in the O–H stretching vibration region (3600 – 3100 cm^{-1}). It was not until month 18 that a weak O–H band was observed. Although the initial structure was absent of H_2O molecules, the coordination architecture suggested MW1-Tb was hydrophilic [433]. A study on the influence of atmospheric moisture on $Cu_3(BTC)_2$ by Singh et al. [435] highlighted that a minimum of 25 minutes of exposure to a dehydrated MOF sample can generate a broad band between 3700 – 2700 cm^{-1} [435]. The difference between MW1-Tb and the MOF reported by Singh et al. [435] is that following the absorption of H_2O there was no peak shifting in MW1-Tb, indicating that there was no adjustment to the MOF structure, and therefore no replacement of metal-ligand coordination. The differences in observed intensities in MW1-Tb over the 24-months could be attributed to baseline drift in the instrument.

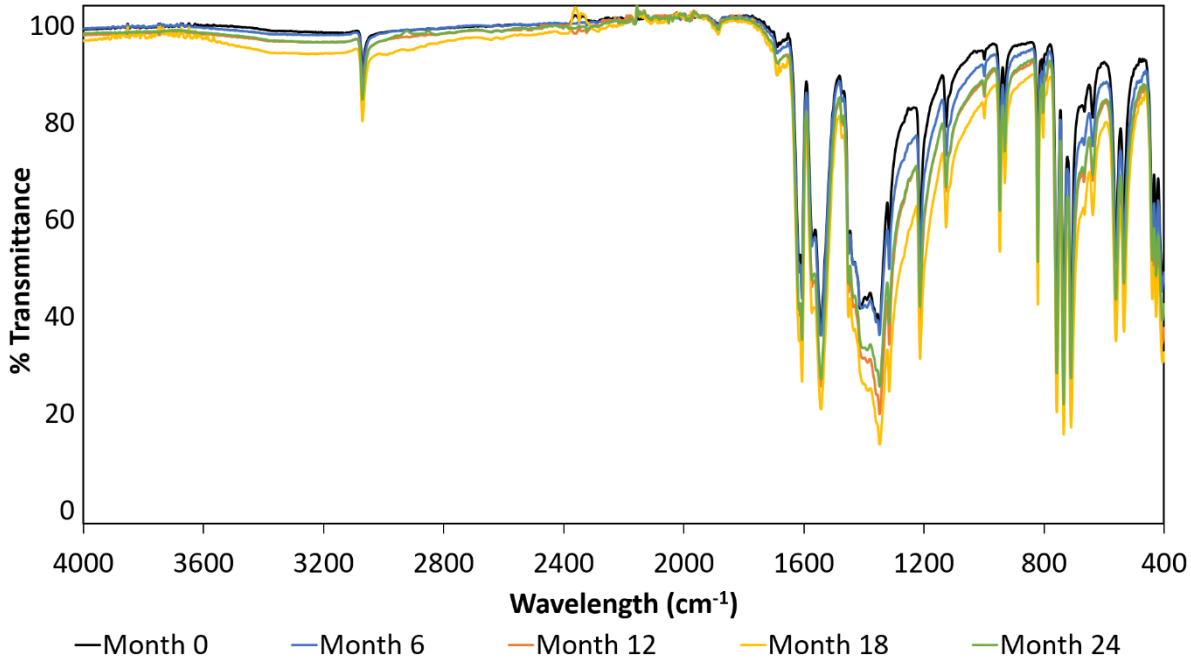

Figure 2-16: Stacked FTIR spectra of MW1-Tb at month 0 (black), month 6 (blue), month 12 (red), month 18 (yellow) and month 24 (green).

Peak shifting and peak loss were also not observed in the MW2-Tb FTIR spectra (*Figure 2-17*). There was evidence of intensity changing throughout the spectra, which can be attributed to baseline drift in the instrument. However, the increasing intensity of the peak between 3460 cm^{-1} and 2820 cm^{-1} could be linked to the absorption of H_2O molecules into the framework [436]. The hygroscopic nature of MW2-Tb is supported by Zhu et al. [437] who exposed a dehydrated $NaLn(dipic)_2{\cdot}7H_2O$ (Ln = Eu^{3+},Gd^{3+} and Tb^{3+}. dipic = DPA) MOF to 100% humidity for 24 hours [437]. The H_2O molecules from

air were observed to absorb into the micro-pores of the framework. Confirmation through TGA and XRD studies highlighted that the presence of H_2O molecules did not affect the patterns [437, 438].

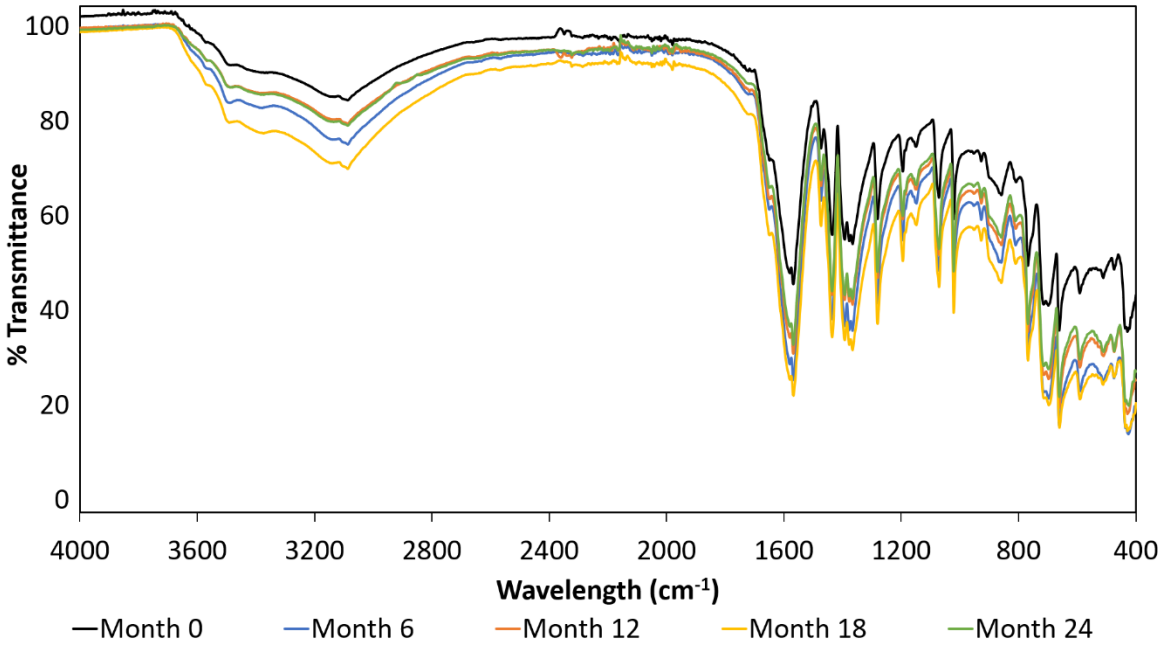

Figure 2-17: Stacked FTIR spectra of MW2-Tb at month 0 (black), month 6 (blue), month 12 (orange), month 18 (yellow) and month 24 (green).

The structural observations encountered over the 24-month chemical stability of the four Tb-MOFs highlighted that these chemicals were structurally unaffected over time. In all MOFs it was observed that the O–H peak was the only change over time and there was no degradation of the ligand bonds in the framework. Overall, this indicated that the MOF exposure to atmospheric air during sampling each month was not resulting in the displacement of bound ligands, but instead introduced guest H_2O molecules into the framework through binding to active sites or permeating into micropores within the framework. Although, the increase of the O–H peak does not negatively impact the functionality of the pure MOF, it is unknown how the retention of H_2O molecules within the framework may affect the interaction between the MOF and the primer or propellant and ultimately affect the discharge process. The assembly of each cartridge is known to be airtight to guarantee the expected shelf-life of the primer and propellant of ammunition. It should be expected that once the MOF is incorporated into the ammunition there is very little opportunity for interaction with moisture from air. To avoid potential impacts of hydrated MOFs during incorporation, this suggested that for incorporation the pure MOF should be completely dried.

2.3.8 UV Photoluminescent Stability

The effect of the MOFs UV photoluminescent properties over time was another important factor to analyse to ensure that traces of LGSR would still be visualised given ammunition can remain unused for some time. To assess the stability of the luminescence two factors were evaluated: spectrophotometer spectra and visual luminescence. It was hypothesised that the inability to retain luminescence over the 24-month period would indicate the MOFs would not be suitable for further incorporation into ammunition. Any radical loss of the transitional peaks or decrease of intensity for the Tb-MOFs would demonstrate instability. With the observed increase in O–H peaks from the FTIR evaluation, there was the possibility that the luminescence would be affected, as guest H_2O molecules have the ability to reduce the luminescent capability of the MOF [437].

2.3.8.1 Varian Cary Eclipse Fluorescence Spectrophotometer Wavelength Optimisation

During initial characterisation, the Tb-MOFs were evaluated at an excitation wavelength of 254 nm or 302 nm, for comparison with corresponding literature, which identified that all MOFs contained the expected four characteristic Tb peaks (Section 2.3.5) [172, 182, 206]. This was due to the maximum excitation for these Tb-MOFs occurring within the UVC range (220 – 260 nm) [439, 440]. However, the decision to visualise LGSR in the UVA wavelength region (using a Labino® lamp containing a 365 nm light source) indicated that optimisation of the spectrophotometer was required to determine a suitable excitation wavelength for the evaluation of all MOFs UV photoluminescence. A *3-D mode* scan was applied to all four Tb-MOFs, which captured the spectral data for each excitation wavelength within the UVA range (Appendix 2). The chosen excitation wavelength of 380 nm was deemed suitable for all MOFs because it contained at least two characteristic Tb peaks. The inability to see the $^5D_4 \rightarrow {}^7F_4$ (585 nm) and $^5D_4 \rightarrow {}^7F_3$ (620 nm) peak transition in SH2-Tb, MW1-Tb and MW3-Tb could be due to the low intensity of these peaks in comparison to the $^5D_4 \rightarrow {}^7F_6$ (485 nm) and $^5D_4 \rightarrow {}^7F_5$ (543 nm) transition peaks and the baseline shift observed. This excitation also presented the least amount of instrument background, with one peak at 520 nm resulting from the composition of the quartz slide containing the MOF. It should be noted that although the data presented in this chapter was analysed at 380 nm on the spectrophotometer, the sample was also subjected to an additional run at 254 nm for confirmation that all characteristic Tb peaks were present each month.

2.3.8.2 Monthly Stability

During the 24 months of luminescence evaluation, it became evident that there was no obvious trend to suggest that the luminescence of the MOFs was decreasing. For SH2-Tb (*Figure 2-18*), the luminescence spectra indicated that the luminescence of the MOF was increasing from month 0 to

month 24, with only a slight decrease in intensity at month 18. The luminescence of the MW-MOFs, MW1-Tb (*Figure 2-19*), MW2-Tb (*Figure 2-20*) and MW3-Tb (*Figure 2-21*); however, did not follow the same intensity pattern as SH2-Tb. The MW-MOFs intensity pattern showed a decrease in the luminescence between month 0 and month 18 followed by an increase in intensity at month 24. It was hypothesised that the intensity of the peaks would lose their sharpness due to a deactivation of the Tb^{3+} ion excited states from the increase of H_2O molecules in the framework, and therefore the luminescence of the MOF would reduce [437]. Instead, the spectral peaks of SH2-Tb and the MW-MOFs retained their overall shape and exhibited minor intensity fluctuations, which were likely to be a result of instrument inter-day variability of the fluorescence spectrophotometer rather than MOF instability. Because the fluorescence spectrophotometer is a highly sensitive and precise instrument, a manual alignment for the powder sample holder prior to use was required. It was decided that the GREENescent™ powder would be used to align the beam to the sample window prior to each use and spectral data was collected to identify the inter-day variability of the instrument due to its known luminescent stability (Appendix 2) was observed to follow the same intensity trend as the samples, respectively. It was observed that there were similarities between the intensity trends observed in the MOFs and GREENescent™ powder spectra. This process identified that the manual alignment process influenced the detected intensity of the Tb^{3+} characteristic peaks, accounting for the discrepancies between SH2-Tb and the MW-MOFs, which were analysed on different days.

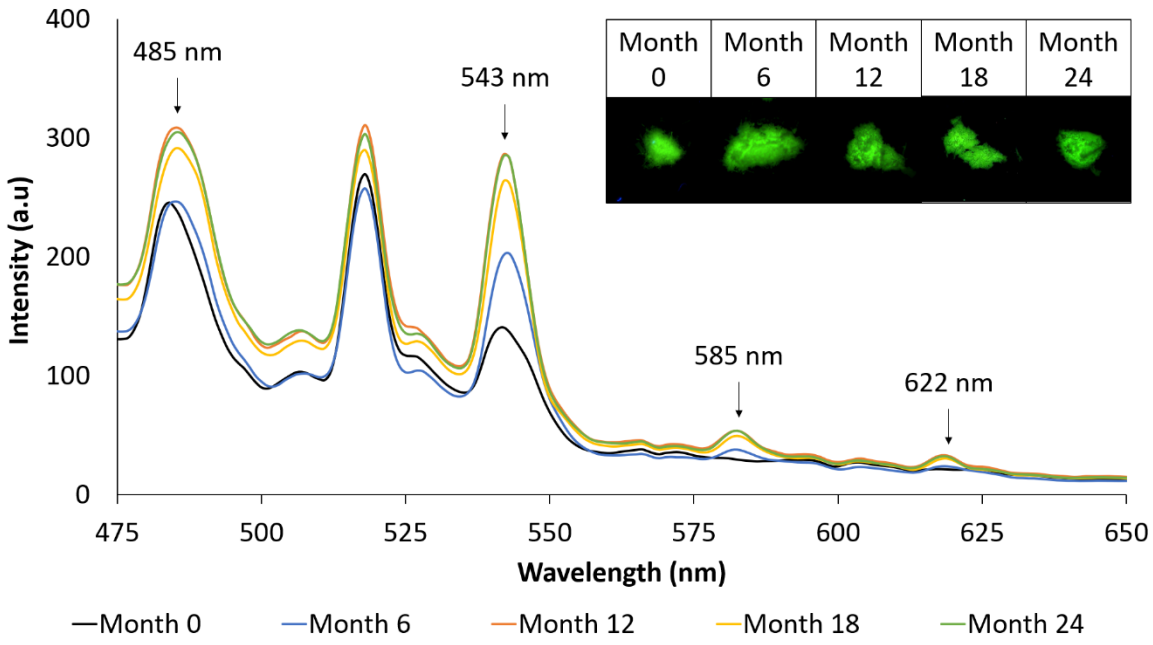

Figure 2-18: Stacked spectrophotometer emission spectra of SH2-Tb at month 0 (black), month 6 (blue), month 12 (orange), month 18 (yellow) and month 24 (green) (λ_{ex} = 380 nm). Insert: Luminescence of SH2-Tb observed in the VSC8000 (λ_{ex} = 365 nm) for corresponding months.

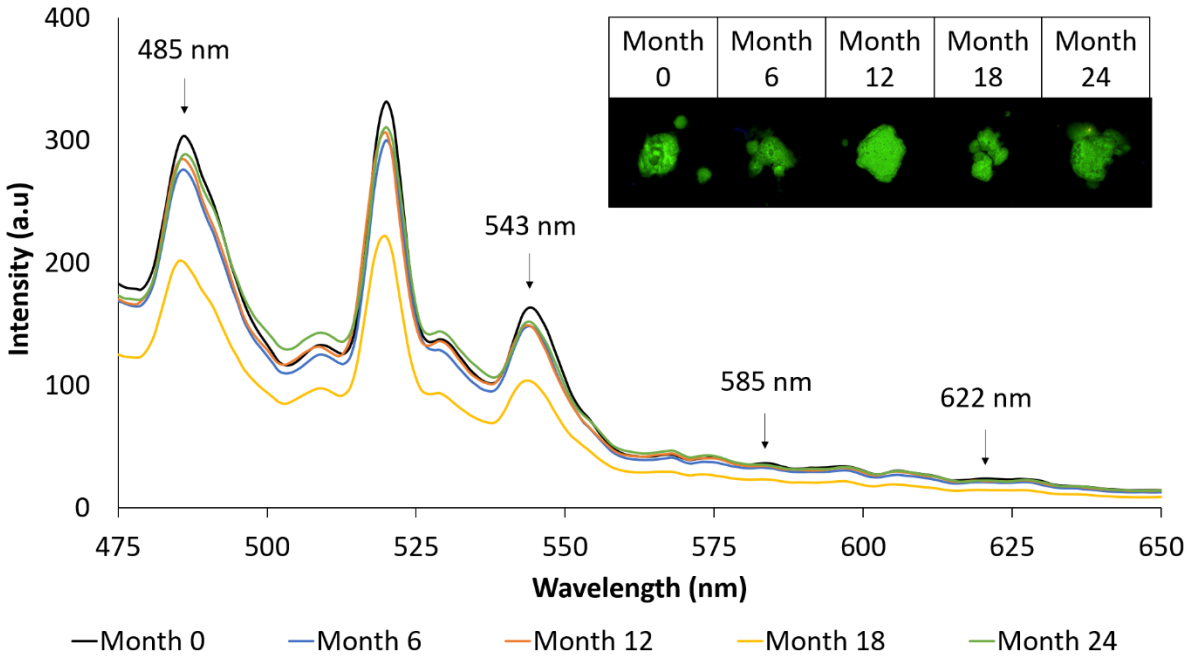

Figure 2-19: Stacked spectrophotometer emission spectra of MW1-Tb at month 0 (black), month 6 (blue), month 12 (orange), month 18 (yellow) and month 24 (green) (λ_{ex} = 380 nm). Insert: Luminescence of MW1-Tb observed in the VSC8000 (λ_{ex} = 365 nm) for corresponding months.

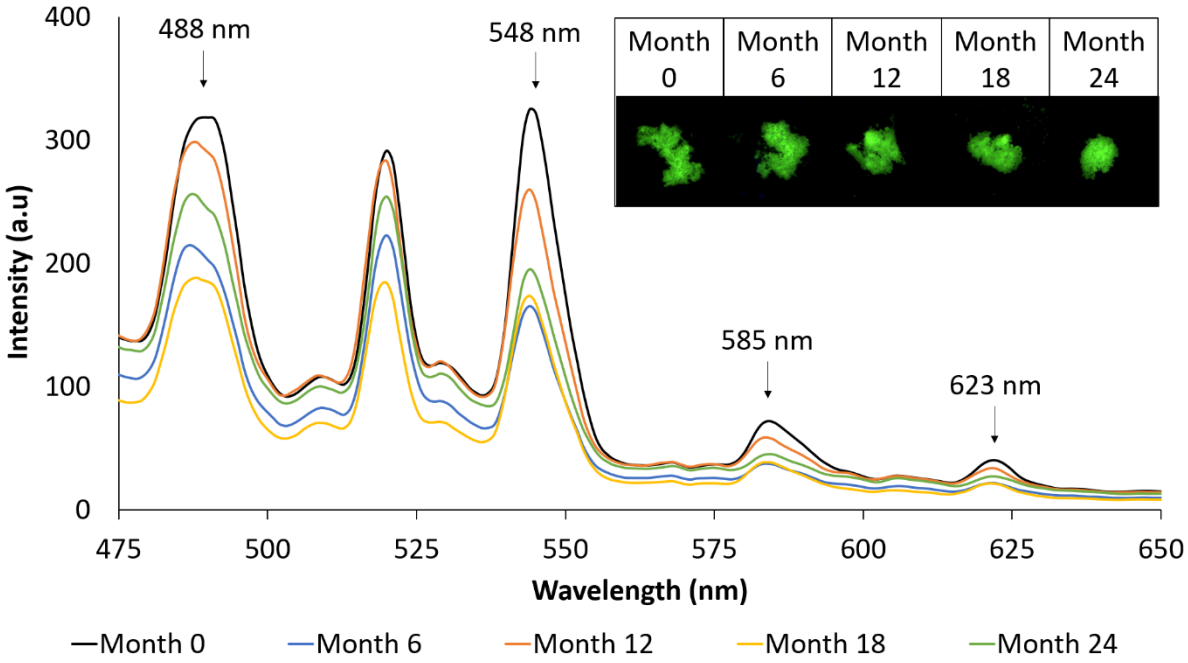

Figure 2-20: Stacked spectrophotometer emission spectra of MW2-Tb at month 0 (black), month 6 (blue), month 12 (orange), month 18 (yellow) and month 24 (green) (λ_{ex} = 380 nm). Insert: Luminescence of MW2-Tb observed in the VSC8000 (λ_{ex} = 365 nm) for corresponding months.

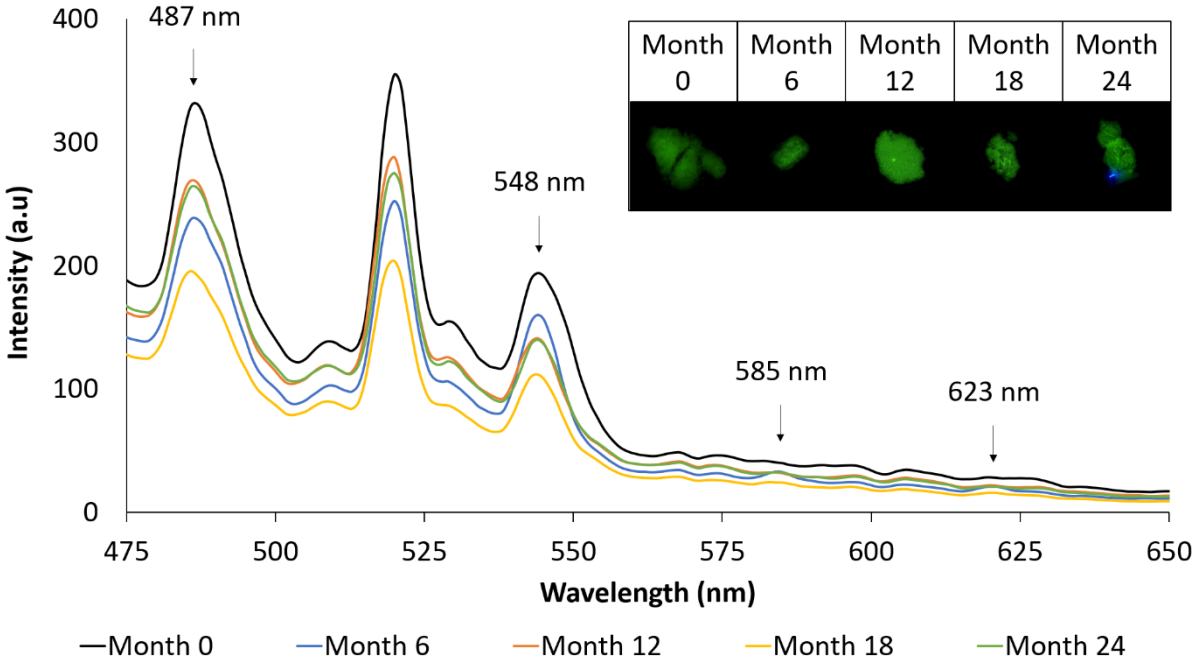

Figure 2-21: Stacked spectrophotometer emission spectra of MW3-Tb at month 0 (black), month 6 (blue), month 12 (orange), month 18 (yellow) and month 24 (green) (λ_{ex} = 380 nm). Insert: Luminescence of MW3-Tb observed in the VSC8000 (λ_{ex} = 365 nm) for corresponding months.

The additional analysis conducted using the VSC, although qualitative, was able to visualise the change in colour over time which might be seen in practice. The fluctuations observed between monthly time points in the spectrophotometer emission spectra were not reflected in the visual luminescence of the pure MOFs observed in the VSC. The observations for the green luminescent colour of the MOFs were objective to the viewer, and overall, the green colour observed in month 0 does not appear to reduce or disappear. There was slight variation in the intensity of the green colour observed, which is seen primarily in month 6 of MW1 (*Figure 2-19*) where the weakest green colour is observed. However, these variations can be attributed to three different factors, including (i) amount of MOF, (ii) surface area of MOF and (iii) shape of the MOF. The general lack of colour loss or weakening indicates that the bonds between the Ln^{3+} ions and ligands were not weakening over time, regardless of the absorption of the guest H_2O molecules into the framework.

The findings from the UV photoluminescent study indicated that exposure to moisture in the air does not affect the luminescence of the MOF. The coordination of ligands with aromatic carboxylate ions and Tb^{3+} ions strengthen the framework resulting in a MOF which is chemically resistant to H_2O [441, 442]. This is supported by Song et al. [443] who evaluated the behaviour of luminescent intensity of $[Tb_3(CBA)_2(HCOO)(\mu_3\text{-}OH)_4(H_2O)]\cdot 2H_2O\cdot 0.5DMF\}_n$ (CBA = 1,1-cyclobutanedicarboxylic acid) after storing the MOF in H_2O for 2 days [443]. Comparing the emission spectrum of this MOF from before

and after immersion in H_2O revealed no change and indicated that this MOF contained excellent stability following immersion in H_2O [443].

The luminescent stability of SH2-Tb, MW1-Tb, MW2-Tb and MW3-Tb over 24-months highlighted that these MOFs would be suitable for incorporation into ammunition. It was confirmed that exposure to atmospheric air during sampling each month does not affect the luminescent visual colour of the MOFs.

2.4 Conclusion

The synthesis, characterisation and stability studies identified four highly luminescent MOFs containing a suitable metal core which could be applied in LGSR visualisation. Of the overall 17 MOFs, 14 novel MOFs were synthesised via SH routes and contained either a Tb^{3+}, Er^{3+}, Ho^{3+}, Gd^{3+} and Y^{3+} metal core. These metal cores were evaluated due to their lack of use in LGSR visualisation, metal core availability in Australia and precursor cost. During the evaluation, 13 novel SH-MOFs were discontinued from additional evaluation due to not meeting the general observation criterion or the UV photoluminescence visualisation criterion. The luminescence characterisation provided the most important information regarding the applicability of the novel MOFs. It was realised that MOFs containing Er^{3+} and Ho^{3+} metal cores cannot emit a visible colour when excited under a UV wavelength. The Gd^{3+} and Y^{3+} metal cores are UV-active; however, only produced a weak luminescence due to the intraligand transition, indicating that if they were incorporated into ammunition, the weak luminescence could prove difficult to identify at a crime scene. This evaluation identified that the chosen metal cores would not be suitable in the application of LGSR visualisation and that MOFs containing a Tb^{3+} metal core produced the most suitable chemical, structural and luminescent properties.

With SH2-Tb being the only highly luminescent novel MOF, additional Tb-MOFs were synthesised via an alternative synthetic route. Three additional Tb-MOFs, one novel and two established, were synthesised via MW-assisted routes and evaluated against the same criteria. All MW-MOFs contained the appropriate chemical, structural and luminescent properties. Additionally, a comparison between the synthetic routes was conducted to highlight whether SH or MW-assisted synthesis produced a better-quality MOF. While there were differences between SH2-Tb and MW3-Tb, they were minimal and did not impact the properties of the MOFs.

The four Tb-MOFs (SH2-Tb, MW1-Tb, MW2-Tb, MW3-Tb) all progressed for further evaluation and undergo a 24-month stability time course, where the chemical and UV photoluminescent properties of the MOFs would be evaluated monthly. As MW1-Tb and MW2-Tb have successfully visualised LGSR in research [4, 22], they were used as a baseline for comparison with SH2-Tb and MW3-Tb to indicate whether the novel MOFs identified in this study are suitable for incorporation into ammunition. During the 24-month stability evaluation, there was evidence of H_2O guest molecules entering the MOF framework through FTIR analysis, resulting from the hygroscopic MOF being exposed to atmospheric air during the overall period of testing. However, it was identified that this addition to the framework did not affect either the bonds or the luminescent properties of the MOFs. It was observed that the intensity of the emission spectra for each MOF fluctuated in intensity over the time

period, but the visual luminescence retained its green colour with no variation in intensity. As the ability of the investigator to see the MOF components is the most important aspect for the application of visualising LGSR, the visual colour of the MOF was an essential aspect of the luminescent stability evaluation.

Overall, in both the chemical and luminescent stability assessments, there was no indication of degradation of the MOF structure throughout the 24-month period. This stability assessment indicated that SH2-Tb, MW1-Tb, MW2-Tb and MW3-Tb show the potential to remain stable once incorporated into ammunition. They were further considered for the remainder of the study.

This page was left intentionally blank

Chapter 3. Evaluation of Metal-Organic Frameworks in the Production of Luminescent Gunshot Residue

3.1 Introduction

The synthesis, characterisation and stability of the pure MOFs highlighted their suitability from a chemical and theoretical perspective. However, to assess the effectiveness of the four suitable Tb-MOFs as a tool for LGSR visualisation, an evaluation of dispersion and impact on the firing process was considered. Following the incorporation of MOFs into ammunition and firearm discharge, literature has indicated that LGSR can be observed to deposit onto the shooter's hands, the firearm, targets and other surfaces in the vicinity of discharge (*Table 3-1*). The ability to visualise LGSR has been possible for a range of variation in the munitions, incorporation method and visualisation sources.

Between the studies, a range of ammunition and firearm combinations have been used to evaluate the ability to visualise LGSR. The evaluation of LGSR behaviour using a Glock 17 firearm and 9 mm Luger CBC (NTA) ammunition was the most common combination encountered in the literature. Most of the LGSR studies were conducted in Brazil where this combination of firearm and ammunition type is common [177, 187]. Taurus® firearms were also commonly used for the evaluation of LGSR behaviour due to being one of the three largest manufacturers of small arms in Brazil [444]. Two studies evaluated the effect of firearm type and LGSR behaviour. Arouca et al.[177] evaluated the effect of six pistol types, containing different barrel lengths and hammer positions, using 9 mm ammunition incorporated with 10 wt% of Eu(BTC). It was observed that the amount of LGSR observed on the shooter was affected by barrel length, and pistols with exposed hammers had a wider distribution (shooter's face and chest). However, the distribution pattern of visible LGSR on the shooter's hand was not able to identify the pistol used [177]. A comparison between a pistol and a revolver was conducted by de Oliveira Silva et al.[189] using different ammunition incorporated with 30 mg of $Eu_{0.1}Tb_{0.9}$(Hbtec). For the .380 pistol, LGSR particles were only visualised on the shooter's hand, forearm and within the firearm, while the 38-calibre revolver was also able to visualise LGSR on the surface of the target. de Oliveira Silva et al. [189] did state that the use of more powerful pistols (which contain a greater discharge energy) can affect the distribution of LGSR particles. Overall, both Arouca et al. [177] and de Oliveira Silva et al. [189] were able to confirm the observations made by Ditrich et al. [53] on GSR distribution. Considering the firearm and ammunition combinations encountered in Australia, it was decided that a combination of Glock 19 semi-automatic pistol and 9 mm Luger Winchester (NTA) ammunition would provide an understanding into how MOFs incorporation could be visualised.

One aspect that is not kept consistent between the studies or discussed in depth is how the incorporation ratio affects the LGSR distribution. Four studies have evaluated the effect of

incorporation ratio on the ease of visibility [12, 78, 190] or projectile behaviour [174], while the remaining studies present findings of a single incorporation ratio. One study indicated an incorporation ratio of 10 wt% resulted in shooting failure (characterised as any FCC that did not eject automatically or when new ammunition was not inserted into the chamber) [174]; however, newer studies have successfully incorporated ammunition with this incorporation ratio of MOF and not identified the same issues [177, 184, 188, 190, 192, 445]. This indicated that there must be a balance between easily visualising LGSR particles without compromising GSR traces and the projectile behaviour. Considering most established MOF types contain different chemical and physical properties, it could be hypothesised that these factors affect the optimal incorporation ratio. The technique adopted to incorporate the MOF into the ammunition may also affect the behaviour of LGSR. Of the studies that indicate their method of incorporation, a majority choose to not homogenise the MOF and ammunition for safety reasons [78, 172, 183], with homogenisation being the least encountered method for mixing the MOF and propellant. For a comprehensive understanding of how the different synthesised MOFs would impact the ease of visualisation, a range of incorporation ratios were evaluated (2 wt% – 10 wt%). Incorporation ratios higher than 10 wt% were not considered due to ejection error concerns highlighted by Weber et al. [174]. To ensure that there was an even distribution of the MOF within the cartridge case, the MOF and propellant were homogenised. This incorporation method was hypothesised to provide the greatest possibility of LGSR particle distribution post-discharge.

The visualisation of LGSR, regardless of MOF type, is typically achieved using UVC light sources (λ_{ex} = 254 nm). The issue with this UV wavelength is the risk of DNA damage or degradation, even in small doses [341, 342]. With the intention of visualising LGSR on a POI's hand, the utility of a UV source that may cause harm to the user should be avoided. In more recent studies [189, 191], UVA wavelengths (λ_{ex} = 380 nm) have been utilised to successfully visualise LGSR particles. Between all studies, regardless of UV wavelength, it was evident that the visualisation of LGSR was possible on each surface of interest. It suggests that the MOFs incorporated into ammunition retain their luminescence following discharge and generation of LGSR. A strong green luminescence was observed for each of the four pure MOFs at this wavelength. For this study, the application of a UVA (λ_{ex} = 365 nm) light source was considered for the visualisation of LGSR. This was a crucial aspect of the study as it would ensure safer UV wavelengths could visualise the luminescence of SH2-Tb, MW1-b, MW2-Tb and MW3-Tb particles.

Table 3-1: Overview of the variables associated with MOF incorporation into ammunition.

MOF	Munitions			Incorporation			Visualisation		Reference
	Ammunition Calibre	Firearm	Number of shots	Ratio	Powder	Homogenised	λ_{ex}	LGSR Surface	
Tb(DPA)(HDPA) Eu(DPA)(HDPA)	.38 SPL .40 S&W	Revolver Pistol	Undefined	1 – 10 wt%	Primer	Non – homogenised	UV light	Hands Firearm Target (10 and 40 cm)	[12]
TbYb(DPA)(HDPA)	.40 S&W	Pistol	Undefined	10 wt%	Propellant	Non – homogenised	UV light	Firearm Target (40 cm)	[172]
$Y_{0.98-x}Er_{0.02}Yb_xVO_4$	9 mm Luger CBC (NTA)	GLOCK 19	1	10 wt%	Propellant	Undefined	254 nm	Hands Firearm Target	[188]
Tb(DPA)(HDPA) Eu(DPA)(HDPA)	9 mm Luger CBC (NTA)	GLOCK 17	2, 4 or 10	2 wt% 10 wt%	Primer	Non – homogenised	254 nm	Hands Car Window Firing Range	[174]
$Eu_2(BDC)(H_2O)_2$ $Tb_2(BDC)(H_2O)_2$ $Zn_2(BDC)(H_2O)_2$	9 mm Luger CBC (NTA)	GLOCK 17	3	4 wt%	Propellant	Undefined	254 nm	Hands Firearm Target	[179]
$Eu(BTC)(H_2O)$ $Eu(BDC)(H_2O)_2$ Eu(DPA)(HDPA)	9 mm Luger CBC (NTA)	GLOCK 17	3	6 wt%	Propellant	Non – homogenised	254 nm	Hands Firearm FCC	[181]
$ZnAl_{1.95}Tb_{0.05}O_4$ $ZnAl_{1.95}Eu_{0.05}O_4$	9 mm Luger CBC (NTA)	GLOCK 17	4	10 wt%	Propellant	Undefined	254 nm	Hands FCC Firing Range	[173]

Table 3-1 continued: Overview of the variables associated with MOF incorporation into ammunition.

MOF	Munitions			Incorporation			Visualisation		Reference
	Ammunition Calibre	Firearm	Number of shots	Ratio	Powder	Homogenised	λ_{ex}	LGSR Surface	
Eu(BTC)	9 mm Luger CBC (NTA)	GLOCK 17	4	10 wt%	Propellant	Non – homogenised	254 nm	Hands	[176]
Dy(DPA)(HDPA)	9 mm Luger CBC (NTA)	GLOCK 17	Undefined	10 wt%	Propellant	Non – homogenised	254 nm	Hands Firearm	[175]
$Y_{0.95}Eu_{0.05}$(BTC) $Y_{0.90}Eu_{0.05}Sm_{0.05}$(BTC) $Y_{0.95}Tb_{0.05}$(BTC) $Y_{0.85}Yb_{0.10}Tb_{0.05}$(BTC) $Y_{0.80}Yb_{0.10}Tb_{0.05}Eu_{0.05}$(BTC)	9 mm Luger CBC (NTA)	GLOCK 17	Undefined	5 wt%	Propellant	Non – homogenised	254 nm	Hands Firearm Firing Range	[182]
$Y_{0.85}Yb_{0.10}Tb_{0.05}$(BTC) $Y_{0.85}Eu_{0.05}$(BTC)	9 mm Luger Sellier & Bellot	GLOCK 17	1	5 wt%	Propellant	Undefined	254 nm	Hands Target (10, 30, 120, 200 and 800 cm)	[178]
Eu(BTC) $Eu_2(BDC)_3(H2O)_2$	9 mm Luger CBC (NTA)	GLOCK 17 Jericho 941F	1	5 wt%	Propellant	Undefined	254 nm	Target (30 cm)	[187]
Eu(DPA)(HDPA) Eu(BTC) $Eu_2(BDC)_3(H2O)_2$	9 mm Luger CBC (NTA)	GLOCK 17 Jericho 941F	1	5 wt%	Propellant	Undefined	N/A	Target (30 cm)	[185]

Table 3-1 continued: Overview of the variables associated with MOF incorporation into ammunition.

MOF	Munitions			Incorporation			Visualisation		Reference
	Ammunition Calibre	Firearm	Number of shots	Ratio	Powder	Homogenised	λ_{ex}	LGSR Surface	
Eu(BTC) $Eu_2(BDC)_3(H2O)_2$ Eu(DPA)(HDPA)	9 mm Luger CBC (NTA)	GLOCK 17 GLOCK 28 S&W 6906 Browning Hi-Power Jericho 941F Taurus® PT 908	1, 2, 3 or 4	5 wt% or 10 wt%	Propellant	Undefined	254 nm	Hands Firing Range Target (6, 30, 60 and 120 cm)	[177]
$Eu(Hbtec)_3$	EXPO (+P) Gold Hex	Imbel 40 GC MD7	2	15 mg 30 mg	Propellant	Undefined	254 nm	Hands Firearm FCC Target (2 m)	[186]
$Tb(Hbtec)_3$	.40 CBC (NTA)	Imbel 40 GC MD7	2	30 mg	Propellant	Non – homogenised	254 nm	Hands Firearm FCC Firing Range Target (2 m)	[183]
$(Eu_2Zr)(btc)_3(Hbtc)_{0.5}.6H_2O$	.380 AUTO EXPO (+P) Gold Hex .380 CBC Auto Treina E00G (NTA)	0.38 calibre Taurus®	Undefined	10 wt%	Propellant	Undefined	UV light	Hands Firearm FCC	[192]

Table 3-1 continued: Overview of the variables associated with MOF incorporation into ammunition.

MOF	Munitions			Incorporation			Visualisation		Reference
	Ammunition Calibre	Firearm	Number of shots	Ratio	Powder	Homogenised	λ_{ex}	LGSR Surface	
$Eu(PIC)_3(NMK)_3$	.38 SPL	0.38 calibre Taurus®	1	2 mg 5 mg 10 mg 25 mg 50 mg	Propellant	Non – homogenised	395 nm	Hands Firearm	[78]
$Eu(tta)_3(\varepsilon\text{-cap})(H_2O)]$	.38 SPL	Taurus® RT 85 2″	1	30 mg	Propellant	Homogenised	380 nm	Firearm FCC Firing Range Target (60 cm)	[191]
$Eu(btfa)_3(\varepsilon\text{-cap})(H_2O)$	.380 AUTO EXPO (+P) Gold Hex	Taurus® 58 HC PLUS							
$Eu_{0.1}Tb_{0.9}(Hbtec)$	.38 SPL CBC	Taurus® RT 85 2″	1	30 mg	Propellant	Undefined	380 nm	Hands Firearm FCC Firing Range Target (60 cm)	[189]
	.380 AUTO EXPO (+P) Gold Hex	Taurus® 58 HC PLUS							
$(Eu_2Zr)(btc)_3(Hbtc)_{0.5}.6H_2O$	.380 AUTO EXPO (+P) Gold Hex GR	Taurus® 638 Pro	Undefined	5wt% 10 wt%	Propellant	Undefined	254 nm	Firearm FCC Firing Range Target (2 m)	[190]
$[Tb(TBZ)_2(NO_3)_3].H_2O$ $[Eu(TBZ)_2(NO_3)_3].H_2O$ $[Gd(TBZ)_2(NO_3)_3].H_2O$	9 mm Luger CBC (NTA)	Taurus® PT 92-AF	2	5 wt%	Propellant	Non – homogenised	254 nm	Hands Firearm/FCC Target (5 m)	[180]

Table 3-1 continued: Overview of the variables associated with MOF incorporation into ammunition.

MOF	Munitions			Incorporation			Visualisation		Reference
	Ammunition Calibre	Firearm	Number of shots	Ratio	Powder	Homogenised	λ_{ex}	LGSR Surface	
Eu(BTC)	9 mm Luger CBC (NTA)	Undefined	1	10 wt%	Propellant	Undefined	254 nm	Leather (2 m) Cotton (2 m) Polyester (2 m) Denim (2 m)	[184]

This chapter aimed to evaluate how the MOFs; SH2-Tb, MW1-Tb, MW2-Tb and MW3-Tb, compared to the established MOFs, while also addressing some of the inconsistencies observed in the literature. To evaluate this, the chapter was separated into three parts: *Visualisation, GSR Stub Evaluation* and *Projectile Performance*. Part 1 evaluated the visualisation of LGSR and set out to compare the luminescence and visualisation capability of the synthesised MOF on the shooter's hand, within the firearm and on the FCC. Part 2 compared the particle observations between the control GSR traces and LGSR traces on collected GSR stubs. Part 3 focused on the performance of the projectile and whether the addition of the MOF within the cartridge case was affecting the discharge process. The projectile velocity, and accuracy and precision were also evaluated to provide insight into the projectile trajectory. Across all parts, the effect of incorporation ratio was explored, with each MOF being evaluated at different ratios (2, 4, 6, 8 and 10 wt%). The comparison of incorporation ratio among different MOF types aims to provide an insight into whether a "one-size-fits-all" approach can be applied to the MOFs or whether each MOF type needs to be evaluated to find its own fit.

3.2 Materials and Munitions

3.2.1 Chemicals and Synthesis

Chemicals required for the synthesis of SH2-Tb, MW1-Tb, MW2-Tb and MW3-Tb were identical to those previously listed in Section 2.2.1. Synthesis of SH2-Tb, MW1-Tb, MW2-Tb and MW3-Tb followed the procedure outlined in Section 2.2.2.2, Section 2.2.2.6, Section 2.2.2.7 and Section 2.2.2.8, respectively. A summary of the experimental design applied to the MOF evaluation as LGSR can be observed in *Figure 3-1*.

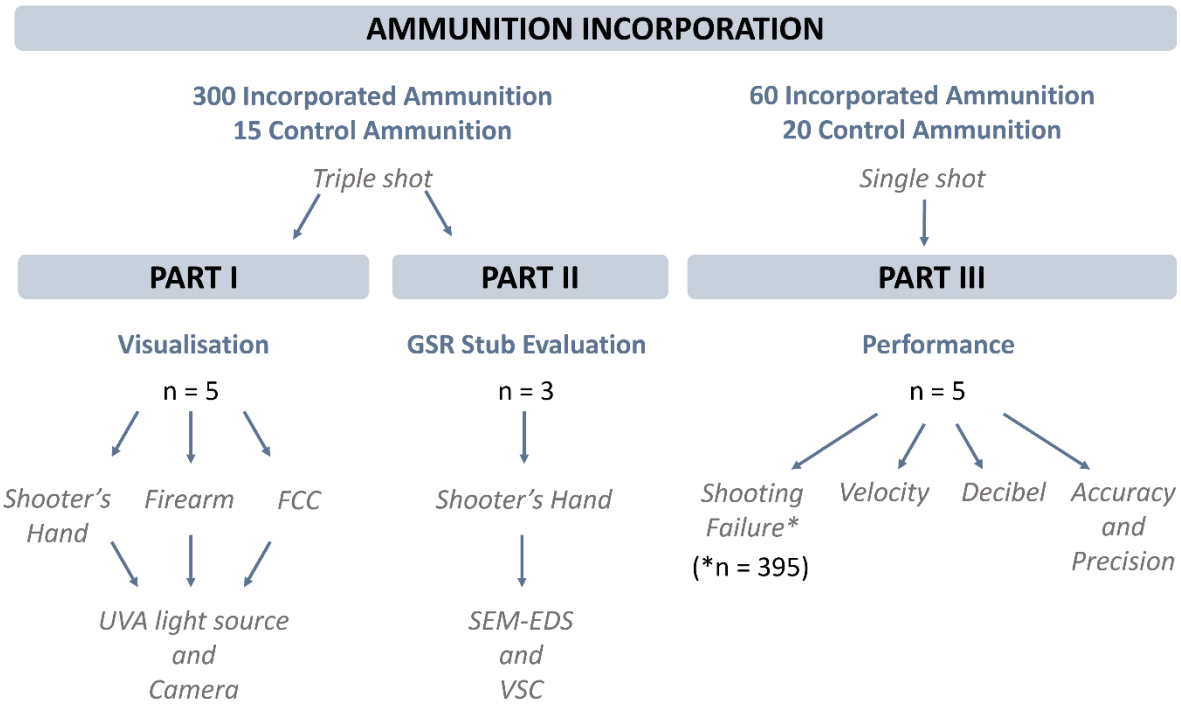

Figure 3-1: Flowchart of experimental design for evaluating the suitability of MOFs as LGSR particles. * indicates that shooting failure was evaluated for all firearm discharge in both Part I (n = 300 + n = 15) and Part III (n = 60 + n = 20).

3.2.2 Firearm and Ammunition

All shots were conducted using a GLOCK 19 (Austria, Germany) in combination with a 9 mm LUGER Winchester SuperX Winclean®147 Gr. Brass Enclosed Base (Melbourne, Australia). For this study, the firearm and ammunition combination was chosen based on the availability and ease of comparison with the literature. It is also a combination frequently encountered among serving officers in Australian policing agencies. A total of 300 incorporated rounds and 15 control rounds of ammunition were stored and discharged at room temperature at the Australian Federal Police (AFP) indoor firing range in Sydney, Australia, for Part 1. Part 2 consisted of 60 incorporated rounds and 20 control

rounds being stored and discharged at room temperature at the Australian Federal Police (AFP) indoor firing range in Canberra, Australia.

3.2.2.1 Ammunition Incorporation

The weight of the propellant was measured and averaged to determine the correct incorporation weight of the MOF for each incorporation ratio (n=5). An additional approach was considered for this study, where the incorporation ratio of MOF would be added to the propellant without the removal of the propellant. This method was chosen over the removal of propellant to reduce the potential impact on the burn rate and, therefore, the generation of NTA GSR and LGSR, as well as the projectile behaviour. For example, in a round containing an incorporation ratio of 2 wt%, the re-assembled ammunition consisted of approximately 0.300 g of propellant and 0.006 g of MOF for a total of 0.306 g of powder. This means the true incorporation ratio of a 2 wt% incorporation would be 1.96%.; however, for simplicity, all incorporation ratios were rounded to the nearest whole number.

The ammunition was disassembled by removing the bullet from the cartridge case using a Frankford Arsenal® Quick-N-EZ Impact Bullet Puller. The propellent was collected in a scintillation vial containing pre-weighed MOF and homogenised through a gentle rolling movement to ensure even dispersion of the MOF. Once homogenised, the incorporated propellent was guided into the cartridge case with the use of a funnel, before being re-assembled with a Lee Classic Cast Breech Lock Press. The ammunition was visualised with the Labino® lamp to ensure each round was clean of contamination, labelled and stored until required for shooting.

3.2.3 Cleaning Process

Prior to discharge, the shooter was required to decontaminate their hands with D-Lead® hand soap before and after cleaning the firearm. Cleaning of the firearm followed the process outlined in the GLOCK maintenance manual [446] and AFP procedures. This included first disassembling the firearm into five main components; the slide, barrel, recoil spring, frame and magazine. Overall, the slide, barrel and recoil spring, these components were first wiped down with a lubricated cleaning patch attached to a cleaning rod, followed by a lubricated nylon bristled brush. A fresh cleaning patch was then used to remove excess lubricant from the components and confirm there were no traces of NTA GSR or LGSR through visualisation under UV. The frame and magazine were wiped with a slightly dampened cleaning cloth until no traces of LGSR remained. During the re-assembly of the firearm, the barrel and slide were lubricated using gun oil.

3.3 PART I: Visualisation

3.3.1 Methods

3.3.1.1 Discharge Process

Once the firearm was cleaned, the shooter moved into the shooting range (primary location) to discharge the firearm. For firearm discharge, the shooter was directed to a pre-cleaned shooting booth, which contained an armrest, to steady the recoil between shots. A target was set up 10 m from distance as a visual mark for shooting.

Five incorporation ratios were evaluated for each MOF (2, 4, 6, 8 and 10 wt%) and a set of control ammunition (unmodified) was evaluated for comparison between GSR and LGSR behaviour. The shooter was instructed to load three rounds of ammunition (control or pre-incorporated) into the firearm magazine. The shooter was directed to discharge all ammunition within their firearm at a target set 10 m from the muzzle in three sequential shots. This process was conducted in quintuplicate (n=5) for each ratio and MOF combination.

After confirming the firearm chamber was empty, the shooter and firearm were directed to a secondary location where a UV light and camera set-up was situated (*Figure 3-2*). All lighting was switched off in the room, to allow the shooter's hands to be visualised with a 365 nm Labino® TrAc Pack PRO (135 Series, 35-Watts). The firearm was visualised and photographed following the collection of potential LGSR from the shooter's hands to ensure no cross-contamination. All photographs of the shooter's hands and firearm were taken using a Canon EOS 700D with a 60 mm macro lens.

All firing range safety protocols enforced by the AFP were followed during each discharge session. The visualisation and collection process of LGSR from the shooter's hand was approved by the University of Technology Sydney Human Research Ethics Committee (HREC; ETH20-5112).

Figure 3-2: UV light source and camera set up to visualise and photograph shooter's hand and firearm post discharge.

3.3.1.2 Post-Discharge Data Analysis

The captured images of the shooter's hands and firearm were analysed, and any visible LGSR particles were counted and their location noted. The median of the LGSR particle count was calculated to give an overview of the five replicates for each MOF and ratio combination. Because of the skewness of the data distribution, the interquartile range was calculated to determine the error between replicates.

The FCC that were ejected from the firearm were collected from the firing range for evaluation back at the laboratory. They were visualised using the Rofin Polilight® PL550XL (λ_{ex} = 350 nm). For all FCCs, images were captured using a Canon EOS 700D under both white light and 365 nm. A total of 11 images were captured per FCC, including four outer sides of the cartridge, one mouth, four inner cartridge and one base image. Unlike the shooter's hands and firearm, due to the abundance of LGSR particles present on the FCC, the individual particles could not be counted in all samples, so instead were subjectively compared to each other based on visual observations.

3.3.2 Results and Discussion

To identify which propellant-to-MOF ratio would provide the best visualisation outcome for the four synthesised MOFs (SH2-Tb, MW1-Tb, MW2-Tb and MW3-Tb), five ratios between 2 wt% and 10 wt% were evaluated against the unmodified ammunition. The visualisation of the LGSR particles identified distinct distribution behaviours in three key areas; the shooter's hands, firearm and FCC.

3.3.2.1 Shooter's Hand

The primary location of interest for traditional GSR to distribute onto has always been the shooter's hands. Following trends outlined in previous literature [12, 78], it was hypothesised that as the ratio of MOF increased, there would be a greater number of LGSR particles visibly deposited onto the shooter's hand. However, this was not supported by the results for any of the synthesised MOFs (SH2-Tb, MW1-Tb, MW2-Tb or MW3-Tb). In 86% of specimens, across all four MOFs ratio combinations, no LGSR particles could be visualised on the shooter's dominant and/or non-dominant hand, as well as forearms or clothing. Specimens where green LGSR particles were able to be visualised did not suggest a MOF-specific or ratio-specific trend (*Figure 3-3*). The highest number of green particles visible to the naked eye on the shooter's hand was four particles. This was observed with SH2-Tb at an incorporation ratio of 10 wt% and MW1-Tb at an incorporation ratio of 4 wt% (*Figure 3-4*). The remaining specimens where visible LGSR particles were observed, contained either one or three green LGSR particles on the shooter's hand. When the LGSR particles were able to be visualised, it was easy to isolate them from other UV luminescent particles due to their distinguishing green luminescence and particle shape. One observation that has not been discussed in LGSR literature is the predominance of fluorescent blue fibres/particles that can be visualised on most surfaces and how it can impact the ability to visualise LGSR particles. Encountering these blue fibres on the shooter's hands are unavoidable as they were identified to be cotton fibres, which are readily transferred from clothing and furniture. While the blue fluorescent fibres did not interfere with the ability to visualise green luminescent particles, there is a chance that due to their size and quantity LGSR could be overlooked if not vigilant.

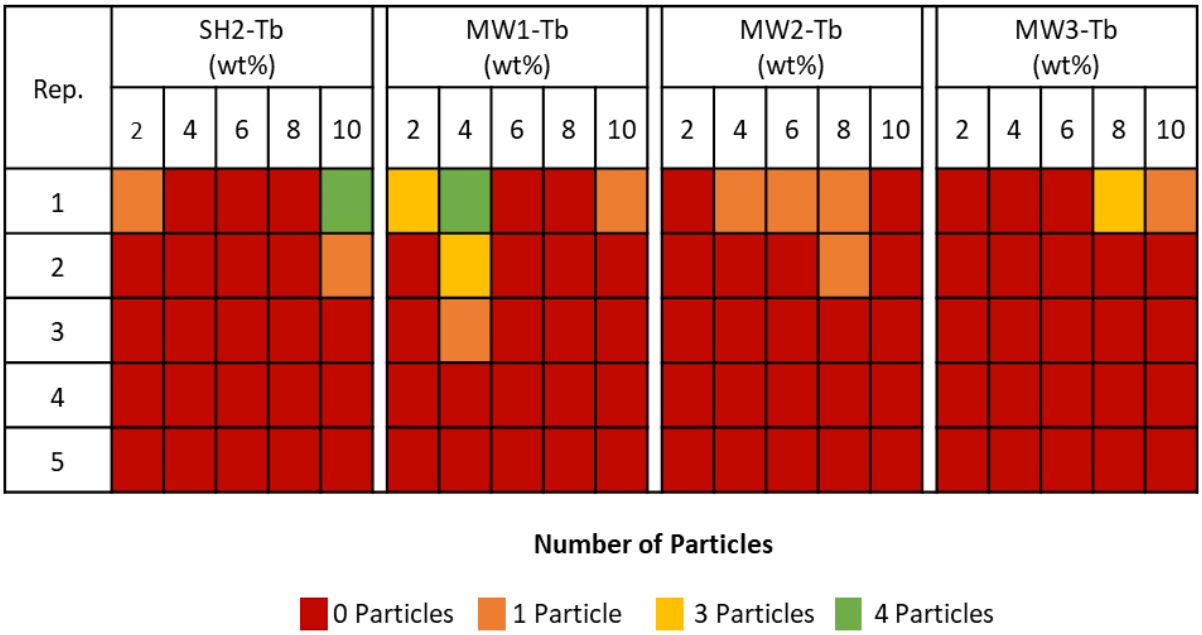

Figure 3-3: Count of visible LGSR particles observed on the shooter's hands (n=5).

Visualising the deposition of LGSR on the shooter's hand proved challenging and was unexpected, considering previous literature had suggested an ease of visualisation. One hypothesis for this observation related to the incorporation process implemented for adding MOF into the cartridge case. One other LGSR study that homogenised the propellant and MOF was conducted by Gomes et al. [191]. It was observed that, after incorporating 30 mg of MOF into ammunition (.38 SPL or .380 AUTO EXPO (+P) Gold Hex), minimal LGSR particles were able to be visualised on the shooter's hand. The greatest abundance of LGSR particles were instead noticed within the firearm and on the FCC. For studies that did not homogenise the MOF and propellant, the dispersion of LGSR particles onto the shooter's hand was identified to be easily visualised. This was confirmed by the images provided which highlighted the greater number of LGSR particles present on the shooter's hands [12, 78, 172, 174-176, 180-183].

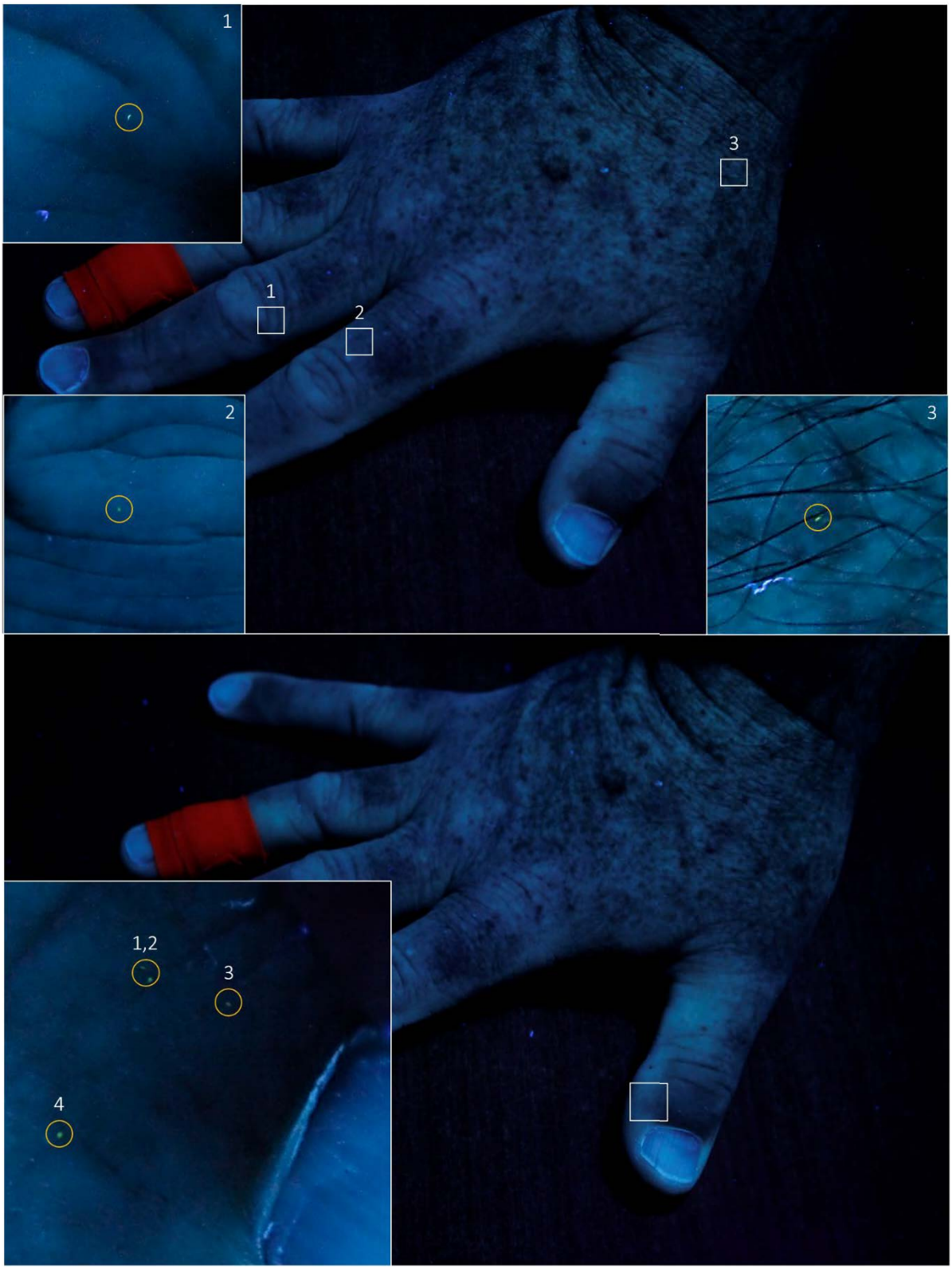

Figure 3-4: Example of maximum distribution patterns observed by the LGSR particles visible under UV light following discharge of ammunition containing 4 wt% of MW1-Tb. Inserts are close up images of the area containing LGSR particles to enhance visibility.

The difference in the MOF addition method could result in a different interaction between the MOF and propellant. The action of homogenisation resulted in a layer of MOF coating each individual propellant grain (pre-discharge) and excess MOF settling within the gaps between the individual propellant. Whereas, it is hypothesised that without homogenising the two components, the MOF settles in the space between the projectile and propellant. This difference in MOF placement within the cartridge case could be affecting the combustion of the propellant once the reaction enters the cartridge case through the flash hole. The MOF coating the propellant could reduce the burn rate of the propellant, which inhibits the combustion, decreases pressure build up and overall disperses less LGSR particles. Any reduction in pressure within the cartridge case would affect the GSR plume exiting the muzzle [447]. The process of not homogenising the MOF and propellant could prevent the inhibition of combustion, suggesting that the GSR plume is generated before combining with the MOF to form LGSR particles. However, a comparison of method would need to be conducted for the four MOFs evaluated to confirm whether the addition process is impacting the ability to visualise LGSR on the shooter's hand.

The observation from the shooter's hands also suggested that the LGSR particles could be too small to observe by the naked eye and/or the LGSR dispersion may have been affected by the addition of the MOF. The stubs were evaluated in the VSC (λ_{ex} = 365 nm) to see whether any LGSR could be visible under different magnifications. Under 60 x magnification it became evident that there were small luminescent green particles present on the stub. A spectroscopic analysis confirmed that the green particles were consistent with the Tb component of the MOF. Overall, analysis of the stub in the VSC highlighted that the LGSR particles were distributing onto the shooter's hand; however, they were too small for an investigator to see without magnification assistance.

3.3.2.2 Firearm

Visualising the LGSR particles deposited on and within the firearm at the firing range was conducted alongside the visualisation and collection of LGSR from the shooter's hands. Unlike the results obtained from the visualisation of the shooter's hand, the LGSR particles were easier to observe on and within the firearm. From the firearm results two observations were made relating to the incorporation ratio and location of LGSR deposition, both of which related to the MOF type.

The first observation focused on the variability between incorporation ratios. It was identified that the LGSR particle trends observed on the firearm fluctuated depending on the MOF type. The variability in LGSR particle counts between the MOFs made it difficult to pinpoint which factors were impacting the results being observed (*Figure 3-5*). SH2-Tb and MW2-Tb followed a similar trend, where incorporation ratios 2 wt%, 6 wt% and 10 wt% resulted in an increase in LGSR particle visible

on the firearm. However, the observation of LGSR particle counts for 4 wt% and 8 wt% being less than the prior incorporation ratio (2 wt% and 6 wt%, respectively) was unexpected. There was no obvious relationship between the MOF ratio and the propellant to suggest why this trend was observed. All MOFs were exposed to the same conditions (storage, incorporation and discharge), with the only notable alteration in the method resulting from the incorporation length (amount of time that passed between MOF incorporation and discharge). Due to discharge scheduling, and to provide the option for comparison with literature, ammunition containing 2 wt%, 6 wt% and 10 wt% ratios were discharged prior to ammunition containing 4 wt% and 8 wt% of MOF. The longest period post-incorporation was 3 months, which corresponded with the incorporation length for the SH2-Tb and MW2-Tb ammunition incorporated with 4 wt% and 8 wt%. This timeframe does not support the possibility for MOF degradation, as the pure MOFs were all observed to retain their chemical and luminescent stability for up to 24 months (Chapter 2). Without evaluating the effect of incorporated ammunition stability for all four MOFs, at all incorporation ratios, it is not clear whether this factor influenced the LGSR dispersion on the firearm. Visualisation of LGSR particles resulting from MW1-Tb highlighted low LGSR counts on the firearm at incorporation ratios of 2wt% and 4 wt% before observing a spike at 6 wt%. This trend in the visible LGSR particles could be attributed to the powder consistency of the MW1-Tb. MW3-Tb was the only MOF to illustrate that by increasing the amount of MOF added to the ammunition, a greater amount of LGSR was able to be visualised post discharge, which is supported by literature [12, 78, 174, 190]. The peak LGSR count observed at the incorporation ratio of 10 wt% was the highest count among all four MOFs.

As a measurement of post-incorporation stability was not performed in this study, an examination into other altering factors was required. The LGSR particle count on the firearm was highest at the 10 wt% for each MOF, except MW1-Tb which had the highest particle count at 6 wt% (no noticeable increase or decrease at increased incorporation ratios). During homogenisation, it was observed that the MOFs generally coated the propellant, with any excess MOF amalgamating into clusters. As incorporation ratios increased, more clusters of MOF within the propellant pre-discharge were observed. Post-discharge, the samples containing the greatest amount of clustering could be linked to higher counts of LGSR particles in the firearm. This was not encountered for MW1-Tb, at incorporation ratio of 2 wt%, which had a high number of clusters and low number of LGSR particles. This suggests that the clustering observed from the MOFs could be impacted by the chosen incorporation methods but may not be the only defining factor in the count of LGSR particles at different incorporation ratios.

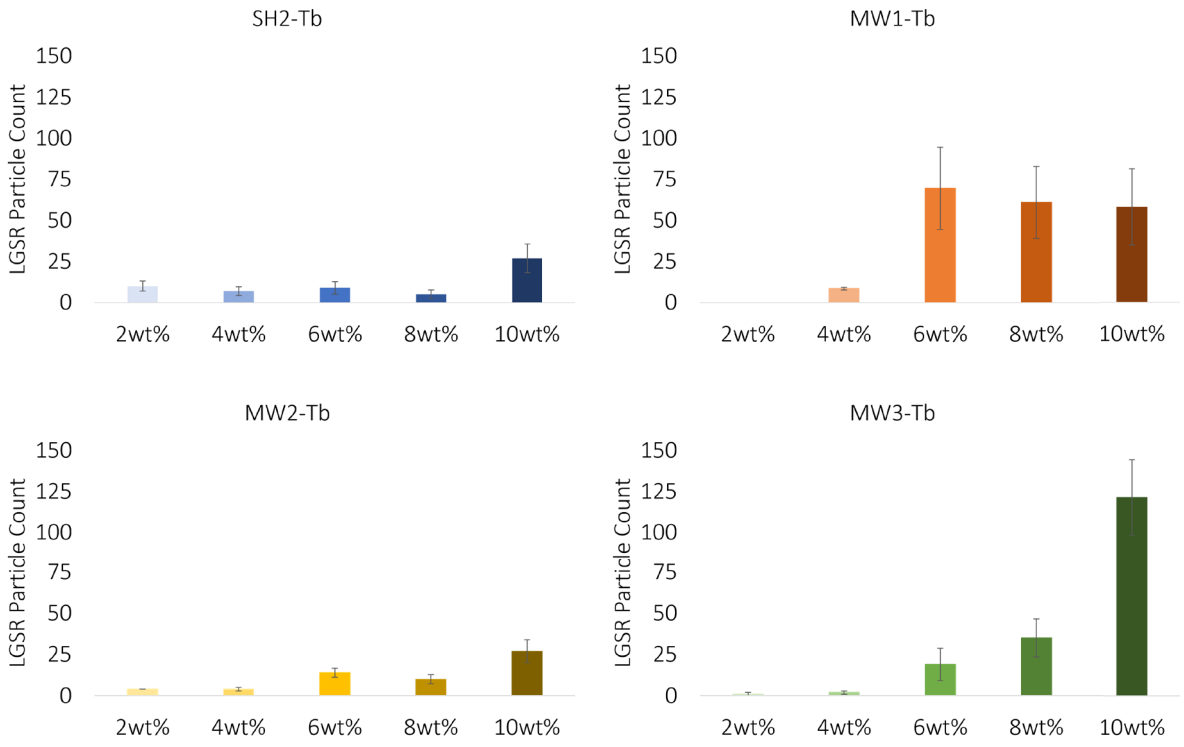

Figure 3-5: Comparison of total count of LGSR particles visible on and within the firearm. Error bars are represented by the interquartile range error (n=5).

The disparity between the different MOFs and the count of LGSR particles observed in the firearm could be attributed to a combination of factors (in addition to the incorporation method), which could include clustering, individual particle morphology and powder consistency (*Figure 3-6*, *Figure 3-7*, *Figure 3-8* and *Figure 3-9*).

When comparing the pure MOF morphology and size, it was observed that SH2-Tb contained a long rod-like morphology (20 – 35 µm), and MW2-Tb contained more of a cuboid shape (22 – 32 µm). MW1-Tb contained a small rod-like morphology (13 – 18 µm), whereas MW3-Tb was oval and the smallest pure MOF (4 – 7 µm) (Chapter 2). It was determined that the morphology of the MOF, does not significantly impact the LGSR count, as even MOFs with the same morphology (SH2-Tb and MW1-Tb) had different trends. The size; however, seemingly did play a role in the trends of LGSR count. The two largest MOFs (SH2-Tb and MW1-Tb) behaved similarly to one another, containing comparable counts and trends for LGSR particles distribution within the firearm. Whereas the smaller MOFs (MW1-Tb and MW3-Tb), had the higher LGSR counts and distinctive trends.

Another physical parameter that could influence the LGSR counts is the powder consistency of the pure MOF. The MOFs with a fluffy powder consistency (SH2-Tb, MW2-Tb and MW3-Tb) had the highest LGSR counts at 10 wt% incorporation ratios, whereas the MOF with a flaky consistency (MW1-Tb) had the highest LGSR count at 6 wt%. The powder consistency also was found to influence the

clustering effect during homogenisation, prior to discharge. MW1-Tb (flaky consistency) was observed to be clustered regardless of incorporation ratio, while the other MOFs (fluffy consistency) only clustered at higher incorporation ratios.

The link between the LGSR particles visible on the firearm and the MOF size suggested that some physical properties may affect the distribution behaviour of LGSR. However, confirmation of this is limited, as there is no evaluation in published literature on MOF powder consistency or morphological properties of the pure MOFs impacting the LGSR visualisation. Only one study by Lucena et al. [173] briefly presents the morphology of their pure MOF, $ZnAl_2O_3:Eu^{3+}$ and stated that while this MOF presents in large aggregates (similar to MW3-Tb), it was still able to generate LGSR on the shooter's hands, firearm and firing range [173]. The variability observed during the visualisation of LGSR particles between different MOFs highlights the importance of considering MOF type and its effect on the LGSR distribution. If the incorporation of MOFs into ammunition was to be implemented into operational ammunition, research should evaluate the MOF properties before, during and after discharge. This observation justifies the need to evaluate the incorporated ammunition each MOF individually.

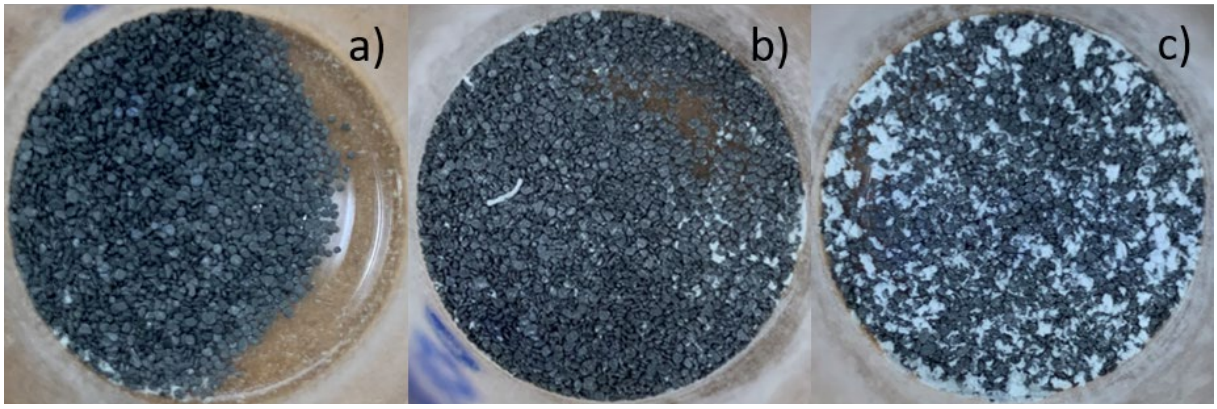

Figure 3-6: Image of SH2-Tb during incorporation with propellant at a) 2 wt%, b) 6 wt% and c) 10 wt%.

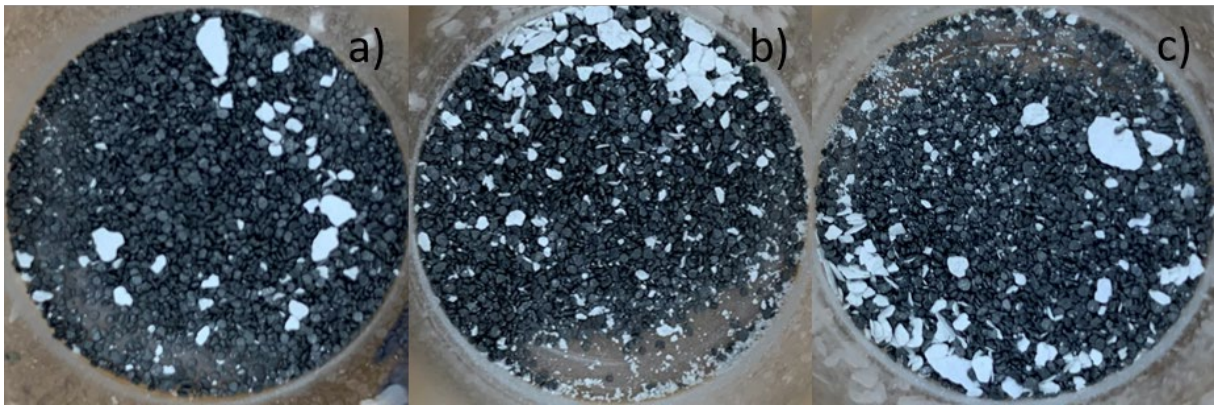

Figure 3-7: Image of MW1-Tb during incorporation with propellant at a) 2 wt%, b) 6 wt% and c) 10 wt%.

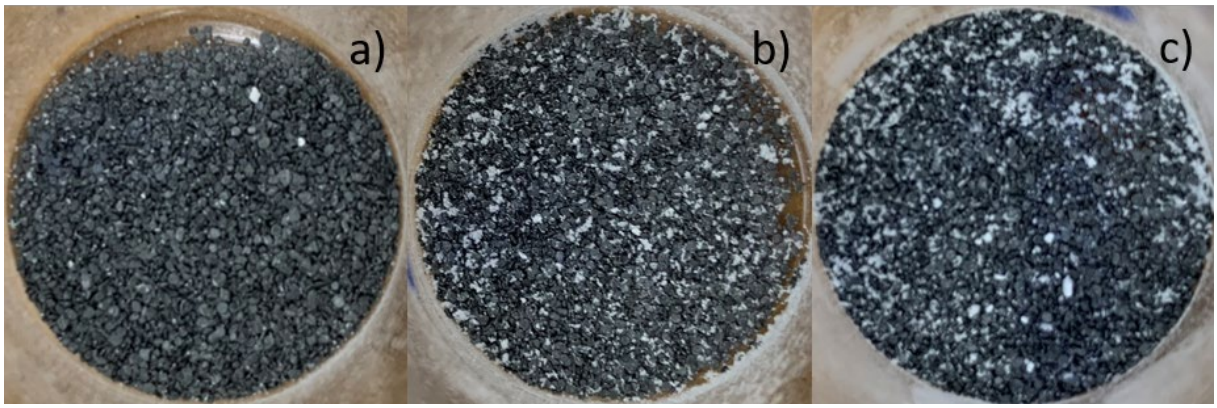

Figure 3-8: Image of MW2-Tb during incorporation with propellant at a) 2 wt%, b) 6 wt% and c) 10 wt%.

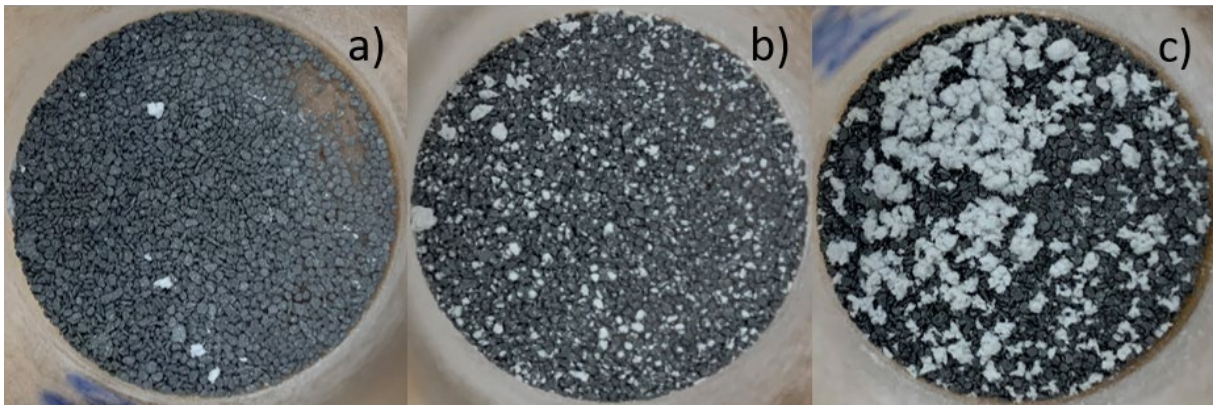

Figure 3-9: Image of MW3-Tb during incorporation with propellant at a) 2 wt%, b) 6 wt% and c) 10 wt%.

The distribution of LGSR particles identified a trend for deposition in different locations of the firearm, which could relate to the powder consistency of the MOF types. For all MOF types, six major areas of the firearm were noted to contain traces of green LGSR particles; (i) frame (handle and trigger), (ii) side of the slide (near grooves), (iii) top of the slide (near ejection port), (iv) barrel (entry and exit), (v) chamber and (vi) breechface. A representation of the LGSR distribution comparison between different locations within the firearm can be seen in *Figure 3-10* for the incorporation ratio of 10 wt%. The LGSR particle counts for all incorporation ratios can be found in Appendix 3.

The areas located on the outside of the firearm (frame and slide) contained the least amount of LGSR particles, while the greatest amount of LGSR was consistently visualised on the breechface of the firearm, and often the particles were grouped instead of being dispersed. Visualising the LGSR deposition on the firearm highlighted that the count of LGSR particles increased the closer to the point of ignition. This suggests that smaller particles are more likely to travel with the plume; however, when clusters of MOF are within the cartridge case the adhesion between particles result in a concentration of LGSR at the point of ignition. These observations are supported by the results from the shooter's hands, hypothesising that the majority of generated LGSR particles are remaining within the chamber instead of travelling in the plume with the firearm. Although, it is expected that

GSR traces would remain within the firearm post-discharge, there has been no research into how much should be expected. A study by Burnett et al. [448] preliminarily evaluated compositional differences in GSR particles collected from the muzzle, bore, cylinder gap and breech of a pistol; however, did not discuss the quantity of GSR particles. To confirm whether the abundance of LGSR visualised is consistent with traditional GSR particles a comparison between traditional GSR and LGSR behaviour should be conducted.

The trends observed from the LGSR counts in different firearm locations provides information regarding the behaviour of the MOF types. Pre-discharge, the visual profile of the homogenised MOF and propellant shows that MOFs containing similar particle sizes and distribution results in similar counts. It was hypothesised, as per previous research, that MOFs containing smaller particle sizes would be observed to travel within the firearm, similarly to GSR particles [27]. However, this was not observed within the data. While SH2-Tb and MW2-Tb were observed to recover the least amount of LGSR (*Figure 3-5*), they show greater distribution along the firearm. The particles post-discharge appear to be travelling within the firearm (*Figure 3-10*) along with the projectile, but not onto the hands of the shooter. During the pure MOF characterisation, these MOFs were observed to contain the largest particle size. As the distance from the point of ignition increases (e.g. slide) there is a decrease in LGSR count (recovered LGSR counts in breechface > chamber ≥ barrel > slide). While these MOFs contain larger individual particle sizes, they are not seen to cluster (during pre-discharge) as frequently.

MW1-Tb follows the same trends as SH2-Tb and MW2-Tb in regard to the travelling distribution of LGSR in the firearm. However, MW1-Tb observed high variability suggesting that the travelling distribution of LGSR is not consistent for this MOF. This was observed for all incorporation ratios. This could be a result of other variables, for example the powder consistency and frequent clustering during homogenisation, which differs from the other MOFs.

Figure 3-5 indicates the greatest recovery of MW3-Tb LGSR was observed on the firearm; however, when exploring the different locations of the firearm (*Figure 3-10*), a large portion of the recovery remains at the point of ignition. Considering the small size of the individual particles, it was expected that this MOF would provide the greatest distribution within the firearm locations. Perhaps this is due to the high counts of clustering of MOF particles observed pre-discharge which is impacting the size of the MOF. For example, the aggregation observed in MW3-Tb (Section 2.3.4) could be leading to easier clustering of excess particles (that do not coat the propellant), which is impacting the ability of the LGSR to travel away from the point of ignition. This is due to the increased mass from the clustering of individual MOF particles hindering their ability to travel.

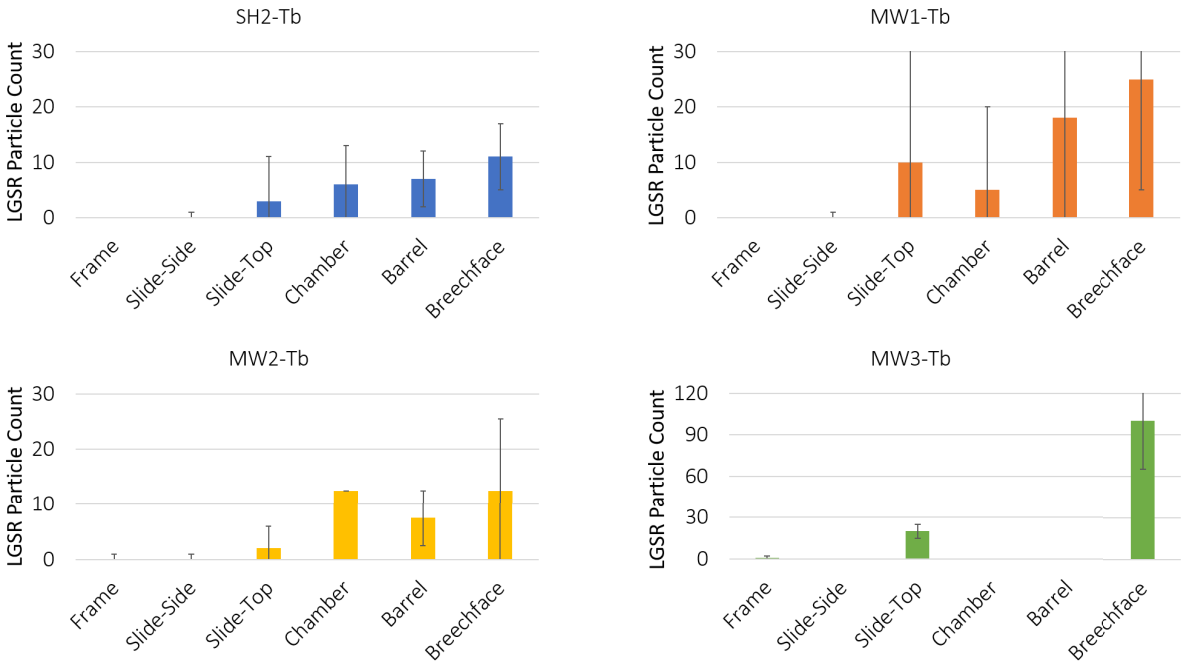

Figure 3-10: Median representation of LGSR particle count within different locations on the firearm at an incorporation ratio of 10 wt%. Error bars are represented by the interquartile range error (n=5).

A comparison can be made between this study and the literature on the visualisation of LGSR particles on the firearm, particularly focusing on the recovery of LGSR particles from the frame [12, 172, 173, 176, 178-180, 183, 186, 188, 189]. This study was able to recover one particle (MW2-Tb and MW3-Tb) from the frame of the firearm (*Figure 3-10*). The studies that evaluated an incorporation ratio of 10 wt% provided mixed information regarding the abundance of LGSR expected to deposit onto the firearm frame. Some literature illustrates a high abundance of LGSR particles distributing onto the frame [172, 178, 188], while other studies visualised less than ten LGSR particles [183, 186, 189]. The differences observed between LGSR abundance did not correlate to firearm or ammunition type, which could suggest that the physical properties of the MOF are influencing the observations.

Within the literature, the purpose of visualising the firearm was subjective, a way to confirm the presence of LGSR regardless of the amount of particles present. This study chose to count the LGSR particles to provide a quantitative approach to the visualisation approach. Although these other studies have evaluated the ability to visualise LGSR on the firearm, there has been no investigation into the quantification of the distribution of LGSR at different locations of the firearm. This would be useful information, as it could suggest if the physical properties of the MOFs are influencing the distribution of the LGSR.

3.3.2.3 Fired Cartridge Case

Once the FCC were ejected and collected, they were visualised in the laboratory to provide further understanding to the distribution behaviour of the LGSR. From the firearm results, it was hypothesised that the LGSR may be easily visible in the FCC, however, it was unknown if the process of ejection from the chamber would result in the loss of LGSR particles. Following visualisation, the amount of LGSR particles were observed to cover the inside of the cartridge case, and due to the abundance of particles were not able to be counted (like for the firearm evaluation). This was prominent in MW1-Tb, which contained the greatest amount of LGSR within and outside the FCC. For SH2-Tb, MW2-Tb and MW3-Tb one distribution trend was observed (Appendix 3), whereas MW1-Tb contained two distinct distribution trends based on the FCC location (*Figure 3-11*). Within the FCC it was observed that as the incorporation ratio increased, there was an obvious increase in the amount of LGSR visible, with FCCs containing 10 wt% MOF being observed with the greatest amount of LGSR. This could suggest that during discharge not all the MOF was being dispersed with the GSR, resulting in lower amounts of LGSR dispersing onto the shooter's hand. For MW1-Tb containing ammunition, specifically 2 wt%, 6 wt% and 10 wt%, a portion of LGSR was also transferred onto the outside of the cartridge case (sides and base). Similar to the firearm results, it could be suggested that the abundance of LGSR particles at the point of ignition is attributed to the powder consistency of the MOF type. For MW1-Tb, which contains a chalky consistency, the large cluster of particles (observed pre-discharge) are unable to travel with the bulk of the GSR plume. In their cluster consistency, the MOFs appear denser than the particles coating the propellant, which could suggest a reason for the abundance of luminescent particles being observed in the FCC. This process is also being observed at higher incorporation ratios for SH2-Tb, MW2-Tb and MW3-Tb, when clusters of their powders are observed pre-discharge; however, in much lower abundances. Interestingly, under white light, a white powdery substance could be observed on the casing, which under excitation with a UV light source, was identified to be the luminescent MOF. Incorporation ratios of 4 wt% and 8 wt% showed a reduced amount of LGSR on the outside of the cartridge case (when compared to the previous incorporation ratio), and instead, the LGSR particles remained within the cartridge case where they were easily visualised as a mass of green luminescent particles. The differences in the ability to visualise LGSR on and within the FCC between MW1-Tb and the other MOFs could be related to the powder consistency observed from the pure MOF.

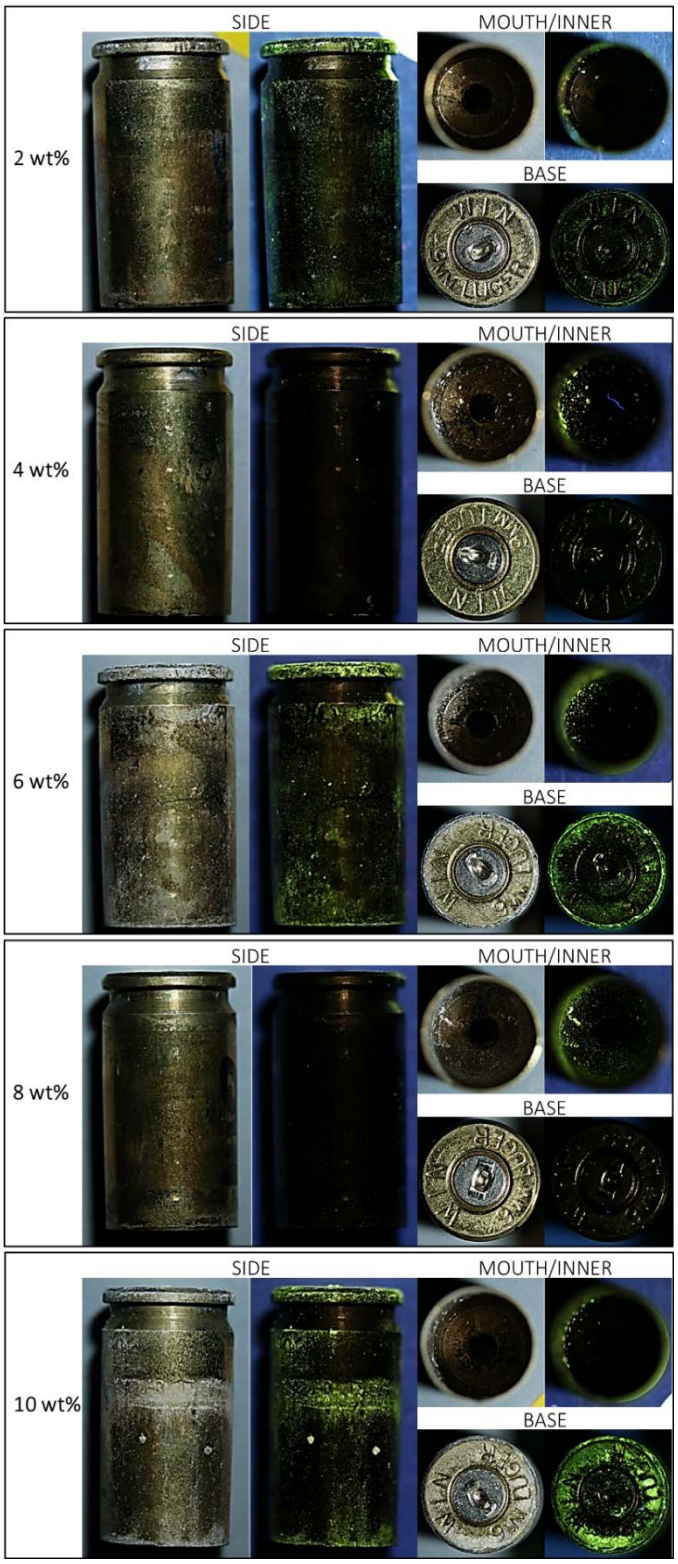

Figure 3-11: Distribution of MW1-Tb LGSR particles at different incorporation ratios on the FCC. Images of the side, mouth and base of MW1-Tb FCC illuminated using white light (left) and the Labino® flood lamp (λ_{ex} = 365 nm, right) using a Canon EOS 700D (ISO = 1600; f-stop = f/2.8; exposure = 1/30 sec.).

3.3.3 Visualisation Overview

The aim of incorporating MOFs into ammunition is to ensure a quick and easy, in-field method of preliminarily identifying traces of GSR on a POI. Overall, the data collected on the visibility of LGSR from the shooter's hand, firearm and cartridge case indicated that the incorporation of MOFs into ammunition influences the discharge process.

The unpredictability of the LGSR deposition onto the shooter's hands contrasted by the strong visual results from the firearm and FCCs suggested that the incorporation of the MOF was affecting the discharge process. In the unmodified ammunition the impact between the firing pin and primer cup causes the primer to explode, creating heat and energy that travels through the flash hole and ignites the propellant. This generates a plume consisting of pressure and GSR particles within the cartridge case, until the maximum threshold is reached. At this point the heat expands the cartridge case to allow the bullet to dislodge and propel forward by the pressure. The plume containing the GSR escapes the firearm through gaps in the frame (predominantly through the muzzle, with some exiting from the ejection port) to disperse onto its surroundings [53]. In the incorporated ammunition, there is a possibility that the MOFs chemical and physical characteristics are impacting the interaction between the heat and energy and the propellant. During the characterisation of the pure MOF, it was identified that each MOF was thermally stable at high temperatures. By coating the propellant, there is a chance that the MOF is acting as an inhibitor, which is affecting the burn rate of the propellant and therefore affecting the generation of pressure and LGSR [447].

In order to confirm whether the incorporation of MOFs into ammunition was impacting the discharge process or LGSR generation or dispersion, the external ballistics of the projectile was evaluated. It was hypothesised that by reducing the pressure being generated within the cartridge case, there would be a change in the velocity and projectile accuracy. Due to the discordant LGSR particle numbers observed from discharging ammunition containing 4 wt% and 8 wt% MOF ratios, it was decided that the external ballistics analysis of these two incorporation ratios would not be conducted.

3.4 PART II: GSR Stub Evaluation

3.4.1 Methods

3.4.1.1 Collection

GSR specimens were collected from the shooter's hand for three discharge scenarios per MOF ratio combination discharge, specimen would be collected in triplicate (*Figure 3-1*). For each discharge scenario, a GSR blank and GSR specimen was collected from the shooter's dominant hand by dabbing the GSR stubs, until all stickiness was lost. The GSR 'blank' was collected after the firearm was loaded and before discharge to understand the background contamination associated with being present within a firing range. Directly after photography, the LGSR samples were collected by dabbing the shooter's dominant hand with GSR stubs, until all stickiness was lost. Certified aluminium pin stubs with a 12 mm diameter double-coated adhesive carbon tab were purchased from Ted Pella, Inc. (Redding, California, USA) for the collection of NTA GSR and LGSR.

3.4.1.2 Analysis

The stubs containing the NTA GSR and LGSR specimens collected from the firing range were stored in a 4-5°C refrigerator until analysis. The specimens were analysed using a Zeiss Evo LS15 SEM (Zeiss, Germany) with an SDD XFlash 5030 detector (Bruker, Germany) and a Diode 5 Channel backscatter detector.

It was not possible to conduct an automated GSR analysis using the GSR Professional Automatic software (Version 1.0, Bruker Quantax) due to calibration errors. Instead, the stubs were manually analysed, which involved locating and imaging different particles within a zone and then manually acquiring the corresponding EDS spectrum under high vacuum (*Table 3-2*).

Table 3-2: SEM-EDS Parameters applied during GSR analysis.

Parameters	SEM	EDS
Magnification	21 x, 500 x, 1000 x, 2000 x	2000 x
Accelerating voltage	25 kV	25 kV
Working Distance	10 mm	10 mm
iProbe	1.0 nA	1.0 nA
Aperture Size	30 µm (large)	30 µm (large)
BSD Gain	High	High

Each stub surface was separated into nine zones. A grid search approach was conducted on zones 4, 5 and 6 at multiple magnifications (x21, x500 and x1000) to locate particles resulting from GSR and/or the MOF (See *A3 - 8* in Appendix 3). Each particle was imaged and analysed at different x magnification. It should be noted that each zone was restricted to an analysis maximum of 20 particles due to the time required for this process for each zone and instrument availability. Although the ammunition being used contained a WinClean composition, a spectral analysis and elemental mapping was conducted and analysed elements pertaining to 'characteristic', 'consistent' and 'commonly associated' with traditional and NTA primers. Additional elements, as indicated by the E1588-20 standard, as well as terbium (Tb), were included in the analysis for all stubs to confirm the presence of the elements in the LGSR specimens (*Table 3-3*) [8].

Table 3-3: List of elements analysed during manual SEM-EDS analysis of traditional GSR, NTA GSR and LGSR stubs according to the E1588-17 Standard. * = characteristic, ^ = consistent, # = commonly associated with and + = additional elements.

Traditional	NTA	Additional Elements
Lead (Pb) * ^ #	Copper (Cu) * +	Chlorine (Cl) +
Antimony (Sb) * ^ #	Gadolinium (Gd) *	Iron (Fe) +
Barium (Ba) * ^ #	Gallium (Ga) *	Nickel (Ni) +
Aluminium (Al) # +	Strontium (Sr) ^	Phosphorus (P) +
Calcium (Ca) * ^ +	Tin (Sn) *	Potassium (K) +
Silicon (Si) * ^ +	Titanium (Ti) * ^	Zirconium (Zr) +
Sulfur (S) ^+	Zinc (Zn) * ^ +	
Tin (Sn) * +		

3.4.2 Results and Discussion

The stubs underwent analysis on the SEM-EDS to confirm the presence of both NTA GSR and LGSR components. The calibration of the *GSR Professional Automatic* software proved unsuccessful and limited this study in quantitatively analysing the stubs according to ASTM E1588-20 standard procedures followed by Australian authorities. Instead, a manual GSR examination was conducted as a proof-of-concept, to identify the morphology and elemental profiles of individual particles.

The control stubs were examined first to identify which of the elements listed in *Table 3-3* were expected to be identified on the GSR stubs. The manual search highlighted that there was a low abundance of spherical particles present on the stub and instead a high abundance of atypical or irregularly shaped particles were observed. The examination of any particle sized within 0.5 – 5.0 µm highlighted particles containing elements from all three categories (traditional, NTA and additional elements) were present on the stub in different abundances. The morphology of the LGSR particles

encountered was consistent with GSR resulting from 9 mm Luger CleanRange® primer in Martiny et al. [59]. The EDS spectrum from each particle provided information regarding the intensity of the counts per second (cps) for each element which varied between particles. The intensity for each element was classified as 'major', 'minor' or 'trace' levels [6, 449]. Atypical particles with an unrecognisable shell shape containing minor elements of Cu and Zn were the most abundantly encountered during the manual GSR examination (*Figure 3-12a* and *Figure 3-12e*). This is likely due to the high percentage of Cu and Zn components within the metal mixture in centrefire loaded ammunition, as well as the from the cartridge case alloy (brass composition), as highlighted in the Winchester material safety data sheet [450]. The abundance of Cu and Zn particles was also encountered by Costa et al. [113] who evaluated two 0.40 clean range ammunition types and attributed the presence of these particles to the alloys used to produce the cartridge. The detection of particles containing a combination of minor level elements (Fe, S and/or Zn) and trace level elements (Al, Ca, Cl, Cr, Cu, K, Ni, P and Ti) was also encountered during the manual GSR examination (*Figure 3-12b, Figure 3-12c, Figure 3-12*f and *Figure 3-12g*). This observation was similar to Romanò et al. [54] who identified particles containing similar minor and trace level elements between three different NTA (two Fiocchi 9 x 21 mm and one GECO 9 x 21 mm). The morphology of these particles; however, were irregular following a shape similar to RUAG SWISS SeCa 9 x 19 mm ammunition evaluated by Doña-Fernández et al. [111]. There was also evidence of irregularly shaped particles with a peeled orange shell containing minor levels of Pb and Sb (*Figure 3-12d* and *Figure 3-12h*). The low abundance of these types of particles could be attributed to contamination as a result of memory effect; however, the material safety data sheet for the SuperX Winclean ammunition suggests there is evidence of Pb being used in the bullet [451], as well as in the metal alloy mixture (see A3 - *10* in Appendix 3). The search of the control stub search did not identify any particle containing Gd, Ga or Sr peaks. It was expected that the ammunition being used would not contain traces of Gd or Ga, as Australian ammunition does not contain these taggants. However, the lack of Sr elemental Kα and Lα peaks at 14.14 KeV and 1.806 KeV, respectively, could be a result of the Sr concentration in this ammunition being below the limit of detection. Considering most elements in the control ammunition were identified at either minor or trace elemental levels, the Sr elemental peaks could be hidden within the noise. All particles examined on the control stubs did not contain traces of Tb.

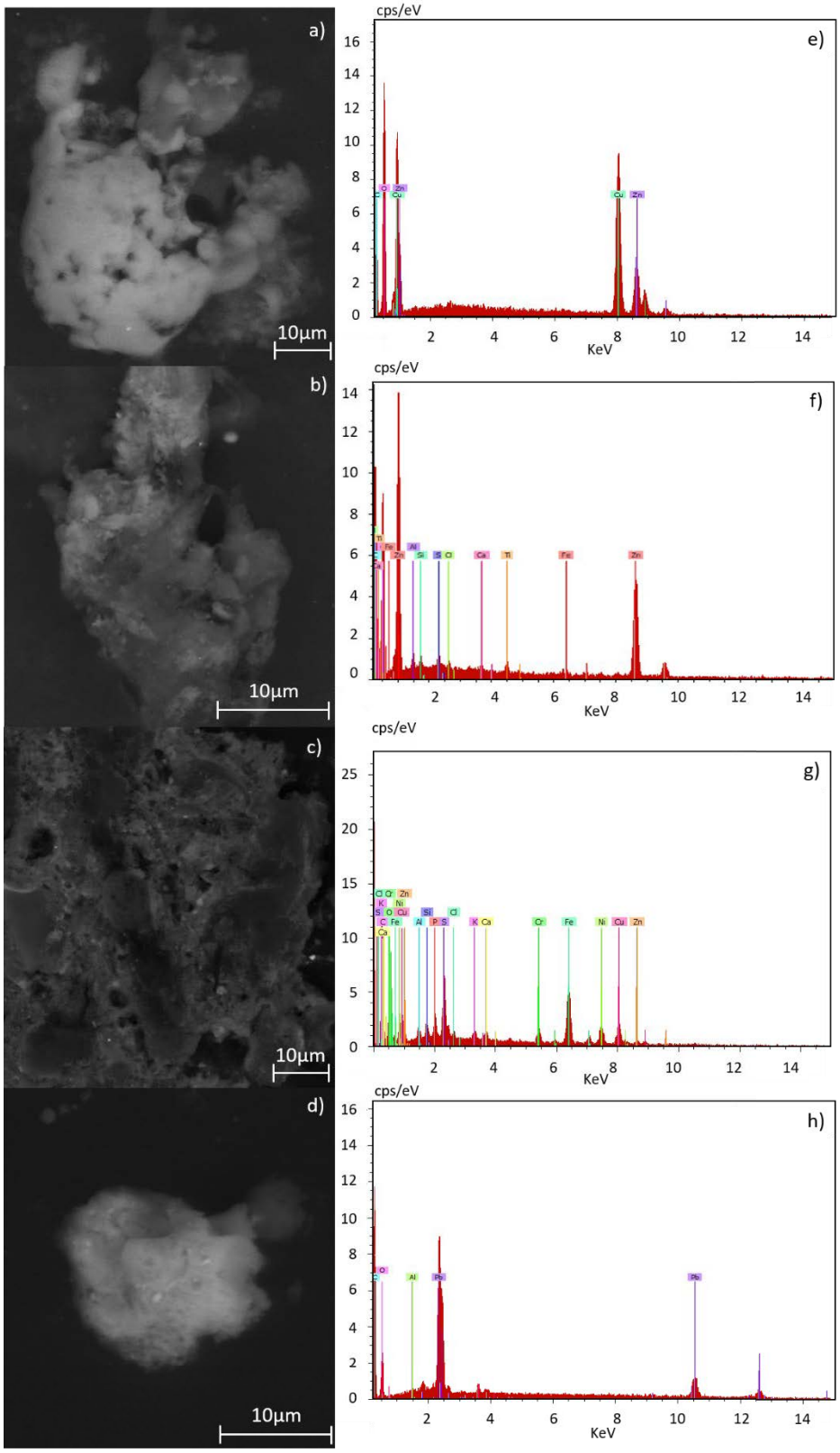

Figure 3-12: Encountered particle morphologies (a-d) and associated elemental composition (e-h) on the control stub. Morphology of particles consist of a) atypical particle, b) irregular particle, c) irregular particle, and d) irregular shape. Abundance of particles decrease further down the list.

The LGSR stubs were observed to contain particles with the same morphology and elemental composition as the control stubs, as well as additional particles containing Tb-MOF particles. The morphology of the discharged SH2-Tb, MW1-Tb and MW3-Tb particles were observed to remain the same as the pure Tb-MOF allowing for simple identification (*Figure 3-13*). This also provided ease for differentiating between GSR particles and Tb-MOF particles which were identified to coexist on the stub with no merging of particles. An additional observation encountered from the manual search of the stubs highlighted that as the incorporation ratio of the MOF increased, it became easier to identify the Tb-MOF particles (*Figure 3-13*). The same observations were not identified on stubs containing MW2-Tb LGSR. The pure MW2-Tb MOF was identified to contain a cuboid morphology; however, the shape of the particle was warped post-discharge. The reason particles containing this morphology were identified as MW2-Tb was due to the associated characteristic Lα and Mα transition peaks of Tb^{3+} ions being detected in the EDS spectrum. As no other study evaluating MW2-Tb MOFs highlighted this occurrence, it is unknown if this phenomenon is common for this MOF type [12]. The change in morphology encountered for MW2-Tb did impact the ease of identification for this MOF.

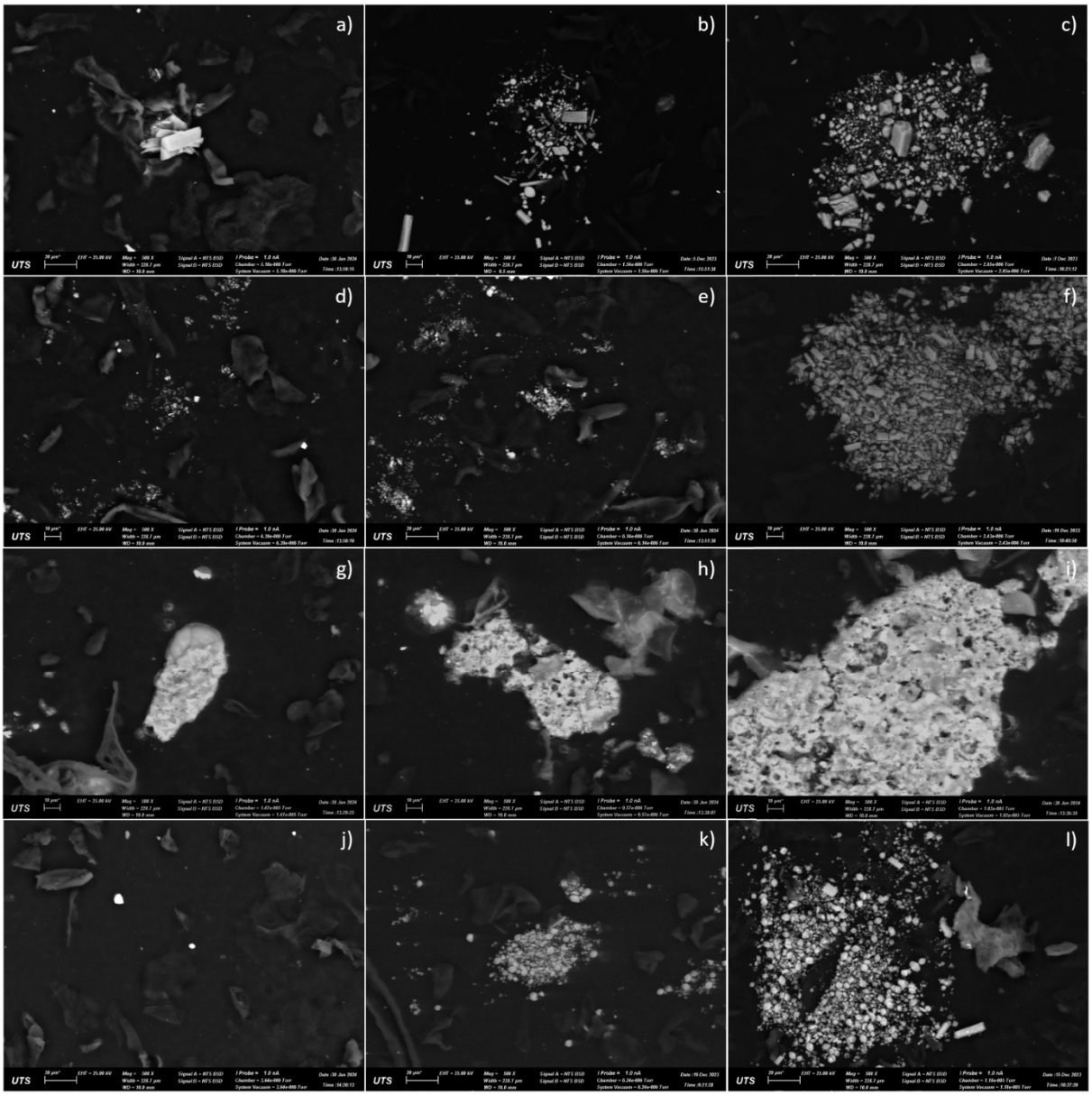

Figure 3-13: Abundance of discharged Tb-MOF on GSR stub. a) SH2-Tb-2 wt%; b) SH2-Tb-6 wt%; c) SH2-Tb-10 wt%; d) MW1-Tb-2 wt%; e) MW1-Tb-6 wt%; f) MW1-Tb-10 wt%; g) MW2-Tb-2 wt%; h) MW2-Tb-6 wt%; i) MW2-Tb-10 wt%; j) MW3-Tb-2 wt%; k) MW3-Tb-6 wt%; l) MW3-Tb-10 wt%.

Without conducting the automated data analysis of the whole GSR stub via SEM-EDS (detection of all individual particles and assignment of particle groups), according to the ASTM E1588-20 standard procedures followed by Australian authorities, it was not possible to identify whether there was any interference to the GSR distribution occurring from the presence of the MOF in the cartridge case. Instead, the data collected from the GSR stubs confirmed the ability for the instrument to be able to detect both GSR particles and MOF particles on the same stub. Additionally, the ability to visually differentiate between the GSR particles and MOF particles coupled with the EDS ability to characteristically identify Tb peaks alongside GSR characterisation indicates that these particles could

be used as a taggant. The introduction of NTA has indicated that the recognised characteristic particles associated with IGSR (spherical Pb-Ba-Sb particles) may not be detectable at some firearm-related scenes [452]. The application of MOFs containing REE as the metal core provides an additional distinctive particle with a characteristic EDS spectrum. The distinctive framework associated with MOFs, along with the implementation of REE as the metal core makes this type of particle differentiable from GSR particles. While it is possible to integrate REE-containing compounds into ammunition, which is seen in Action 4 SXF (Sintox Forensis) from RUAG (Gd_2O_3) [453], SECA SXF from RUAG (GaCuSn) [61, 453], QD-PEP 2.0 (II) from MEN (Gd_2O_3) [61, 453] and FIOCCHI-RIS from Fiocchi (Sm_2O_3) [161], the associated GSR particles are not distinctive (identified as spherical). Differentiating between GSR based on both MOF morphology and REE provides a stronger support for investigators to link the traces collected to the discharge of a firearm. The ability to confirm luminescence (visual and spectral) on the GSR stub under VSC magnification will also assist the interpretation of the analytical results and provide better support that the specimen collected is indicative of firearm discharge.

3.5 PART III: Projectile Performance

3.5.1.1 Set Up

To assess the projectile behaviour post-discharge, the firearm was secured into a vice to ensure the firearm was held in place during discharge and to alleviate any variation attributed to the shooter (*Figure 3-14*). A BR-3503 Doppler radar antenna (Infinition Inc., Canada) was used to capture and measure the velocity of the projectile in flight. It functions at 35.5GHz and was chosen over a chronograph due to its designation for short-range applications. It captures both the projectile muzzle velocity and the velocity of the projectile along its trajectory. The Doppler radar was used in combination with a JB-6e Junction Box (Infinition Inc., Canada) to reliably process and transfer the acquired velocity data. A combination of an AT-01 Acoustic Transducer (Infinition Inc., Canada) and a 4941-A-011 pressure-field microphone (Brüel & Kjær, Denmark) to synchronise the sound and velocity of the projectile. TestCenter 6 Doppler processing software (Infinition Inc., Canada) was used to collect and analyse the velocity data. The target was set up at a distance of 10 m from muzzle to collect accuracy data of the projectile. The firearm was equipped with a laser light (mounted to the rail) to ensure the firearm muzzle was lined up to the same point of aim (POA) target between each discharge. The target was replaced after five replicate shots was conducted for each MOF incorporation ratio.

Figure 3-14: Chronograph and firearm set up aimed perpendicularly at the target (10 m distance between muzzle and target), in an indoor firing range.

3.5.1.2 Discharge Process

To identify the range of effects the incorporation of MOFs has on the behaviour of the projectile following discharge, three incorporation ratios (2 wt%, 6 wt%, and 10 wt%) and the unmodified ammunition were evaluated for each MOF. Prior to discharge, the shooter was required to clean the firearm according to Section 3.2.3. The firearm was then loaded with a single round of ammunition before being loaded into the vice and discharged. This was conducted in quintuplicate for each MOF and ratio combination, before a new target was placed at a distance of 10 m from muzzle. The velocity and accuracy data were collected simultaneously for each discharge.

3.5.1.3 Post-Discharge Data Analysis

An evaluation into shooting failure (ejection of FCC) was conducted each time the firearm was discharged. To determine the rate of shooting failure, the ejection of FCC from the GLOCK 19 firearm was recorded as being either automatic (removed by the extractor) or manual (required shooter to assist).

The velocity (in m/s) of the projectile was collected on the TestCenter 6 Doppler processing software following the projectile from the time it exited the muzzle of the barrel until it reached the back of

the range. The software analysed the performance of the projectile to provide the average velocity over the course of 10 m. The velocity of the projectile from ammunition containing MOF were compared to the projectile from unmodified ammunition to identify the variation in speed from the additional components in the cartridge case. The standard error of the mean was calculated for each MOF and ratio combination. The sound measurement readings were collected on the PULSE™ LabShop software (Brüel & Kjær, Denmark) at the time of discharge. Only the maximum decibel readings from the initial discharge sound were recorded.

The accuracy of the projectile was determined by comparing the location of the MOF projectile in relation to the location of the traditional projectile. The location (x-, y-coordinates) of each shot was measured (in cm) from the centre of the target. The location of each projectile penetration was calculated (and averaged) from the POA target. The averaged MOF projectile location was normalised against the location of the control projectile to determine the effect the addition of the MOF has on the projectile accuracy. The standard error of the mean was calculated for each MOF and ratio combination.

3.5.2 Results and Discussion

Evaluating the performance of the firearm and projectile during the discharge of incorporated ammunition is an important aspect to consider in conjunction with the evaluation of LGSR. Shooting failure, velocity, sound measurement and accuracy testing were conducted to understand how the discharge process and projectile performance were being impacted by the presence of the MOF as observed by the deposition of the LGSR on the shooter's hand, firearm and FCC. The high level of risk associated with the use of firearms requires ammunition performance to be evaluated for the safety of its users (law enforcement or civilians) through quality testing of the repeatability and constancy in the projectile trajectory and aim.

3.5.2.1 Shooting Failure

The location of FCCs at a crime scene provides investigators with information regarding the use of a firearm and can be applied to determine a shooters position. For GLOCK 19 firearms, the ejection of FCCs is an automatic process. Once the projectile propels forward, the FCC is extracted from the chamber of the pistol and an unfired round of ammunition is feed into the chamber ready for the next discharge. This study recorded the ejection (automatic or manual) for each FCC to identify whether the incorporation of MOF was affecting the firearm mechanisms.

During discharge, the automatic ejection of the FCC and ammunition feeding were observed for any indication of shooting failure. In all shots recorded, less than 10% of shots resulted in the FCC failing

to eject automatically, with 8% of these occurring for MW3-Tb. These results differ from Weber et al. [174], who observed 100% of failure when incorporating 10 wt% of either Ln(DPA)(HDPA) or $ZnAl_2O_4$:Ln MOF into ammunition and suggested that the shooting failure is related to the changes of mass and space within the cartridge case. The results from SH2-Tb, MW1-Tb, MW2-Tb and MW3-Tb indicated that this reasoning may not affect the shooting failure observed. Instead, the observation of shooting failure is more likely to be a result of the re-assembly process of the ammunition round considering no other LGSR study has indicated that this was encountered.

3.5.2.2 Velocity

The unmodified ammunition was evaluated to identify the baseline velocity for this combination of firearm and ammunition, which was used as a comparison with the incorporated ammunition. For all MOF types, increasing the incorporation ratio resulted in a decrease in the projectile velocity (*Figure 3-15*). A mean decrease of all MOFs from the control velocity of 21.5% (± 2.75%), 33.4% (± 9.23%) and 40.9% (± 6.70%) was observed for incorporation ratios of 2 wt%, 6 wt% and 10 wt%, respectively. It was also observed that increasing the mass of the MOF was affecting the repeatability of the shots, suggesting that the MOF type may affect the velocity. This velocity observation was similar to literature by Weber et al. [174] who suggested that the trend observed was a result of changes in ammunition mass and/or the reduction of free space within the cartridge. Weber et al. [174] further indicated that regardless of this decrease in velocity, the overall incorporation of MOFs in ammunition is still a viable option following the correct balancing of incorporation ratio, propellant (type and weight) and primer [174]. However, according to NATO Standard AEP-97, a decrease in velocity greater than 1.26% (approx. 4 m/s) for 9 mm x 19 ammunition implies that the ammunition does not meet the baseline standards [454]. It was evident that for the unmodified ammunition velocity all replicate shots were tightly concentrated at 282 m/s (± 1.99 m/s), which is in line with the AEP-97. However, the incorporation of any MOF resulted in a minimum velocity reduction of 21.5% (35 m/s). Given the thermally stable property of the MOFs, the data suggests that by coating the propellant, the MOF could be inhibiting the ignition process. This was affecting the propellant burn rate, the generation of pressure within the cartridge case and negatively impacted the performance of the projectile. Another observation could be made from *Figure 3-15* based on the variability of the velocity clustering between the MOF types and replicate shots (n=5) at higher incorporation ratios. For the control projectiles, the velocity clustering was tightly gathered within 3 m/s. At incorporation ratio of 2 wt% the velocity cluster increases to within 9 m/s of each other, whereas the velocity clustering becomes more spread out at higher incorporation ratios of 6 wt% (30 m/s) and 10 wt% (21 m/s). While some degree of variation is expected between replicate shots, the level exhibited by the higher incorporation ratios falls outside the acceptable standard deviation range (<4 m/s) [454].

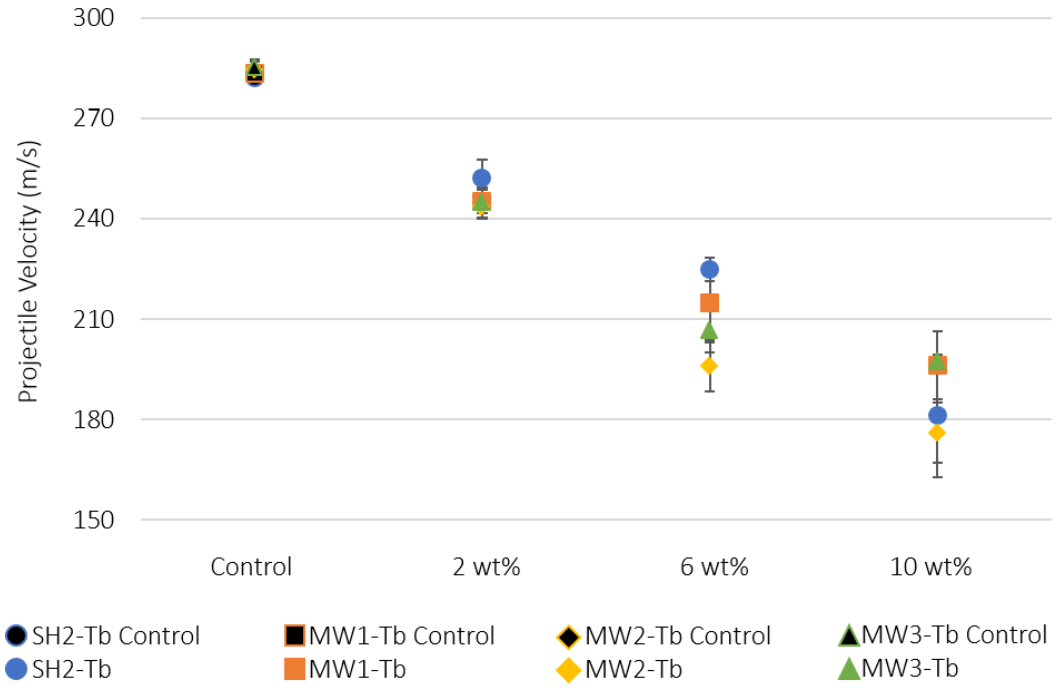

Figure 3-15: Ratio effect on the velocity comparison of MOF-incorporated ammunition and the unmodified ammunition (control). Error is represented by the standard error of mean (n=5).

During homogenisation, the MOF was observed to coat the propellant and any excess MOF settled within gaps between the propellant. The MOF could be acting as an inhibitor during ignition due to its heat resistant property. This suggests that during discharge the heat from the primer detonation takes longer to interact with the propellant and delays the generation of pressure and LGSR. The MOF coating may also be impacting the burn temperature within the cartridge case resulting in the propellant not burning to completion before the projectile exits the muzzle and remains unburnt in the chamber, FCC, or barrel of the firearm. This change in temperature can lead to a change in the velocity of the projectile [455].

To a lesser extent, there could be a lack of oxygen within the cartridge case that is reducing the impact of the detonation and altering the pressure build up within the cartridge case. This reduction of oxygen could occur from either the excess MOF using up space within in the cartridge case, or the MOF is absorbing oxygen into its framework as H_2O molecule and reducing the amount of oxygen left within the cartridge case. It is unknown whether it is only one of these processes or a combination of all hypotheses is resulting in the reduction of pressure generated to propel the projectile forward, causing a reduction in velocity. However, it should be highlighted that the homogenisation incorporation process is a point of differentiation between this study and existing literature [455].

3.5.2.3 Sound Measurement

Sound measurement readings of each shot were collected simultaneously with the velocity data. For all shots (control and incorporated), the initial maximum sound reading was 169 dB (± 1 dB). Although the same maximum sound readings (initial discharge sound) were identified for all shots, it should be noted that during discharge the investigators were able to identify audible differences between the control and incorporated ammunition discharge. During analysis, it was highlighted that in order to understand the impact between changes in ammunition (or firearms) and sound impact, a time-domain graph is required which follows the sound of the shot after discharge. The time-domain graph provides the waveforms, post initial discharge, which provides information about sound reflection from nearby facades and butt hitting. A study by Matys et al. [456] highlights the importance of the time-domain graph in the differentiation of discharge sound from different firearm types. For five out of the eight firearms (mixture of rifles, shotguns and pistols) tested, the initial maximum sound reading was approximately 143 dB and the differentiable information between the firearm being observed in the time-domain graph [456]. This highlights that without additional information from the sound reading, it is difficult to pinpoint the differences between that could support or deny the hypotheses for velocity. Unfortunately, the time-domain graph was not able to be collected for this study, and without this data it is not possible to identify the similarities or differences in the waveforms post-discharge for incorporated ammunition.

3.5.2.4 Accuracy and Precision

The evaluation of the projectile accuracy and precision was conducted to confirm the findings outlined by the velocity of the projectile. When using the unmodified ammunition, the intended amount of pressure generated within the cartridge case propels the projectile forward at a consistent velocity. As the projectile begins to exit the muzzle, the firearm barrel lifts slightly so that the projectile begins its trajectory at an angle of elevation. As the projectile travels along the flight path, it reaches a point where the air resistance and gravitational effect causes it to begin travelling in a downwards curved path known as the angle of fall until it perforates the target at the point of aim (POA) [457]. The accuracy of the projectile is impacted by the projectile velocity; however, is also dependent on a range of other factors including gravity, angle of elevation, target and projectile materials, and the projectiles drag coefficient [458].

The baseline determination of the accuracy and precision was conducted through the evaluation of the control projectile perforation, which was used for comparison with the incorporated projectiles. The control projectiles had a standard deviation of ± 0.59 cm (y-axis) and ± 1.5 cm (x-axis). According to NATO Standard AEP-97, the vertical and horizontal precision of 9 mm x 19 ammunition projectiles

should contain a standard deviation of ≤ 2.5 cm when the muzzle to target distance is 46 m [454]. Comparing the unmodified ammunition and the AEP-97 standard indicates that the control projectile sits within acceptable precision limits.

The accuracy of the MOF incorporated projectiles was identified based on the deviation from the control (POA), while the precision was observed through the repeatability of multiple projectiles and is represented through the error bars as the standard error of mean. No apparent trend could be identified based on either the incorporation ratio or MOF type (*Figure 3-16*). Once the MOFs were incorporated into the ammunition, both the accuracy and precision of the projectile was negatively impacted. All MOF incorporated projectiles were observed to perforate the target at locations below the control indicating that the flight path of these projectiles was being impacted. For projectiles from ammunition containing MW1-Tb and MW3-Tb it was observed that as the incorporation ratio increased, the distance between the control projectile and the MOF projectile perforations increased along the y-axis. Projectiles from SH2-Tb showed that incorporation ratio of 10 wt% were the closest projectiles to the POA; however, the precision of the projectiles show a large amount of overlap with the SH2-Tb incorporation ratios 2 wt% and 6 wt%. This indicates that for this MOF the incorporation ratio did not impact the deviation from the control POA. Similarly, MW2-Tb showed no trend for its incorporation ratios, which were all found to perforate at similar y-axis locations.

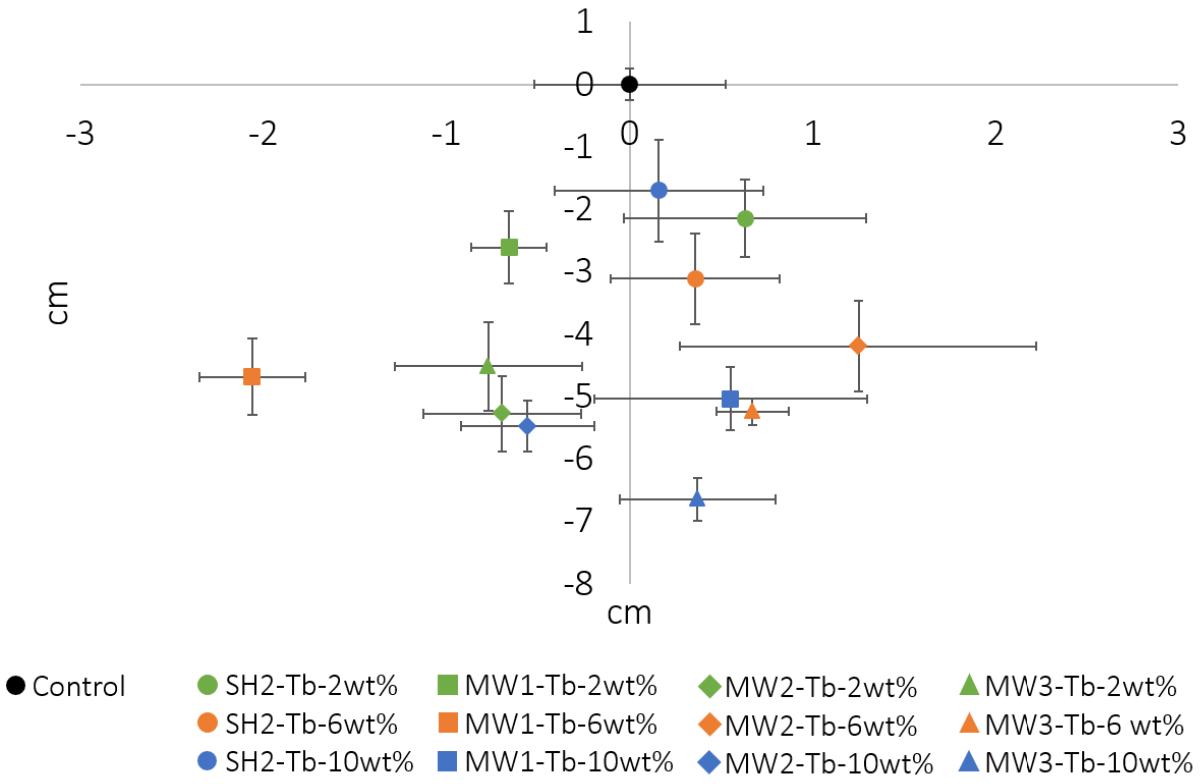

Figure 3-16: Normalised projectile perforation location for each MOF and incorporation ratio in relation to the unmodified ammunition projectile. Colour represents incorporation ratio and shape represents MOF. Error is represented by the standard error of mean (n=5).

With the position of the firearm and target, as well as the room conditions remaining consistent, it left little room for unknown variables other than the incorporation of the MOF into the ammunition to affect the trajectory of the projectile. Once the projectile velocity is impacted, although the flight distance and target material remain the same, the projectile did not have enough velocity once it exited the muzzle to pushing it along the normal flight path (*Figure 3-17*). Without the required velocity the projectile angle of elevation was reduced impacting its flight path. The additional impact of air resistance and gravitational effect caused the projectile to begin travelling in a downwards began to fall sooner and as a result the projectile deviated from the POA.

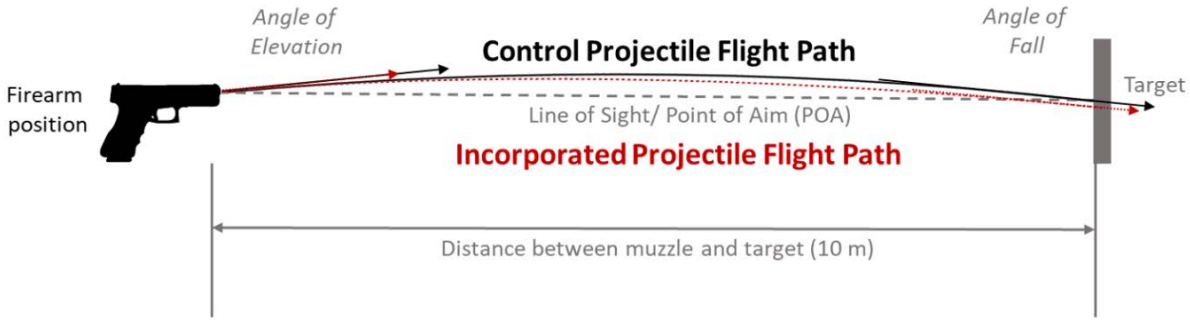

Figure 3-17: Hypothesised flight paths of the control and incorporated projectiles.

3.5.3 Projectile Performance Overview

Evaluating the performance of the projectile from incorporated ammunition provides an understanding into how the discharge process was being impacted by the presence of the MOF. By expanding knowledge into how the MOF is interacting with the propellant it can direct future research into new areas.

The assessment of velocity, sound measurement and accuracy were conducted simultaneously. The audible sound of discharge can infer information regarding firearm and ammunition [456], while speed of the projectile in motion is known to influence the projectile flight path, which affects the POA [5]. In the unmodified ammunition the detonation caused by the firing pin colliding with the primer cup results in an explosion that travels into the cartridge case. The interaction between the explosion and the propellant causes an increase in gas within the cartridge case, and as a result high pressure waves are formed, allowing the projectile to travel through the barrel, propel through the air and impact a target. It was the interaction between each of these process that make firearms a dangerous, yet precise and effective tool. The incorporation of the MOF into the ammunition affected this process by changing the rate of each interaction and further impacting the behaviour of the projectile. The observations from the velocity and accuracy highlight that the incorporation of MOFs into ammunition is affecting the processes within the cartridge case that were affecting the generation of LGSR. The evaluation of the external ballistics from the incorporated projectiles supports that the incorporation of MOFs into ammunition was impacting the discharge process, which further impacts the distribution and generation of LGSR. The addition of MOFs was observed to affect the velocity of the projectiles, likely through impacting the generation of the required pressure for the projectile movement. This reduction in velocity was then seen to affect the flight plan associated with the projectile after it leaves the barrel of the firearm.

It was obvious from the visualisation of the firearm and FCC that increasing the incorporation ratio of MOFs in ammunition does result in easier visualisation of LGSR on the item. However, from the velocity, and, accuracy and precision of the projectiles, as the incorporation ratio increases, there is more variability observed in the projectile behaviour.

3.6 Conclusion

This chapter evaluated four different MOFs; SH2-Tb, MW1-Tb, MW2-Tb and MW3-Tb, and their impact when incorporated into ammunition. Both a visual evaluation on the generation of LGSR and an external ballistics evaluation through the velocity and accuracy of the projectile were conducted.

The results from the visualisation of the shooter's hands indicated that with these four synthesised MOFs it would be difficult to identify whether a firearm was discharged. From the visualisation of LGSR on the shooter's hand, no overall recommendation can be made regarding the effect MOF type has on the incorporation ratio. Although this investigation identified that LGSR does not distribute to the shooter's hands in high quantities for easy visualisation, it did highlight that these MOFs can still be used in the identification process of GSR analysis through the characteristic detection of Tb^{3+} ions.

The visualisation of the firearm and FCCs illustrated that LGSR was easier to visualise closer to the point of ignition. The majority of the LGSR was remaining at the point of ignition (chamber and cartridge), with very few LGSR observed in the plume region at the muzzle or distributing onto the shooter's hands. Increasing the incorporation ratio resulted in more LGSR being visualised. The observations from visualising LGSR particles highlighted that there could be a number of factors (incorporation ratio, morphology and powder consistency) that are impacting the behaviour of GSR distribution.

Overall, the visualisation of LGSR suggested that the incorporation of MOFs into ammunition was affecting the generation of pressure during discharge. However, it was also evident that the physical characteristics of the MOF type may play a role in the extent of the impact.

Unlink previous literature, the incorporation of MOFs into ammunition was not identified to be a contributing factor to the observation of shooting failure. The low rate of manual FCC ejection from the firearm did not correlate to a particular MOF or incorporation ratio. Instead, it was suggested that this could be attributed to the re-assembled ammunition, inferring that care is required during this process.

The projectile performance highlighted a reduction in velocity and accuracy when MOFs were incorporated into ammunition. The sound measurement evaluation could not provide additional information into the impact MOFs had on the discharge process, but further evaluation could be beneficial. These results suggest that these four MOFs were affecting the propellant burn rate, which could influence the generation of the required pressure for discharge or the generation of LGSR. The current homogenisation process applied to the ammunition is not suitable for this application of

incorporating MOFs into ammunition. It illustrates that the incorporation of MOFs has the ability to impact the safety of the general public if the firearm was used. It can also impact the overall analysis of firearm-related crime scenes by affecting basic reconstruction of scene through affected points of projectile perforations.

The evaluation of the incorporation ratio suggests that due to the MOF chemical and physical properties, each MOF must be evaluated to identify its optimal incorporation ratio. Every synthesised MOF will require both visual and an external ballistic evaluation to ensure that the incorporation of the MOF does not impact the baseline standards set for firearms and ammunition. The four MOFs evaluated in this study would not be ideal for future incorporation into ammunition which would be employed in the real world.

This page was left intentionally blank

Chapter 4. General Discussion and Future Direction

4.1 General Discussion

Firearm-related crimes are an ongoing issue in society. In a traditional firearm-related investigation, investigators rely on information gathered from the scene (via the presence of a projectile, FCC, firearm, or an associated trace) to infer whether a firearm was discharged. The incorporation of MOFs into ammunition can be beneficial to forensic science practices from improving the visualisation of GSR traces at the crime scene through to assisting in the distinction between GSR traces and environmental contaminants. Collecting GSR traces from a POI, firearm, or crime scene, will continue to be a part of standard operating procedures, so the ability to easily see the traces, which are invisible to the naked eye would assist investigators in the collection process. Literature has indicated that the incorporation of MOFs into ammunition has the potential to improve the in-field collection of specimens, leading to a reduction of specimens requiring laboratory analysis through a more targeted collection process [95, 193]. Visualising LGSR also has the potential to be used for scene reconstruction in conjunction with the identification of projectiles and FCC positions, which can lead to the determination of shooter position, distance from target and even differentiate between shooters (ammunition encoding) [12, 78, 172-192]. Before MOFs can be considered for incorporation into ammunition from a manufacturing perspective, several factors need to be further evaluated, including, MOF suitability in a forensic context and their effect on firearm functionality.

This study evaluated a range of luminescent MOFs containing a mixture of different REE metal cores and ligands to identify suitable particles which could be used to visualise GSR traces. The optimal LGSR particles should contain a strong luminescence when excited with a UVA light source (320 –400 nm) as this wavelength range carries reduced risk associated with skin exposure in comparison to UVC rays [341-343]. Within the literature, Eu- and Tb-MOFs are frequently encountered (*Table 1-8*), as they provide a strong luminance when excited at UVC wavelengths; however, there has been little investigation into the properties of different REE metal cores. The present study investigated five REE metal cores (Tb^{3+}, Er^{3+}, Ho^{3+}, Gd^{3+} and Y^{3+}), which highlighted that the metal core influenced the luminescent properties encountered under UVA conditions. The ligand dictated the rigidity of the structure and provided the distinctive chemical framework and the synthetic route applied during synthesis influenced the particle morphology. Together, these features ensure that each MOF type is specific. This was confirmed during SEM-EDS analysis when the morphology of LGSR particles (particularly from SH2-Tb, MW1-Tb and MW3-Tb) were easily distinguishable from NTA-GSR particles. The outcomes of this study highlight that any future research into the synthesis of suitable MOFs should not focus solely on the chemical and/or physical properties. Additional criteria focusing on the forensic context (impact to firearm discharge and projectile behaviour) may ensure that researchers

are evaluating suitable MOFs appropriately. The four MOFs (SH2-Tb, MW1-Tb, MW2-Tb and MW3-Tb) incorporated into ammunition addressed all the criteria (chemically and thermally stable, as well as, containing strong luminescence) but were still observed to negatively impact the performance of the LGSR visibility and projectile performance. This indicated that there are other factors (particle size and morphology, powder consistency, interaction with propellant and/or discharge process) that need to be considered before any MOF is deemed viable for incorporation into ammunition. The impacts observed from the addition of MOFs into ammunition suggest that current forensic practices for detecting GSR traces at the crime scene (i.e. colourimetric tests) should still be considered the optimal technology. Although current techniques contain their own set of limitations (not specific to GSR particles [146, 147, 459] and have the potential to destroy specimen [21, 34, 76]), the difficulty encountered in visualising LGSR on the shooter's hand highlights that the MOFs evaluated in this body of work are not suitable for this purpose.

This study identified that not all MOFs are suitable as a preliminary visualisation technique at the crime scene. The difficulty encountered with visualising green luminescent particles on the shooter's hands suggested that the additional particles in the cartridge case were impacting the discharge process. To confirm whether the internal ballistics process within the cartridge case was being impacted during ignition, the behaviour of the projectile in motion was observed. Previous work examining MOF incorporated projectile behaviour had solely focused on the impact on velocity [174]. Weber et al. [174] showed that incorporated ammunition decreased projectile velocity and increased shooting failure. In this body of work the impact of incorporated ammunition was evaluated by evaluating shooting failure, velocity, sound measurement and accuracy and precision to confirm if the discharge process was being impacted. Overall, the results showed that the velocity of the projectile was impacted by the internal ballistics within the cartridge case during ignition. Accuracy and precision of the projectile are important factors for firearm discharge as they measure the quality of the firearm and ammunition [460]. The lower velocity led to a reduction in accuracy for all MOF ratios, highlighting that the introduction of these MOFs reduces the safety associated with firearms. As any fluctuation in the functionality of a firearm could have a detrimental effect, to either the shooter, target or any bystanders. The impact observed in the projectile trajectory highlights that these four MOFs are not suitable to be considered for ammunition incorporation.

Considering the results, unless the challenges encountered within this study are addressed, specifically the LGSR visualisation and projectile behaviour, the possibility for incorporating MOFs into operational ammunition may not be achieved. It has been stated that MOF incorporation into ammunition could assist investigators at firearm-related scenes by visualising the deposition of LGSR

particles post discharge. To unlock the potential of this research, the behaviour of the discharge process needs to be further investigated and evaluated.

4.2 Future Work

This study has highlighted that the addition of MOFs into ammunition affects the discharge process and therefore has the ability to impact the functionality of firearms. For the application of MOFs to visualise GSR to become a viable option, research has to shift focus onto the performance of the firearm and projectile. The range of MOFs that are suitable for this application can continue to expand (ability for ammunition encoding); however, every new and established MOFs needs to be evaluated to identify how they impact the discharge process.

4.2.1 MOF Synthesis

To date, research has synthesised and evaluated MOFs containing nine different REE metal cores; however, two of the REEs (Eu and Tb) provide superior luminescence. Evaluating the remainder of the REE, at a UV wavelength (specifically UVA) also provides a holistic understanding into which metal cores are the most suitable for this application. From this study, four REE were deemed unsuitable due to their luminescent properties. The identification of additional REE that are deemed suitable for incorporation provides the opportunity for ammunition encoding. The ability to differentiate between different MOFs based on their REE metal cores and unique structural frameworks are the reason these luminescent particles are ideal for this type of application.

In addition to compositional differences within the MOFs, it would also be valuable to synthesise MOFs via alternative routes. This study highlighted that there were observable differences in particle size and morphology between SH and MW-assisted MOFs, even when their components and molar ratios were not altered. Altering the synthetic route generated MOFs with different morphologies and sizes, without affecting the properties (structural or luminescent). This study identified that MW3-Tb (smaller morphology) was observed in higher abundance on the firearm than SH2-Tb (larger morphology). A deep evaluation into understanding how the MOF morphology and size impacts the discharge process could provide insight into some factors that need to be considered when synthesising MOFs for visualising GSR. At a spectroscopic level, this avenue has the potential to differentiate between LGSR types which could be used to differentiate between firearm holders (law enforcement or civilians) and ammunition type (calibre or manufacturers).

4.2.2 Shelf-life of incorporated ammunition

Evaluation of the pure MOF initially, prior to incorporation, highlighted that the MOF would be able to withstand degradation, without wasting ammunition resources. With the four pure Tb-MOFs proving to be stable for 24-months, the stability of the MOF post-incorporation should be evaluated. This avenue of research is valuable as it will indicate whether the behaviour of the incorporated MOF behave similarly to the pure MOFs (stable for up to 24-months) or if the interaction with the propellant alters the MOF stability over time. This would provide definitive information into whether the evaluated MOF is suitable for incorporation into ammunition for extended incorporation lengths.

The stability of the pure MOFs highlighted that, for future research, it would also be beneficial to increase the time range to gain a better understanding of the long-term stability of MOFs. Ensuring the stability of the MOFs is aligned with the shelf-life of conventional ammunition will determine whether the addition of these chemicals is a suitable long-term option for ammunition.

4.2.3 Incorporation process

The chosen method of homogenising the MOF and propellant provided different results to most of the literature, with only Gomes et al. [191] indicating the difficulty associated with observing LGSR on the shooter's hand. To confirm whether the action of homogenisation plays a role in the ability of visualising LGSR, it is recommended to re-evaluate the four synthesised MOFs by changing the incorporation method to non-homogenisation. A non-homogenisation approach would involve adding the MOF into the cartridge case without the additional action of mixing the MOF and propellant. This comparison between homogenisation and non-homogenisation of the four Tb-MOFs will highlight whether the behaviour of the LGSR dispersion follows similar trends. If the trends observed for the non-homogenised ammunition are similar it would indicate that there is another factor that impacts the ability to visualise these four Tb-MOFs on the shooter's hand.

Another factor that could be impacting the dispersion of LGSR is the physical properties of the MOFs (i.e. morphology). This study highlighted that between the four MOFs, each contained different particle morphologies and sizes. The variation in results between the different MOFs suggests the possibility that these physical features are influencing the discharge process. As the only four MOFs to be evaluated based on their morphology, it would be beneficial for an assessment into the morphology and size of the established MOFs in literature. This would indicate whether the dispersion of the LGSR or behaviour of the projectile are affected by particle differences and highlight what MOF properties are optimal for incorporation into ammunition.

4.2.4 Performance

Evaluating the performance of the firearm, ammunition and projectile during discharge should become the priority for future LGSR examinations. For all established MOFs applied for visualising LGSR an evaluation into how they affect the projectile behaviour will indicate whether similar trends observed by Weber et al. and in this study are followed. It provides insight into how the particles from the MOFs interact with the different ballistic components during firearm discharge.

Although this study was not able to easily visualise the transfer of LGSR particles onto the shooter's hand, the GSR examination (via SEM-EDS) did highlight the presence of small LGSR particles. Transfer and persistence of GSR traces are essential to the investigator during the reconstruction of events and interpretation of results [41], and should be a prominent consideration when evaluating MOF suitability as LGSR. It has been identified that IGSR and OGSR contain distinctive transfer and persistence behaviours, which could lead to different observations being made for LGSR due to differences in physical properties [40, 54]. Three LGSR studies did investigate the transfer and persistence of LGSR particles (specifically the primary, secondary and tertiary transfer of LGSR [177], persistence of LGSR after handwashing [174] and persistence of LGSR on clothing[184]). However, the focus of these studies was to identify the individual behaviour of the specific LGSR, without comparing the behaviours with traditional GSR. An investigation into how LGSR transfers and persists in comparison to IGSR and OGSR could indicate whether the addition of the MOF can provide additional or congruent information to aid the investigator during the reconstruction of events

Addressing the above future work suggestions could improve the results observed from this study and can provide researchers with an understanding of the how different factors can influence the ability to implement this research into a forensic setting. To date, all MOFs applied for visualisation of LGSR have been deemed suitable for this application, regardless of their composition or morphology, or the firearm and ammunition combination. This study has highlighted that there are unknown factors that suggest not all MOFs are suitable and further research is required to identify what these factors are relevant before implementation into real-world scenarios.

Chapter 5. Conclusion

The greatest limitation encountered by GSR investigators in firearm-related scenes is the difficulty associated with seeing these traces due to their minute size. Often, the collection of the GSR traces on a POI is not conducted at the crime scene, so investigators must consider the impact of transfer and persistence of these traces during interpretation. The incorporation of MOFs into ammunition has been evaluated since 2011 as a method that can preliminarily visualise the location of LGSR on a shooter or within the surrounding vicinity of firearm discharge simplifying the collection process. This project aimed to contribute to the available information by developing low-cost MOFs that could be incorporated into ammunition and used to visualise GSR post discharge. Four objectives were evaluated to advance the understanding of MOF type and the impact they have on the discharge process.

Chapter 2 focused on identifying a range of suitable MOFs for incorporation into ammunition based on the characterisation of their chemical and luminescent properties, as well as their ability to remain stable over time. The first objective was to synthesise and characterise a range of MOFs using SH or MW-assisted synthetic routes. A total of 17 MOFs were synthesised, of which 13 were deemed unsuitable for incorporation into ammunition due to their cost or luminescent properties (weak or no luminescence when excited under UVA conditions). Only four MOFs, each containing Tb metal cores, were identified as being suitable for incorporation based on their strong green luminescence. This objective suggested that some REE metal cores do not produce a strong enough luminescence when excited using a UVA wavelength (λ_{ex} = 320 nm – 400 nm) and further, indicating that not all REE can be integrated into a MOF framework and expected to contain a strong luminescence. The original goal was to identify a novel metal core which had not been evaluated as a luminescent MOF for visualisation of GSR. While the Er- and Ho-MOFs were reported to be luminescent under a specific context in the literature, when applied to forensic conditions it was identified that these MOFs were UV-inactive. For the Gd- and Y-MOFs, a weak blue luminescence was observed under forensic conditions; however, these particles would not be differentiable visually with background contamination and could introduce challenges in the field. This is important information for research as it highlights not all REEs can be implemented for this luminescent application.

Evaluating the stability of the pure MOFs was also conducted to recognise any deficient behaviour in the MOF properties prior to incorporation into ammunition. The second objective identified the chemical and luminescent stability of the four luminescent Tb-MOFs over a period of 24-months and provided encouraging results with each MOF retaining adequate luminescence at the end of the evaluation process. The structural and luminescent spectral data, as well as the visual luminescent colour, of each MOF did not indicate a general trend of degradation in the peaks or

bands, highlighting the overall stability of the MOFs. There was evidence of fluctuation in the FTIR and fluorescence spectrophotometer spectral intensities between the months; however, this was attributed to intra-day instrument variability. One observation that was not due to instrument variability and was observed in all four Tb-MOFs was the increased presence of H_2O, observed in the FTIR spectra. This broadening and increase in intensity of the O–H band was attributed to the hygroscopic nature of the MOFs through exposure to air during monthly analysis. While it is undefined whether this interaction with moisture would occur when enclosed within the cartridge case, it is hypothesised that it would not interact with the MOF to the extent observed in Chapter 2. This evaluation provided insight into the behaviour of the MOFs stability, which could affect its suitability for long-term incorporation into ammunition.

With the identification of four suitable Tb-MOFs, a new batch of MOFs were synthesised for incorporation into ammunition. Chapter 3 outlined the applicability of using the four Tb-MOFs in the generation of LGSR through a visual assessment on the deposition of LGSR and an evaluation of the performance of the projectile via velocity and accuracy assessments. The third objective evaluated the capability of visualising LGSR particles on the shooter's hands, firearm, and FCC. The results from the shooter's hands were inconsistent with previous literature but did highlight new considerations when altering ammunition. Between the four Tb-MOFs, it was observed that the number of visible LGSR particles deposited decreased as the distance from the point of ignition increased (FCC > firearm > shooter's hand). Within literature, the preferred method of incorporating did not involve homogenisation, suggesting that this process could also be factored into the results observed. It was hypothesised that the MOF coating the propellant could be preventing the burn rate and resulting in small amounts of LGSR travelling outside of the firearm.

Another observation made during the visualisation of LGSR was the variation in count abundance between the four different Tb-MOFs. MW1-Tb was observed to contain the highest abundant LGSR particle count, which was hypothesised to be attributed to the distinguishing chalky powder consistency. MW3-Tb was observed in high LGSR counts for higher incorporation ratios (10 wt%), due to a clustering effect prominent during ammunition loading. The abundance of SH2-Tb and MW2-Tb were much lower in comparison because of less clustering of the MOF within the cartridge case during homogenisation. This suggested that the physical properties of the MOF could play a role in the interactions affecting the discharge process, highlighting the need to independently evaluate each MOF to find its own optimal conditions for ammunition.

Another observation during the visualisation of the FCC, was the effect of post-incorporation time to discharge. The ammunition which was left combined with the MOF for a longer incorporation

length was observed to have a lower amount of visible luminescence. The reason behind this difference in visible LGSR is unclear, but it could be suggested that, if any, the interactions between the MOF and propellant have more time to occur. Although the visualisation of the LGSR on the shooter's hands was not easily visible, the exploratory GSR analysis on the SEM-EDS did determine that the collected stubs were positive for Tb elements. With the movement towards replacing traditional ammunition [461], the use of REE as a sustainable characteristic indicator to substitute for the lack of Pb-Ba-Sb particles in NTA would assist the interpretation of the results. Terbium is not identified in the environment or occupationally as a source of contamination and if identified in a GSR specimen has the potential to be deemed characteristic.

The difficulty in visualising LGSR on the shooter's hand suggested that the discharge process was being impacted by the addition of the MOF. The fourth objective focused on how the addition of the MOF within the cartridge case affected the discharge process through the evaluation of the projectile behaviour. It was observed that as the incorporation ratio of MOF increased within the ammunition, the velocity of the projectile decreases, while the accuracy and precision of the projectile in the target were also negatively impacted. These observations were consistent with literature, but also supported the ideas proposed in the third objective, which suggested the addition of the MOF within the ammunition was impacting the discharge process.

This research has highlighted that further research is needed before MOFs can be implemented into ammunition. Literature has indicated that the introduction of MOFs into ammunition leads to the visualisation of LGSR on areas of interest (shooter's hands, firearm, and target) and can be used in event reconstruction (position and distance determination of shooters). However, progress is required to identify how the MOF interacts with the propellant and how this can impact the behaviour of GSR generation and deposition, as well as the projectile flight path at a firearm-related scene. Once these limitations are overcome, the application of MOFs for LGSR visualisation would be a valuable tool for investigators at a firearm-related crime scene. The benefits of encountering LGSR would be vast as the presence of these particles can be implemented into investigative procedures and aid law enforcement in numerous ways. The visualisation of LGSR at the crime scene can be used as a pre-screening tool for collection and also aid in event reconstruction, particularly if ammunition encoding is implemented. The identification of the unique characteristics associated with the MOF in the LGSR particles during laboratory analysis will give support to the interpretation of the collected specimen.

Appendices

Appendix 1: Ethics and Consent Forms

UTS UNIVERSITY OF TECHNOLOGY SYDNEY

PARTICIPANT INFORMATION SHEET
INVESTIGATION OF METAL-ORGANIC FRAMEWORKS AS GUNSHOT RESIDUE TAGGANTS (ETH20-5112)

WHO IS DOING THE RESEARCH?

My name is Analisa Chiaravalle and I am a student at UTS. My supervisors are Alison Beavis and Scott Chadwick, and they can be contacted at a.beavis@unsw.edu.au and scott.chadwick@uts.edu.au, respectively.

WHAT IS THIS RESEARCH ABOUT?

This research aims to assess the safety and viability of incorporating metal-organic frameworks (MOFs) into ammunition as a visualisation technique for gunshot residue (GSR) detection. The MOF will be incorporated into the ammunition and following the discharge of a firearm the luminescent GSR (LGSR) will be evaluate through different forensic aspects. This study will assist forensic interpretation at firearm-related scenes because it will aid investigators in visualising GSR, which will indicate whether a firearm was discharged at a crime scene or not.

WHY HAVE I BEEN ASKED?

You have been invited to participate in this study because you contain a current firearm license, as well as extensive training and expertise in firearm safety and firearm safety protocols.

IF I SAY YES, WHAT WILL IT INVOLVE?

If you decide to participate, you will be invited to:

Assist in the loading of ammunition. Each ammunition which you will be asked to discharge, will be loaded previously with the MOF. As a result of your experience, you will be asked to assist in the appropriate and safe techniques required for loading ammunition. This process should take approximately 10 minutes per ammunition and should take approximately 6 hours.

Assist in the discharging of firearms and visualisation of LGSR. Prior to each discharge, you will be required to wash your hands, which will then be visualised with a UV lamp ($\lambda > 350 – 380$ nm). You will then be asked to load the firearm with the ammunition incorporated with the MOF and discharge your firearm (either a single time or consecutively). Following each discharge your hands will again be visualised with the UV lamp. An image of your hands will be taken, using a CANON EOS Camera, to capture the amount of LGSR that has been deposited. This process will take approximately 10 minutes per discharge and will be conducted multiple times. You will be asked to discharge firearms a total of 1000 times, which will take approximately 170 hours (across the period of this research). Upon leaving the firing range, the images will be uploaded into a password protected folder. The images on the camera SD card will then be erased. The images will be re-named according to the weapon, ammunition, hand and blank/sample on the computer. Each image will then be opened in an image editor software (such as Photoshop or GNU Image Manipulation Program (GIMP)) to analyse the amount of LGSR present on the participant's hand (low, moderate, high, etc). The combination of UV light and camera barrier filter will ensure that no identifiable features from your hands (fingerprint or palm prints) will be visible in the photographs.

For the initial 120 rounds the LGSR deposited on your hands will be collected for further testing in the laboratory. You will be required to discharge a firearm, and subsequently your hands will be visualised and photographed before the LGSR is collected with carbon adhesive stubs. The remaining rounds will not require your hands to be stubbed.

UTS UNIVERSITY OF TECHNOLOGY SYDNEY

ARE THERE ANY RISKS/INCONVENIENCE?

Yes, there are some risks/inconveniences involved.

There is always a chance that the firearm could malfunction. The firearms will be purchased for the purpose of this project. Due to your expertise in firearm safety, the firearms will be stored at a facility of your choice, as well as be cleaned, maintained, and serviced by you at any time you think is necessary.

The ammunition being used will be incorporated with MOFs. While there is no literature that has indicated these chemicals causing a reaction to skin, there is a slight possibility. Between each discharge, you will be asked to wash your hands to minimise the amount of time the chemical is deposited on your hands. If you experience any irritation, testing will stop immediately.

The UV lamp that will be used will be fitted with a UVA wavelength range (this UV radiation is what you experience daily from the sun). To minimise any negative effects, you will be exposed to the UV lamp for a very short exposure time (< 30 seconds per visualisation). If you experience any irritation, testing will stop immediately.

The research will be undertaken at a firing range of your choice, and you should be made aware that while your identity will be protected and remain confidential for the purpose of published/unpublished data, there may be other patrons at the firing range on the days that we will attend and see you.

COVIDSafe Information:

It is encouraged that, while participating in face-to-face activities during this research, good hand hygiene and appropriate physical distancing (maintaining 1.5 metres or more between yourself and others) is maintained at all times. Please ensure that you implement measures to respond to COVID-19 according to the Australian Government COVID-19 guidelines and consider downloading the COVIDSafe app. For your safety and for others, if you are feeling unwell prior to face-to-face contact, please notify myself or my supervisors and do not attend any physical face-to-face activities.

DO I HAVE TO SAY YES?

Participation in this study is voluntary. The decision to take part in this research is up to you.

WHAT WILL HAPPEN IF I SAY NO?

If you decide not to participate, it will not affect your relationship with the researchers or the University of Technology Sydney.

If you wish to withdraw from the study once it has started, you can do so at any time without having to give a reason, by contacting Analisa Chiaravalle at analisa.chiaravalle@student.uts.edu.au. If you withdraw from the study, and do not permit the images collected to be used, all images will be deleted and any analysis results will be erased. If you do permit the already collected and analysed images, you should be aware that data collected up to the time you withdraw will form part of the research project results.

CONFIDENTIALITY

By signing the consent form you consent to the research team collecting and using images of you hands collected at the firing range for this research project. All this information will be treated confidentially. All personal information will be accessed only by myself and my supervisors and will not be a key component of this study. It will only be disclosed with your permission, except as required by law.

The images captured may be used in future publications and future research, however, the information will be provided in such a way that you cannot be identified.

UTS UNIVERSITY OF TECHNOLOGY SYDNEY

WHAT IF I HAVE CONCERNS OR A COMPLAINT?

If you have concerns about the research that you think I or my supervisor can help you with, please feel free to contact us at analisa.chiaravalle@sudent.uts.edu.au, a.beavis@unsw.edu.au or scott.chadwick@uts.edu.au.

You will be given a copy of this form to keep.

NOTE:
This study has been approved by the University of Technology Sydney Human Research Ethics Committee [UTS HREC]. If you have any concerns or complaints about any aspect of the conduct of this research, please contact the Ethics Secretariat on ph.: +61 2 9514 2478 or email: Research.Ethics@uts.edu.au, and quote the UTS HREC reference number. Any matter raised will be treated confidentially, investigated and you will be informed of the outcome.

CONSENT FORM
INVESTIGATION OF METAL-ORGANIC FRAMEWORKS IN GUNSHOT RESIDUE (ETH20-5112)

I _____ *[participant's name]* agree to participate in the research project Investigation Of Metal-Organic Frameworks in Gunshot Residue (ETH20-5112) being conducted by Analisa Chiaravalle at the University of Technology Sydney, located at 15 Broadway, Ultimo NSW 2007.

I have read the Participant Information Sheet or someone has read it to me in a language that I understand.

I understand the purposes, procedures and risks of the research as described in the Participant Information Sheet.

I have had an opportunity to ask questions and I am satisfied with the answers I have received.

I freely agree to participate in this research project as described and understand that I am free to withdraw at any time without affecting my relationship with the researchers or the University of Technology Sydney.

I understand that I will be given a signed copy of this document to keep.

I agree for my hands to be photographed for this research and that the photographs may be published.

I agree that the research data and photographs gathered from this project may be published in a form that:
☐ Does not identify me in any way
☐ May be used for future research purposes

I am aware that I can contact Analisa Chiaravalle by phone on [redacted] or email at analisa.ahiaravalle@student.uts.edu.au if I have any concerns about the research.

_____ ____/____/____
Name and Signature [participant] Date

_____ ____/____/____
Name and Signature [researcher or delegate] Date

Appendix 2: Chapter 2

SECTION II: Characterisation Method

5.1.1 Characterisation Excitation Wavelengths

Table A2 - 1: Characterisation excitation wavelength for each MOF as indicated in the literature. * Reference literature was not available during characterisation, so a 3D mode scan was conducted to identify maximum excitation spectrum in the UV range.

MOF	Excitation Wavelength (nm)	Reference
SH1-Tb	-	-
SH1-Er	-	-
SH2-Tb	254	[206]
SH2-Er	235	[206]
SH2-Ho	235	[206]
SH2-Gd	290	[385]
SH2-Y	315	[385]
SH3-Gd	380	[367]
SH4-Gd	340	[368]
SH5-Tb	254 and 381	[369]
SH5-Er*	310	-
SH5-Ho*	310	-
SH5-Gd	366	[369]
SH5-Y	420	[369]
MW1-Tb	254	[172]
MW2-Tb	302	[182]
MW3-Tb	254	[206]

SECTION II: Characterisation Results

5.1.2 XRD

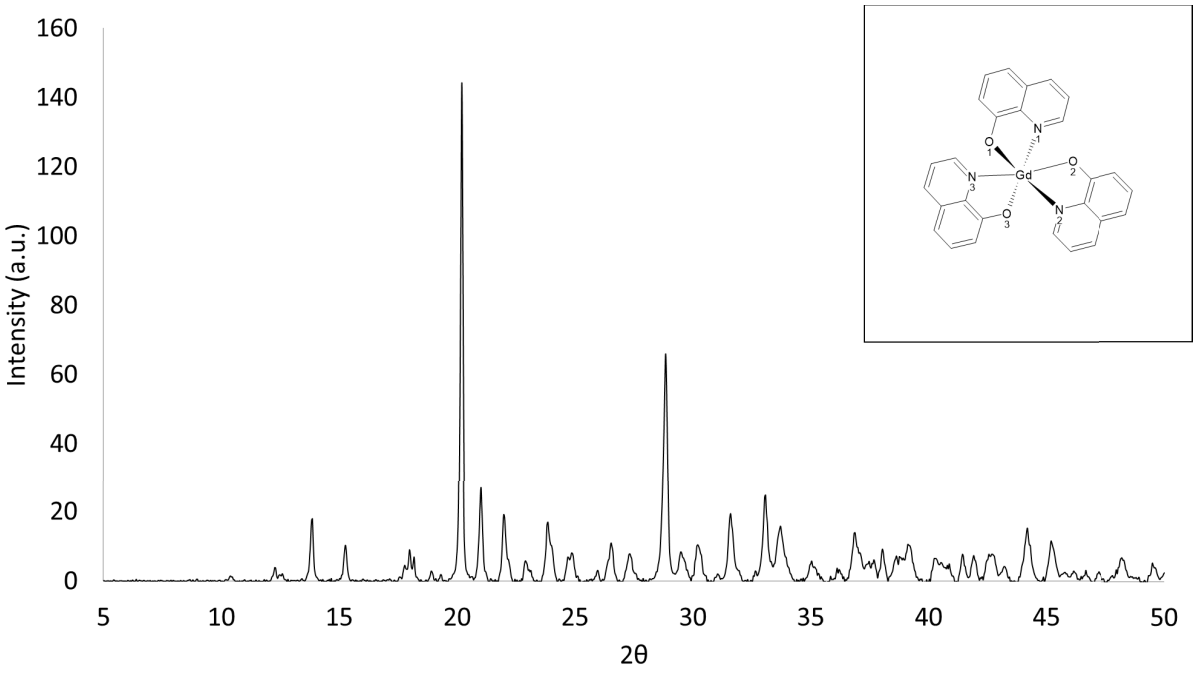

A2 - 1: XRD pattern of as-prepared SH4-Gd. The insert represents the expected structure of the MOF as indicated by literature.

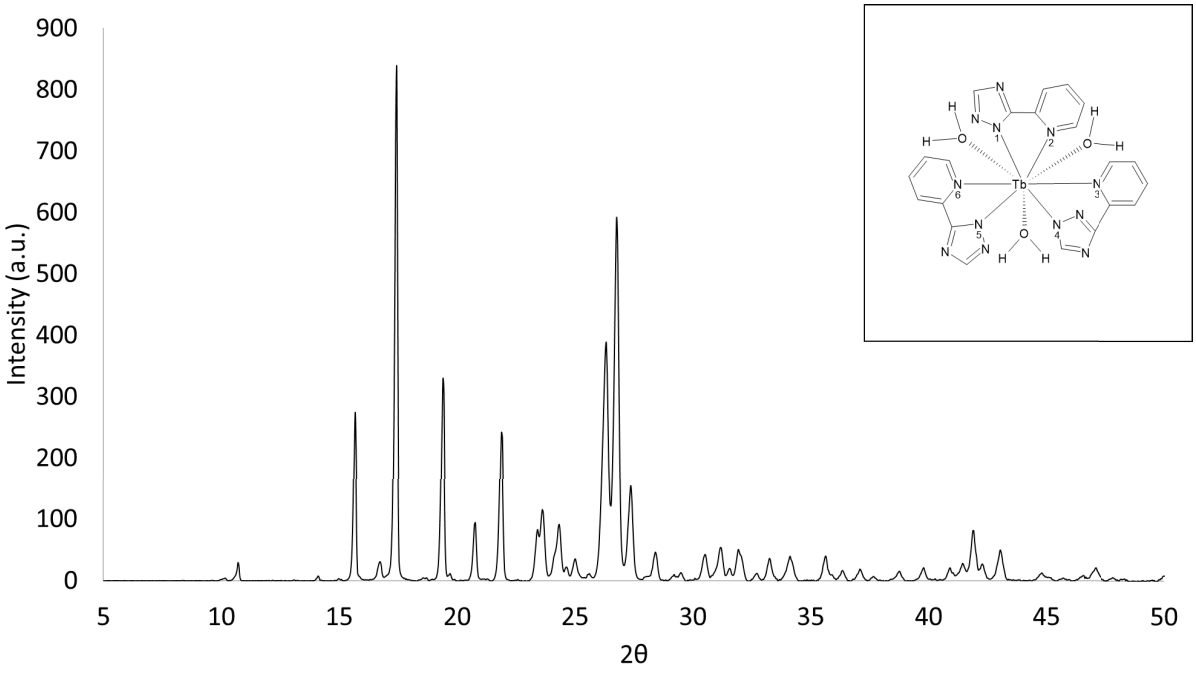

A2 - 2: XRD pattern of as-prepared SH5-Tb. The insert represents the expected structure of the MOF as indicated by literature.

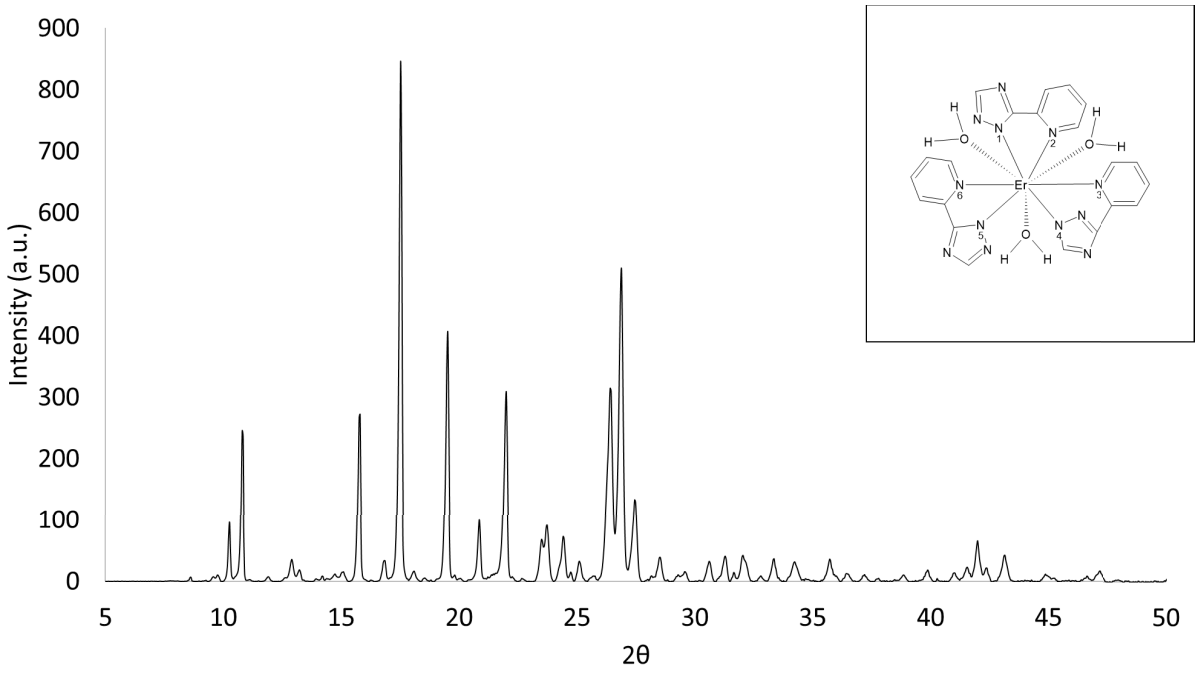

A2 - 3: XRD pattern of as-prepared SH5-Er. The insert represents the expected structure of the MOF as indicated by literature.

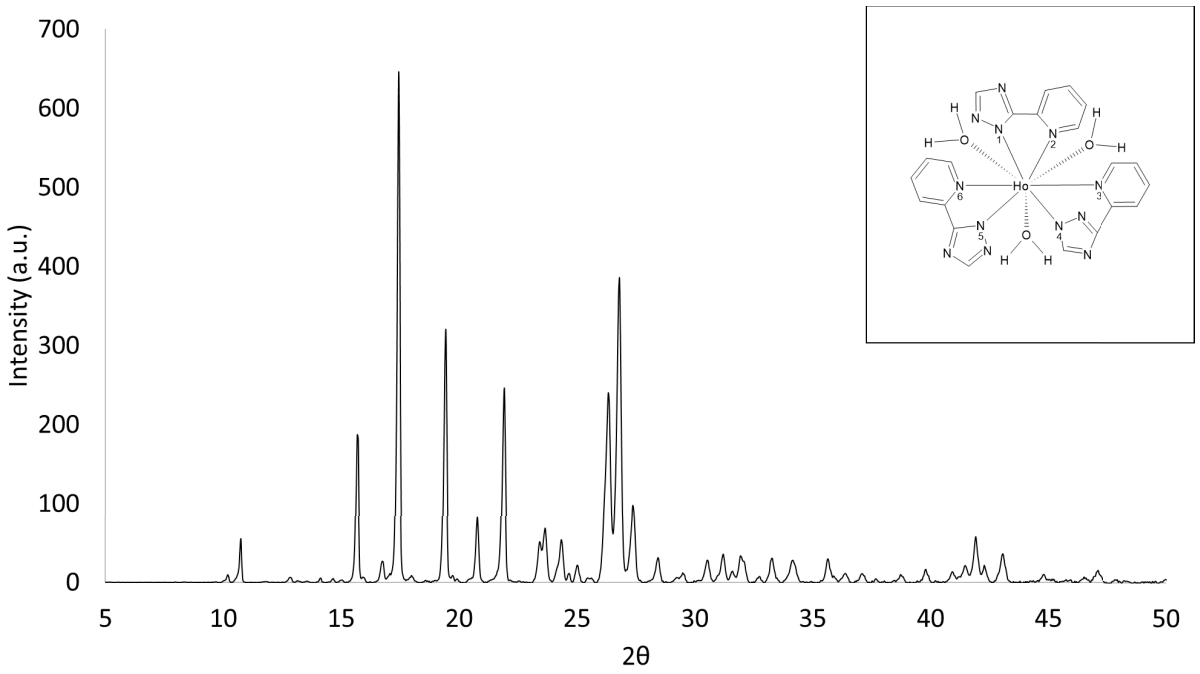

A2 - 4: XRD pattern of as-prepared SH5-Ho. The insert represents the expected structure of the MOF as indicated by literature.

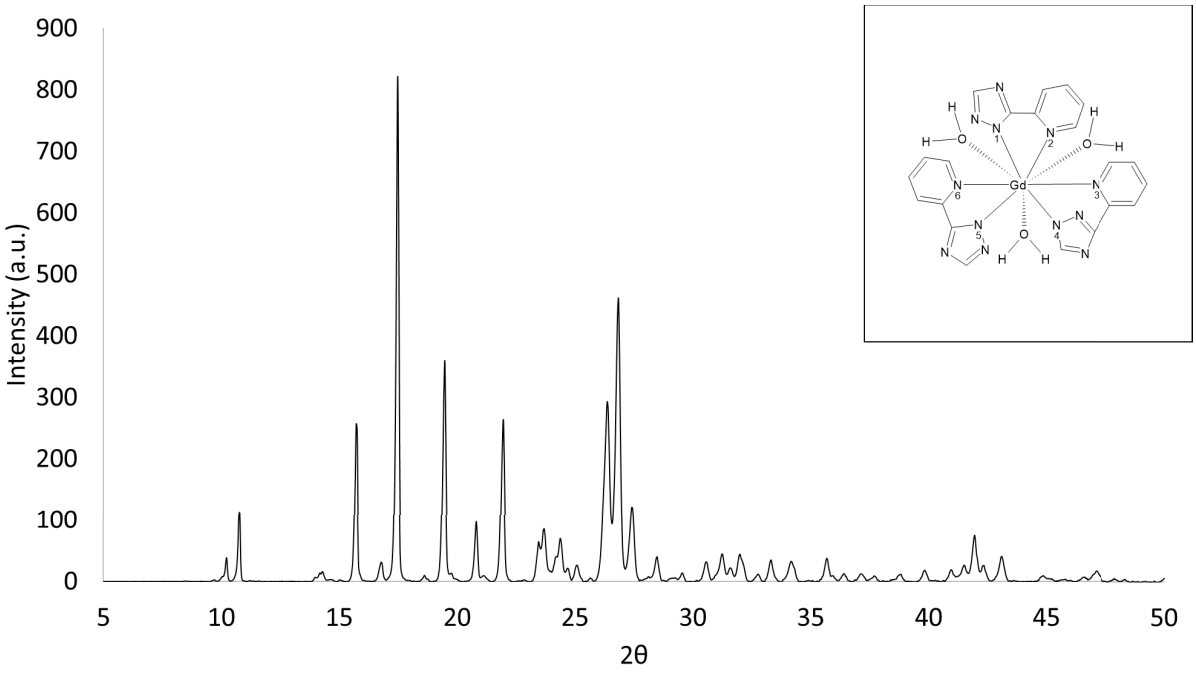

A2 - 5: XRD pattern of as-prepared SH5-Gd. The insert represents the expected structure of the MOF as indicated by literature.

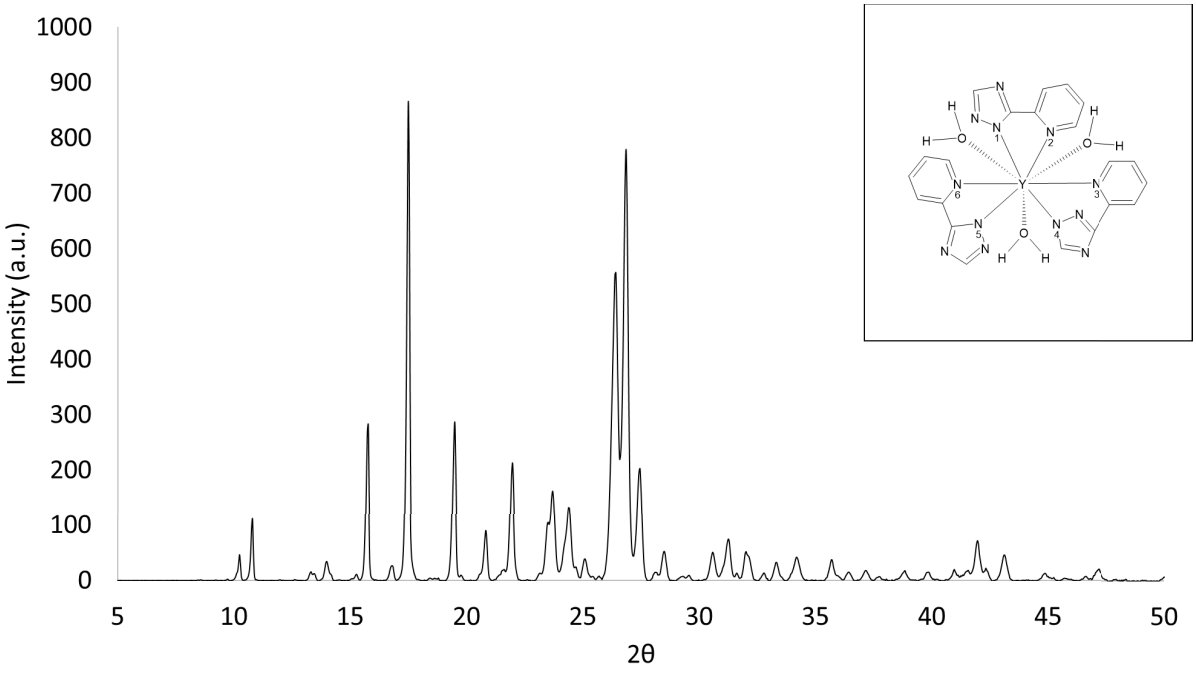

A2 - 6: XRD pattern of as-prepared SH5-Y. The insert represents the expected structure of the MOF as indicated by literature.

5.1.3 FTIR

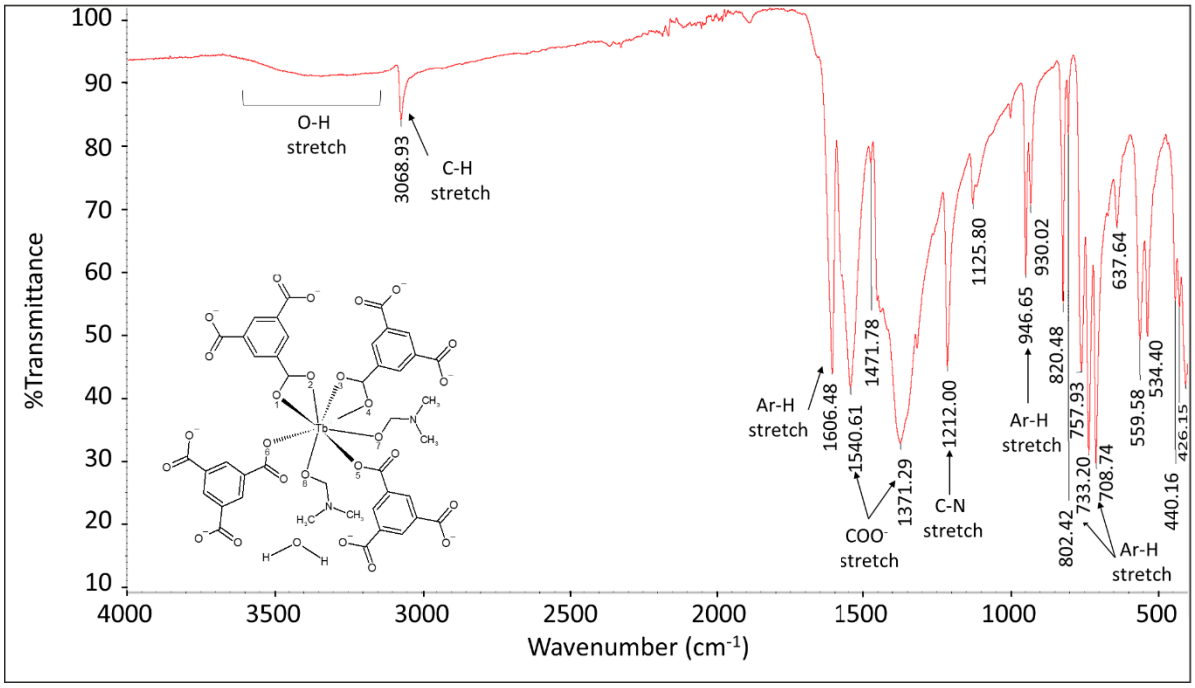

A2 - 7: Annotated FTIR of SH2-Tb including peak allocation. The insert represents the expected structure of the MOF as indicated by literature.

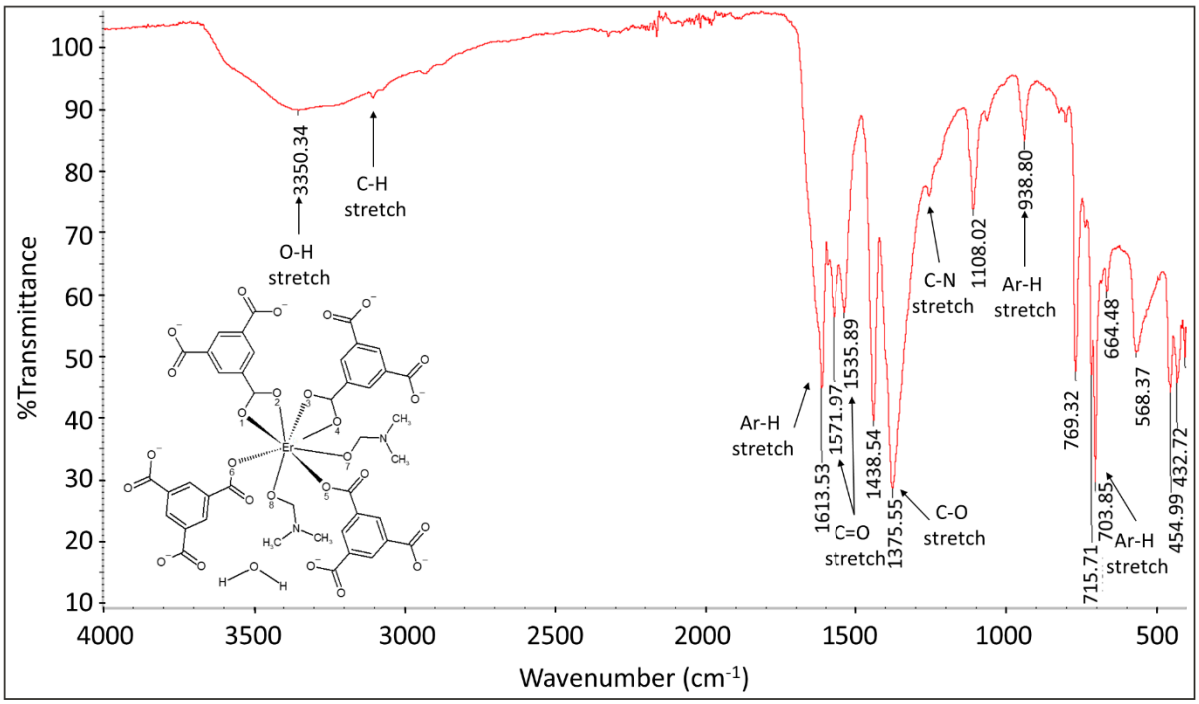

A2 - 8: Annotated FTIR of SH2-Er including peak allocation. The insert represents the expected structure of the MOF as indicated by literature.

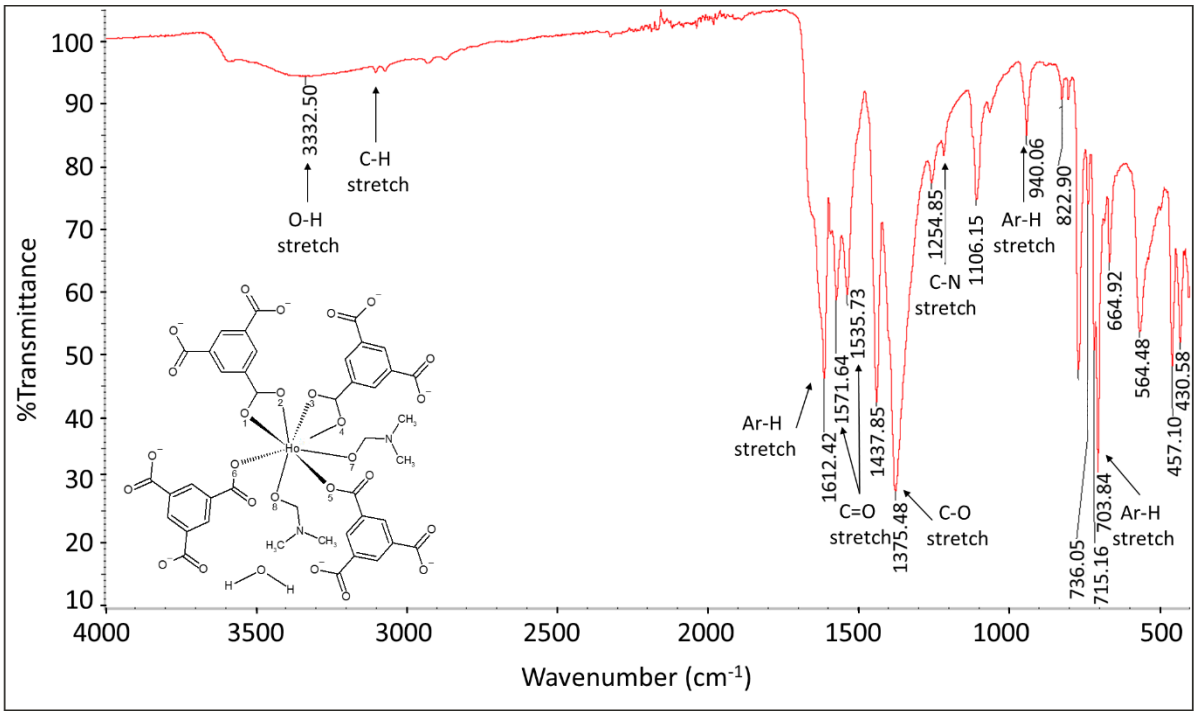

A2 - 9: Annotated FTIR of SH2-Ho including peak allocation. The insert represents the expected structure of the MOF as indicated by literature.

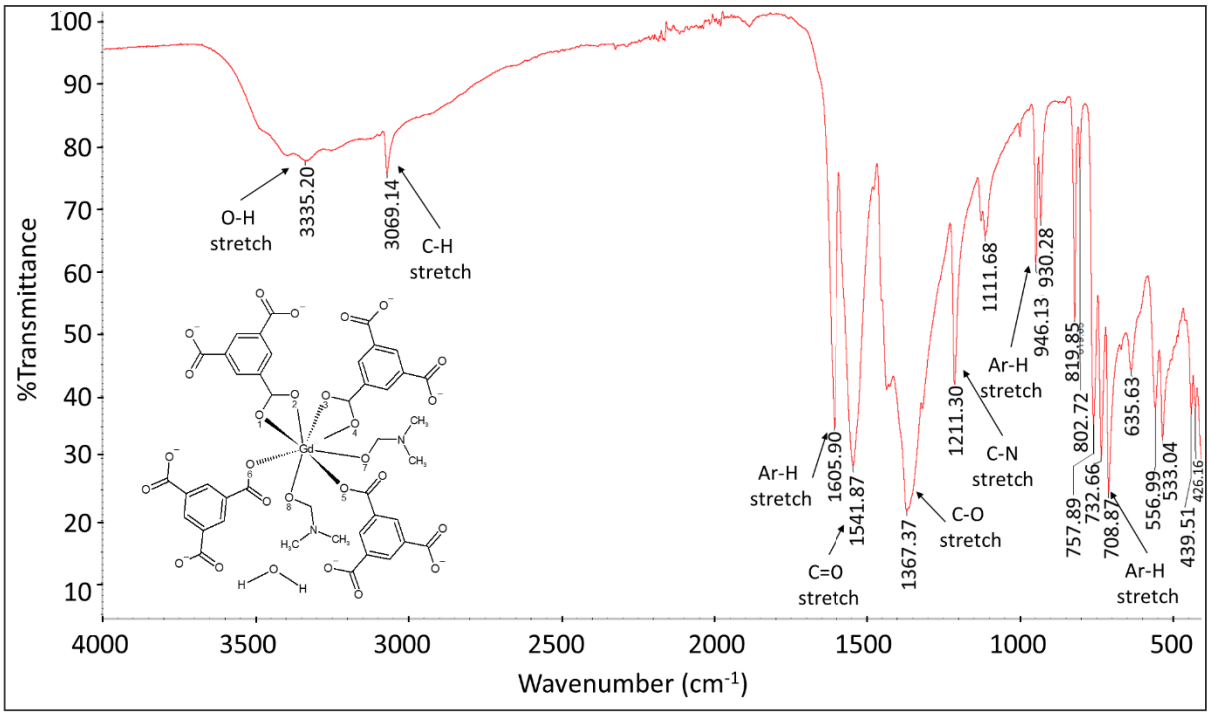

A2 - 10: Annotated FTIR of SH2-Gd including peak allocation. The insert represents the expected structure of the MOF as indicated by literature.

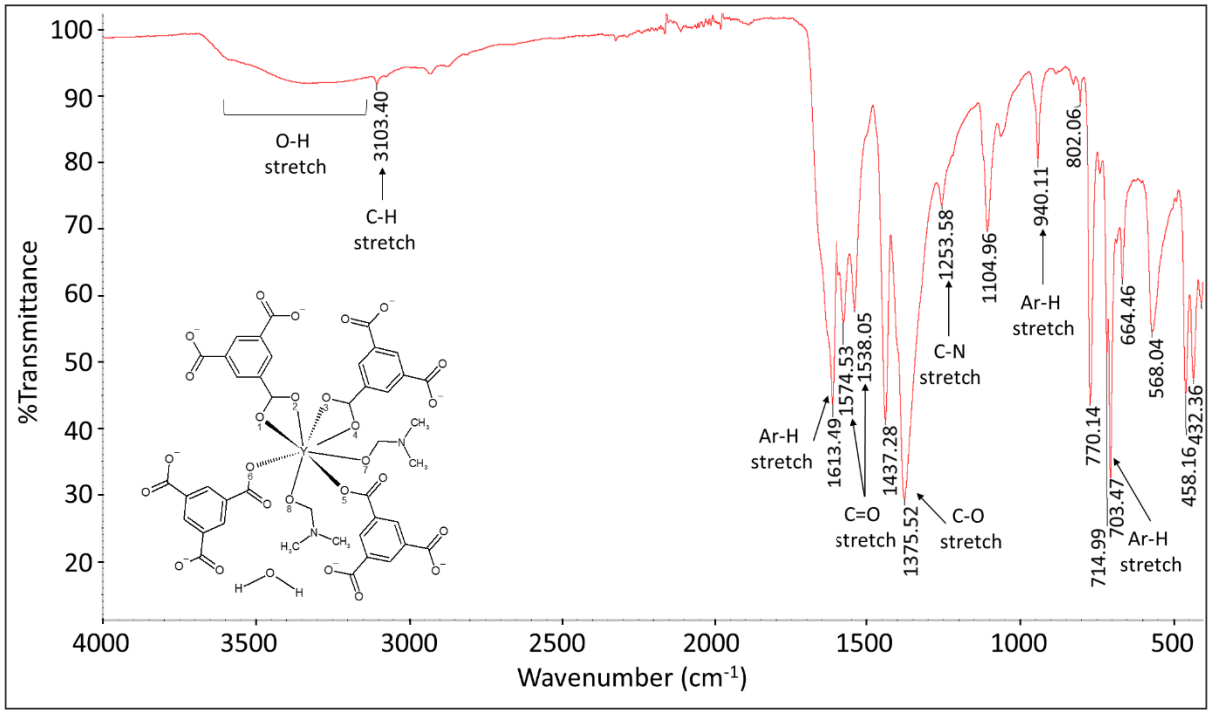

A2 - 11: Annotated FTIR of SH2-Y including peak allocation. The insert represents the expected structure of the MOF as indicated by literature.

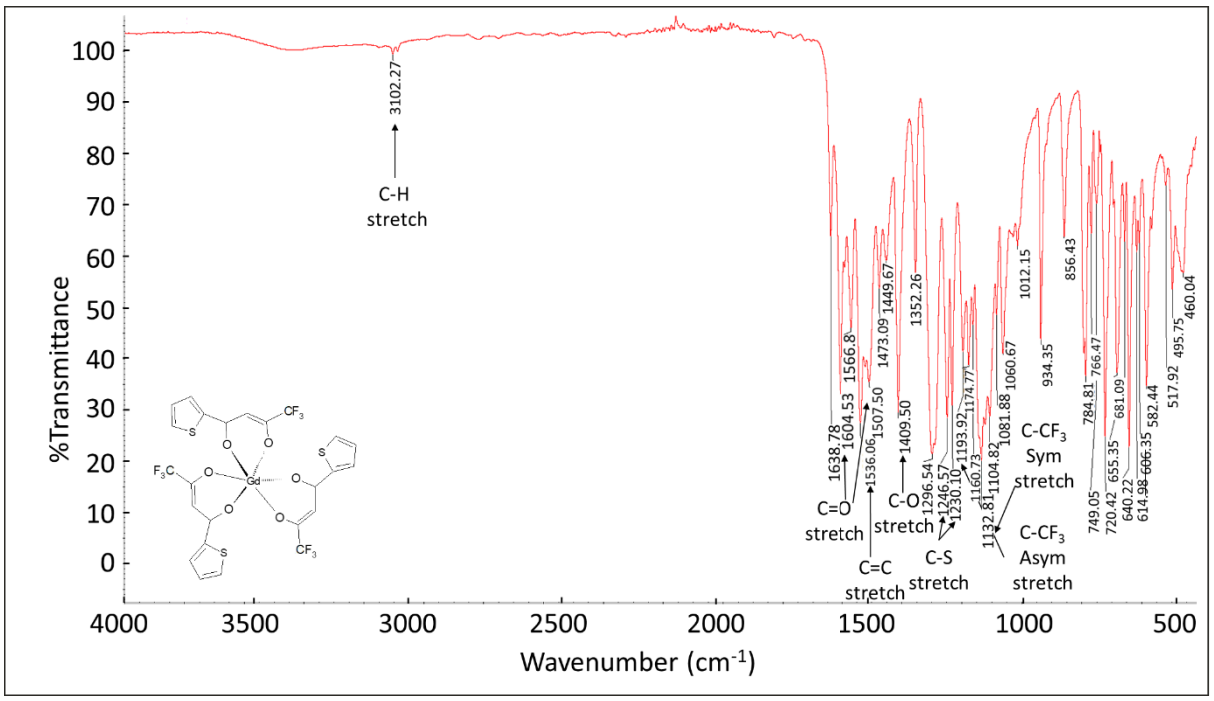

A2 - 12: Annotated FTIR of SH3-Gd including peak allocation. The insert represents the expected structure of the MOF as indicated by literature.

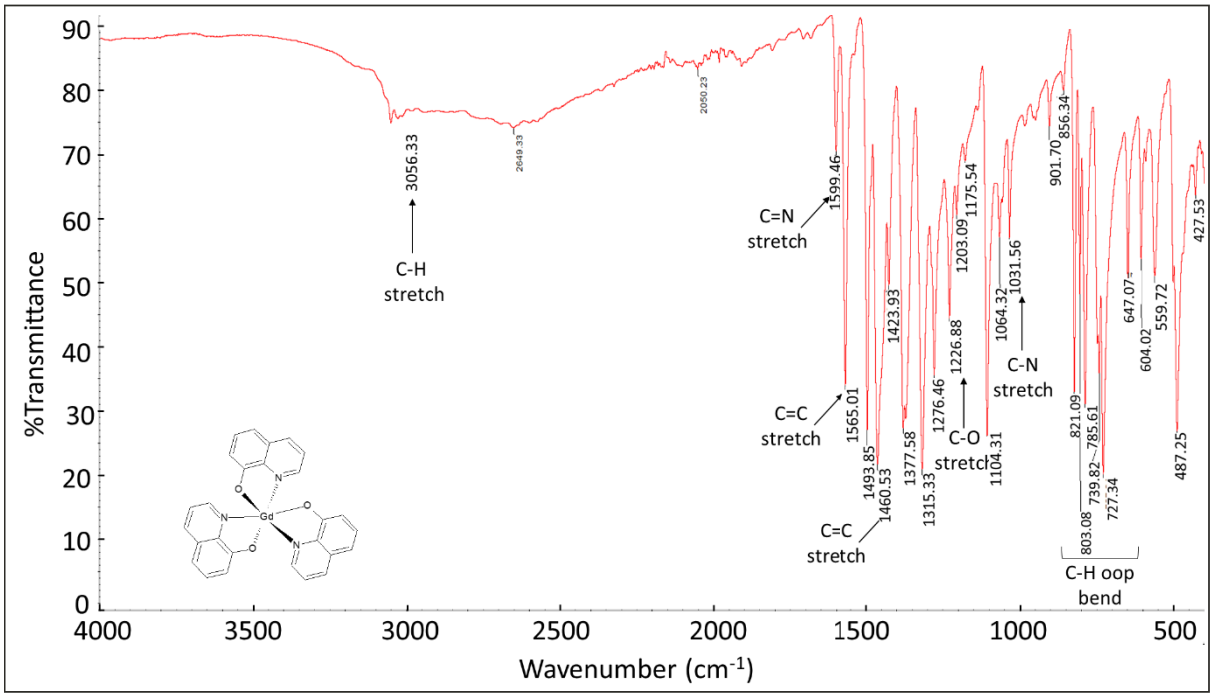

A2 - 13: Annotated FTIR of SH4-Gd including peak allocation. The insert represents the expected structure of the MOF as indicated by literature.

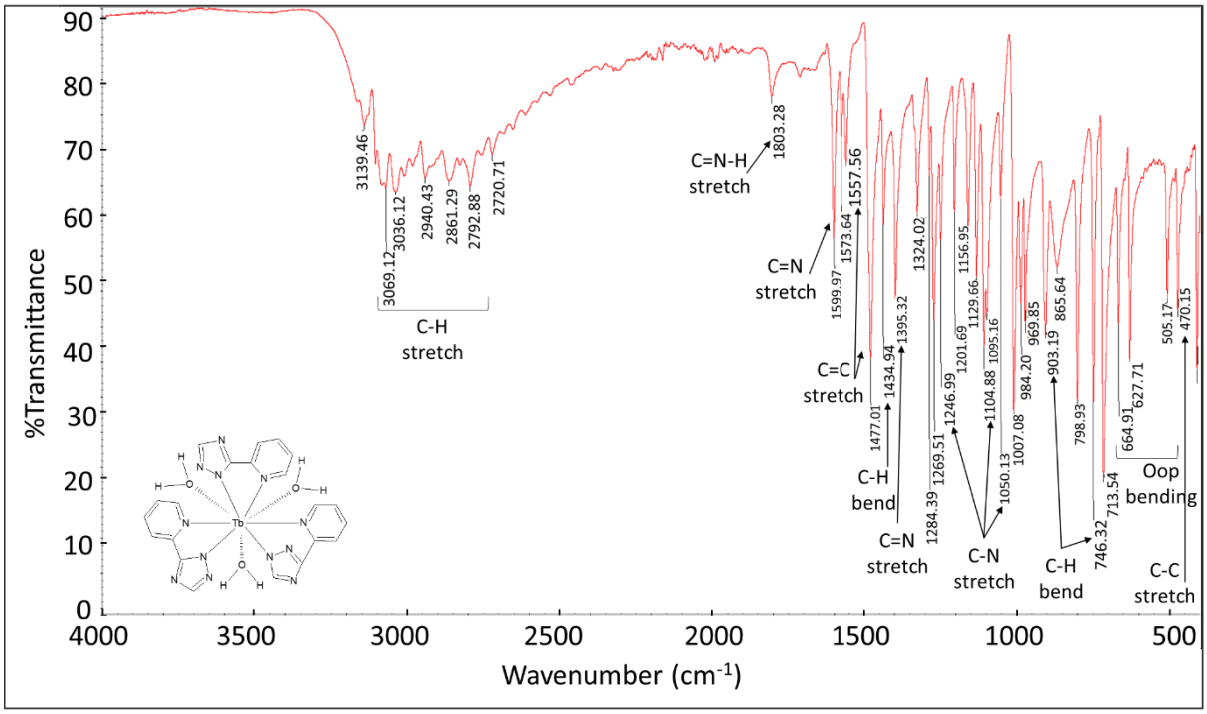

A2 - 14: Annotated FTIR of SH5-Tb including peak allocation. The insert represents the expected structure of the MOF as indicated by literature.

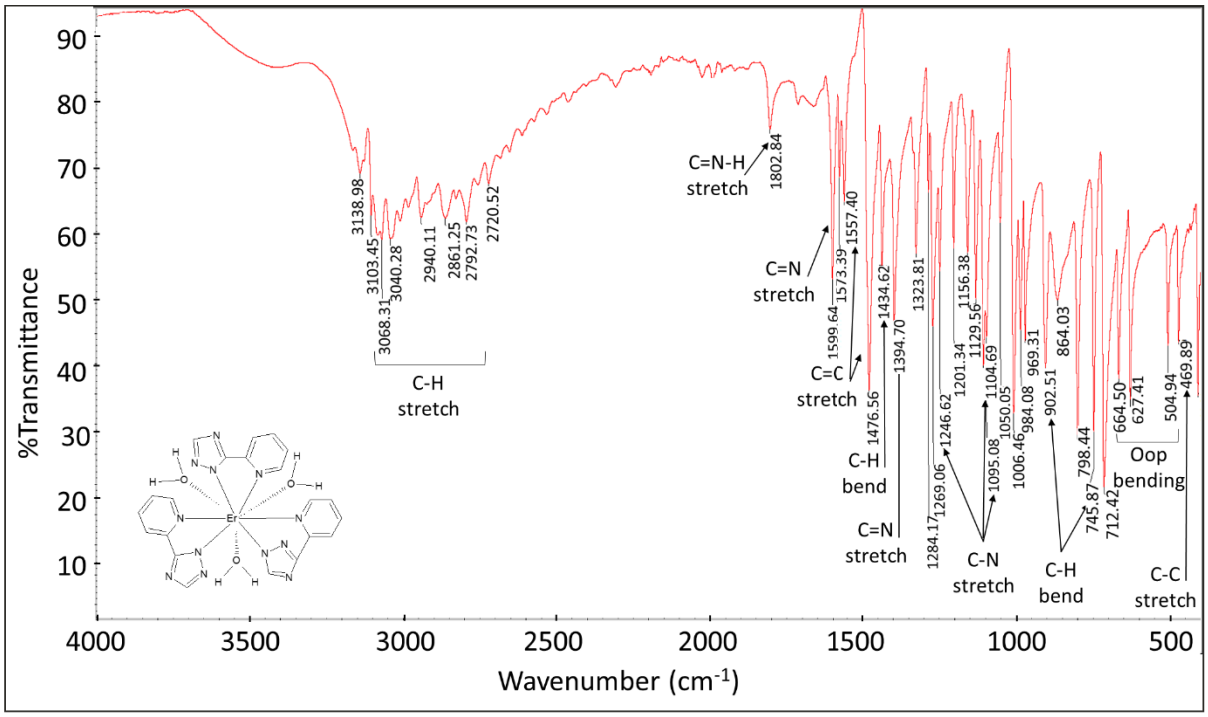

A2 - 15: Annotated FTIR of SH5-Er including peak allocation. The insert represents the expected structure of the MOF as indicated by literature.

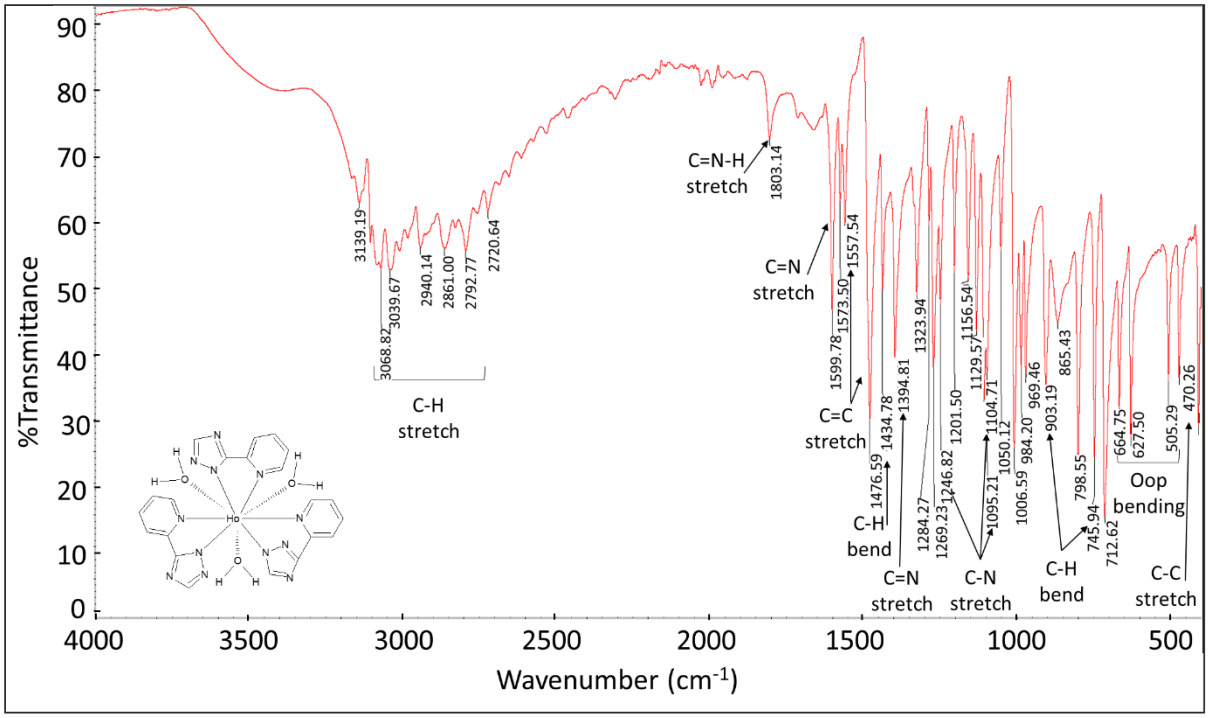

A2 - 16: Annotated FTIR of SH5-Ho including peak allocation. The insert represents the expected structure of the MOF as indicated by literature.

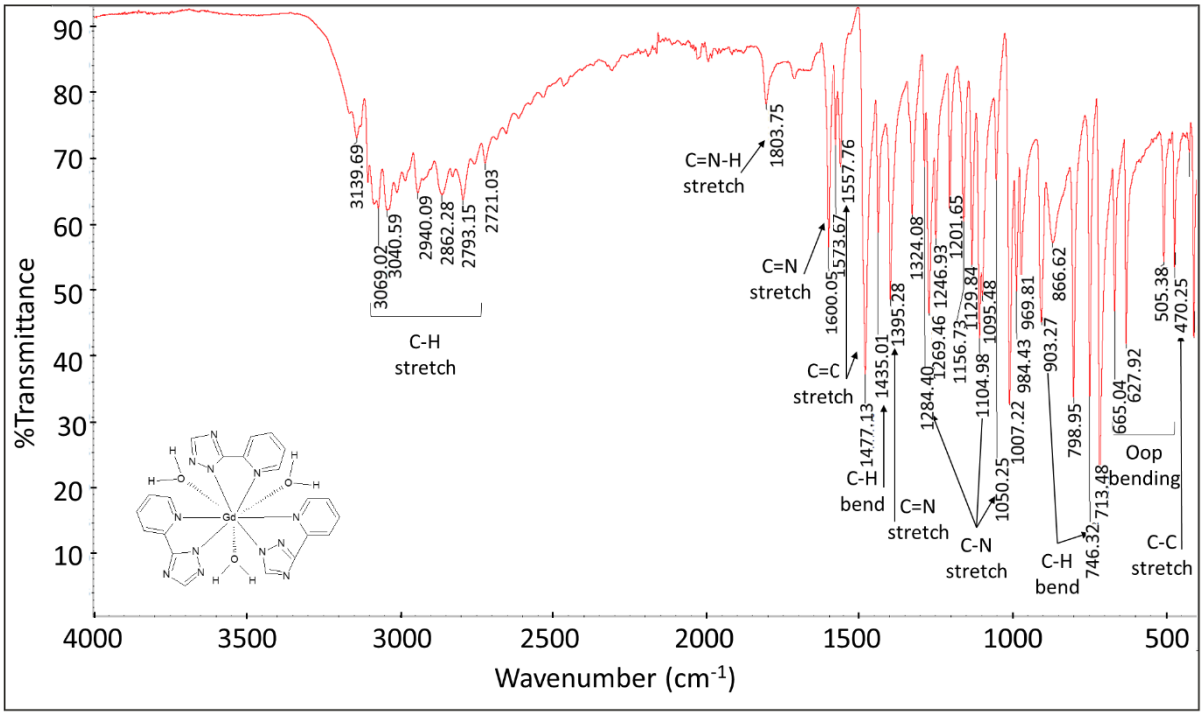

A2 - 17: Annotated FTIR of SH5-Gd including peak allocation. The insert represents the expected structure of the MOF as indicated by literature.

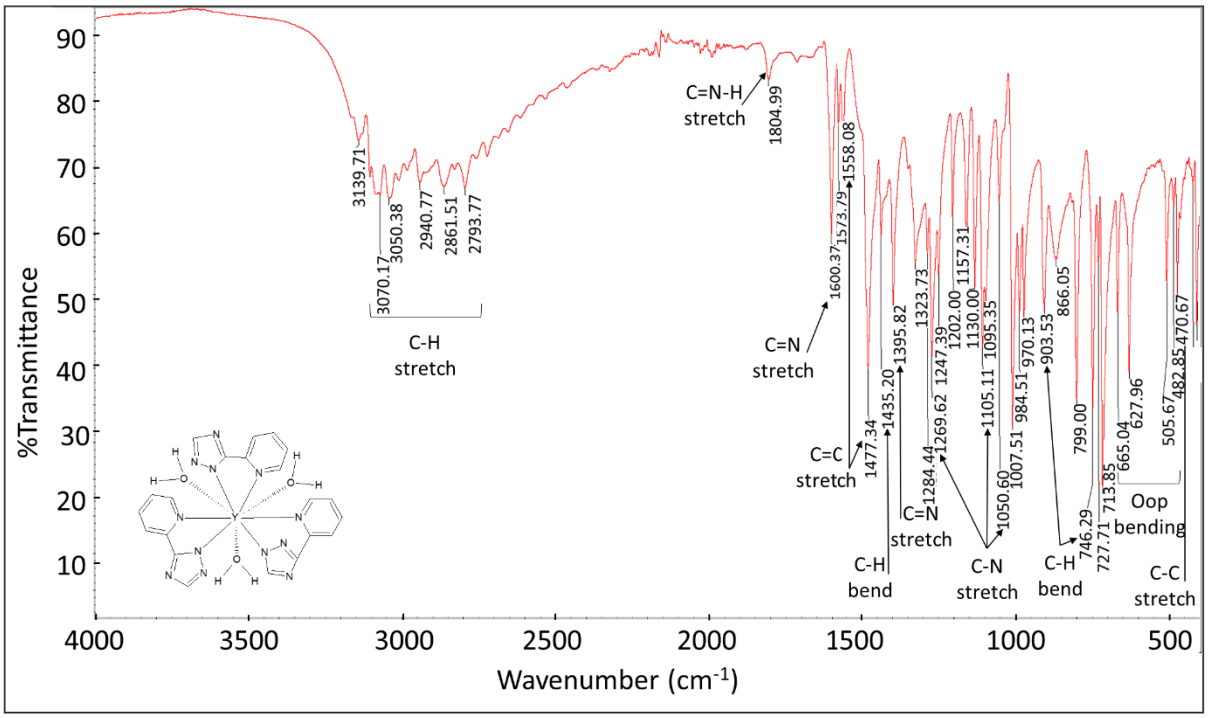

A2 - 18: Annotated FTIR of SH5-Y including peak allocation. The insert represents the expected structure of the MOF as indicated by literature.

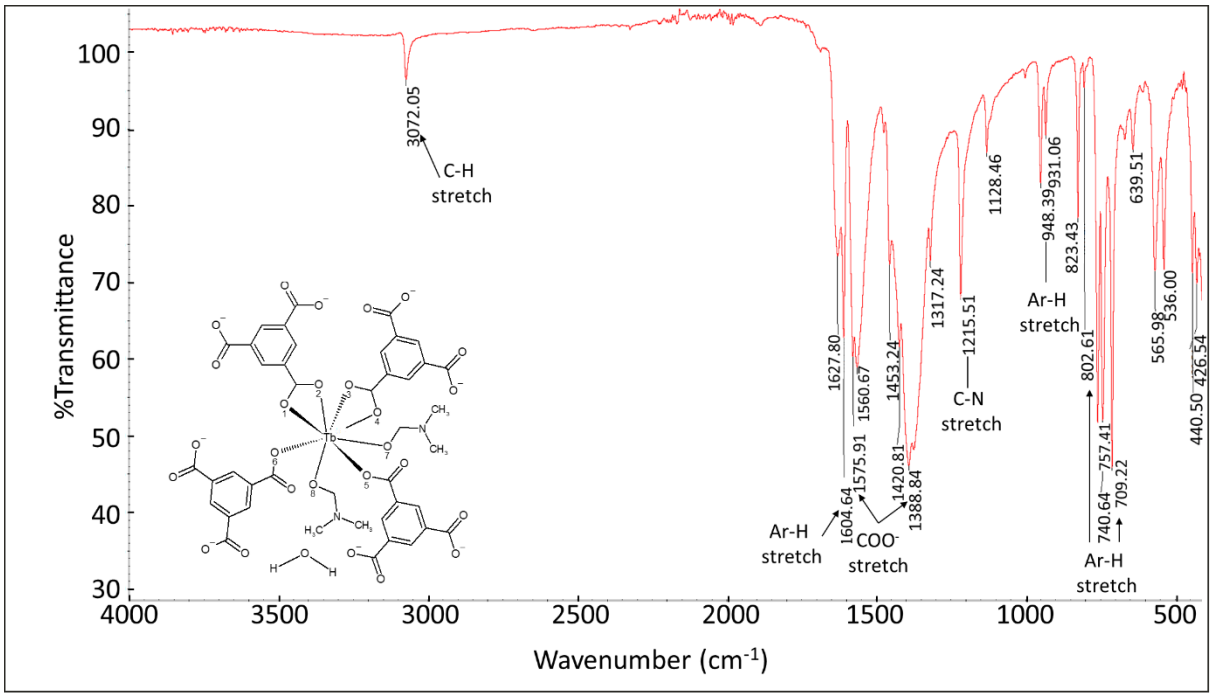

A2 - 19: Annotated FTIR of MW1-Tb including peak allocation. The insert represents the expected structure of the MOF as indicated by literature.

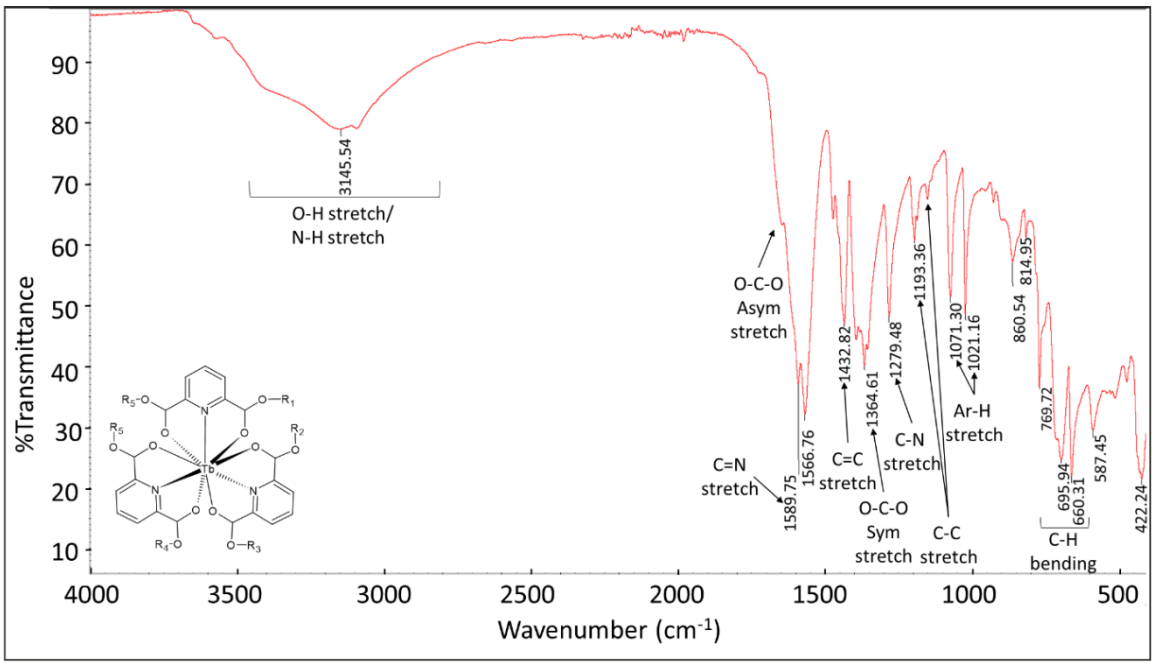

A2 - 20: Annotated FTIR of MW2-Tb including peak allocation. The insert represents the expected structure of the MOF as indicated by literature.

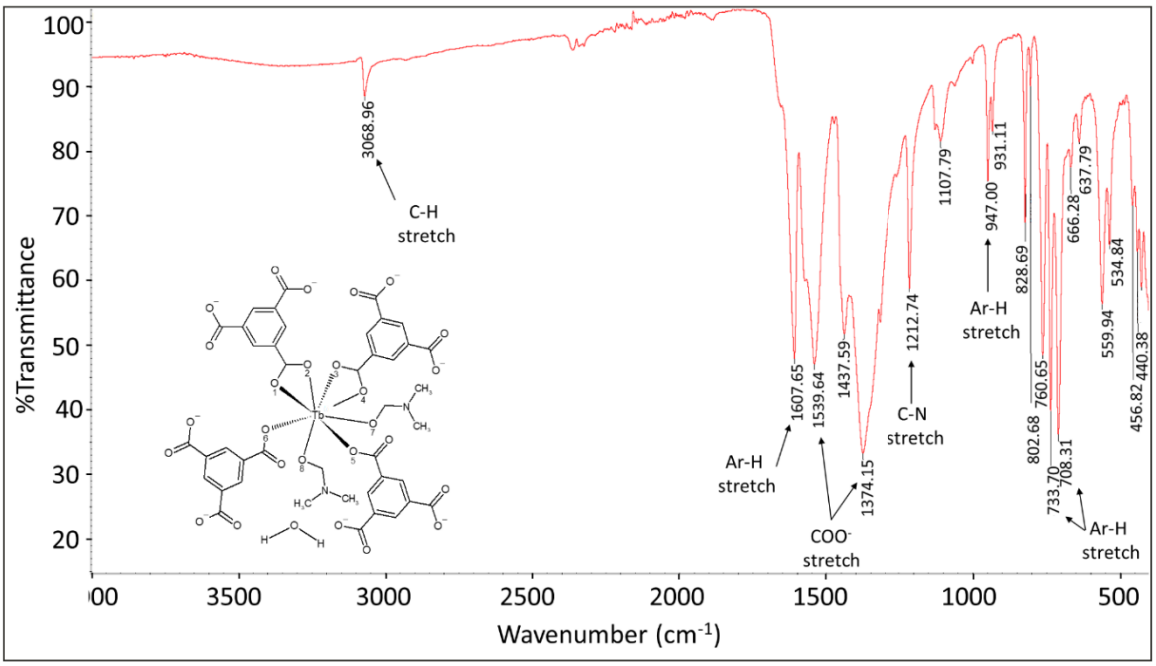

A2 - 21: Annotated FTIR of MW3-Tb including peak allocation. The insert represents the expected structure of the MOF as indicated by literature.

5.1.4 SEM-EDS

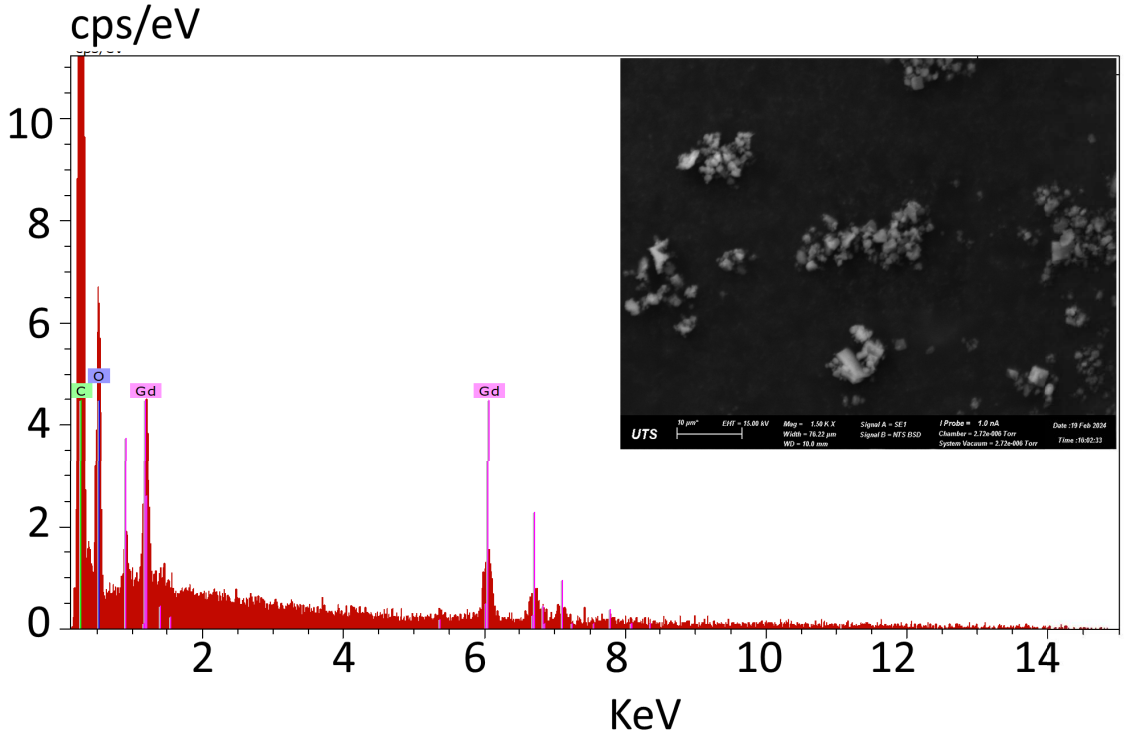

A2 - 22: EDS spectra of SH4-Gd. The insert represents the SEM image collected at 15.00 kV, mag = 1.5 K and WD = 10 mm.

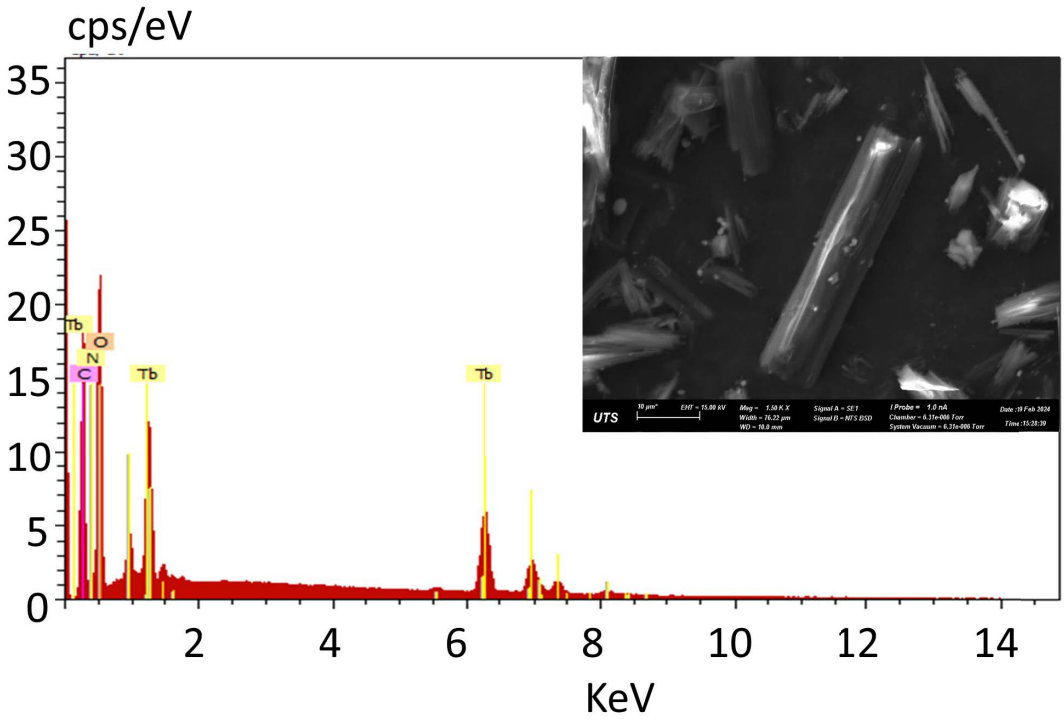

A2 - 23: EDS spectra of SH5-Tb. The insert represents the SEM image collected at 15.00 kV, mag = 1.5 K and WD = 10 mm.

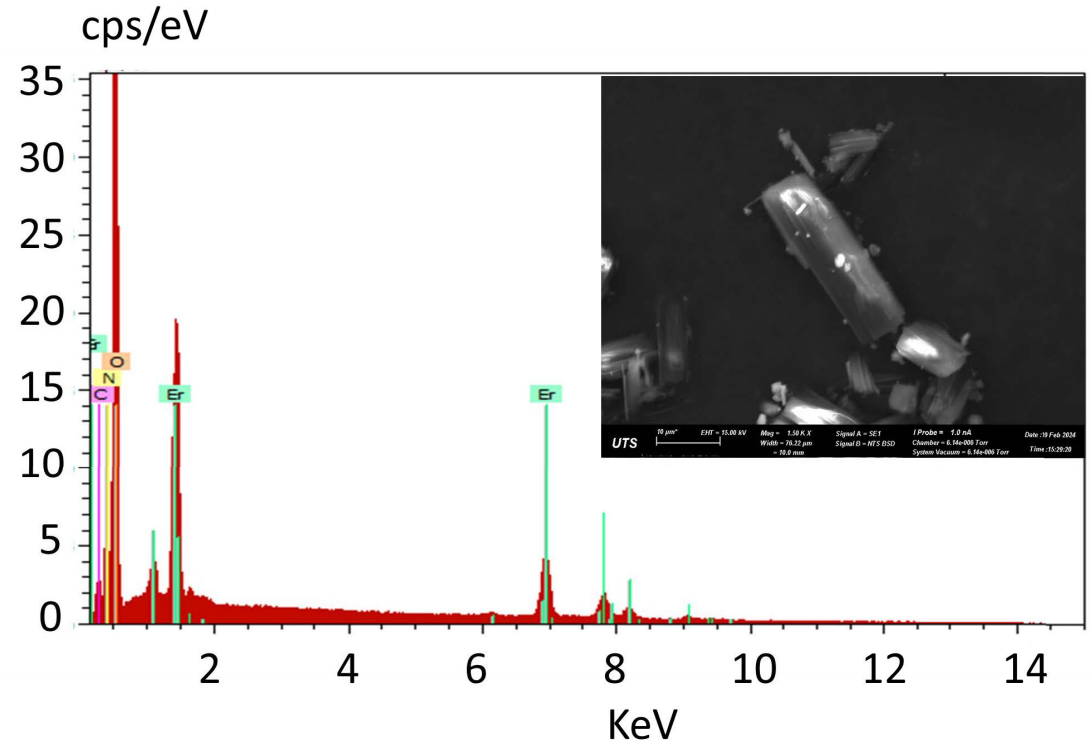

A2 - 24: EDS spectra of SH5-Er. The insert represents the SEM image collected at 15.00 kV, mag = 1.5 K and WD = 10 mm.

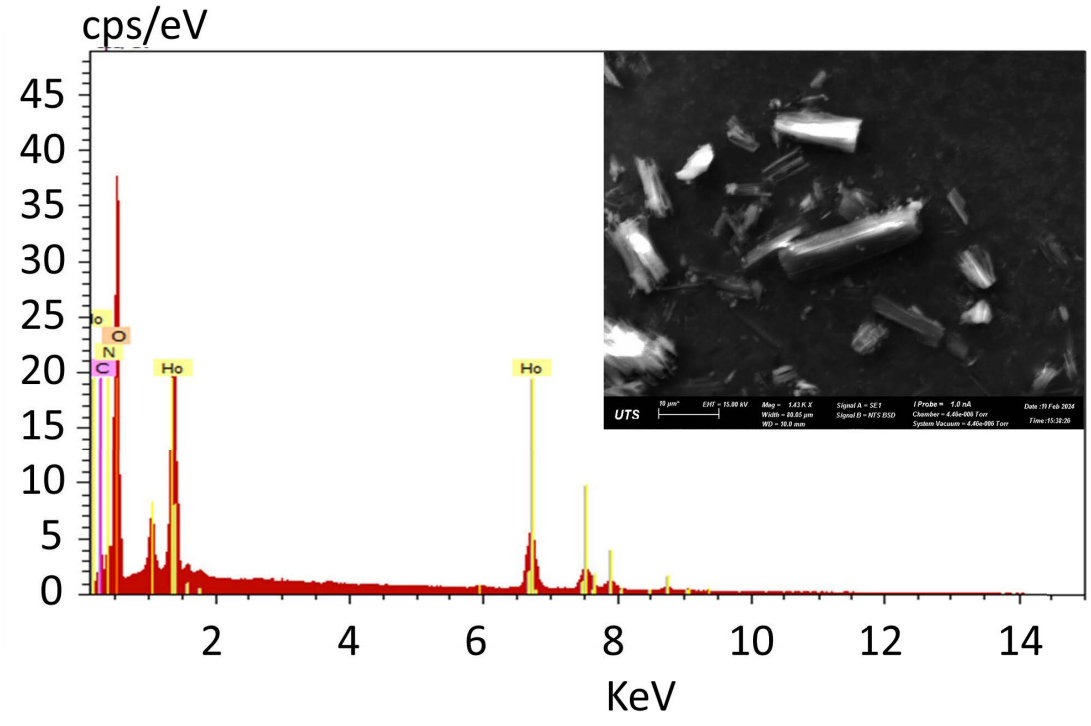

A2 - 25: EDS spectra of SH5-Ho. The insert represents the SEM image collected at 15.00 kV, mag = 1.5 K and WD = 10 mm.

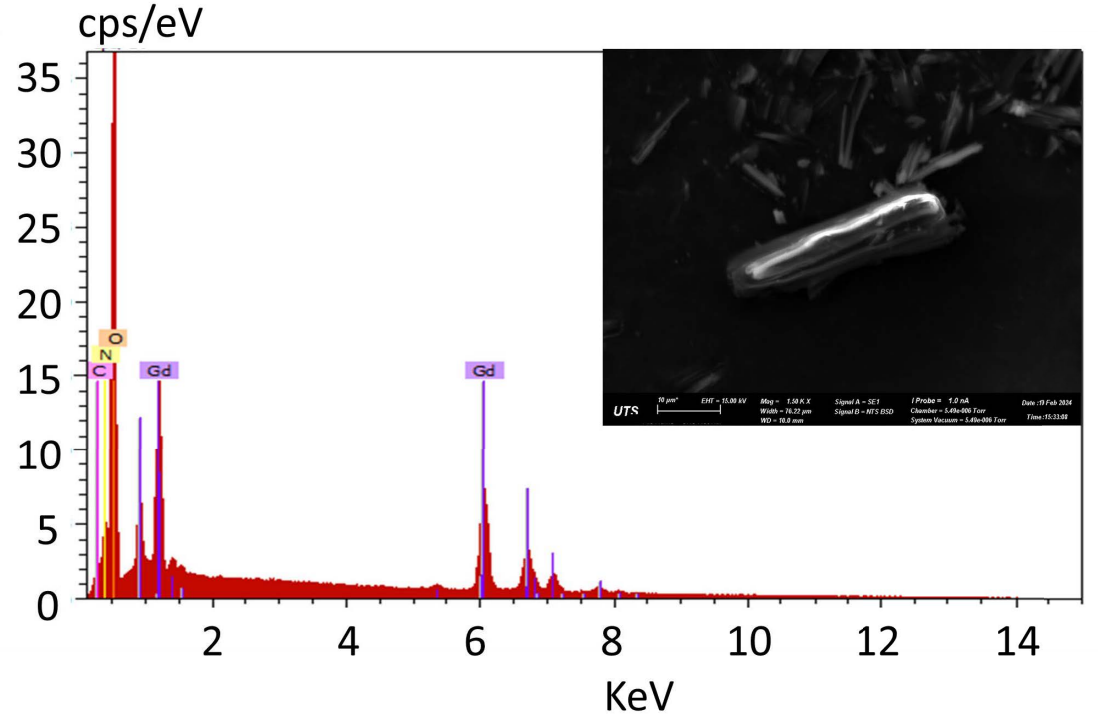

A2 - 26: EDS spectra of SH5-Gd. The insert represents the SEM image collected at 15.00 kV, mag = 1.5 K and WD = 10 mm.

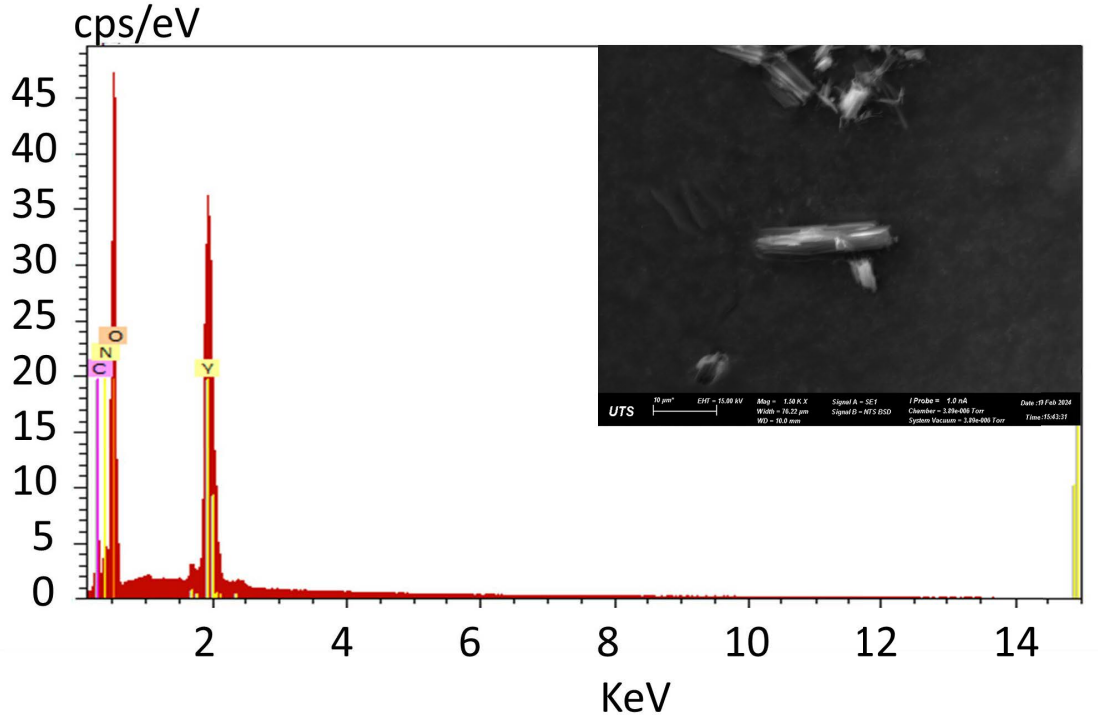

A2 - 27: EDS spectra of SH5-Y. The insert represents the SEM image collected at 15.00 kV, mag = 1.5 K and WD = 10 mm.

5.1.5 TGA

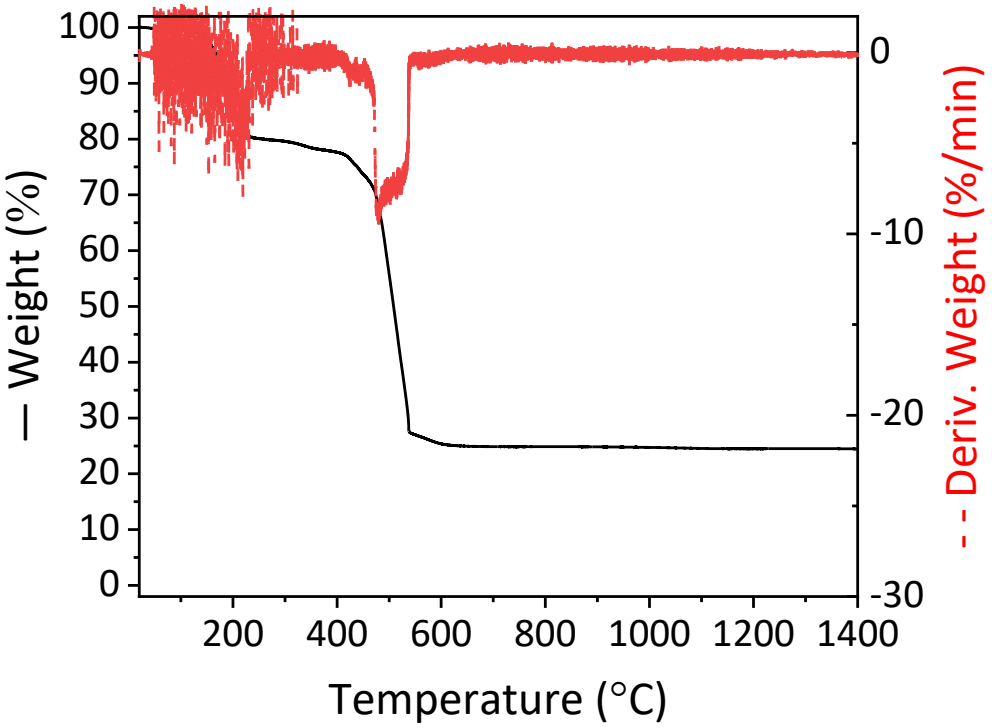

A2 - 28: TGA curves (black solid line) and DTA plots (red dotted line) of SH4-Gd.

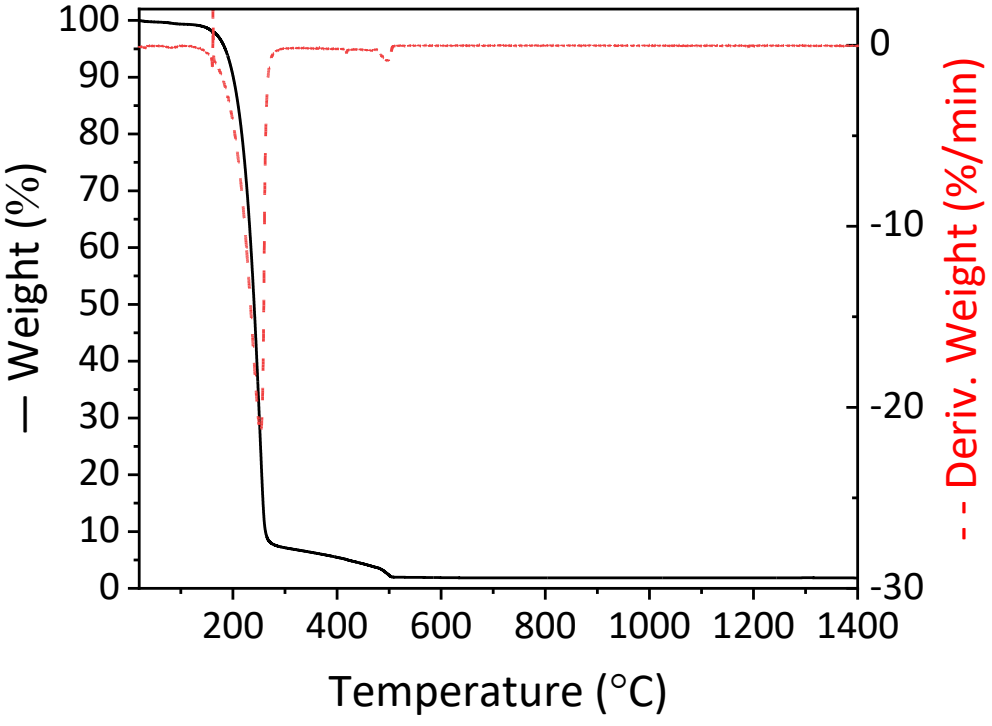

A2 - 29: TGA curves (black solid line) and DTA plots (red dotted line) of SH5-Tb.

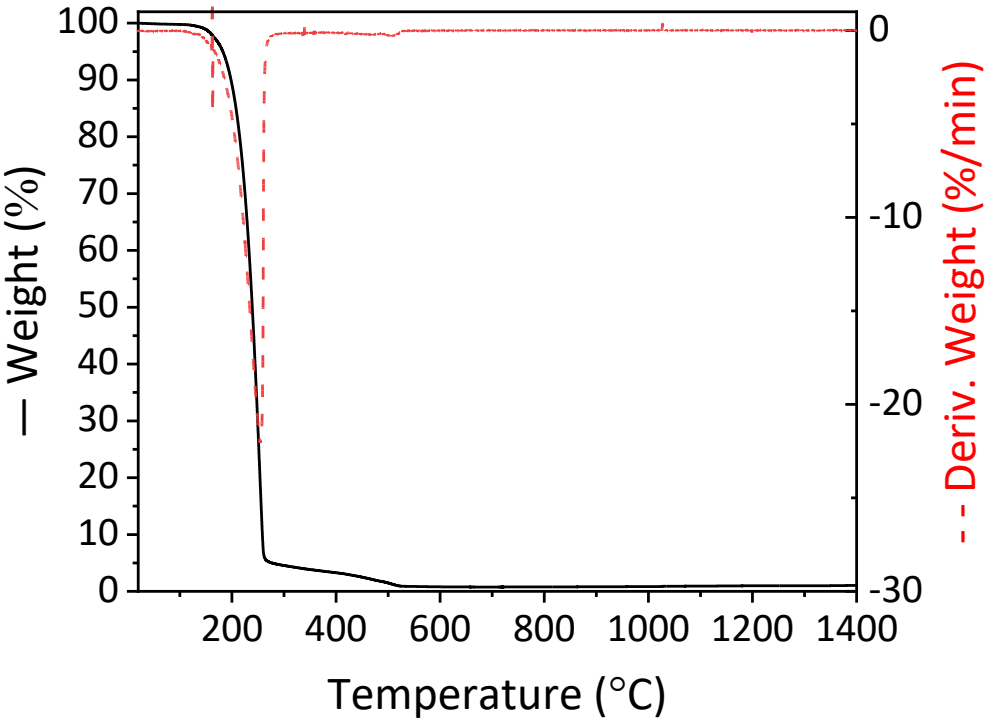

A2 - 30: TGA curves (black solid line) and DTA plots (red dotted line) of SH5-Er.

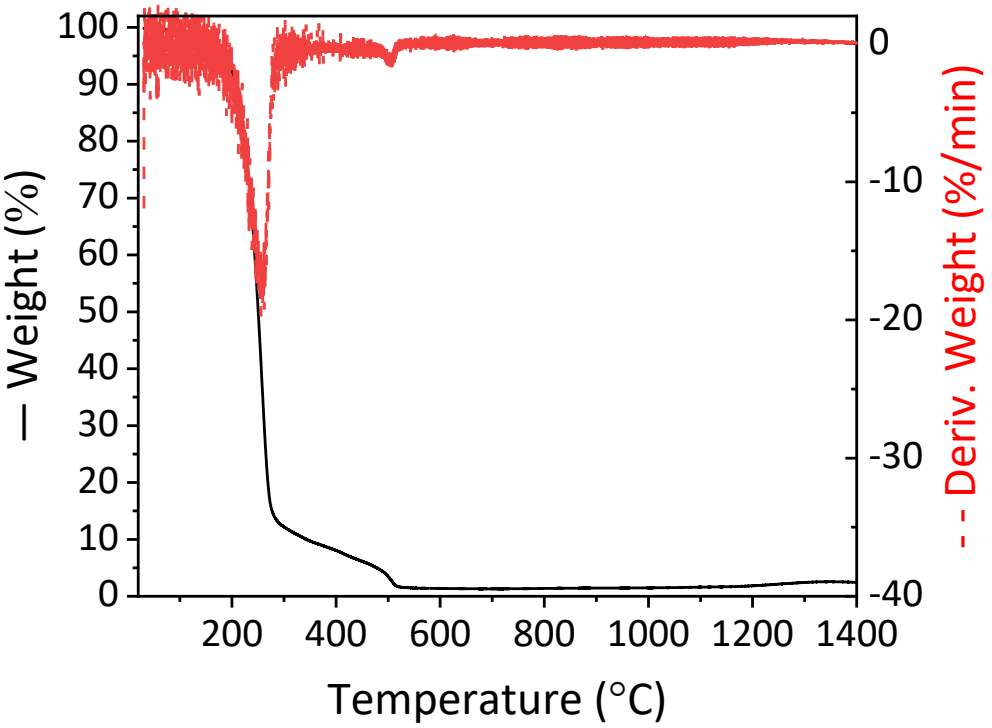

A2 - 31: TGA curves (black solid line) and DTA plots (red dotted line) of SH5-Ho.

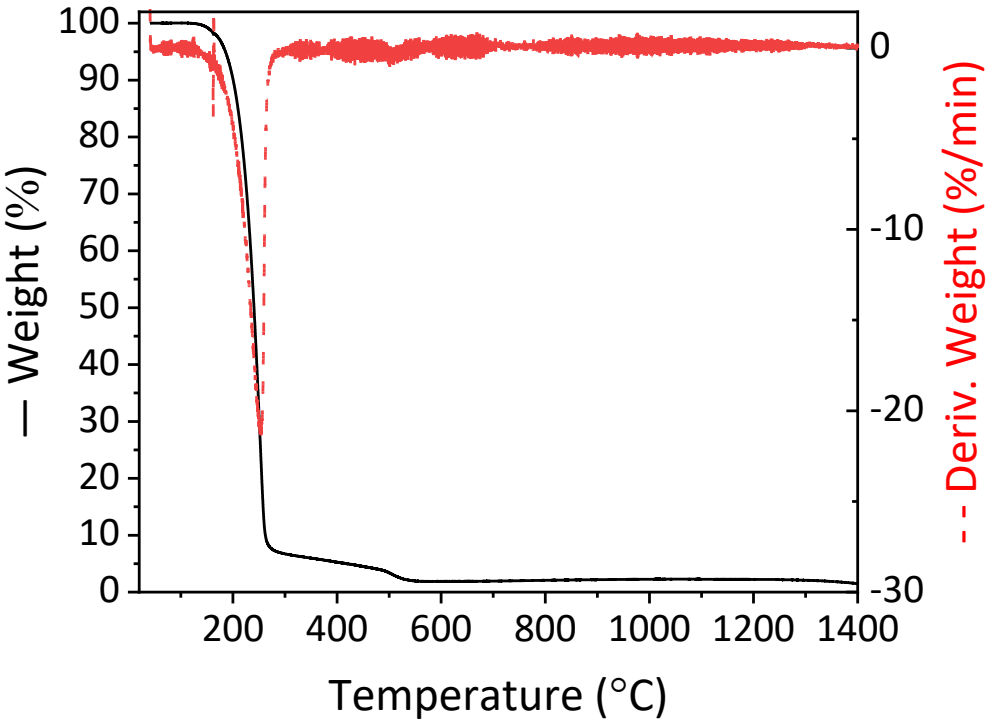

A2 - 32: TGA curves (black solid line) and DTA plots (red dotted line) of SH5-Gd.

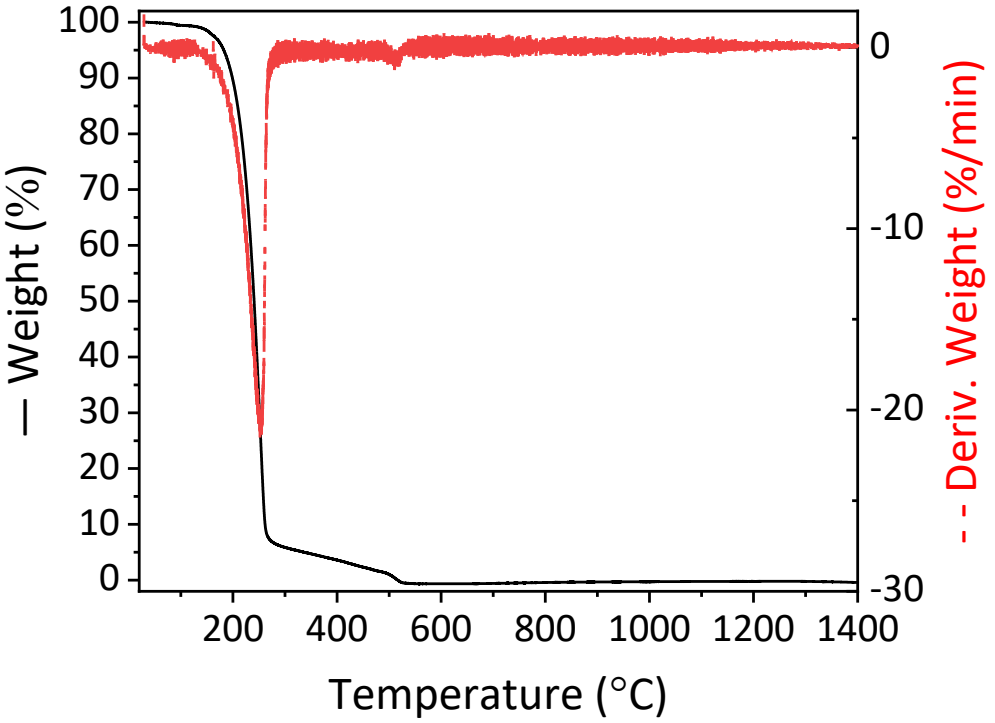

A2 - 33: TGA curves (black solid line) and DTA plots (red dotted line) of SH5-Y.

5.1.6 UV Photoluminescence

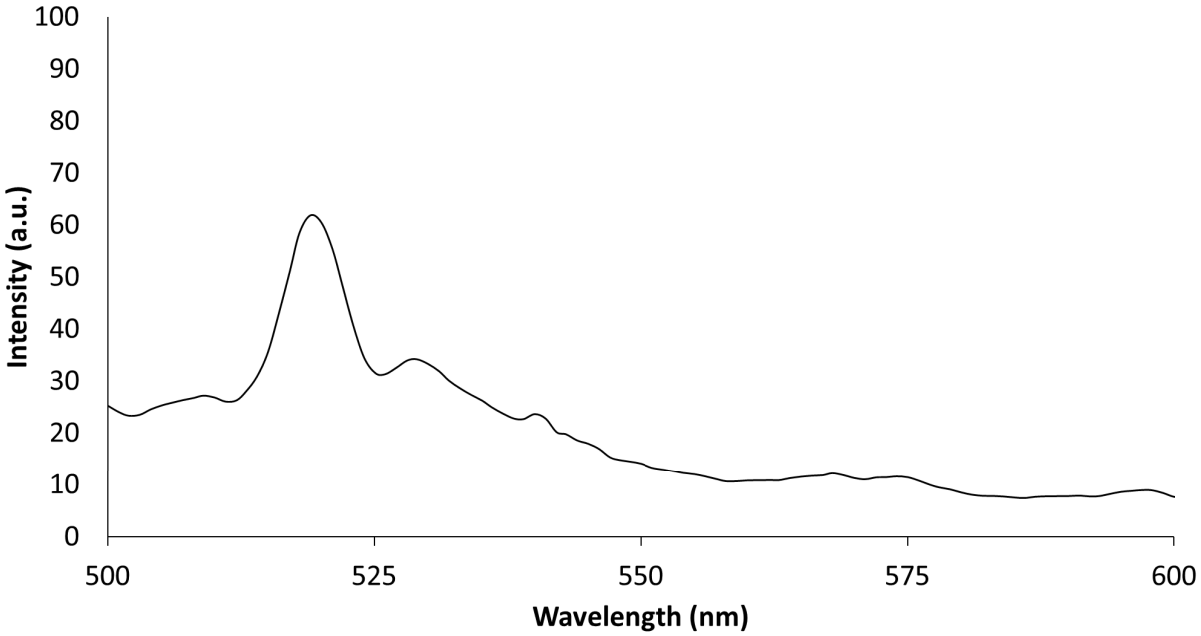

A2 - 34: Photoluminescence emission of quartz slide (λ_{ex} = 380 nm).

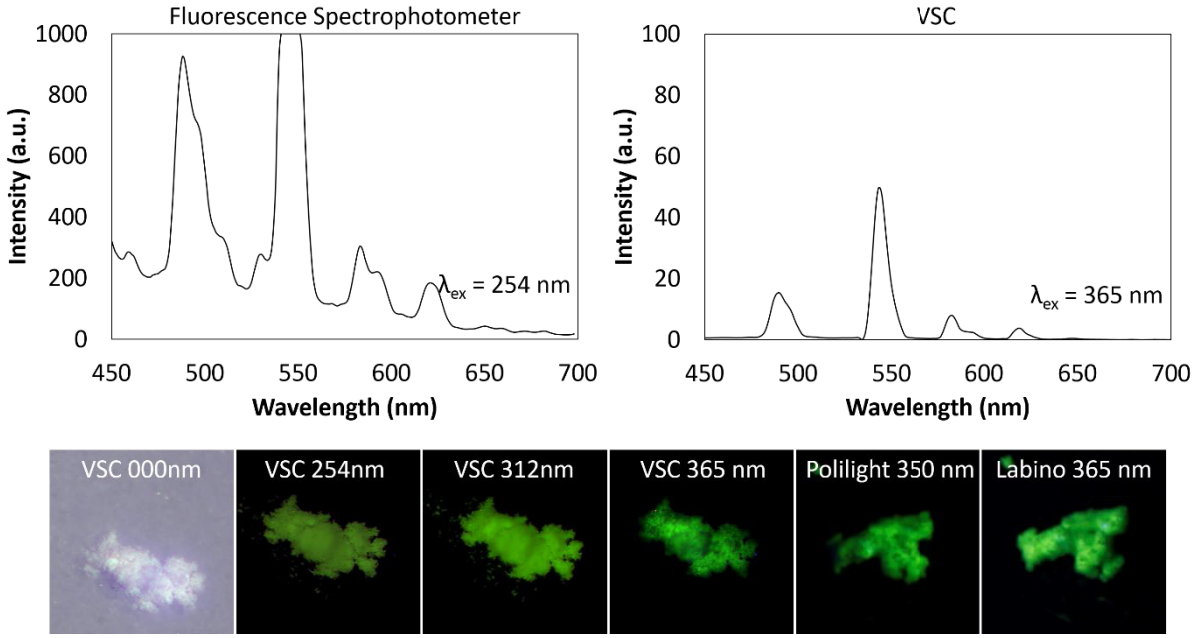

A2 - 35: Photoluminescence emission spectra of SH2-Tb captured from the spectrophotometer (left) and VSC (right). The inserts represent the pure MOF samples in the VSC (λ_{ex} = 365 nm; ISO = 100; integration time = 500 ms; iris = 100% and mag = 60x), Polilight® (λ_{ex} = 350 nm; ISO = 100; f-stop = = f/2.8; exposure = 1/30 sec) and Labino® Lamp (λ_{ex} = 350 nm; ISO = 100; f-stop = = f/2.8; exposure = 1/30 sec).

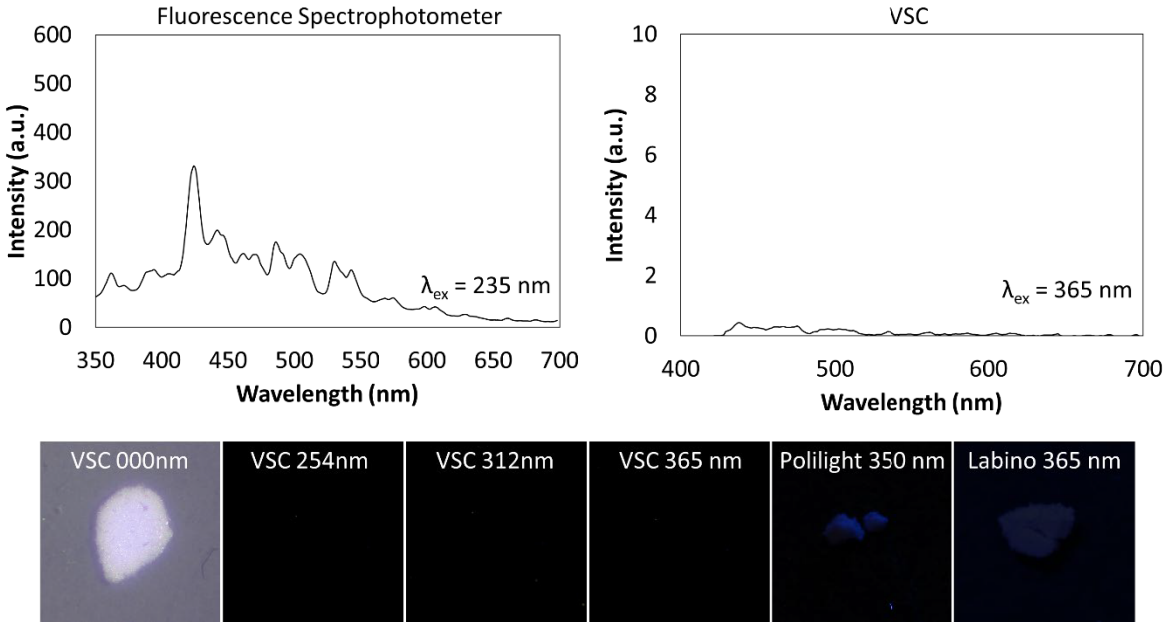

A2 - 36: Photoluminescence emission spectra of SH2-Er captured from the spectrophotometer (left) and VSC (right). The inserts represent the pure MOF samples in the VSC (λ_{ex} = 365 nm; ISO = 100; integration time = 500 ms; iris = 100% and mag = 60x), Polilight® (λ_{ex} = 350 nm; ISO = 100; f-stop = = f/2.8; exposure = 1/30 sec) and Labino® Lamp (λ_{ex} = 350 nm; ISO = 100; f-stop = = f/2.8; exposure = 1/30 sec).

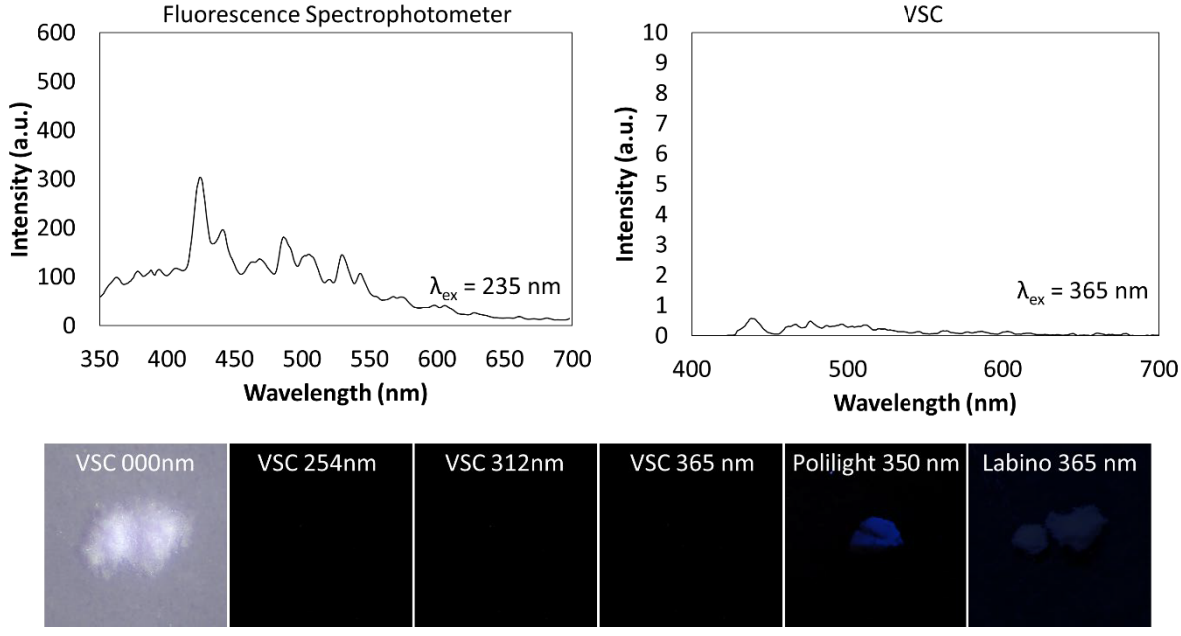

A2 - 37: Photoluminescence emission spectra of SH2-Ho captured from the spectrophotometer (left) and VSC (right). The inserts represent the pure MOF samples in the VSC (λ_{ex} = 365 nm; ISO = 100; integration time = 500 ms; iris = 100% and mag = 60x), Polilight® (λ_{ex} = 350 nm; ISO = 100; f-stop = = f/2.8; exposure = 1/30 sec) and Labino® Lamp (λ_{ex} = 350 nm; ISO = 100; f-stop = = f/2.8; exposure = 1/30 sec).

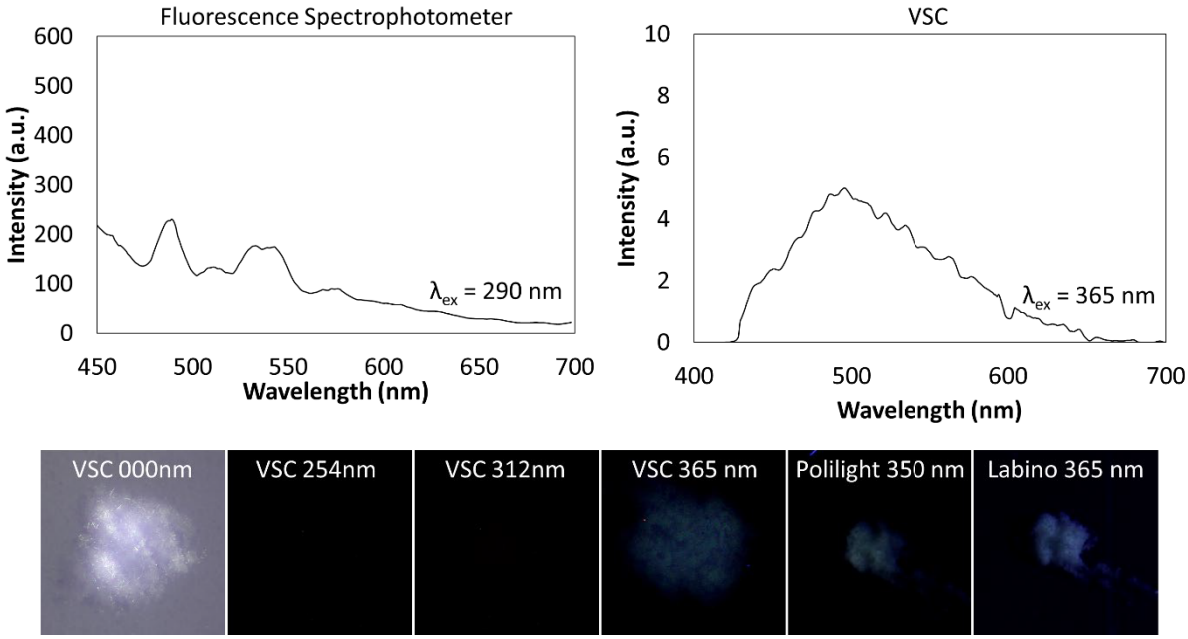

A2 - 38: Photoluminescence emission spectra of SH2-Gd captured from the spectrophotometer (left) and VSC (right). The inserts represent the pure MOF samples in the VSC (λ_{ex} = 365 nm; ISO = 100; integration time = 500 ms; iris = 100% and mag = 60x), Polilight® (λ_{ex} = 350 nm; ISO = 100; f-stop = = f/2.8; exposure = 1/30 sec) and Labino® Lamp (λ_{ex} = 350 nm; ISO = 100; f-stop = = f/2.8; exposure = 1/30 sec).

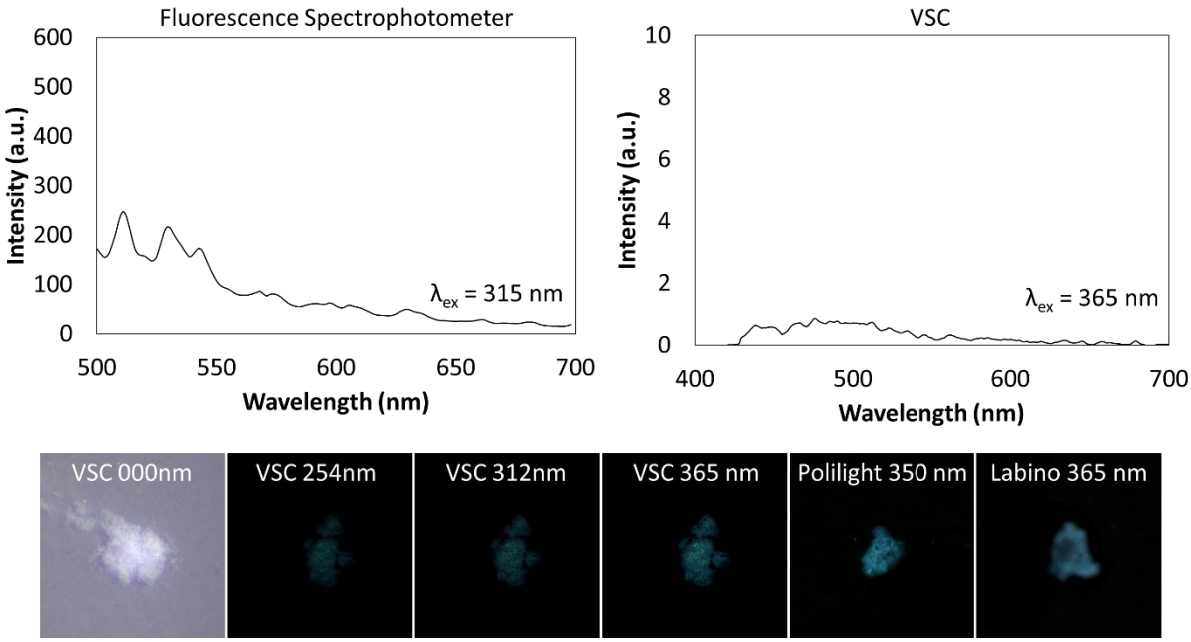

A2 - 39: Photoluminescence emission spectra of SH2-Y captured from the spectrophotometer (left) and VSC (right). The inserts represent the pure MOF samples in the VSC (λ_{ex} = 365 nm; ISO = 100; integration time = 500 ms; iris = 100% and mag = 60x), Polilight® (λ_{ex} = 350 nm; ISO = 100; f-stop = = f/2.8; exposure = 1/30 sec) and Labino® Lamp (λ_{ex} = 350 nm; ISO = 100; f-stop = = f/2.8; exposure = 1/30 sec).

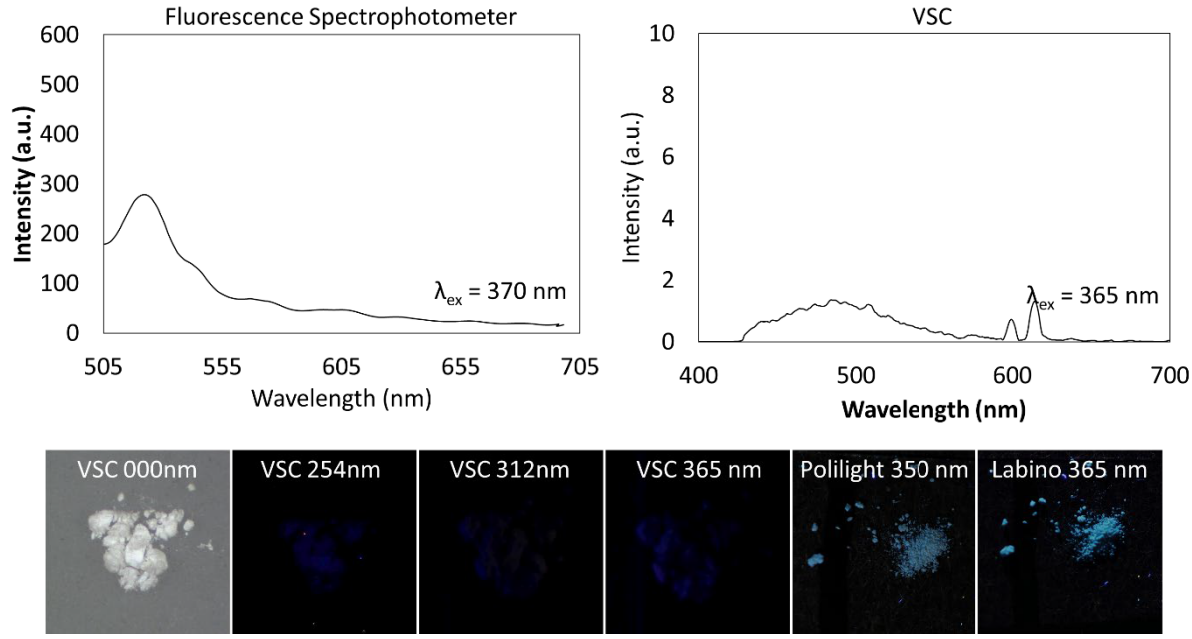

A2 - 40: Photoluminescence emission spectra of SH3-Gd captured from the spectrophotometer (left) and VSC (right). The inserts represent the pure MOF samples in the VSC (λ_{ex} = 365 nm; ISO = 100; integration time = 500 ms; iris = 100% and mag = 60x), Polilight® (λ_{ex} = 350 nm; ISO = 100; f-stop = = f/2.8; exposure = 1/30 sec) and Labino® Lamp (λ_{ex} = 350 nm; ISO = 100; f-stop = = f/2.8; exposure = 1/30 sec).

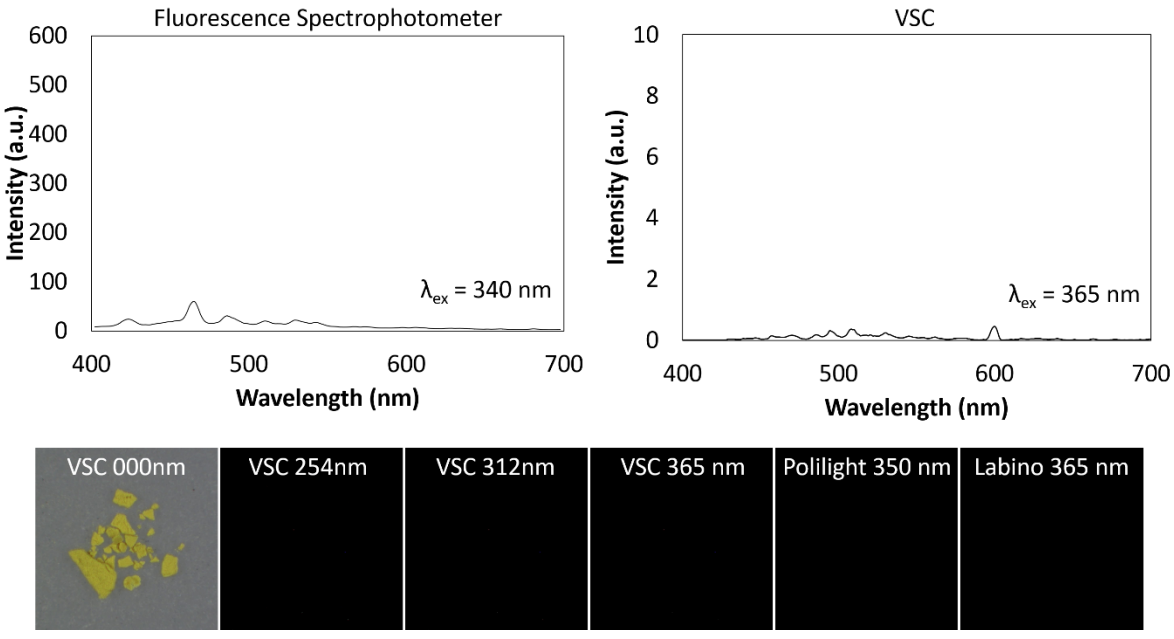

A2 - 41: Photoluminescence emission spectra of SH4-Gd captured from the spectrophotometer (left) and VSC (right). The inserts represent the pure MOF samples in the VSC (λ_{ex} = 365 nm; ISO = 100; integration time = 500 ms; iris = 100% and mag = 60x), Polilight® (λ_{ex} = 350 nm; ISO = 100; f-stop = = f/2.8; exposure = 1/30 sec) and Labino® Lamp (λ_{ex} = 350 nm; ISO = 100; f-stop = = f/2.8; exposure = 1/30 sec).

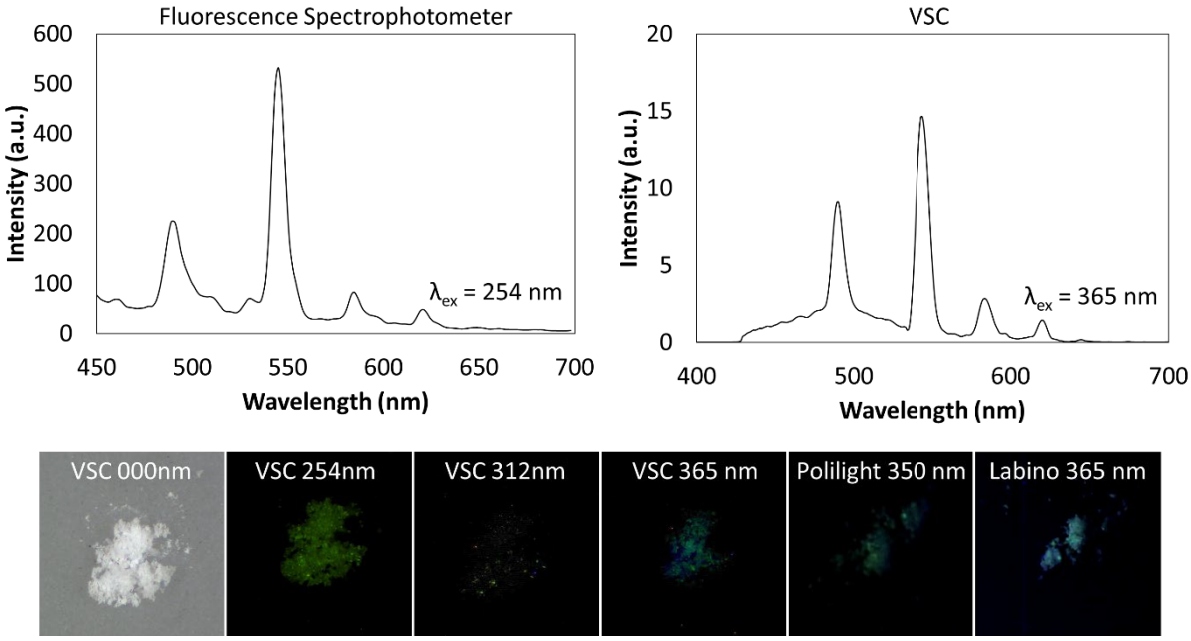

A2 - 42: Photoluminescence emission spectra of SH5-Tb captured from the spectrophotometer (left) and VSC (right). The inserts represent the pure MOF samples in the VSC (λ_{ex} = 365 nm; ISO = 100; integration time = 500 ms; iris = 100% and mag = 60x), Polilight® (λ_{ex} = 350 nm; ISO = 100; f-stop = = f/2.8; exposure = 1/30 sec) and Labino® Lamp (λ_{ex} = 350 nm; ISO = 100; f-stop = = f/2.8; exposure = 1/30 sec).

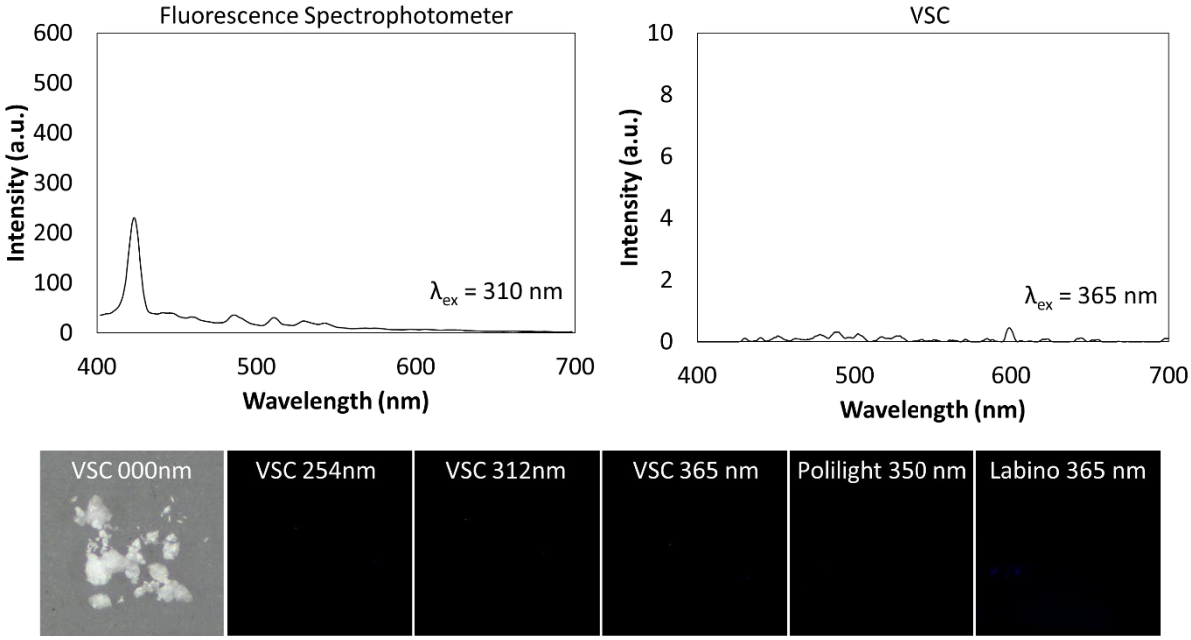

A2 - 43: Photoluminescence emission spectra of SH5-Er captured from the spectrophotometer (left) and VSC (right). The inserts represent the pure MOF samples in the VSC (λ_{ex} = 365 nm; ISO = 100; integration time = 500 ms; iris = 100% and mag = 60x), Polilight® (λ_{ex} = 350 nm; ISO = 100; f-stop = = f/2.8; exposure = 1/30 sec) and Labino® Lamp (λ_{ex} = 350 nm; ISO = 100; f-stop = = f/2.8; exposure = 1/30 sec).

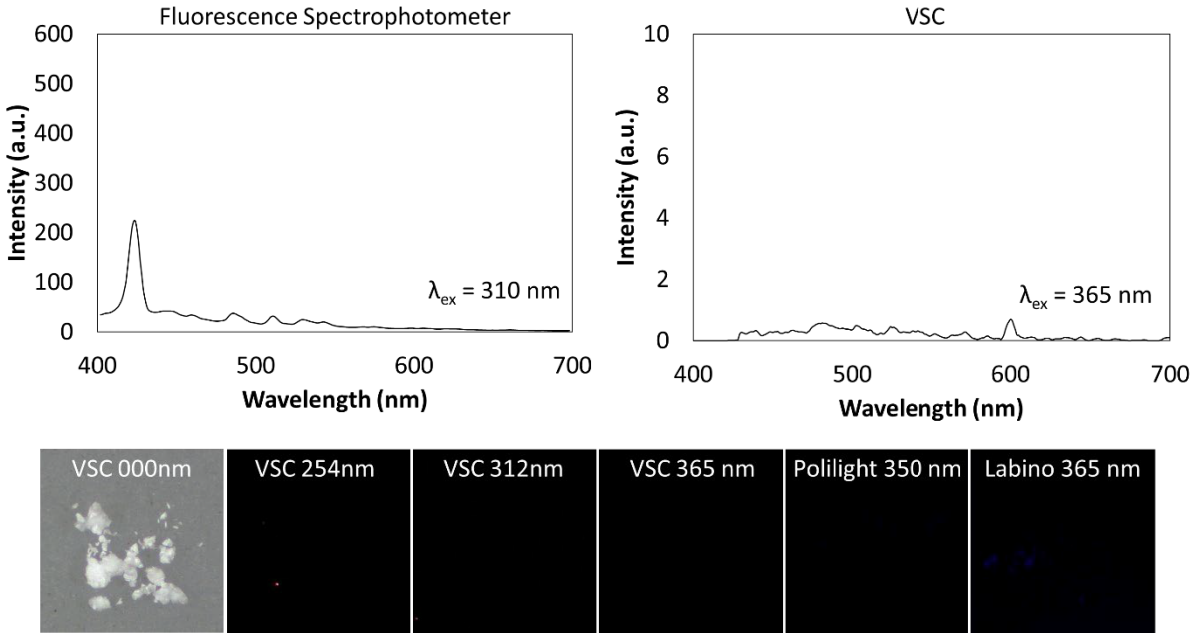

A2 - 44: Photoluminescence emission spectra of SH5-Ho captured from the spectrophotometer (left) and VSC (right). The inserts represent the pure MOF samples in the VSC (λ_{ex} = 365 nm; ISO = 100; integration time = 500 ms; iris = 100% and mag = 60x), Polilight® (λ_{ex} = 350 nm; ISO = 100; f-stop = = f/2.8; exposure = 1/30 sec) and Labino® Lamp (λ_{ex} = 350 nm; ISO = 100; f-stop = = f/2.8; exposure = 1/30 sec).

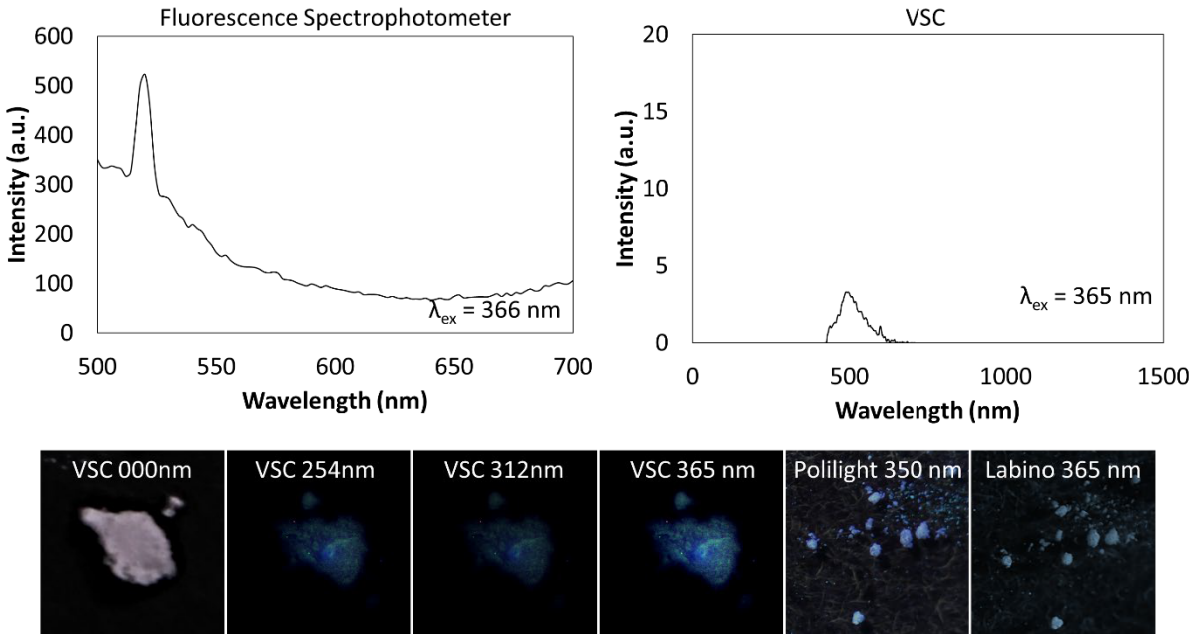

A2 - 45: Photoluminescence emission spectra of SH5-Gd captured from the spectrophotometer (left) and VSC (right). The inserts represent the pure MOF samples in the VSC (λ_{ex} = 365 nm; ISO = 100; integration time = 500 ms; iris = 100% and mag = 60x), Polilight® (λ_{ex} = 350 nm; ISO = 100; f-stop = = f/2.8; exposure = 1/30 sec) and Labino® Lamp (λ_{ex} = 350 nm; ISO = 100; f-stop = = f/2.8; exposure = 1/30 sec)

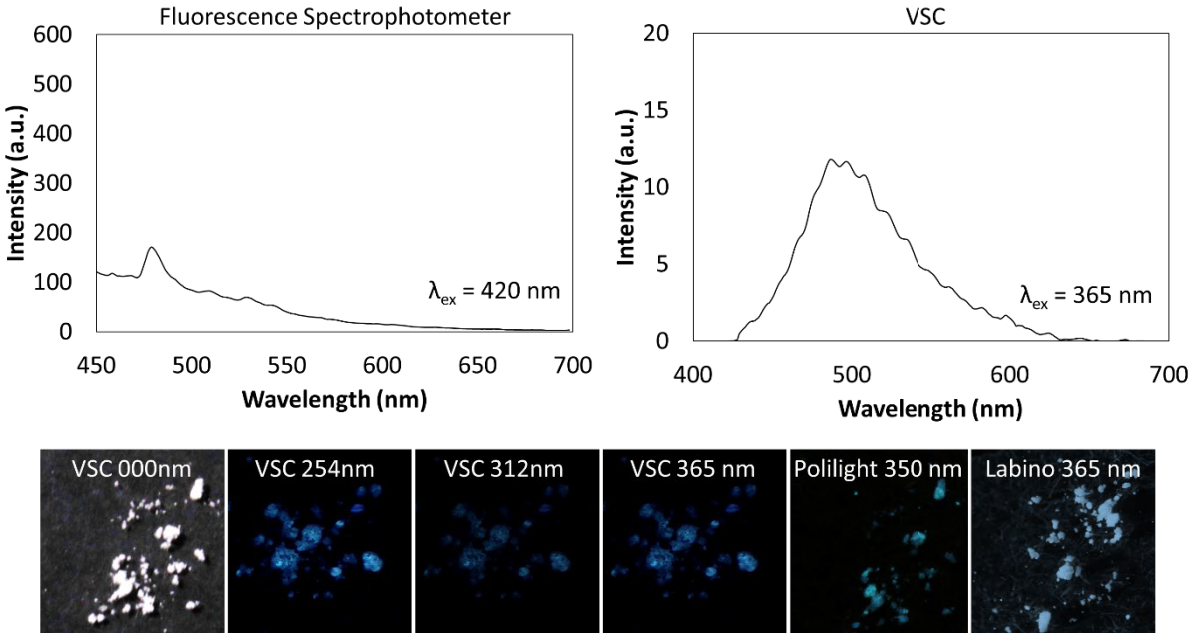

A2 - 46: Photoluminescence emission spectra of SH5-Y captured from the spectrophotometer (left) and VSC (right). The inserts represent the pure MOF samples in the VSC (λ_{ex} = 365 nm; ISO = 100; integration time = 500 ms; iris = 100% and mag = 60x), Polilight® (λ_{ex} = 350 nm; ISO = 100; f-stop = = f/2.8; exposure = 1/30 sec) and Labino® Lamp (λ_{ex} = 350 nm; ISO = 100; f-stop = = f/2.8; exposure = 1/30 sec).

SECTION III: Stability

5.1.7 FTIR Stability

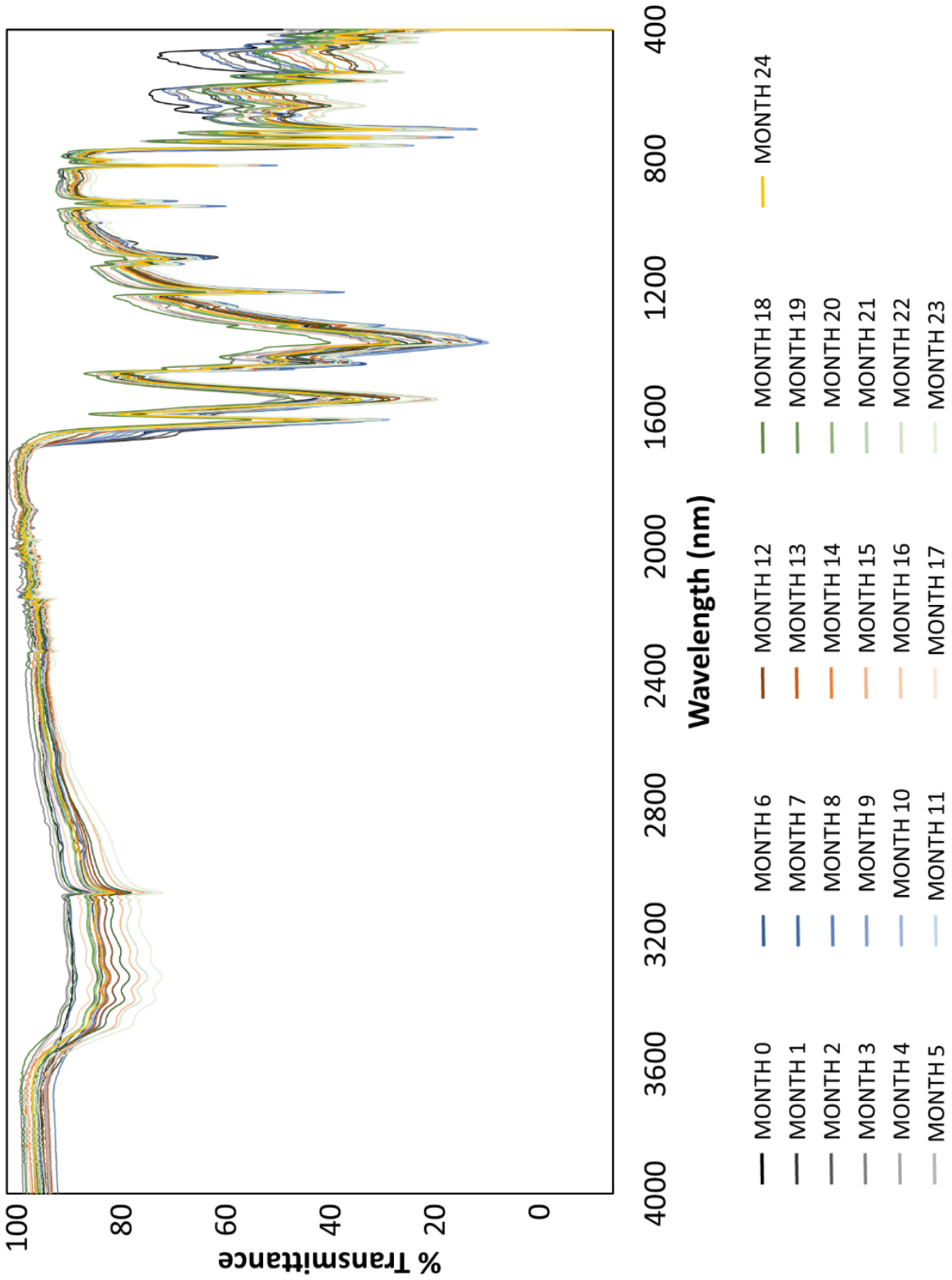

A2 - 47: Monthly FTIR spectrum for SH2-Tb.

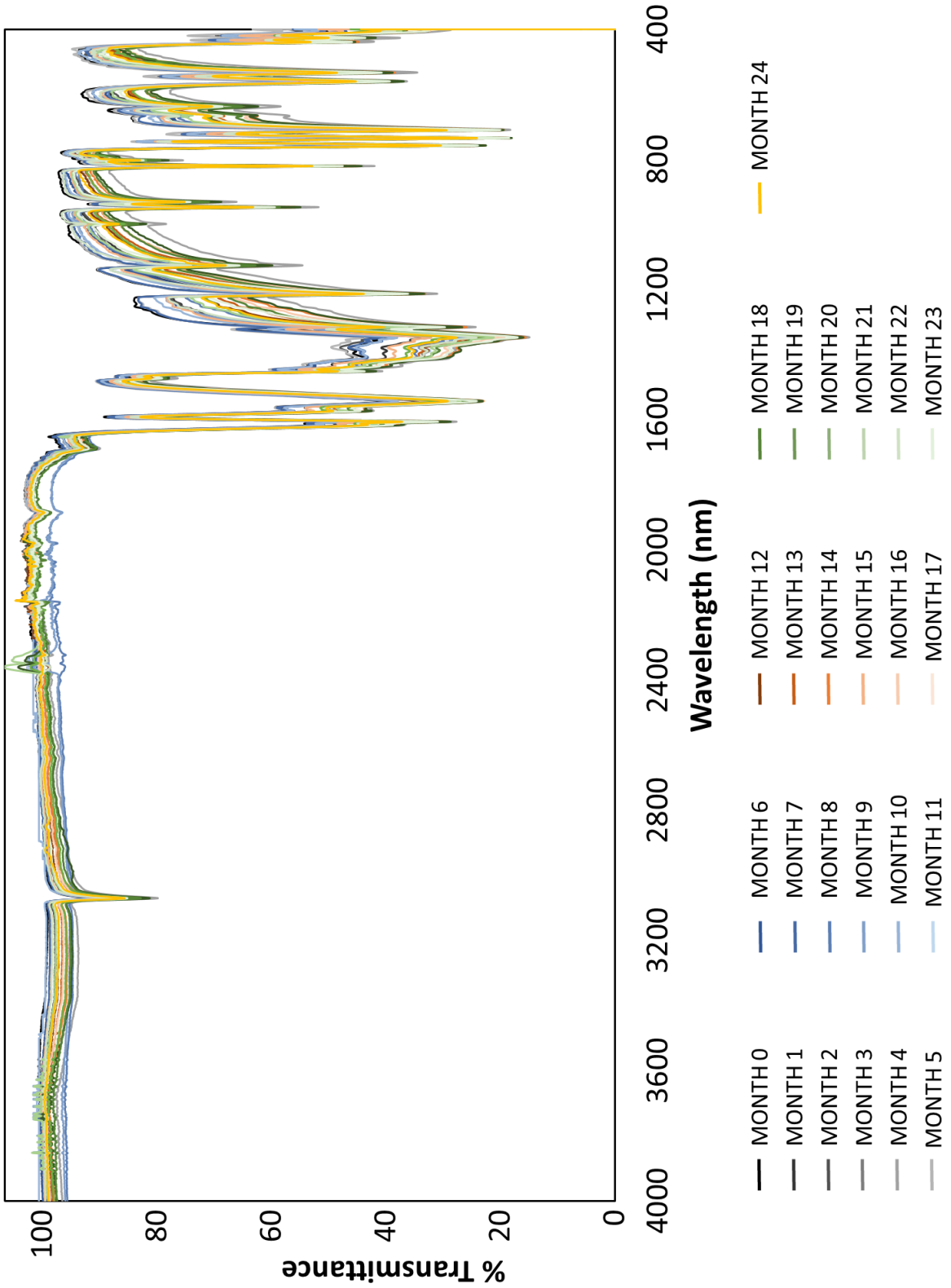

A2 - 48: Monthly FTIR spectrum for MW1-Tb.

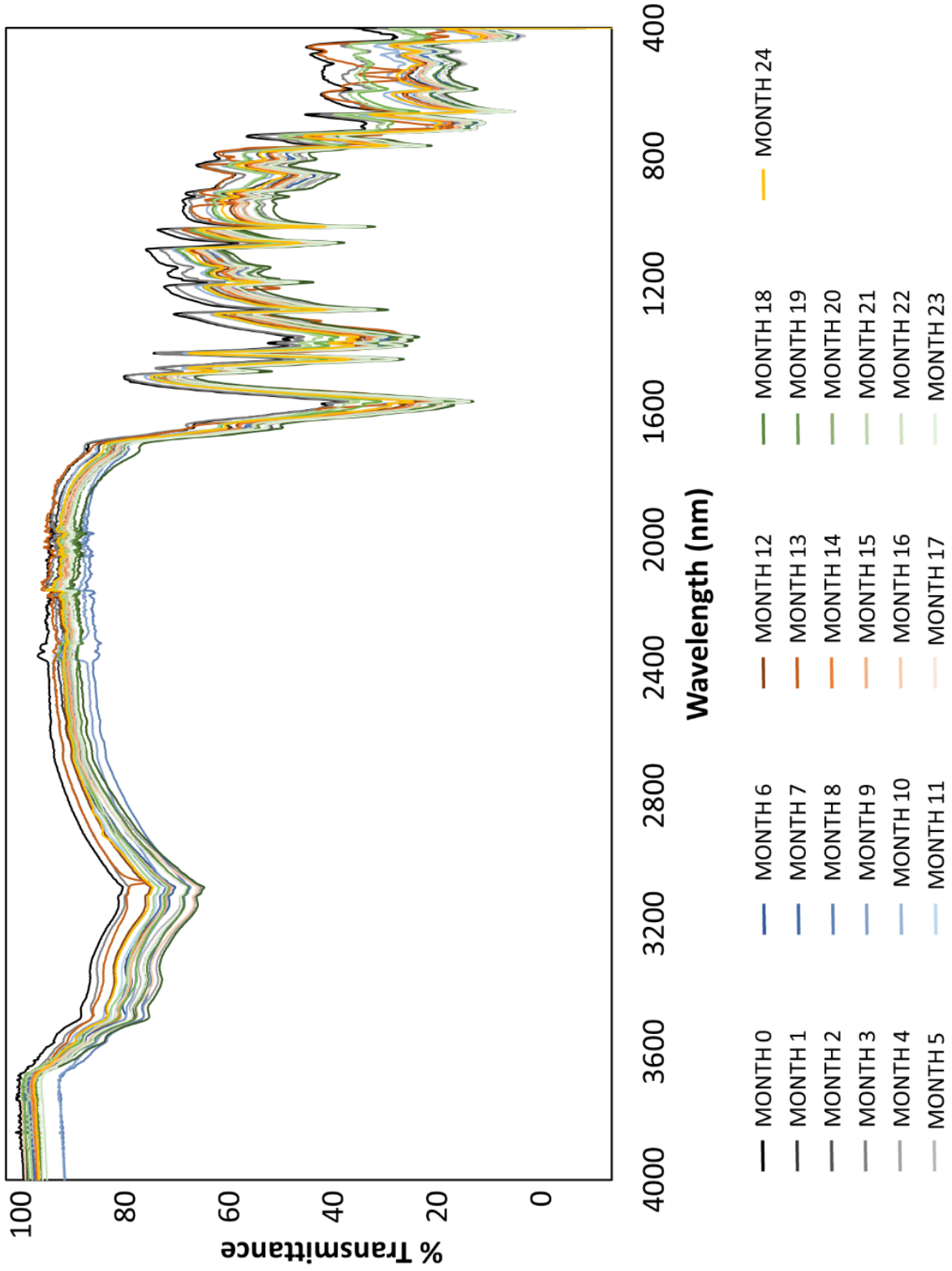

A2 - 49: Monthly FTIR spectrum for MW2-Tb.

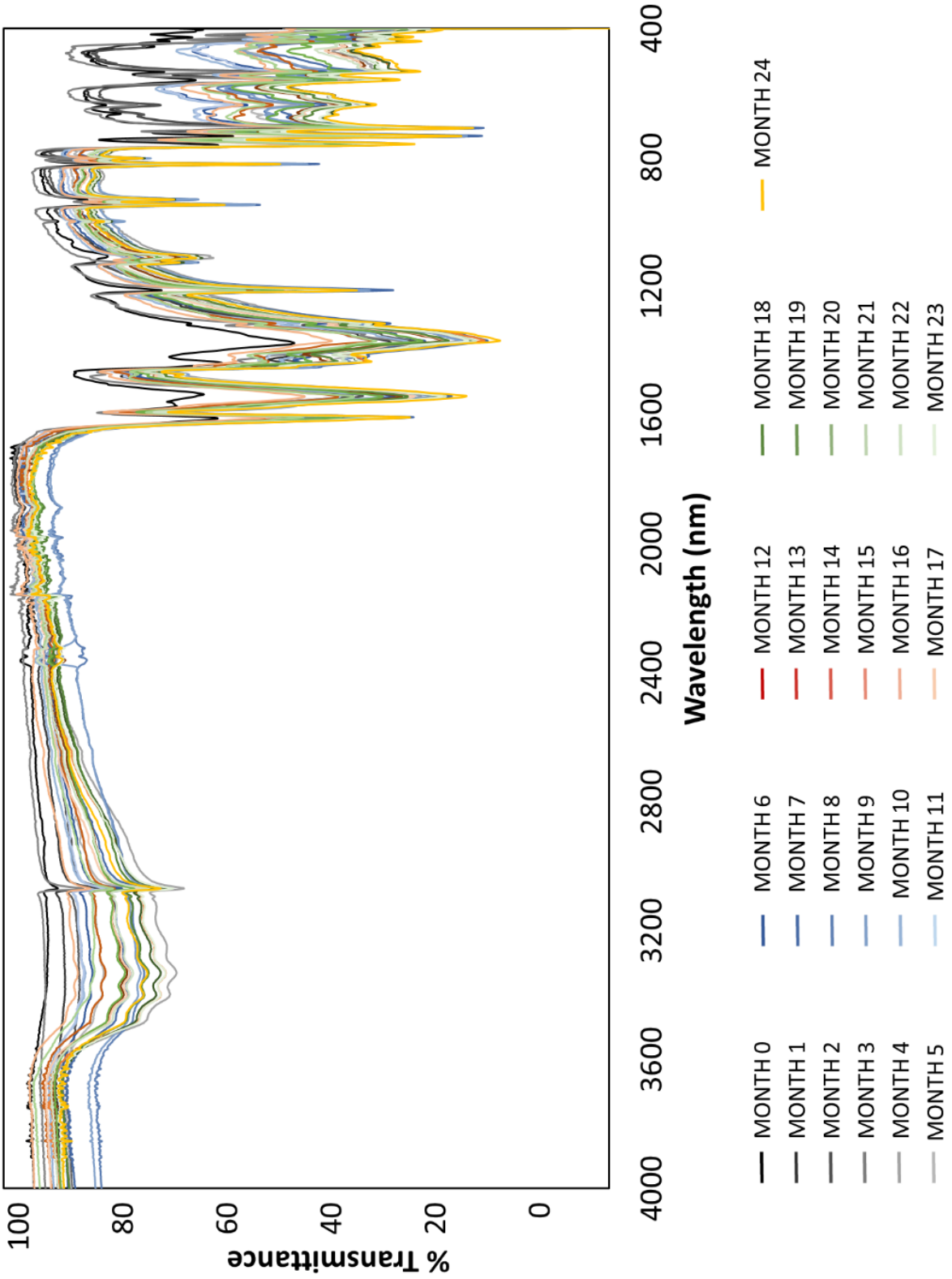

A2 - 50: Monthly FTIR spectrum for MW3-Tb.

5.1.8 Spectrophotometer Wavelength Optimisation

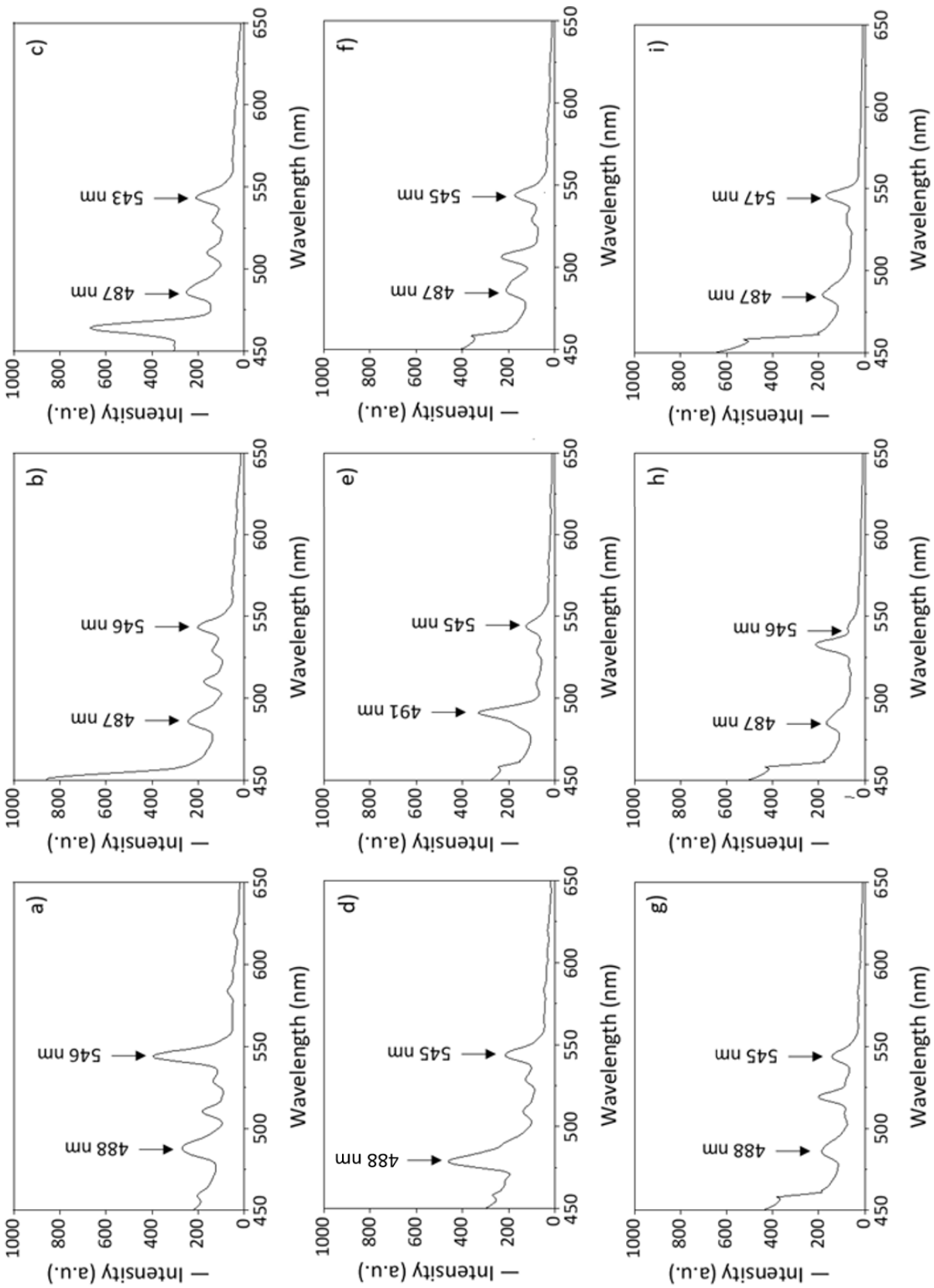

A2 - 51: Mapping of photoluminescence emissions of SH2-Tb. λ_{ex} = a) 320 nm; b) 330 nm; c) 340 nm; d) 350 nm; e) 360 nm; f) 370 nm; g)380 nm; h) 390 nm and i) 400 nm.

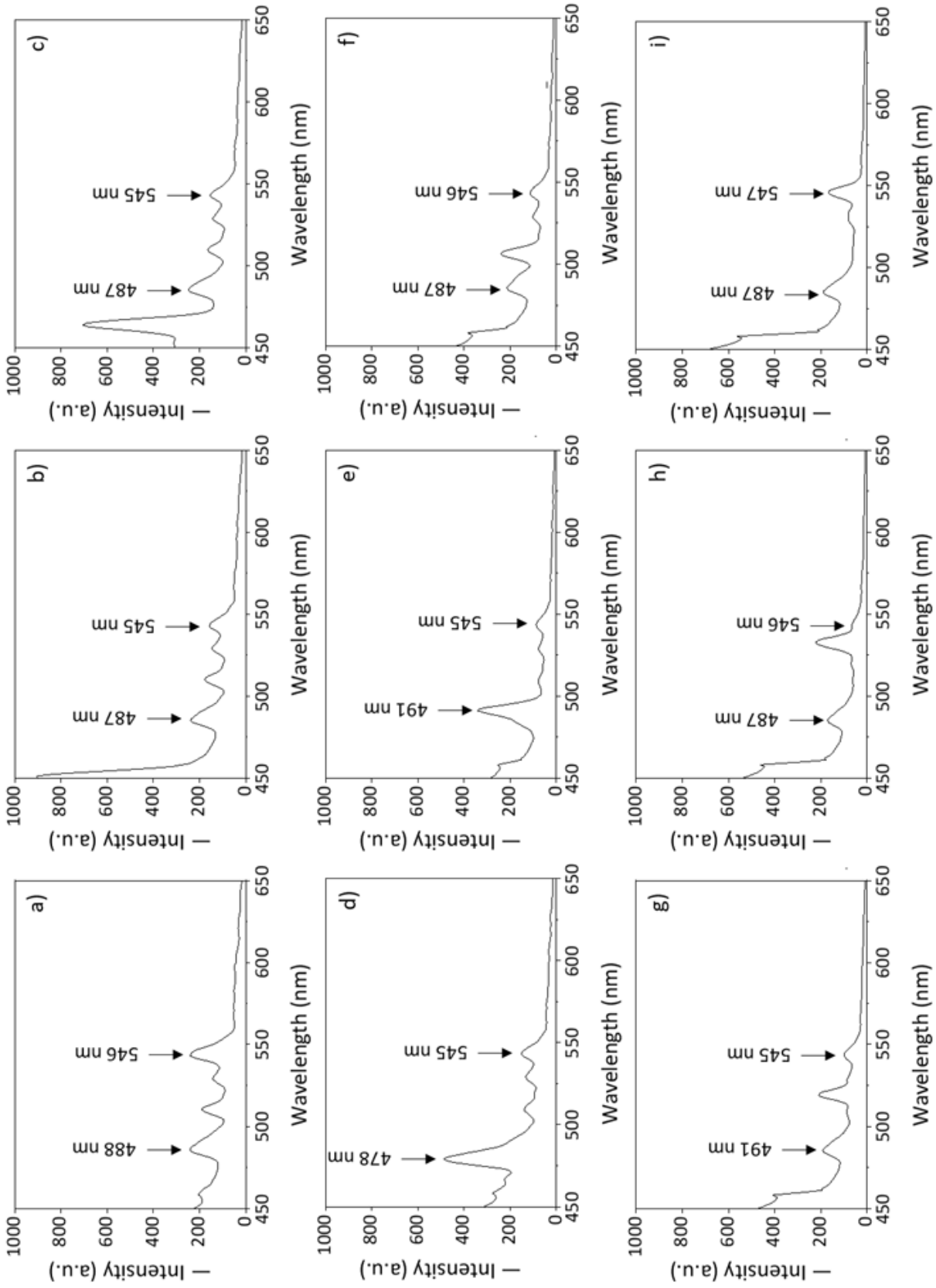

A2 - 52: Mapping of photoluminescence emissions of MW1-Tb. λ_{ex} = a) 320 nm; b) 330 nm; c) 340 nm; d) 350 nm; e) 360 nm; f) 370 nm; g)380 nm; h) 390 nm and i) 400 nm.

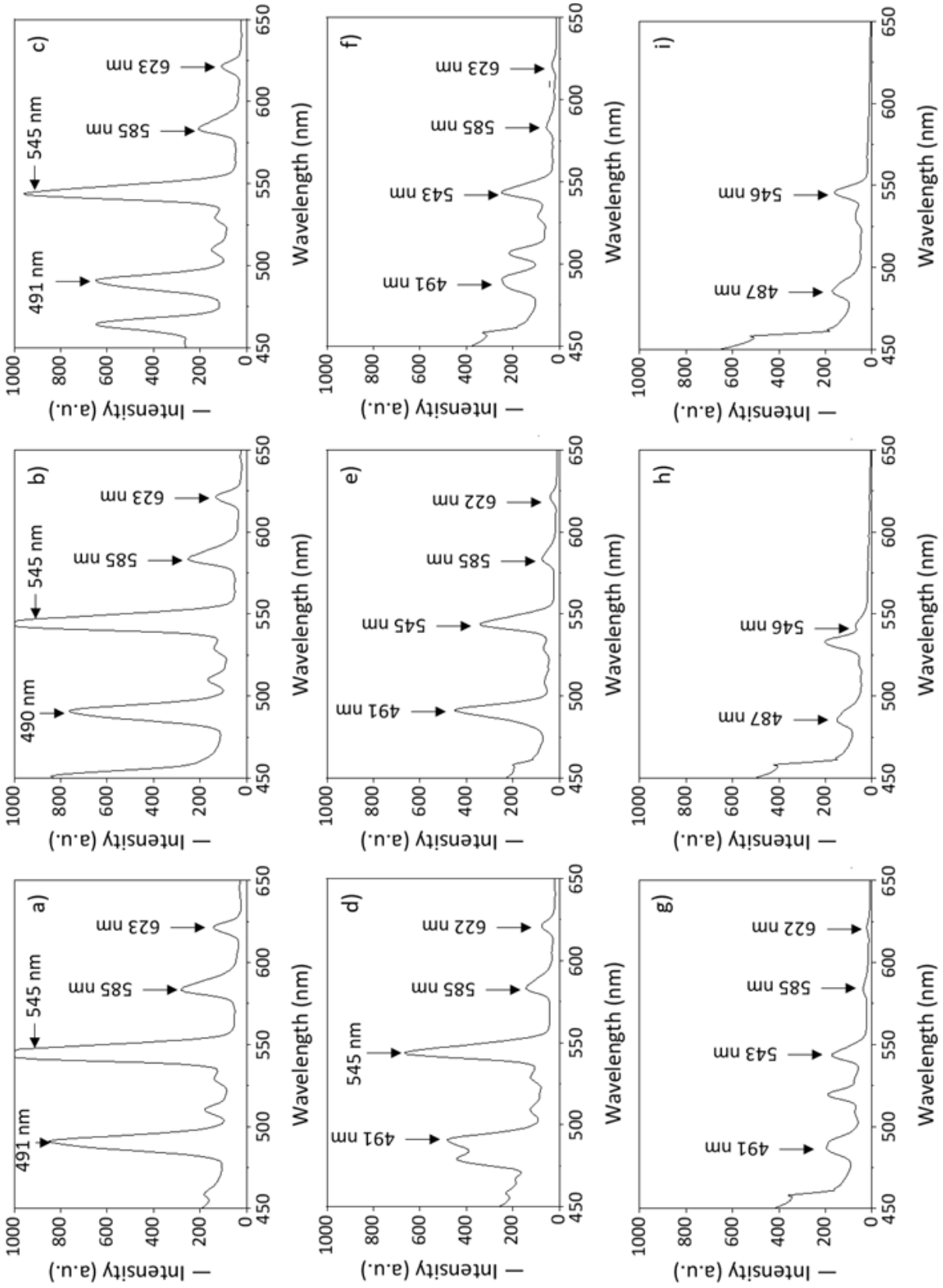

A2 - 53: Mapping of photoluminescence emissions for MW2-Tb. λ_{ex} = a) 320 nm; b) 330 nm; c) 340 nm; d) 350 nm; e) 360 nm; f) 370 nm; g)380 nm; h) 390 nm and i) 400 nm.

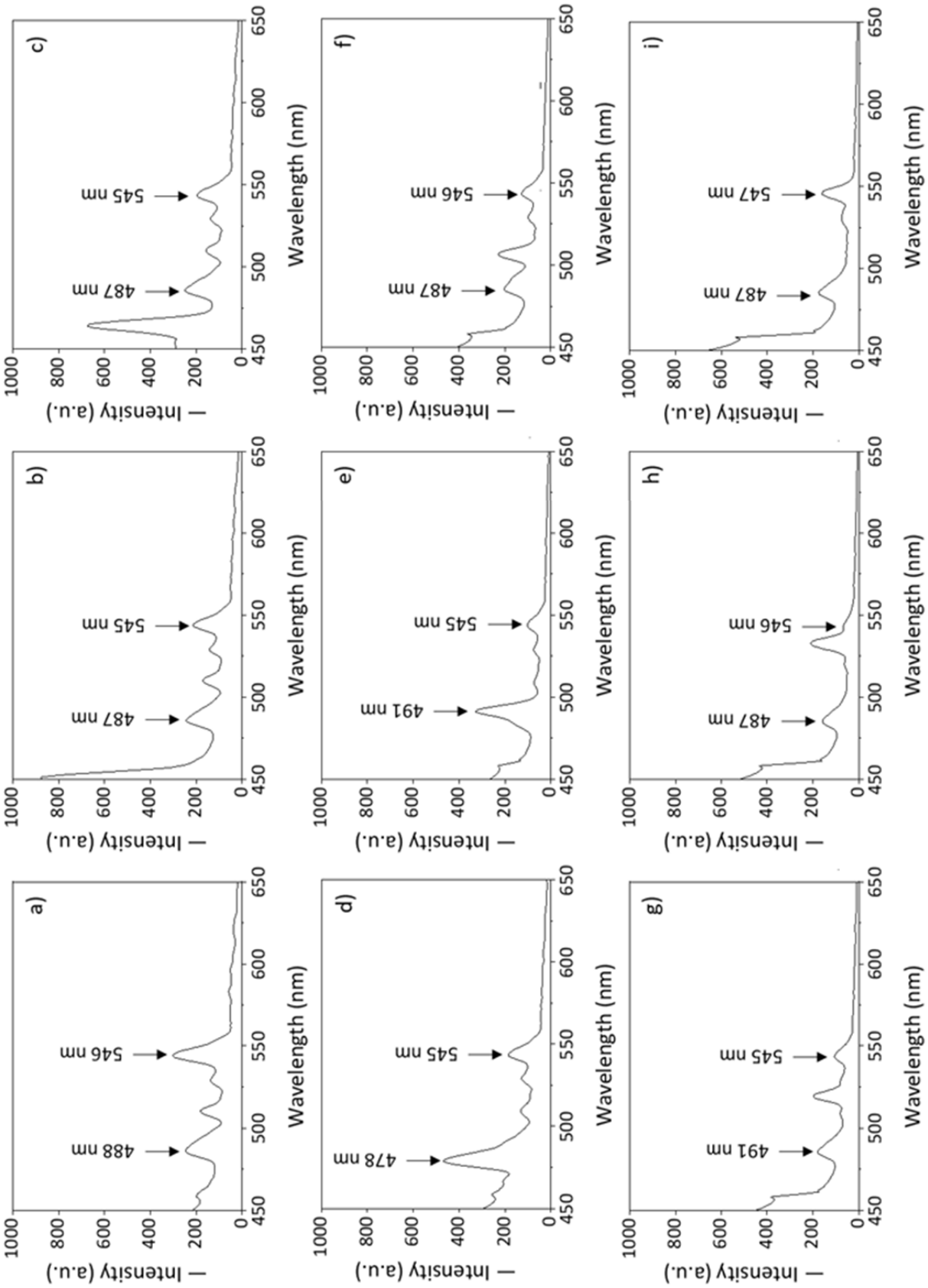

A2 - 54: Mapping of photoluminescence emissions for MW3-Tb. λ_{ex} = a) 320 nm; b) 330 nm; c) 340 nm; d) 350 nm; e) 360 nm; f) 370 nm; g)380 nm; h) 390 nm and i) 400 nm.

5.1.9 Fluorescence Stability

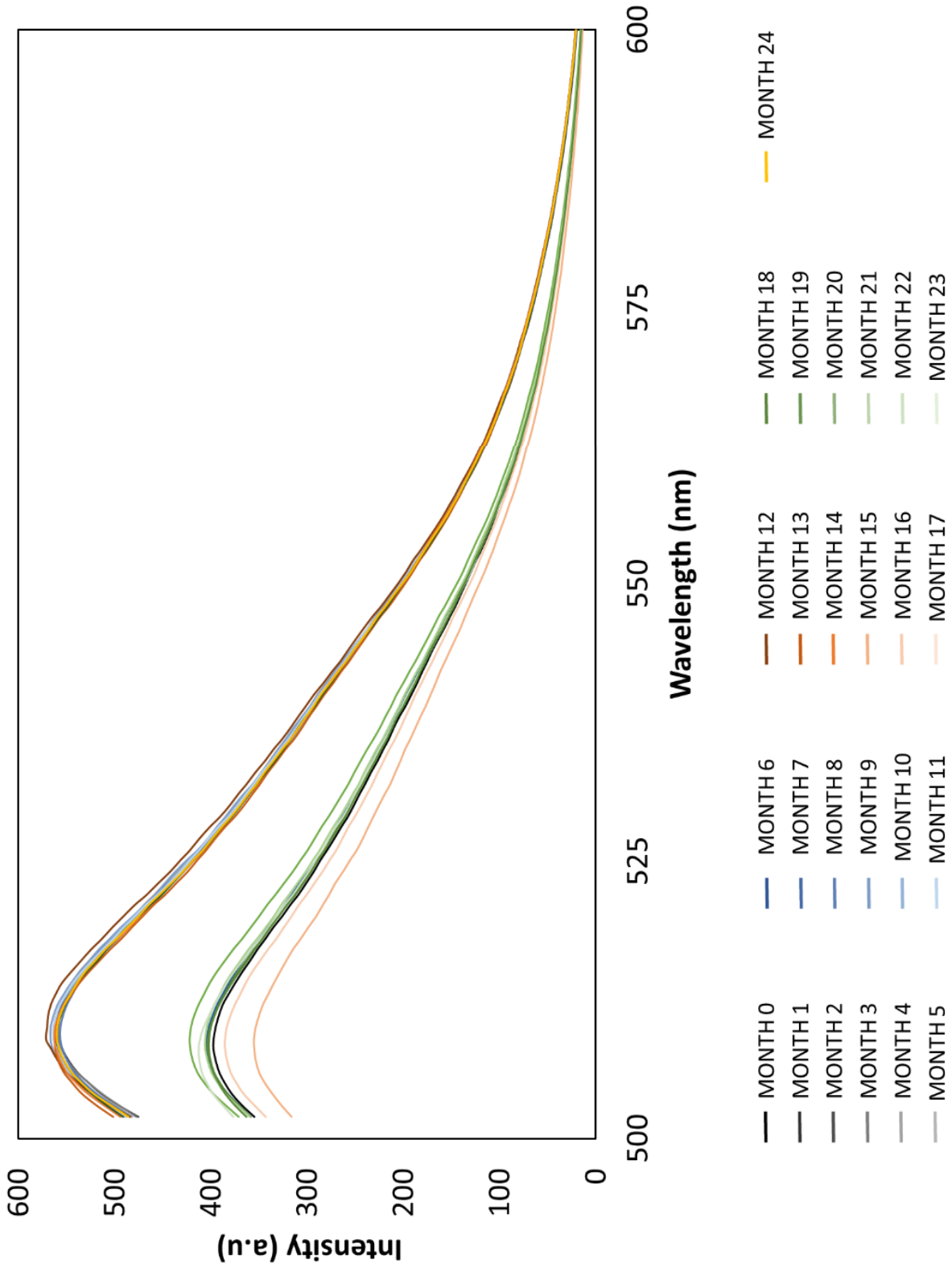

A2 - 55: Monthly photoluminescence emissions of Sirchie GREENCHARGETM Fluoro-Magnetic Print Powder for SH2-Tb.

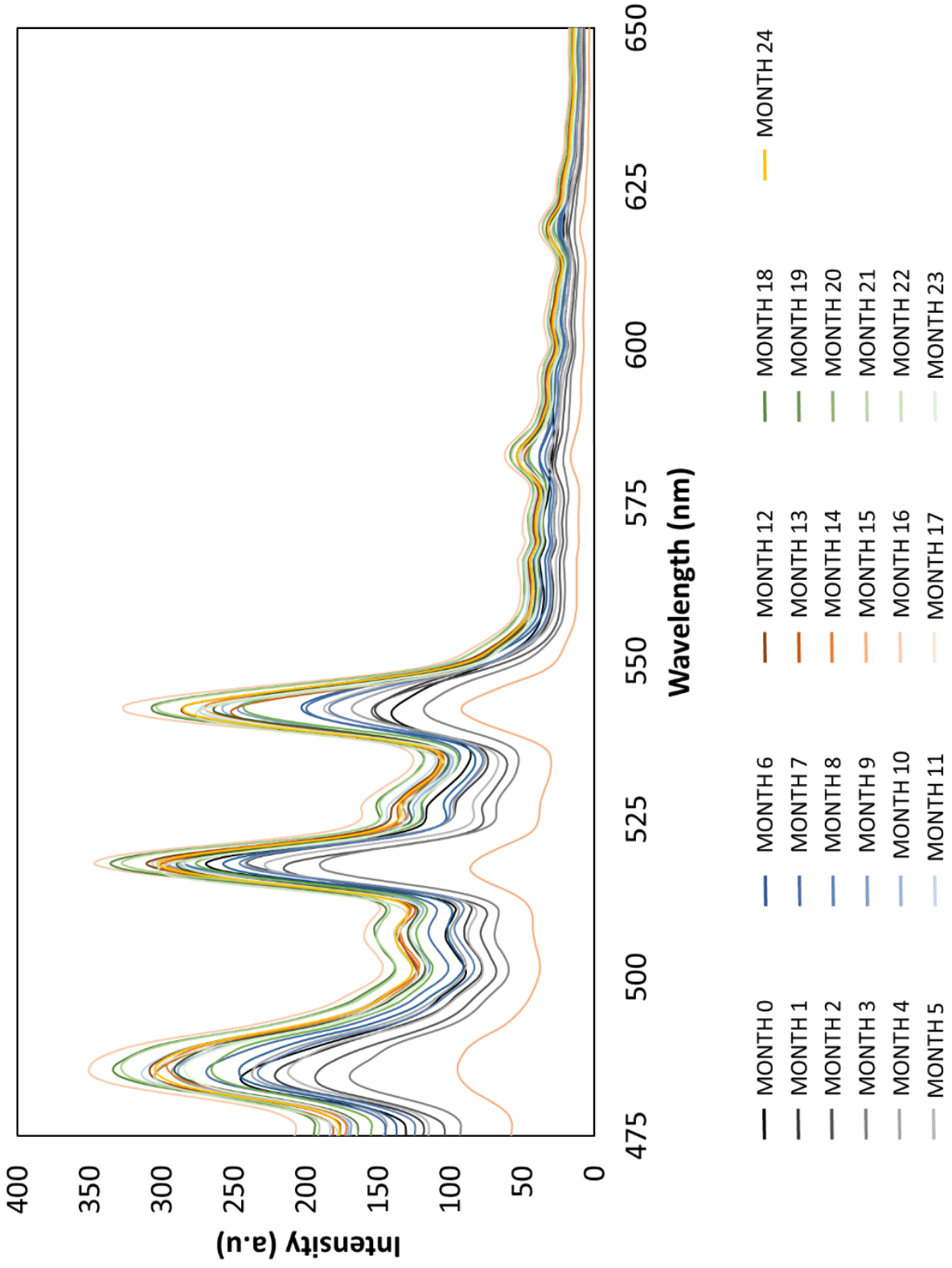

A2 - 56: Monthly photoluminescence emissions of SH2-Tb.

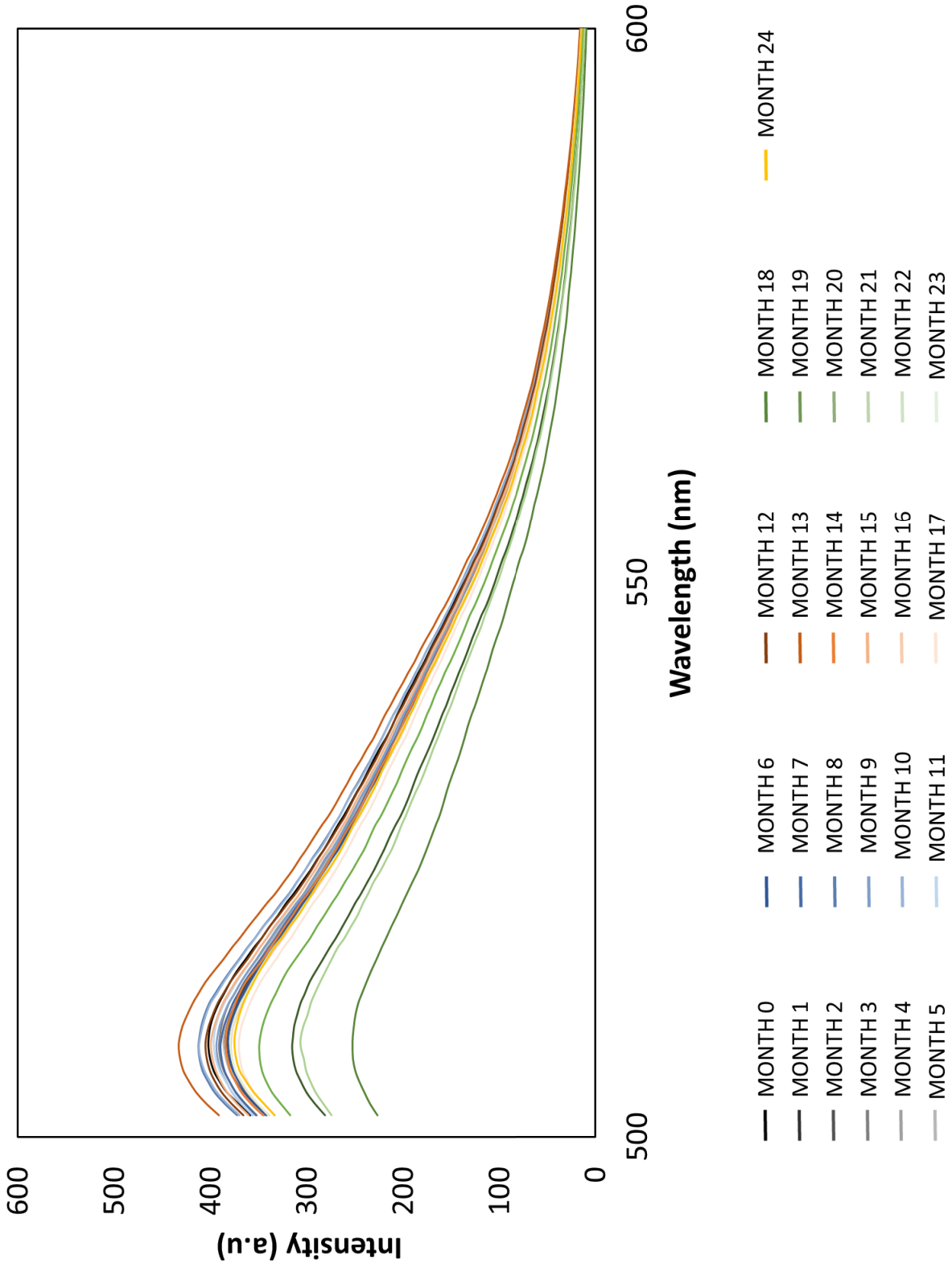

A2 - 57: Monthly photoluminescence emissions of Sirchie GREENCHARGETM Fluoro-Magnetic Print Powder for MW-Tb MOFs.

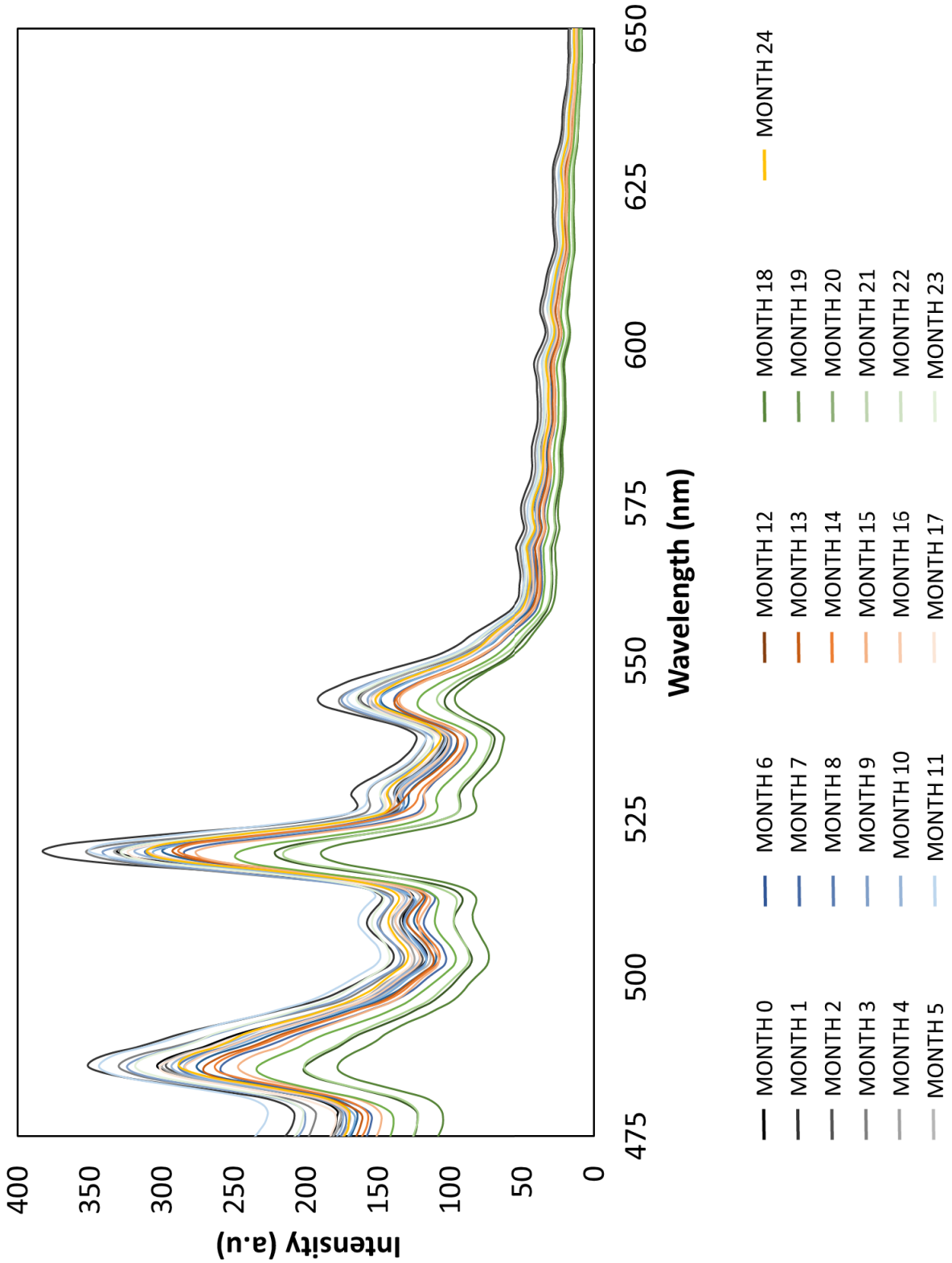

A2 - 58: Monthly photoluminescence emissions of MW1-Tb.

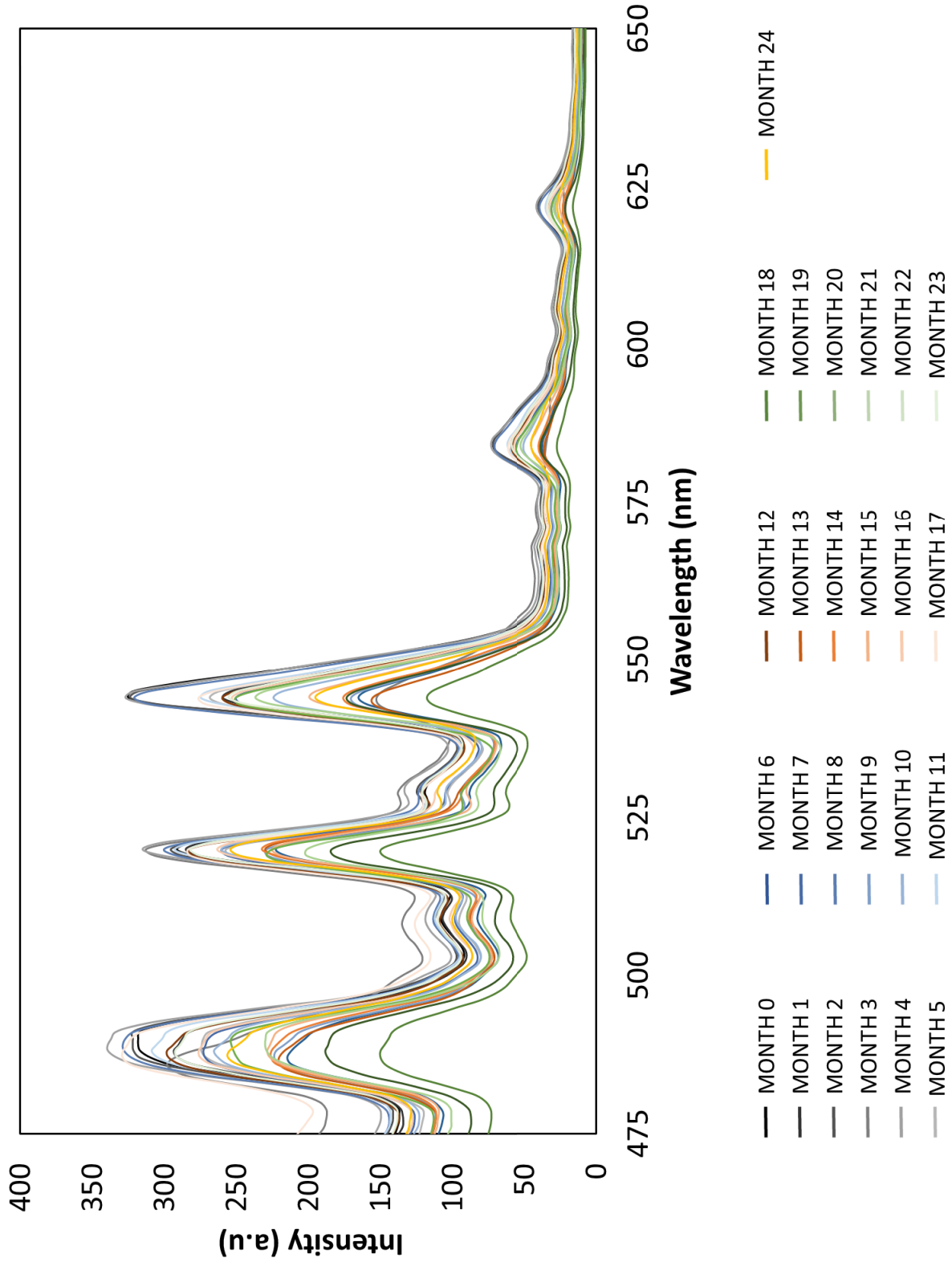

A2 - 59: Monthly photoluminescence emissions of MW2-Tb.

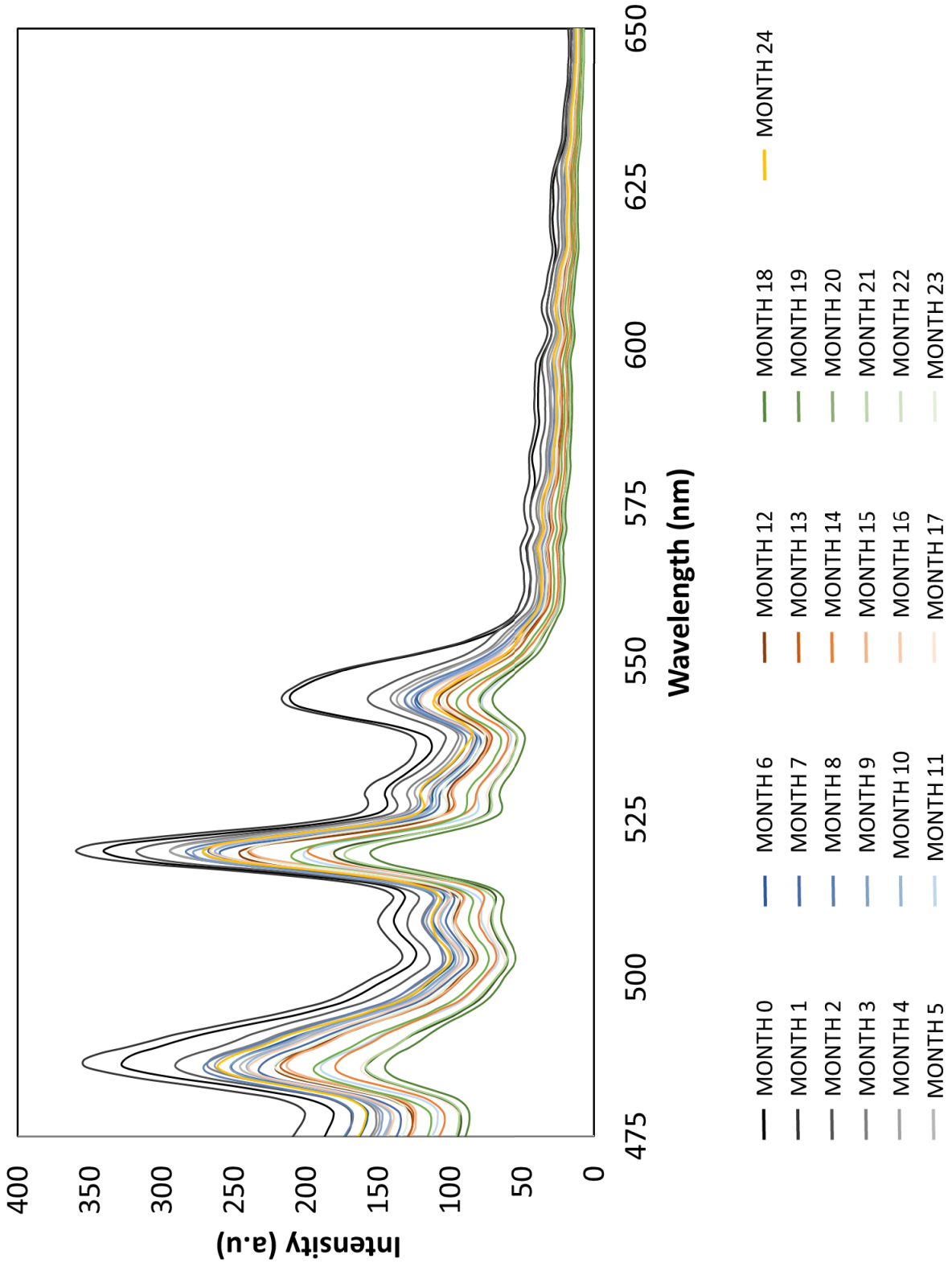

A2 - 60: Monthly photoluminescence emissions of MW3-Tb.

5.1.10 VSC Stability

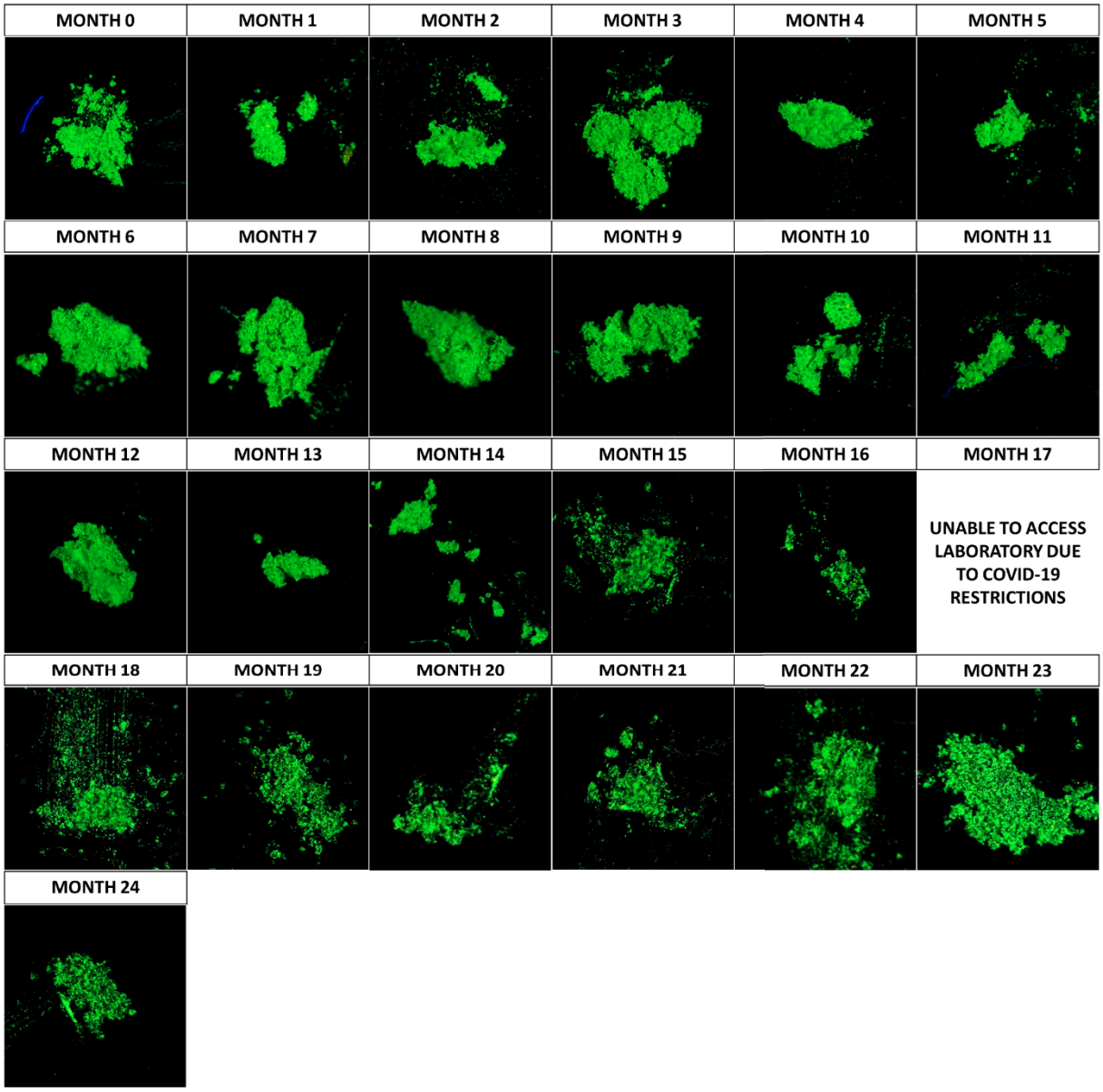

A2 - 61: Monthly visual luminescence of Sirchie GREENCHARGETM Fluoro-Magnetic Print Powder for SH2-Tb in the VSC (λ_{ex} = 365 nm; ISO = 100; integration time = 500 ms; iris = 100% and mag = 60x).

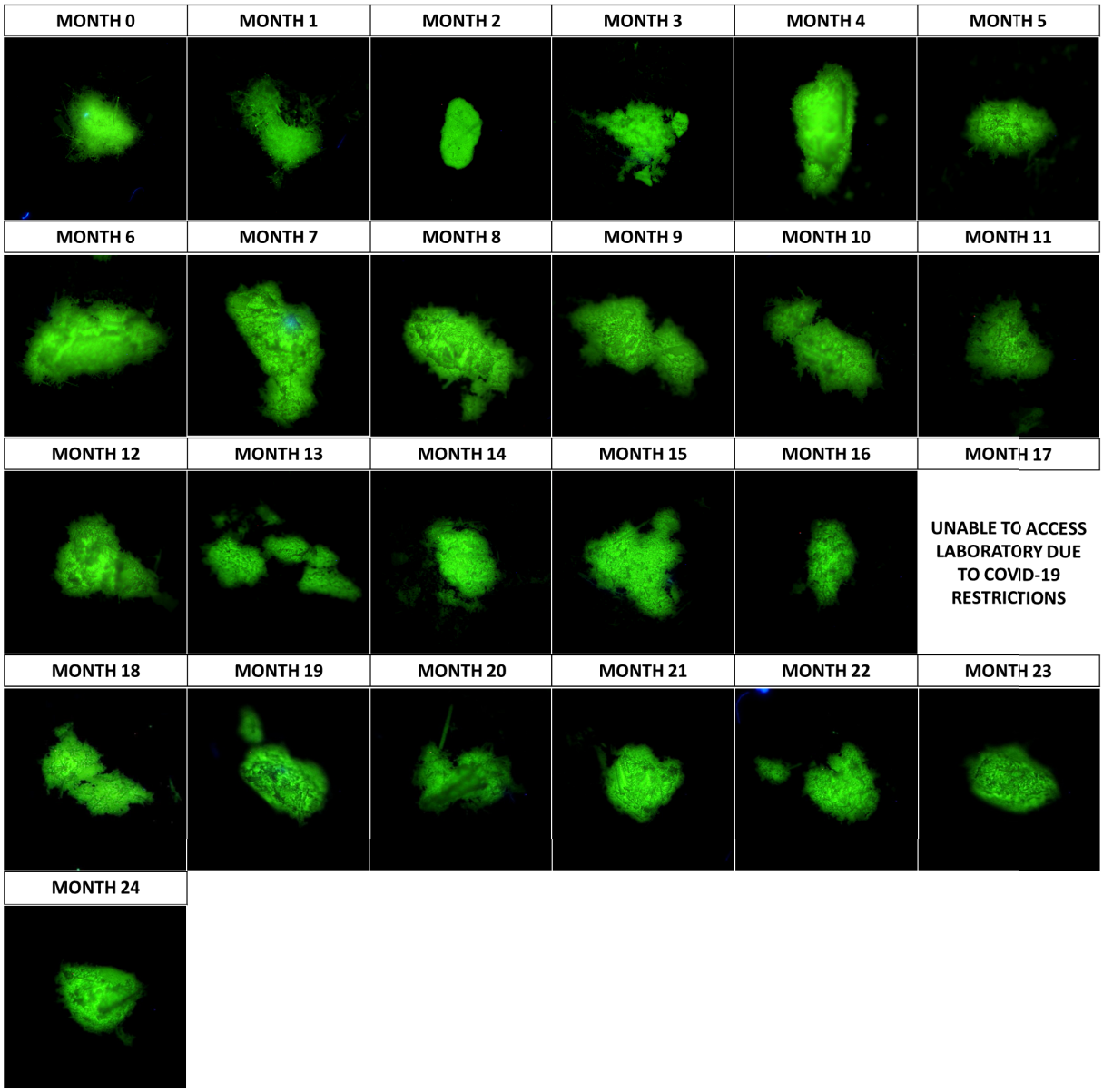

A2 - 62: Monthly visual luminescence of SH2-Tb in the VSC (λ_{ex} = 365 nm; ISO = 100; integration time = 500 ms; iris = 100% and mag = 60x).

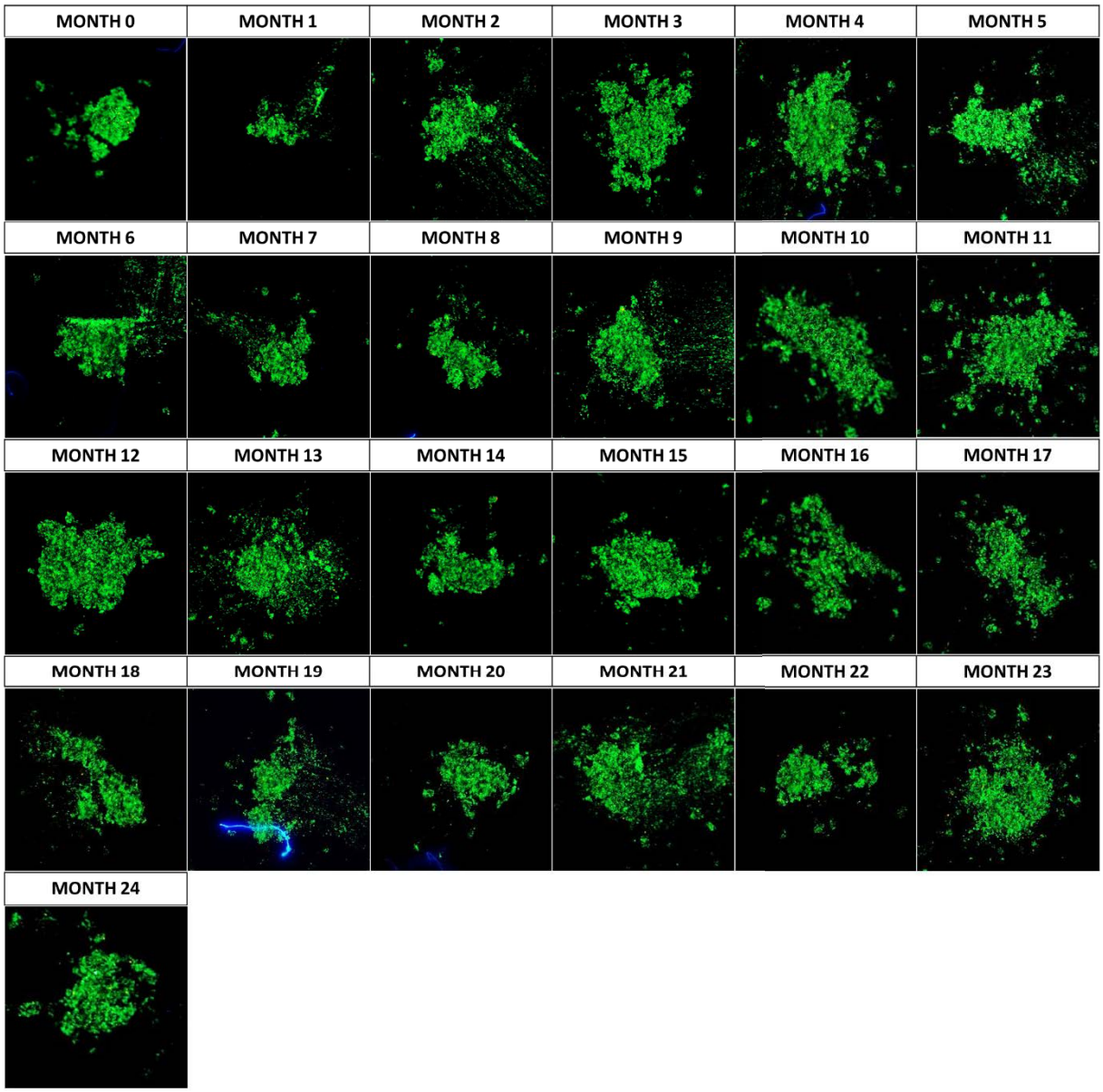

A2 - 63: Monthly visual luminescence of Sirchie GREENCHARGETM Fluoro-Magnetic Print Powder for MW-Tb MOFs in the VSC (λ_{ex} = 365 nm; ISO = 100; integration time = 500 ms; iris = 100% and mag = 60x).

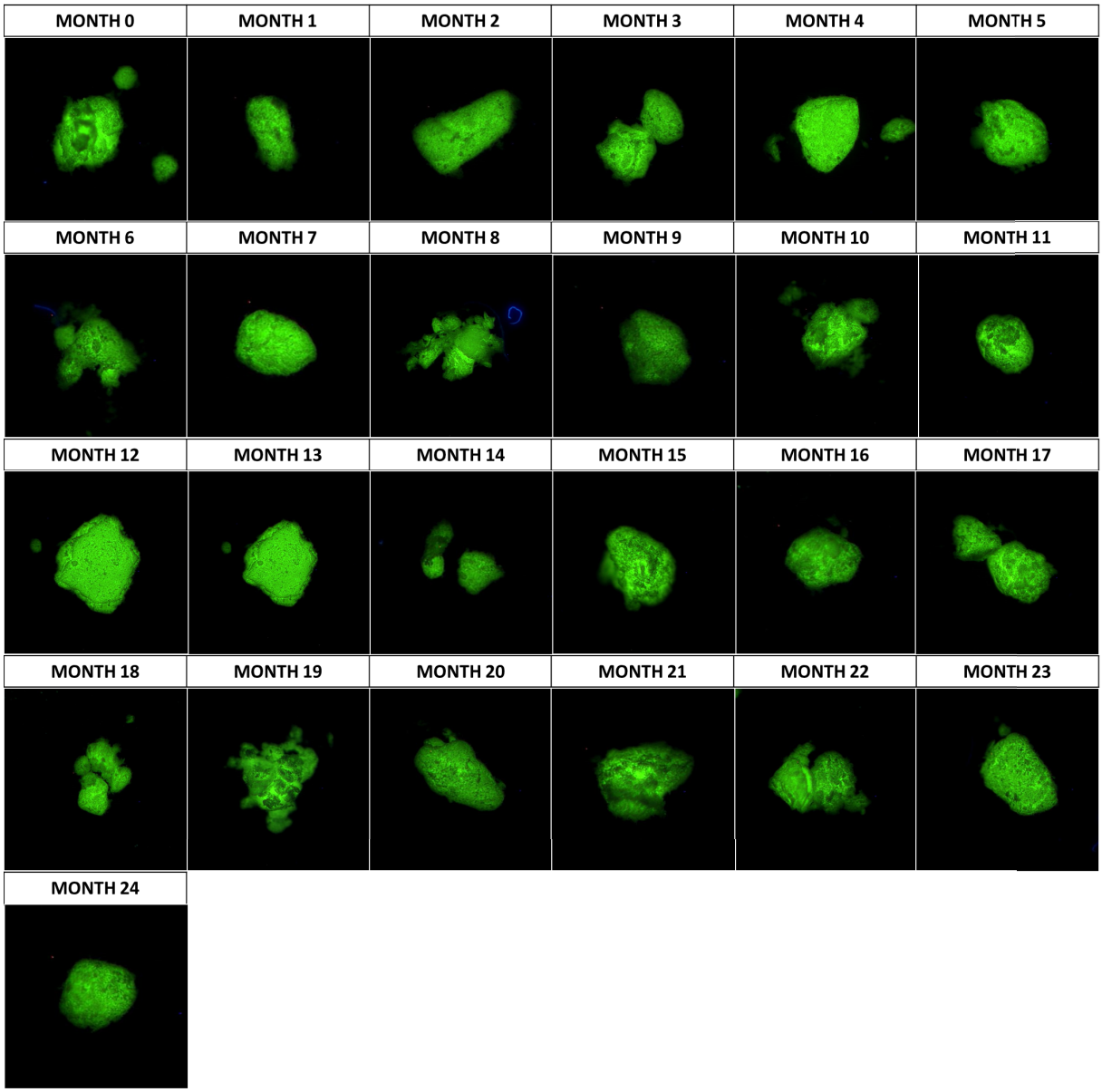

A2 - 64: Monthly visual luminescence of MW1-Tb in the VSC (λ_{ex} = 365 nm; ISO = 100; integration time = 500 ms; iris = 100% and mag = 60x).

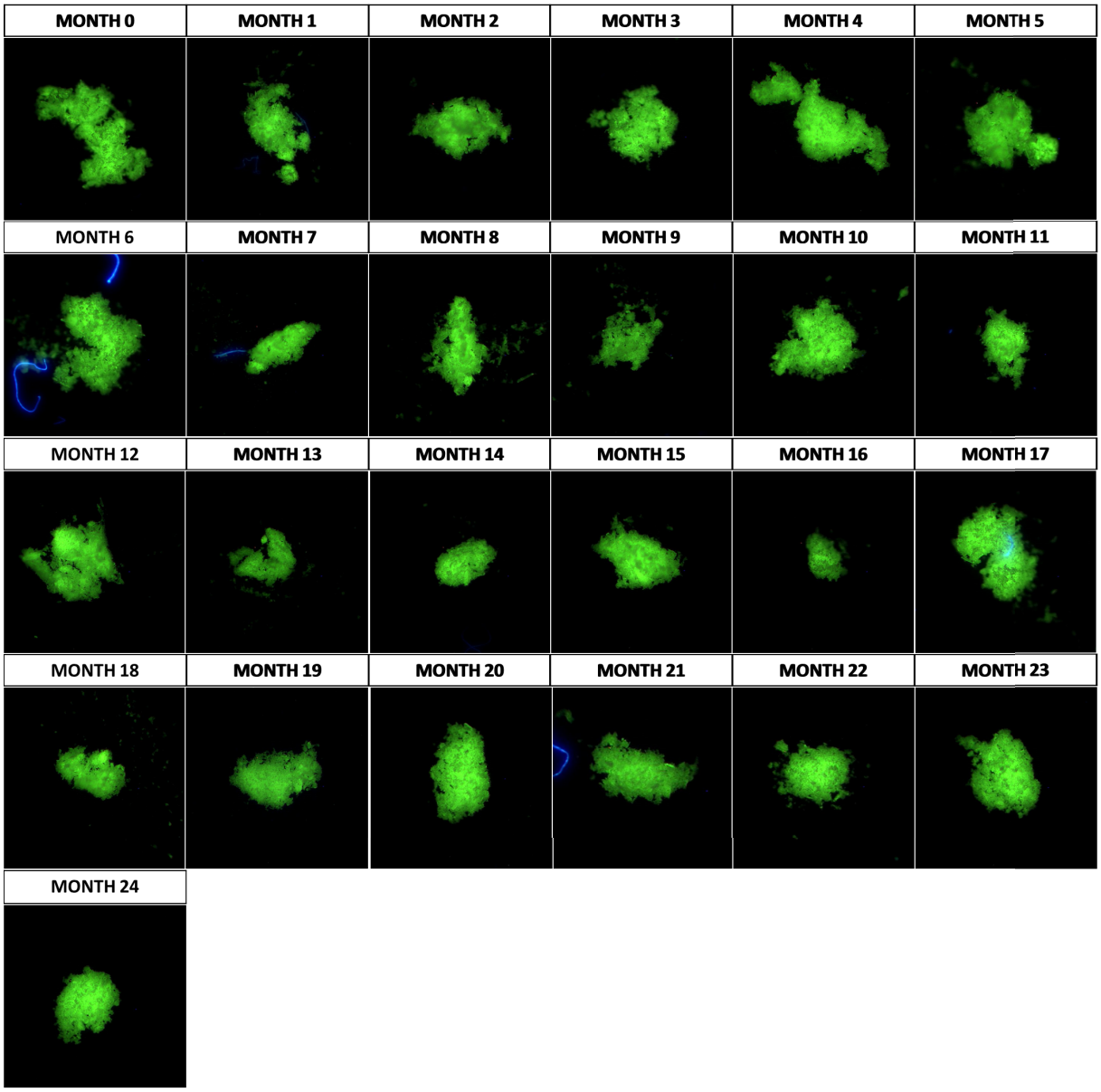

A2 - 65: Monthly visual luminescence of MW2-Tb in the VSC (λ_{ex} = 365 nm; ISO = 100; integration time = 500 ms; iris = 100% and mag = 60x).

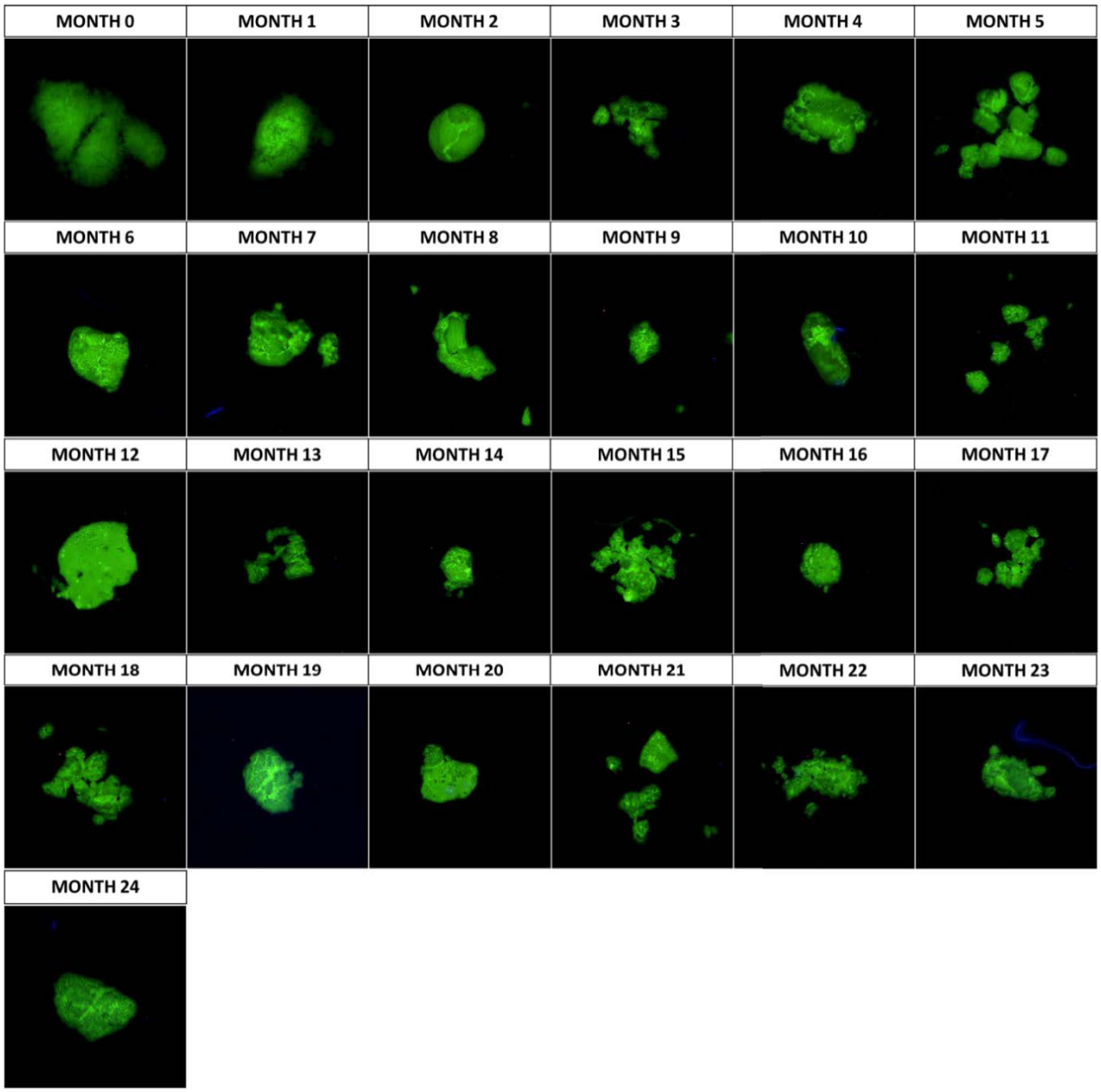

A2 - 66: Monthly visual luminescence of MW3-Tb in the VSC (λ_{ex} = 365 nm; ISO = 100; integration time = 500 ms; iris = 100% and mag = 60x).

Appendix 3: Chapter 3

5.1.11 Firearm

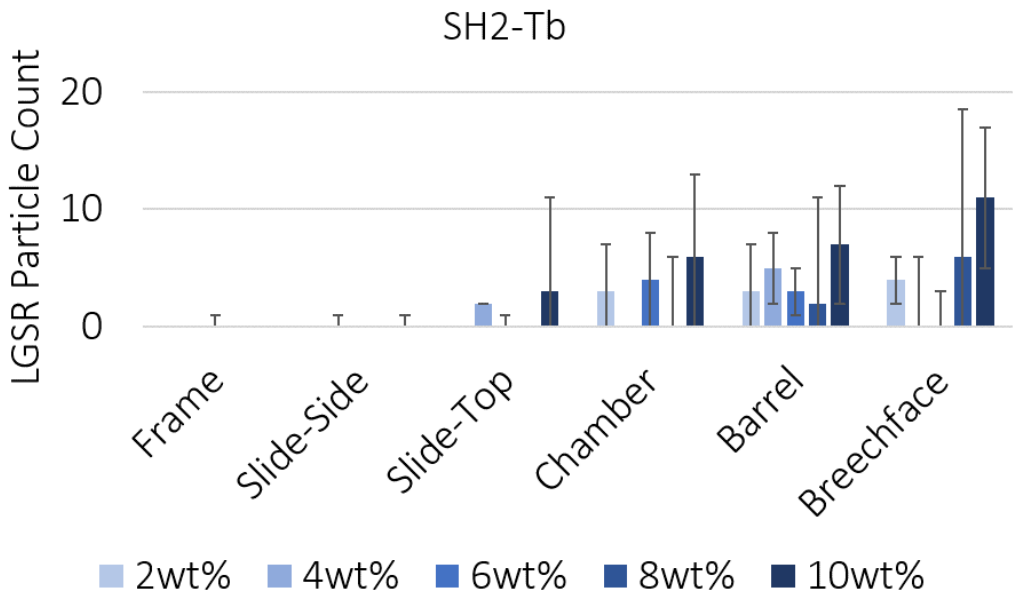

A3 - 1: Median representation of SH2-Tb LGSR particle count within different locations on the firearm at all incorporation ratios. Error bars are represented by the interquartile range error (n=5).

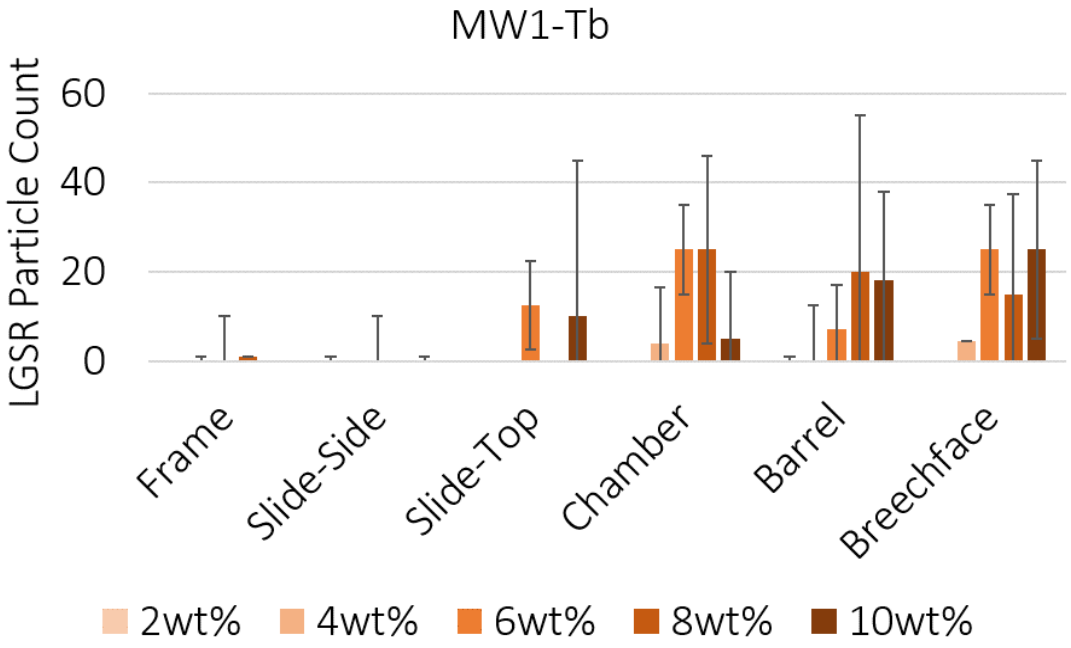

A3 - 2: Median representation of MW1-Tb LGSR particle count within different locations on the firearm at all incorporation ratios. Error bars are represented by the interquartile range error (n=5).

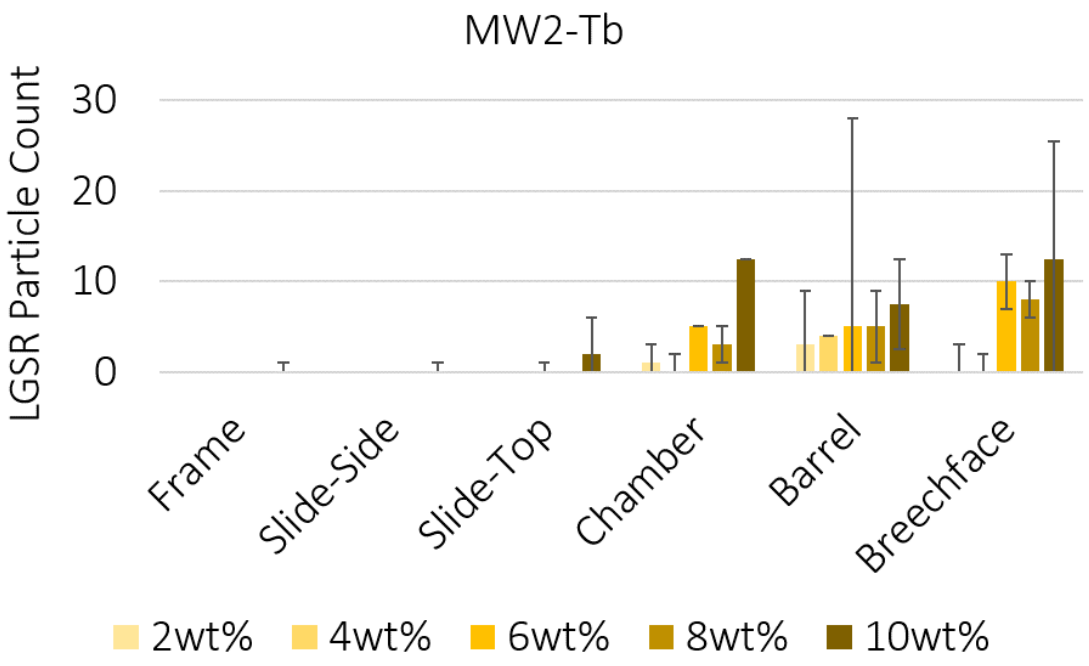

A3 - 3: Median representation of MW2-Tb LGSR particle count within different locations on the firearm at all incorporation ratios. Error bars are represented by the interquartile range error (n=5).

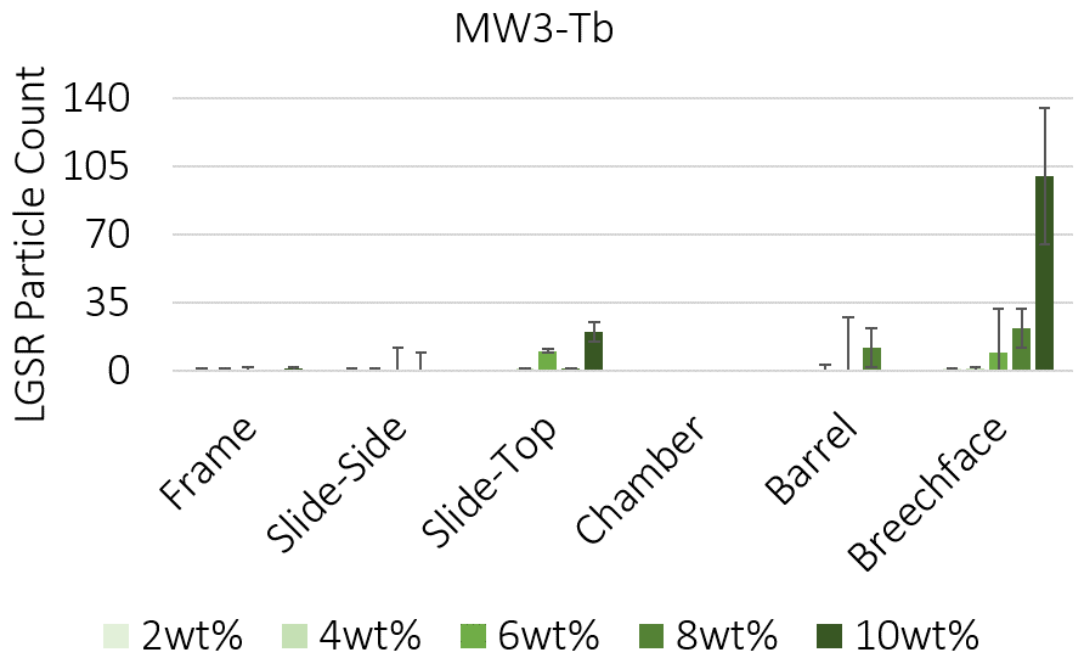

A3 - 4: Median representation of MW3-Tb LGSR particle count within different locations on the firearm at all incorporation ratios. Error bars are represented by the interquartile range error (n=5).

5.1.12 FCC

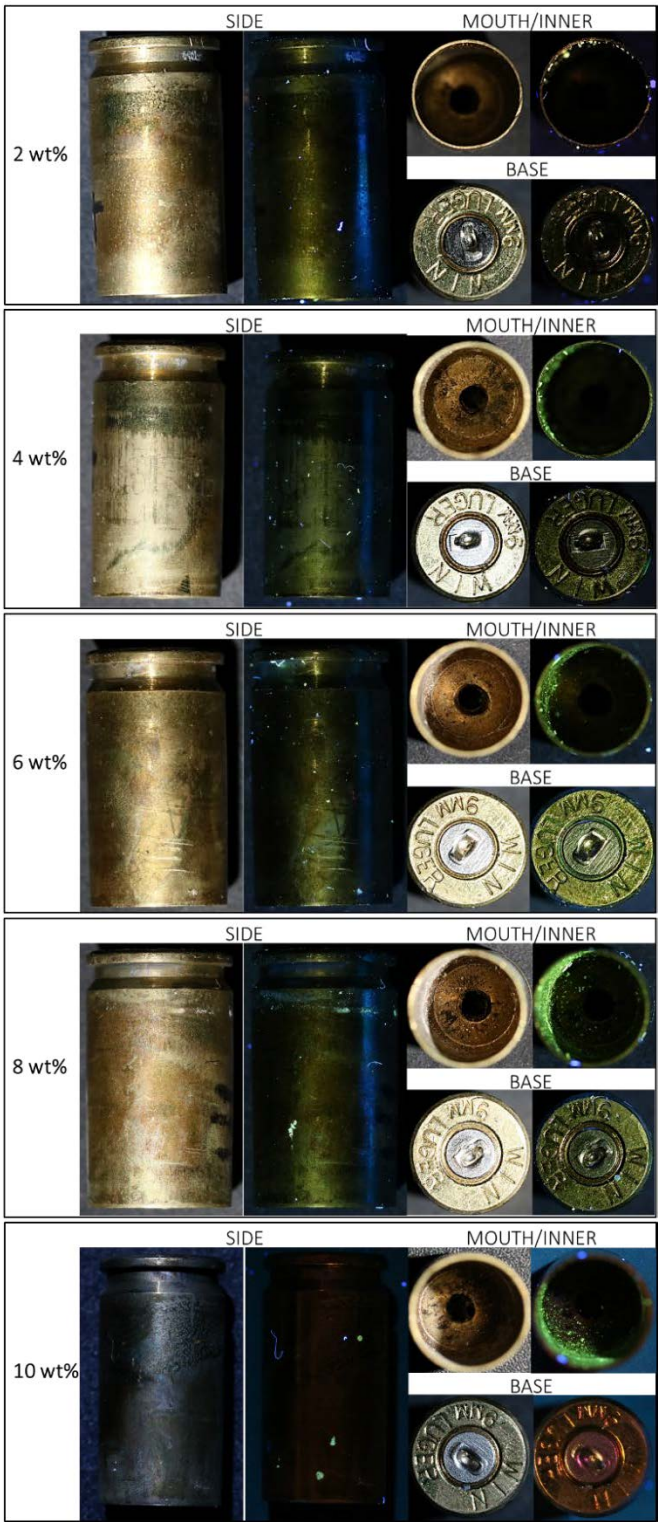

A3 - 5: Effect of ratio incorporated into ammunition on LGSR distribution on FCC. Images of the side, mouth and base of SH2-Tb FCC illuminated using white light (left) and the Labino® flood lamp (λex = 365 nm, right) using a Canon EOS 700D (ISO = 1600; f-stop = = f/2.8; exposure = 1/30 sec.). Note:// Images of SH2-Tb-10 wt% were captured with the same camera and light source settings, but on different days.

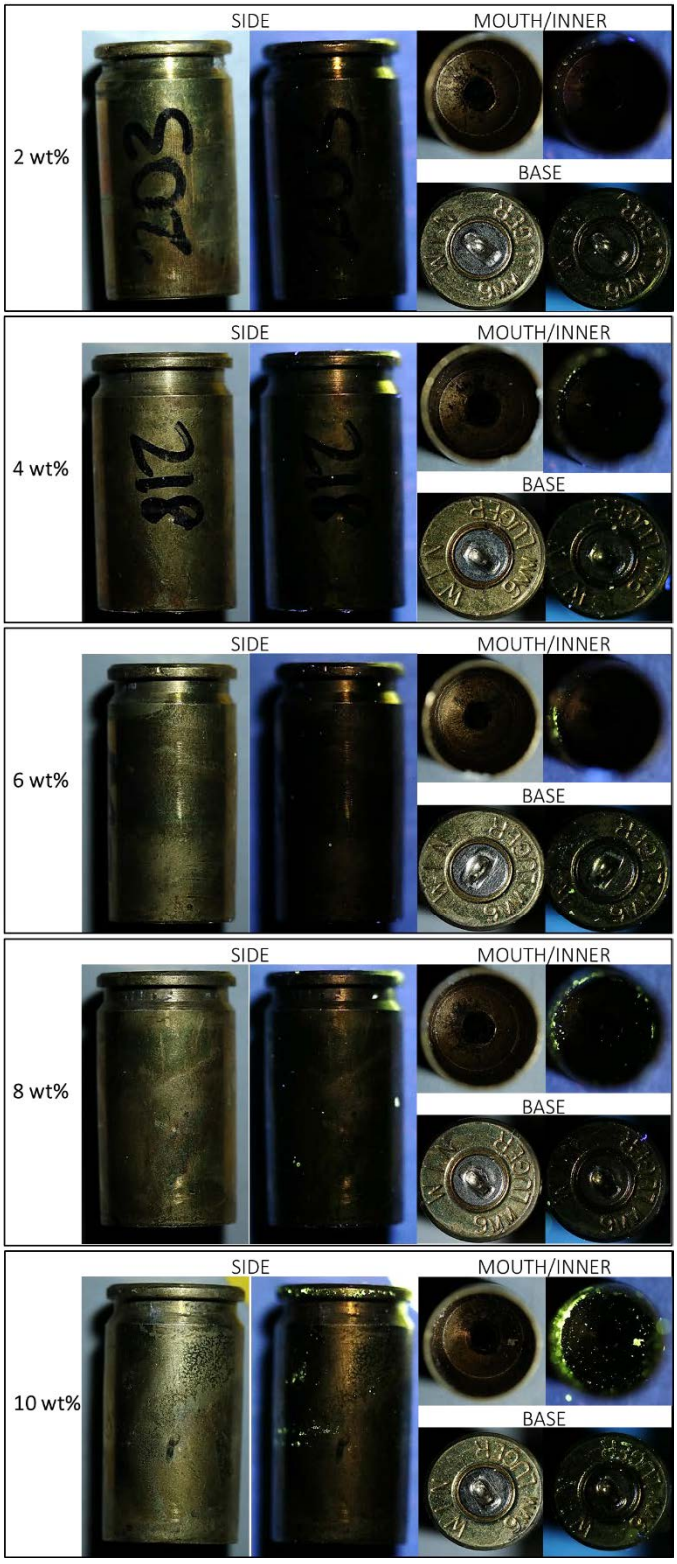

A3 - 6: Effect of ratio incorporated into ammunition on LGSR distribution on FCC. Images of the side, mouth and base of MW2-Tb FCC illuminated using white light (left) and the Labino® flood lamp (λex = 365 nm, right) using a Canon EOS 700D (ISO = 1600; f-stop = = f/2.8; exposure = 1/30 sec.).

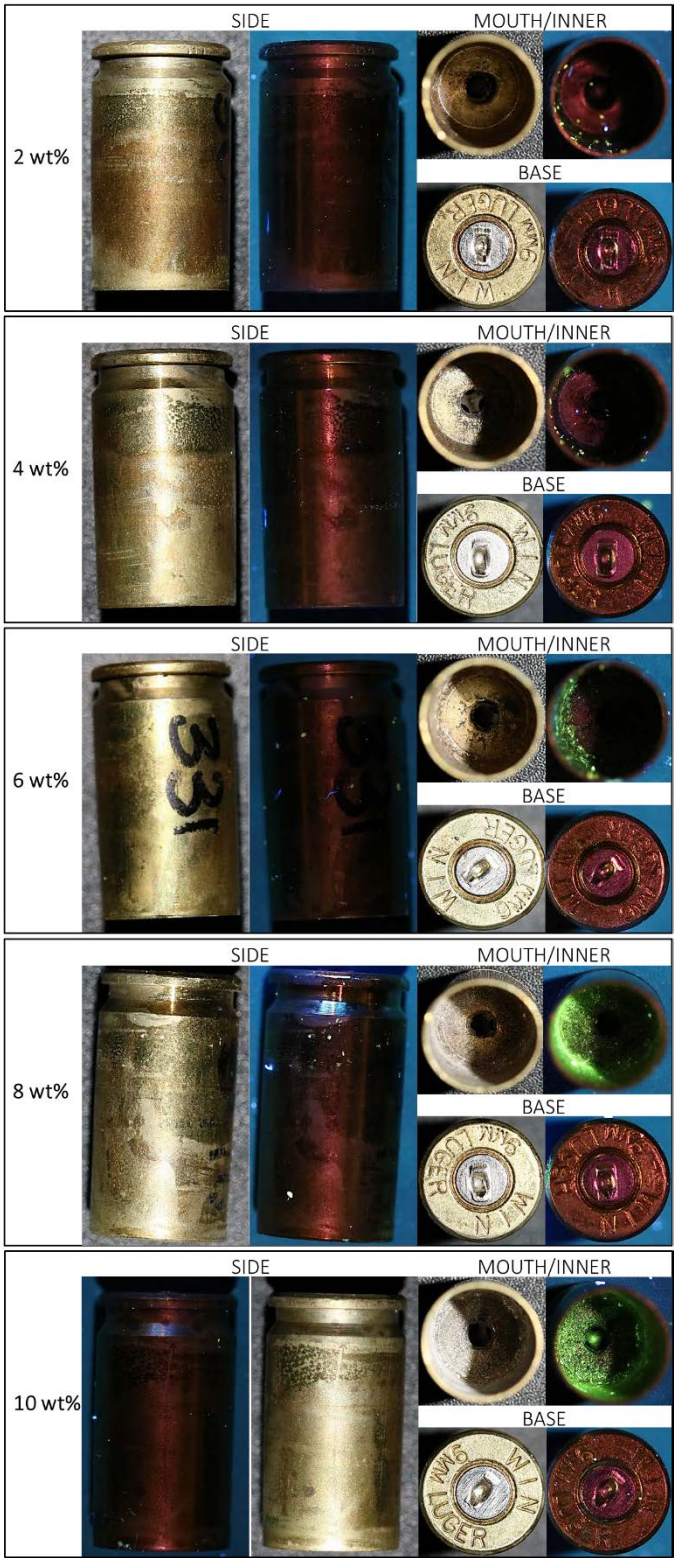

A3 - 7: Effect of ratio incorporated into ammunition on LGSR distribution on FCC. Images of the side, mouth and base of MW3-Tb FCC illuminated using white light (left) and the Labino® flood lamp (λex = 365 nm, right) using a Canon EOS 700D(ISO = 1600; f-stop = = f/2.8; exposure = 1/30 sec.).

5.1.13 GSR Stub

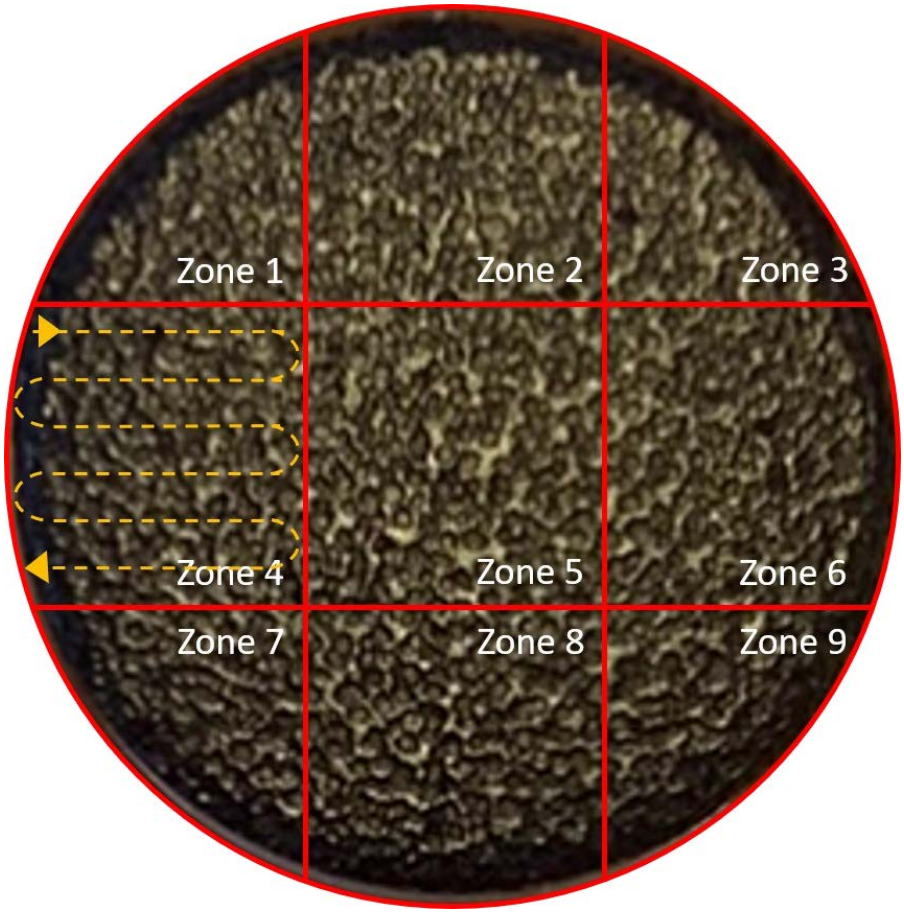

A3 - 8: Representative allocation of zones and example of searching pattern applied to SEM-EDS analysis on GSR stub

Olin WINCHESTER AMMUNITION

MATERIAL SAFETY DATA SHEET

Olin MSDS No.: **00050.0001**	Revision Date: **1/1/13**
Revision No.: **28**	Supercedes: 8/29/12

1. PRODUCT AND COMPANY IDENTIFICATION

Product Name: CENTERFIRE LOADED ROUNDS
Chemical Name: Mixture – Metal Alloy
Synonyms: Super-X Centerfire Rifle: 218 Bee, 22 Hornet, 22-250 Remington, 222 Remington, 223 Remington, 225 Winchester, 243 Winchester, 6mm Remington, 25-06 Remington 25-20 Winchester, 25-35 Winchester, 250 Savage, 257 Roberts + P, 264 Winchester Mag., 270 Winchester, 284 Winchester, 7mm Mauser (7 x 57), 7mm Remington Mag., 30 Carbine, 30-30 Winchester, 30-06 Spring- field, 30-40 Krag, 300 Winchester Mag., 300 H & H Magnum, 300 Savage, 303 Savage, 303 British, 307 Winchester, 308 Winches- ter, 32 Win. Special, 32-20 Winchester, 8mm Mauser (8 x57), 338 Winchester Mag., 35 Remington, 356 Winchester, 357 Magnum, 358 Winchester, 375 Winchester, 375 H & H Magnum, 38-40 Winchester, 38-55 Winchester, 44 Remington Magnum, 44-40 Winchester, 45-70 Government, 458 Winchester Mag, 280 Remington, Supreme 243 Winchester, Supreme 22-250 Remington, Supreme 270 Winchester, Supreme 280 Remington, Supreme 7mm Remington Magnum, Supreme 30-30 Winchester, Supreme 308 Winchester, Supreme 30-06 Springfield, Supreme 300 Winchester Magnum, 223 Remington 55 gr. Pointed Soft Point Varminator, 22-250 Remington, 55 gr. Pointed Soft Point Varminator, 22 Hornet, 46 gr. Hollowpoint, Varminator, 243 Winchester, 100 gr. Power Point, Varminator, 222 Remington, 50 gr. Pointed Soft Point, Varminator, 220 Swift, 55 gr. Pointed Soft Point Varminator, 25-06 Remington, 90 gr. Positive Expanding Point, Varminator, 454 Casull, 260 gr. Jacketed Flat Point, 454 Casull, 300 gr. Jacketed Flat Point, 30-06 Springfield, 150 gr. Fail Safe, 280 Remington, 140 gr. Fail Safe, 7MM Remington Magnum, 140 gr. Fail Safe, 220 Swift, 40 gr. Ballistic Silvertip, 22-250 Remington, 50 gr. Ballistic silver- tip, 222 Remington, 40 gr. Ballistic Silvertip, 223 Remington, 50 gr. Ballistic Silvertip, 243 Winchester, 55 gr. Ballistic Silvertip, 25-06 Remington, 115 gr. Ballistic Silvertip, 270 Winchester, 130 gr. Ballistic Silvertip, 280 Remington, 140 gr. Ballistic Silvertip, 7mm Remington Magnum, 150 gr. Ballistic Silvertip, 30-06 Springfield, 150 gr. Ballistic Silvertip, 30-06 Springfield, 168 gr. Ballistic Silvertip, 300 Winchester Magnum, 180 gr. Ballistic Silvertip, 308 Winchester, 150 gr. Ballistic Silvertip, 308 Winchester, 168 gr. Ballistic Silvertip, 338 Winchester Magnum, Cal .50 - Long Range Sniper, E-Tip, 5.56mm 64gr Bonded Solid Base, 5.56mm 62gr Open Tip, 5.56mm 62gr Open Tip Reduced Lead.

Military Centerfire Rifle: 5.56mm Ball M193 55 gr. full metal jacket, 5.56mm Penetrator M855 62 gr. full metal jacket, 7.62mm NATO Ball M80 147 gr. full metal jacket, Caliber 50 Ball M33 650 gr. full metal jacket, 5.56mm Penetrator M855A1 62 gr. Full Metal Jacket.

Super-X Centerfire Pistol/Revolver: 25 Automatic (6.35mm) Expanding Point and Full Metal Case; 30 Luger (7.65mm) Full Metal Case; 30 Carbine Hollow Soft Point and Full Metal Case; 32 Smith & Wesson Lead Round Nose and Long Lead Round Nose; 32 Short and Long Colt Lead Round Nose; 32 Automatic Silvertip Hollow Point and Full Metal Case; 38 Smith & Wesson Lead Round Nose, 380 Automatic Silvertip Hollow Point and Full Metal Case; 38 Special Silvertip Hollow Point, Lead Round Nose, Lead Semi-Wad Cutter, Metal Point, Silvertip Hollow Point + P, Jacketed Hollow Point + P, Lead Hollow Point + P, Lead Semi-Wad Cutter + P, Match Lead Mid-Range Match; 9mm Luger(Parabellum): Full Metal Jacket Encapsulated, Full Metal Case, Silvertip Hollow Point; 38 Super Automatic Silvertip Hollow point + P, Full Metal Case + P; 357 Magnum Jacketed Hollow Point, Silvertip Hollow Point, Lead Semi-Wad Cutter, Jacketed Soft Point; 10mm Automatic Silvertip Hollow Point; 41 Remington Magnum Silvertip Hollow Point, Lead Semi-Wad Cutter, Jacketed Soft Point, Jacketed Hollow Point; 44 Smith & Wesson Special Silvertip Hollow Point, Hollow Soft Point; 44 Remington Magnum Silvertip Hollow Point, Hollow Soft Point, Lead Semi-Wad Cutter(Med. Vel. & Gas Check); 45 Automatic Silvertip Hollow Point + P, Full Metal Case, Super-Match Full Metal Case Semi-Wad Cutter; 45 Colt Silvertip Hollow Point, Lead Round Nose; 45 Winchester Magnum: Jacketed Soft Point, Full Metal Case; Black Talon; 40 Smith and Wesson: Silvertip Hollow Point, Full Metal Jacket Truncated Cone, Full Metal Jacket Encapsulated, Jacket Hollow Point, Full Metal Jacket, Supreme 357 Magnum 180 gr. Partition Bullet, Supreme 44 Magnum 250 gr. Partition Bullet, 180 gr. SXT, 165 gr. SXT; Ranger Talon, 40 Cal. 180 gr. JHP; Ranger Talon, 40 Cal. 165 gr. JHP; Ranger Talon, 45 Auto, 230 gr. JHP; Ranger Talon, 9mm, 147 gr. JHP; Ranger, 9mm Luger, 147 gr., FMJ-E; Winclean (BEB), Ranger Bonded Handgun Ammunition; 223 Remington 60 gr. Partition; 380 Automatic T-Series, 357 SIG
Chemical Family: Metal mixture

MSDS #00050.0001

A3 - 9: Excerpt of centerfire loaded rounds material safety data sheet (page 1 of 7) as taken from Winchester Ammunition [450]. Identifies ammunition applicable for A3 – 3.

2. COMPOSITION / INFORMATION ON INGREDIENTS

CAS Number	Components	% By Weight	EINECS/ ELINCS #	EU Classification	
				Symbol	R-Phrase
7439-92-1	Lead	0.5 - 60	231-100-4	T, N*	R1-33-50/53-62
7440-50-8	Copper	25 - 60	231-159-6	None	None
7440-66-6	Zinc	4 - 20	231-175-3	F (as dust or powder)	R 15-17
9004-70-0	Nitrocellulose	10 - 20	Not listed	E*	R 2
55-63-0	Nitroglycerin	1 - 2	200-240-8	E, T+, N	R 3-26/27/28-33-51-53

*This material is not listed in Annex 1 of Directive 88/379/EEC. Olin has classified the material according to the conventional method based upon information from similar materials.

A3 - 10: Composition information for centerfire loaded rounds listed in A3 – 9, as taken from Winchester Ammunition [450]

References

1. Negin, J., Alpers, P., Nassar, N., and Hemenway, D., *Australian Firearm Regulation at 25–Success, Ongoing Challenges, and Lessons for the World.* New England journal of medicine, 2021. **384**(17): p. 1581-1582.DOI: https://doi.org/10.1056/NEJMp2102574.
2. Bureau of Crime Statistics and Research, *Offences Involving Weapons*. 2023.
3. Hueske, E.E., *Gunshot Residue Testing*. Practical Analysis and Reconstruction of Shooting Incidents. 2006: CRC Press. 199-222.
4. Pandey, P.K., Harshey, A., Yadav, M.M., and Srivastava, A., *Essentials of Forensic Ballistics*, in *Textbook of Forensic Science*. 2023, Springer. p. 425-468.
5. Haag, M.G. and Haag, L.C., *Shooting Incident Reconstruction*. second ed. 2011, Oxford, UK: Academic press.
6. Wallace, J.S., *Chemical Analysis of Firearms, Ammunition and Gunshot Residue*. 2018: CRC Press.
7. Miller, M.T., *Exercise N - Visualization and Enhancement: Chemical Evidence*, in *Crime Scene Investigation Laboratory Manual (Second Edition)*, M.T. Miller, Editor. 2018, Academic Press. p. 109-119.
8. American Society for Testing and Materials, *ASTM E1588-20 Standard Practice for Gunshot Residue Analysis by Scanning Electron Microscopy/Energy Dispersive XRay Spectrometry.* ASTM International, 2020.DOI: https://doi.org/10.1520/E1588-20.
9. American Society for Testing and Materials, *ASTM WK72856 New Practice for Standard Practice for the Collection, Preservation, and Analysis of Organic Gunshot Residue.* ASTM International, 2021.
10. Organisation of Scientific Area Committees for Forensic Science, *Standard Practice for the Analysis of Organic Gunshot Residue (OGSR) by Liquid Chromatography-Spectrometry (LC-MS), OSAC 2022-S-0003.* Draft OSAC Proposed Standard, 2021.
11. Rhodes, C., Beavan, E., and Smith, P., *A Preliminary Evaluation Study to Determine the Effectiveness of Infra-Red Photography for the Rapid Visualisation of Gun Shot Residue on Fabric.* Journal of Forensic Science & Criminology, 2019. **7**(1).DOI: https://doi.org/10.1016/j.aca.2007.07.024.
12. Weber, I.T., de Melo, A.J.G., Lucena, M.A.d.M., Rodrigues, M.O., and Alves Junior, S., *High Photoluminescent Metal Organic Frameworks as Optical Markers for the Identification of Gunshot Residues.* Analytical Chemistry, 2011. **83**(12): p. 4720-4723.DOI: https://doi.org/10.1021/ac200680a.
13. Romolo, F.S., *Advances in Analysis of Gunshot Residue*, in *Emerging Technologies for the Analysis of Forensic Traces*. 2019, Springer International Publishing. p. 183-202.
14. Blakey, L.S., Sharples, G.P., Chana, K., and Birkett, J.W., *Fate and Behavior of Gunshot Residue—A Review.* Journal of Forensic Sciences, 2018. **63**(1): p. 9-19.DOI: https://doi.org/10.1111/1556-4029.13555.
15. Wray, J.L., McNeil, J., and Rowe, W., *Comparison of Methods for Estimating Range of Fire Based on the Spread of Buckshot Patterns.* Journal of Forensic Science, 1983. **28**(4): p. 846-857.DOI: https://doi.org/10.1520/JFS11591J.
16. Feeney, W., Vander Pyl, C., Bell, S., and Trejos, T., *Trends in Composition, Collection, Persistence, and Analysis of IGSR and OGSR: A Review.* Forensic Chemistry, 2020: p. 100250.DOI: https://doi.org/10.1016/j.forc.2020.100250.

17. Rijnders, M.R., Stamouli, A., and Bolck, A., *Comparison of GSR Composition Occurring at Different Locations around the Firing Position.* Journal of Forensic Sciences, 2010. **55**(3): p. 616-623.DOI: https://doi.org/10.1111/j.1556-4029.2009.01292.x.
18. Blakey, L.S., Sharples, G.P., Chana, K., and Birkett, J.W., *The Fate and Behaviour of Gunshot Residue: Recreational Shooter Distribution.* Australian Journal of Forensic Sciences, 2019. **6451**(6): p. 1668-1672.DOI: https://doi.org/10.1111/1556-4029.14126.
19. Minzière, V.R., Gassner, A.L., Gallidabino, M., Roux, C., and Weyermann, C., *The Relevance of Gunshot Residues in Forensic Science.* Wiley Interdisciplinary Reviews: Forensic Science, 2023. **5**(1): p. e1472.DOI: https://doi.org/10.1002/wfs2.1472.
20. Meng, H.h. and Caddy, B., *Gunshot Residue Analysis - A Review.* Journal of Forensic Sciences, 1997. **42**(4): p. 553-570.DOI: https://doi.org/10.1520/JFS14167J.
21. Dalby, O., Butler, D., and Birkett, J.W., *Analysis of Gunshot Residue and Associated Materials - A Review.* Journal of Forensic Sciences, 2010. **55**(4): p. 924-943.DOI: https://doi.org/10.1111/j.1556-4029.2010.01370.x.
22. Goudsmits, E., Sharples, G.P., and Birkett, J.W., *Recent Trends in Organic Gunshot Residue Analysis.* Trends in Analytical Chemistry, 2015. **74**: p. 46-57.DOI: https://doi.org/10.1016/j.trac.2015.05.010.
23. Shrivastava, P., Jain, V., and Nagpal, S., *Gunshot Residue Detection Technologies—A Review.* Egyptian Journal of Forensic Sciences, 2021. **11**(1): p. 1-21.DOI: https://doi.org/10.1186/s41935-021-00223-9.
24. Taudte, R.V., Beavis, A., Blanes, L., Cole, N., Doble, P., and Roux, C., *Detection of Gunshot Residues using Mass Spectrometry.* BioMed Research International, 2014. **2014**.DOI: https://doi.org/10.1155/2014/965403.
25. Monturo, C., *Chapter 3 - Ammunition*, in *Forensic Firearm Examination*, C. Monturo, Editor. 2019, Academic Press. p. 21-71.
26. Bevan, J. and Pézard, S., *Basic Characteristics of Ammunition: From Handguns to MANPADS*, in *Targeting Ammunition: A Primer.* 2006, Small Arms Survey. p. 17-45.
27. Kara, İ., *The Relationship Between Gunshot-Residue Particle Size and Boltzmann Distribution.* Forensic Sciences Research, 2020. **7**(1): p. 47-52.DOI: https://doi.org/10.1080/20961790.2020.1713433.
28. Monturo, C., *Chapter 5 - Firearm Manufacturing Techniques*, in *Forensic Firearm Examination*. 2019, Academic Press. p. 95-142.
29. Muster, M., Hameed, A., and Wood, D., *Dynamic Qualitative Bolt Force Measurements for Investigating Influence Factors on the Pushout Effect of Small Calibre Ammunition.* AIP Advances, 2019. **9**(6): p. 065020.DOI: https://doi.org/10.1063/1.5092167.
30. Muster, M., Hameed, A., Wood, D., and Wasmer, K., *Push-out Force and Impulse Measurement of Seven Types of Small Arms Ammunition with Three Different Surface States.* AIP Advances, 2019. **9**(11): p. 115016.DOI: https://doi.org/10.1063/1.5128440.
31. Goudsmits, E., Blakey, L.S., Chana, K., Sharples, G.P., and Birkett, J.W., *The Analysis of Organic and Inorganic Gunshot Residue from a Single Sample.*

Forensic Science International, 2019. **299**: p. 168-173.DOI: https://doi.org/10.1016/j.forsciint.2019.03.049.

32. Pun, K.-M. and Gallusser, A., *Macroscopic Observation of the Morphological Characteristics of the Ammunition Gunpowder.* Forensic Science International, 2008. **175**(2): p. 179-185.DOI: https://doi.org/10.1016/j.forsciint.2007.06.021.
33. Karahacane, D.S., Dahmani, A., and Khimeche, K., *Raman Spectroscopy Analysis and Chemometric Study of Organic Gunshot Residues Originating from Two Types of Ammunition.* Forensic Science International, 2019. **301**: p. 129-136.DOI: https://doi.org/10.1016/j.forsciint.2019.05.022.
34. Chang, K.H., Jayaprakash, P.T., Yew, C.H., and Abdullah, A.F.L., *Gunshot Residue Analysis and its Evidential Values: A Review.* Australian Journal of Forensic Sciences, 2013. **45**(1): p. 3-23.DOI: https://doi.org/10.1080/00450618.2012.691546.
35. Benito, S., Abrego, Z., Sánchez, A., Unceta, N., Goicolea, M.A., and Barrio, R.J., *Characterisation of Organic Gunshot Residues in Lead-Free Ammunition Using a New Sample Collection Device for Liquid Chromatography–Quadrupole Time-Of-Flight Mass Spectrometry.* Forensic Science International, 2015. **246**: p. 79-85.DOI: https://doi.org/10.1016/j.forsciint.2014.11.002.
36. Gassner, A.L., Ribeiro, C., Kobylinska, J., Zeichner, A., and Weyermann, C., *Organic Gunshot Residues: Observations About Sampling and Transfer Mechanisms.* Forensic Science International, 2016. **266**: p. 369-378.DOI: https://doi.org/10.1016/j.forsciint.2016.06.029.
37. Taudte, R.V., Roux, C., Blanes, L., Horder, M., Kirkbride, K.P., and Beavis, A., *The Development and Comparison of Collection Techniques for Inorganic and Organic Gunshot Residues.* Analytical and Bioanalytical Chemistry, 2016. **408**(10): p. 2567-2576.DOI: https://doi.org/10.1007/s00216-016-9357-7.
38. Goudsmits, E., Sharples, G.P., and Birkett, J.W., *Preliminary Classification of Characteristic Organic Gunshot Residue Compounds.* Science & Justice, 2016. **56**(6): p. 421-425.DOI: https://doi.org/10.1016/j.scijus.2016.06.007.
39. Mach, M., Pallos, A., and Jones, P., *Feasibility of Gunshot Residue Detection via its Organic Constituents. Part I: Analysis of Smokeless Powders by Combined Gas Chromatography-Chemical Ionization Mass Spectrometry.* Journal of Forensic Science, 1978. **23**(3): p. 433-445.DOI: https://doi.org/10.1520/JFS10690J.
40. Maitre, M., Horder, M., Kirkbride, K.P., Gassner, A.-L., Weyermann, C., Roux, C., and Beavis, A., *A Forensic Investigation on the Persistence of Organic Gunshot Residues.* Forensic Science International, 2018. **292**: p. 1-10.DOI: https://doi.org/10.1016/j.forsciint.2018.08.036.
41. Maitre, M., Kirkbride, K., Horder, M., Roux, C., and Beavis, A., *Thinking Beyond the Lab: Organic Gunshot Residues in an Investigative Perspective.* Australian Journal of Forensic Sciences, 2018: p. 1-7.DOI: https://doi.org/10.1080/00450618.2018.1457718.
42. Gassner, A.-L., Manganelli, M., Werner, D., Rhumorbarbe, D., Maitre, M., Beavis, A., Roux, C.P., and Weyermann, C., *Secondary Transfer of Organic Gunshot Residues: Empirical Data to Assist the Evaluation of Three Scenarios.* Science & Justice, 2019. **59**(1): p. 58-66.DOI: https://doi.org/10.1016/j.scijus.2018.08.007.
43. Gallidabino, M.D., Barron, L.P., Weyermann, C., and Romolo, F.S., *Quantitative Profile–Profile Relationship (QPPR) Modelling: a Novel Machine Learning Approach to Predict and Associate Chemical Characteristics of Unspent*

Ammunition from Gunshot Residue (GSR). Analyst, 2019. **144**(4): p. 1128-1139.DOI: https://doi.org/10.1039/C8AN01841C.

44. Maitre, M., Chadwick, S., Kirkbride, K.P., Gassner, A.-L., Weyermann, C., Beavis, A., and Roux, C., *An Investigation on the Secondary Transfer of Organic Gunshot Residues.* Science & Justice, 2019. **59**(3): p. 248-255.DOI: https://doi.org/10.1016/j.scijus.2019.01.007.
45. Manganelli, M., Weyermann, C., and Gassner, A.-L., *Surveys of Organic Gunshot Residue Prevalence: Comparison between Civilian and Police Populations.* Forensic Science International, 2019. **298**: p. 48-57.DOI: https://doi.org/10.1016/j.forsciint.2019.02.050.
46. Bell, S. and Feeney, W., *Single Shot, Single Sample, Single Instrument Detection of IGSR and OGSR using LC/MS/MS.* Forensic Science International, 2019. **299**: p. 215-222.DOI: https://doi.org/10.1016/j.forsciint.2019.04.002.
47. Taudte, R.V., Roux, C., Bishop, D.P., Fouracre, C., and Beavis, A., *High-Throughput Screening for Target Compounds in Smokeless Powders using Online-SPE Tandem Mass Spectrometry.* Australian Journal of Forensic Sciences, 2019. **53**(1): p. 16-26.DOI: https://doi.org/10.1080/00450618.2019.1629019.
48. Ott, C.E., Dalzell, K.A., Calderón-Arce, P.J., Alvarado-Gámez, A.L., Trejos, T., and Arroyo, L.E., *Evaluation of the Simultaneous Analysis of Organic and Inorganic Gunshot Residues Within a Large Population Data Set Using Electrochemical Sensors.* Journal of Forensic Sciences, 2020. **65**(6): p. 1935-1944.DOI: https://doi.org/10.1111/1556-4029.14548.
49. Bonnar, C., Moule, E.C., Lucas, N., Seyfang, K.E., Dunsmore, R.P., Popelka-Filcoff, R.S., Redman, K., and Kirkbride, K.P., *Tandem Detection of Organic and Inorganic Gunshot Residues using LC-MS and SEM-EDS.* Forensic Science International, 2020. **314**: p. 110389.DOI: https://doi.org/10.1016/j.forsciint.2020.110389.
50. Gassner, A.-L. and Weyermann, C., *Prevalence of Organic Gunshot Residues in Police Vehicles.* Science & Justice, 2020. **60**(2): p. 136-144.DOI: https://doi.org/10.1016/j.scijus.2019.09.009.
51. Minzière, V.R., Werner, D., Schneider, D., Manganelli, M., Jung, B., Weyermann, C., and Gassner, A.L., *Combined Collection and Analysis of Inorganic and Organic Gunshot Residues.* Journal of Forensic Sciences, 2020. **65**(4): p. 1102-1113.DOI: https://doi.org/10.1111/1556-4029.14314.
52. Lucas, N., Cook, M., Wallace, J., Kirkbride, K.P., and Kobus, H., *Quantifying Gunshot Residues in Cases of Suicide: Implications for Evaluation of Suicides and Criminal Shootings.* Forensic Science International, 2016. **266**: p. 289-298.DOI: https://doi.org/10.1016/j.forsciint.2016.06.006.
53. Ditrich, H., *Distribution of Gunshot Residues – The Influence of Weapon Type.* Forensic Science International, 2012. **220**(1): p. 85-90.DOI: https://doi.org/10.1016/j.forsciint.2012.01.034.
54. Romanò, S., De-Giorgio, F., D'Onofrio, C., Gravina, L., Abate, S., and Romolo, F.S., *Characterisation of Gunshot Residues from Non-Toxic Ammunition and their Persistence on the Shooter's Hands.* International Journal of Legal Medicine, 2020. **134**: p. 1083-1094.DOI: https://doi.org/10.1007/s00414-020-02261-9.
55. Seyfang, K.E., Kobus, H.J., Popelka-Filcoff, R.S., Plummer, A., Magee, C.W., Redman, K.E., and Kirkbride, K.P., *Analysis of Elemental and Isotopic Variation in Glass Frictionators from 0.22 Rimfire Primers.* Forensic Science International, 2018. **293**: p. 47-62.DOI: https://doi.org/10.1016/j.forsciint.2018.10.017.

56. Arnemo, J.M., Andersen, O., Stokke, S., Thomas, V.G., Krone, O., Pain, D.J., and Mateo, R., *Health and Environmental Risks from Lead-Based Ammunition: Science versus Socio-Politics.* EcoHealth, 2016. **13**(4): p. 618-622.DOI: https://doi.org/10.1007/s10393-016-1177-x.
57. Cromie, R., Newth, J., and Strong, E., *Transitioning to Non-Toxic Ammunition: Making Change Happen.* Ambio, 2019. **48**(9): p. 1079-1096.DOI: https://doi.org/10.1007/s13280-019-01204-y.
58. Green, R.E. and Pain, D.J., *Risks to Human Health from Ammunition-derived Lead in Europe.* Ambio, 2019. **48**(9): p. 954-968.DOI: https://doi.org/10.1007/s13280-019-01194-x.
59. Martiny, A., Campos, A.P., Sader, M.S., and Pinto, M.A.L., *SEM/EDS Analysis and Characterization of Gunshot Residues from Brazilian Lead-Free Ammunition.* Forensic Science International, 2008. **177**(1): p. 9-17.DOI: https://doi.org/10.1016/j.forsciint.2007.07.005.
60. Donghi, M., Mason, K., and Romolo, F.S., *Detecting Gunshot Residue from Sellier & Bellot Nontox Heavy Metal-free Primer by in situ Cathodoluminescence.* Journal of Forensic Sciences, 2019. **64**(6): p. 1658-1667.DOI: https://doi.org/10.1111/1556-4029.14110.
61. Niewoehner, L., Buchholz, N., and Merkel, J., *New Ammunitions for the German Police.* Scanning, 2005. **27**(2): p. 69.
62. Polovková, J., Šimonič, M., and Szegényi, I., *Study of Gunshot Residues from Sintox® Ammunition Containing Marking Substances.* Egyptian Journal of Forensic Sciences, 2015. **5**(4): p. 174-179.DOI: https://doi.org/10.1016/j.ejfs.2014.09.003.
63. Schwoeble, A. and Exline, D.L., *Current Methods in Forensic Gunshot Residue Analysis*. 2000: CRC Press.
64. Reyes, L.C., López, C.E., Barrios, A.B., Soto, C.G., Ibáñez, C., and Díaz, F.J., *Development and Application of a New Nose Hairs Sample Collection Device for GSR Particles by Scanning Electron Microscopy with Energy Dispersive X-ray Spectroscopy (SEM-EDS).* Forensic Science International, 2018. **290**: p. 42-48.DOI: https://doi.org/10.1016/j.forsciint.2018.06.029.
65. Houck, M.M. and Siegel, J.A., *Firearms and Tool Marks*, in *Fundamentals of Forensic Science*. 2015, Academic Press.
66. Hofstetter, C., Maitre, M., Beavis, A., Roux, C.P., Weyermann, C., and Gassner, A.-L., *A Study of Transfer and Prevalence of Organic Gunshot Residues.* Forensic Science International, 2017. **277**: p. 241-251.DOI: https://doi.org/10.1016/j.forsciint.2017.06.013.
67. Fojtášek, L. and Kmječ, T., *Time Periods of GSR Particles Deposition after Discharge - Final Results.* Forensic Science International, 2005. **153**(2-3): p. 132-135.DOI: https://doi.org/10.1016/j.forsciint.2004.09.127.
68. Luten, R., Neimke, D., Barth, M., and Niewoehner, L., *Investigating Airborne GSR Particles by the Application of Impactor Technology.* Forensic Chemistry, 2018. **8**: p. 72-81.DOI: https://doi.org/10.1016/j.forc.2018.02.005.
69. Brożek-Mucha, Z., *Scanning Electron Microscopy and X-ray Microanalysis for Chemical and Morphological Characterisation of the Inorganic Component of Gunshot Residue: Selected Problems.* BioMed Research International, 2014. **2014**: p. 428038-428038.DOI: https://doi.org/10.1155/2014/428038.
70. Cecchetto, G., Giraudo, C., Amagliani, A., Viel, G., Fais, P., Cavarzeran, F., Feltrin, G., Ferrara, S.D., and Montisci, M., *Estimation of the Firing Distance Through*

Micro-CT Analysis of Gunshot Wounds. International Journal of Legal Medicine, 2011. **125**(2): p. 245-251.DOI: https://doi.org/10.1007/s00414-010-0533-6.

71. Fojtášek, L., Vacínová, J., Kolář, P., and Kotrlý, M., *Distribution of GSR Particles in the Surroundings of Shooting Pistol.* Forensic Science International, 2003. **132**(2): p. 99-105.DOI: https://doi.org/10.1016/S0379-0738(03)00018-5.
72. Carreras, L.F. and Palma, L.A.M., *Ejection Patterns of Shot Residues made from 9 mm Parabellum Gun, 9 mm Short Gun,. 38 Revolver and 7.62 mm Cetme Rifle.* Forensic Science International, 1998. **96**(2-3): p. 143-172.DOI: https://doi.org/10.1016/S0379-0738(98)00117-0.
73. Vachon, C.R. and Martinez, M.V., *Understanding Gunshot Residue Evidence and its Role in Forensic Science.* The American Journal of Forensic Medicine and Pathology, 2019. **40**(3): p. 210-219.DOI: https://doi.org/10.1097/PAF.0000000000000483.
74. Miller, M.T. and Massey, P., *Chapter 8 - Reconstruction Activities*, in *The Crime Scene*. 2019, Academic Press. p. 179-227.
75. Geusens, N., Nys, B., and Charles, S., *Implementation and Optimization of the Sodium-Rhodizonate Method for Chemographic Shooting Distance Estimation.* Journal of Forensic Sciences, 2019. **64**(4): p. 1169-1172.DOI: https://doi.org/10.1111/1556-4029.13984.
76. Kersh, K.L., Childers, J.M., Justice, D., and Karim, G., *Detection of Gunshot Residue on Dark-Colored Clothing Prior to Chemical Analysis.* Journal of Forensic Sciences, 2014. **59**(3): p. 754-762.DOI: https://doi.org/10.1111/1556-4029.12409.
77. Werner, D., Gassner, A.-L., Marti, J., Christen, S., Wyss, P., and Weyermann, C., *Comparison of Three Collection Methods for the Sodium Rhodizonate Detection of Gunshot Residues on Hands.* Science & Justice, 2020. **60**(1): p. 63-71.DOI: https://doi.org/10.1016/j.scijus.2019.09.004.
78. Destefani, C.A., Motta, L.C., Vanini, G., Souza, L.M., A Filho, J.F., Macrino, C.J., Silva, E.M., Greco, S.J., Endringer, D.C., and Romão, W., *Europium-Organic Complex as Luminescent Marker for the Visual Identification of Gunshot Residue and Characterization by Electrospray Ionization FT-ICR Mass Spectrometry.* Microchemical Journal, 2014. **116**: p. 216-224.DOI: https://doi.org/10.1016/j.microc.2014.05.009.
79. Andreola, S., Gentile, G., Battistini, A., Cattaneo, C., and Zoja, R., *Forensic Applications of Sodium Rhodizonate and Hydrochloric Acid: a New Histological Technique for Detection of Gunshot Residues.* Journal of Forensic Sciences, 2011. **56**(3): p. 771-774.DOI: https://doi.org/10.1111/j.1556-4029.2010.01689.x.
80. Glattstein, B., Vinokurov, A., Levin, N., and Zeichner, A., *Improved Method for Shooting Distance Estimation. Part 1. Bullet Holes in Clothing Items.* Journal of Forensic Sciences, 2000. **45**(4): p. 801-806.DOI: https://doi.org/10.1520/JFS14773J.
81. Berger, J., Upton, C., and Springer, E., *Evaluation of Total Nitrite Pattern Visualization as an Improved Method for Gunshot Residue Detection and its Application to Casework Samples.* Journal of Forensic Sciences, 2019. **64**(1): p. 218-222.DOI: https://doi.org/10.1111/1556-4029.13802.
82. Jaluddin, S.N., Zain, Z.M., Halim, M.I.A., Safian, M.F., Rani, M.A.A., and Subri, M.S.M., *Preliminary Evaluation of Gunshot Residue (GSR) Using 3-Aminophenol as a Substitute in Modified Griess Test.* Indonesian Journal of Chemistry, 2021. **21**(6): p. 1550-1559.DOI: https://doi.org/10.22146/ijc.68265.

83. Gandy, L., Najjar, K., Terry, M., and Bridge, C., *A Novel Protocol for the Combined Detection of Organic, Inorganic Gunshot Residue.* Forensic Chemistry, 2018. **8**: p. 1-10.DOI: https://doi.org/10.1016/j.forc.2017.12.009.
84. Lin, A.C.Y., Hsieh, H.M., Tsai, L.C., Linacre, A., and Lee, J.C.I., *Forensic Applications of Infrared Imaging for the Detection and Recording of Latent Evidence.* Journal of Forensic Sciences, 2007. **52**(5): p. 1148-1150.DOI: https://doi.org/10.1111/j.1556-4029.2007.00502.x.
85. Zapata, F., López-López, M., Amigo, J.M., and García-Ruiz, C., *Multi-Spectral Imaging for the Estimation of Shooting Distances.* Forensic Science International, 2018. **282**: p. 80-85.DOI: https://doi.org/10.1016/j.forsciint.2017.11.025.
86. Ortega-Ojeda, F., Torre-Roldán, M., and García-Ruiz, C., *Short Wave Infrared Chemical Imaging as Future Tool for Analysing Gunshot Residues Patterns in Targets.* Talanta, 2017. **167**: p. 227-235.DOI: https://doi.org/10.1016/j.talanta.2017.02.020.
87. Głomb, P., Romaszewski, M., Cholewa, M., and Domino, K., *Application of Hyperspectral Imaging and Machine Learning Methods for the Detection of Gunshot Residue Patterns.* Forensic Science International, 2018. **290**: p. 227-237.DOI: https://doi.org/10.1016/j.forsciint.2018.06.040.
88. Marsh, N., *Forensic Photography: A Practitioner's Guide*. 2014: Wiley Blackwell.
89. Marin, N. and Buszka, J.M., *Forensic Photography Techniques*. Alternate Light Source Imaging. 2014: Taylor & Francis.
90. Barrera, V., Fliss, B., Panzer, S., and Bolliger, S., *Gunshot Residue on Dark Materials: A Comparison between Infrared Photography and the Use of an Alternative Light Source.* International Journal of Legal Medicine, 2019. **133**(4): p. 1115-1120.DOI: https://doi.org/10.1007/s00414-018-1965-7.
91. Vecellio, M., *Comparison of Gunshot Residue Visualization with Alternative Light Sources and Infrared Light.* Journal of Forensic and Crime Investigation, 2020. **3**(1): p. 104.
92. Vecellio, M., *Visualization of Gunshot Residue on Dark Fabric: A Comparison of Infrared Photography and an Alternate Light Source.* Journal of Forensic Identification, 2022. **72**(2): p. 157-173.
93. Husak, J., *Noninvasive, Visual Examination for the Presence of Gunshot Residue on Human Skin.* Journal of Forensic Sciences, 2022. **67**(3): p. 1191-1197.DOI: https://doi.org/10.1111/1556-4029.14954.
94. Atwater, C.S., Durina, M.E., Durina, J.P., and Blackledge, R.D., *Visualization of Gunshot Residue Patterns on Dark Clothing.* Journal of Forensic Sciences, 2006. **51**(5): p. 1091-1095.DOI: https://doi.org/10.1111/j.1556-4029.2006.00226.x.
95. Charles, S., Geusens, N., Vergalito, E., and Nys, B., *Interpol Review of Gunshot Residue 2016–2019.* Forensic Science International: Synergy, 2020. **2**: p. 416-428.DOI: https://doi.org/10.1016/j.fsisyn.2020.01.011.
96. Taudte, R.V., Roux, C., and Beavis, A., *Stability of Smokeless Powder Compounds on Collection Devices.* Forensic Science International, 2017. **270**: p. 55-60.DOI: https://doi.org/10.1016/j.forsciint.2016.11.027.
97. Reid, L., Chana, K., Bond, J.W., Almond, M.J., and Black, S., *Stubs Versus Swabs? A Comparison of Gunshot Residue Collection Techniques.* Journal of Forensic Sciences, 2010. **55**(3): p. 753-756.DOI: https://doi.org/10.1111/j.1556-4029.2010.01332.x.

98. Merli, D., Amadasi, A., Mazzarelli, D., Cappella, A., Castoldi, E., Ripa, S., Cucca, L., Cattaneo, C., and Profumo, A., *Comparison of Different Swabs for Sampling Inorganic Gunshot Residue from Gunshot Wounds: Applicability and Reliability for the Determination of Firing Distance.* Journal of Forensic Sciences, 2019. **64**(2): p. 558-564.DOI: https://doi.org/10.1111/1556-4029.13870.
99. Zuy, Y., Sweck, S.O., Dockery, C.R., and Potts, G.E., *HPLC Detection of Organic Gunshot Residues Collected with Silicone Wristbands.* Analytical Methods, 2020. **12**(1): p. 85-90.DOI: https://doi.org/10.1039/c9ay02305d.
100. Castro, S.V., Lima, A.P., Rocha, R.G., Cardoso, R.M., Montes, R.H., Santana, M.H., Richter, E.M., and Munoz, R.A., *Simultaneous Determination of Lead and Antimony in Gunshot Residue using a 3D-Printed Platform Working as Sampler and Sensor.* Analytica Chimica Acta, 2020. **1130**: p. 126-136.DOI: https://doi.org/10.1016/j.aca.2020.07.033.
101. Sobreira, C., Klu, J.K., Cole, C., Nic Daéid, N., and Ménard, H., *Reviewing Research Trends—A Scientometric Approach Using Gunshot Residue (GSR) Literature as an Example.* Publications, 2020. **8**(1): p. 7.DOI: https://doi.org/10.3390/publications8010007.
102. Fambro, L.A., Miller, E.T., Vandenbos, D.D., and Dockery, C.R., *Characterization of Lead-Free Gunshot Residue Analogs.* Analytical Methods, 2016. **8**(15): p. 3132-3139.DOI: https://doi.org/10.1039/c6ay00725b.
103. Burnett, B.R., Nunziata, F., and Gentile, C., *Examination of Firearm Gunpowders by Scanning Electron Microscopy/Energy Dispersive X-ray Analysis.* Journal of Forensic Sciences, 2020. **66**(2): p. 709-718.DOI: https://doi.org/10.1111/1556-4029.14621.
104. Aliste, M., Arranz, S., Sánchez-Ortega, A., Sampedro, M.C., Unceta, N., Gómez-Caballero, A., Vallejo, A., Goicolea, M.A., and Barrio, R.J., *Particle Analysis for the Detection of Gunshot Residue (GSR) in Nasal Samples Using Scanning Laser Ablation and Inductively Coupled Plasma-Mass Spectrometry (SLA-ICPMS).* Journal of Forensic Sciences, 2020. **65**(4): p. 1094-1101.DOI: https://doi.org/10.1111/1556-4029.14278.
105. Brünjes, R., Schüürman, J., Kammer, F.v.d., and Hofmann, T., *Rapid Analysis of Gunshot Residues with Single-Particle Inductively Coupled Plasma Time-Of-Flight Mass Spectrometry.* Forensic Science International, 2022. **332**: p. 111202.DOI: https://doi.org/10.1016/j.forsciint.2022.111202.
106. Yüksel, B., Şen, N., Ögünç, G.I., and Erdoğan, A., *Elemental Profiling of Toxic and Modern Primers using ICP-MS, SEM-EDS, and XPS: An Application in Firearm Discharge Residue Investigation.* Australian Journal of Forensic Sciences, 2023. **55**(4): p. 529-546.DOI: https://doi.org/10.1080/00450618.2022.2043436.
107. Szakas, S.E., Menking-Hoggatt, K., Trejos, T., and Gundlach-Graham, A., *Elemental Characterization of Leaded and Lead-Free Inorganic Primer Gunshot Residue Standards Using Single Particle Inductively Coupled Plasma Time-of-Flight Mass Spectrometry.* Applied Spectroscopy, 2022. **77**(8): p. 873-884.DOI: https://doi.org/10.1177/00037028221142624.
108. Tarifa, A. and Almirall, J.R., *Fast Detection and Characterization of Organic and Inorganic Gunshot Residues on the Hands of Suspects by CMV-GC–MS and LIBS.* Science & Justice, 2015. **55**(3): p. 168-175.DOI: https://doi.org/10.1016/j.scijus.2015.02.003.

109. Vander Pyl, C., Ovide, O., Ho, M., Yuksel, B., and Trejos, T., *Spectrochemical Mapping using Laser Induced Breakdown Spectroscopy as a More Objective Approach to Shooting Distance Determination.* Spectrochimica Acta Part B: Atomic Spectroscopy, 2019. **152**: p. 93-101.DOI: https://doi.org/10.1016/j.sab.2018.12.010.
110. Vander Pyl, C., Morris, K., Arroyo, L., and Trejos, T., *Assessing the Utility of LIBS in the Reconstruction of Firearm Related Incidents.* Forensic Chemistry, 2020. **19**: p. 100251.DOI: https://doi.org/10.1016/j.forc.2020.100251.
111. Doña-Fernández, A., Rodriguez-Pascual, J.A., Andres-Gimeno, I., Gutiérrez-Redomero, E., Valtuille-Fernández, E., and Gomez-Laina, F.J., *Assessing the Shooting Distance of Lead-Free Ammunition Regardless of Composition using Laser Induced Breakdown Spectroscopy.* Forensic Sciences Research, 2023.DOI: https://doi.org/10.1093/fsr/owad022.
112. Santos, A., Ramos, P., Fernandes, L., Magalhães, T., Almeida, A., and Sousa, A., *Firing Distance Estimation Based on the Analysis of GSR Distribution on the Target Surface using ICP-MS - An Experimental Study with a 7.65 mm× 17mm Browning Pistol (. 32 ACP).* Forensic Science International, 2015. **247**: p. 62-68.DOI: https://doi.org/10.1016/j.forsciint.2014.12.006.
113. Costa, R.A., Motta, L.C., Destefani, C.A., Rodrigues, R.R.T., do Espírito Santo, K.S., Aquije, G.M.F.V., Boldrini, R., Athayde, G.P.B., Carneiro, M.T.W.D., and Romão, W., *Gunshot residues (GSR) Analysis of Clean Range Ammunition using SEM/EDX, Colorimetric Test and ICP-MS: A Comparative Approach between the Analytical Techniques.* Microchemical Journal, 2016. **129**: p. 339-347.DOI: https://doi.org/10.1016/j.microc.2016.07.017.
114. Doña-Fernández, A., de Andres-Gimeno, I., Santiago-Toribio, P., Valtuille-Fernández, E., Aller-Sanchez, F., and Heras-González, A., *Real-Time Detection of GSR Particles from Crime Scene: A Comparative Study of SEM/EDX and Portable LIBS System.* Forensic Science International, 2018. **292**: p. 167-175.DOI: https://doi.org/10.1016/j.forsciint.2018.09.021.
115. Fambro, L.A., Vandenbos, D.D., Rosenberg, M.B., and Dockery, C.R., *Laser-Induced Breakdown Spectroscopy for the Rapid Characterization of Lead-Free Gunshot Residues.* Applied Spectroscopy, 2017. **71**(4): p. 699-708.DOI: https://doi.org/10.1177/0003702816689099.
116. Silva, M.J., Cortez, J., Pasquini, C., Honorato, R.S., Paim, A.P.S., and Pimentel, M.F., *Gunshot Residues: Screening Analysis by Laser-Induced Breakdown Spectroscopy.* Journal of the Brazilian Chemical Society, 2009. **20**(10): p. 1887-1894.DOI: https://doi.org/10.1590/S0103-50532009001000017.
117. López-López, M., Alvarez-Llamas, C., Pisonero, J., García-Ruiz, C., and Bordel, N., *An Exploratory Study of the Potential of LIBS for Visualizing Gunshot Residue Patterns.* Forensic Science International, 2017. **273**: p. 124-131.DOI: https://doi.org/10.1016/j.forsciint.2017.02.012.
118. Profumo, A., Capucciati, A., Mattino, A., Donghi, M., and Merli, D., *A Simple Voltammetric Method to Evaluate the Firing Distance Through Determination of Nitrocellulose.* Talanta, 2024. **266**: p. 125040.DOI: https://doi.org/10.1016/j.talanta.2023.125040.
119. Minzière, V.R., Robyr, O., and Weyermann, C., *Should Inorganic or Organic Gunshot Residues be Analysed First?* Forensic Science International, 2023. **348**: p. 111600.DOI: https://doi.org/10.1016/j.forsciint.2023.111600.

120. Khandasammy, S.R., Rzhevskii, A., and Lednev, I.K., *A Novel Two-Step Method for the Detection of Organic Gunshot Residue for Forensic Purposes: Fast Fluorescence Imaging followed by Raman Microspectroscopic Identification.* Analytical Chemistry, 2019. **91**(18): p. 11731-11737.DOI: https://doi.org/10.1021/acs.analchem.9b02306.
121. Doty, K.C. and Lednev, I.K., *Raman Spectroscopy for Forensic Purposes: Recent Applications for Serology and Gunshot Residue Analysis.* TrAC Trends in Analytical Chemistry, 2018. **103**: p. 215-222.DOI: https://doi.org/10.1016/j.trac.2017.12.003.
122. Bueno, J., Halámková, L., Rzhevskii, A., and Lednev, I.K., *Raman Microspectroscopic Mapping as a Tool for Detection of Gunshot Residue on Adhesive Tape.* Analytical and Bioanalytical Chemistry, 2018. **410**(28): p. 7295-7303.DOI: https://doi.org/10.1007/s00216-018-1359-1.
123. López-López, M., Ferrando, J.L., and García-Ruiz, C., *Comparative Analysis of Smokeless Gunpowders by Fourier transform Infrared and Raman Spectroscopy.* Analytica Chimica Acta, 2012. **717**: p. 92-99.DOI: https://doi.org/10.1016/j.aca.2011.12.022.
124. López-López, M.a., Delgado, J.J., and García-Ruiz, C., *Ammunition Identification by Means of the Organic Analysis of Gunshot residues using Raman Spectroscopy.* Analytical Chemistry, 2012. **84**(8): p. 3581-3585.DOI: https://doi.org/10.1021/ac203237w.
125. Mou, Y., Lakadwar, J., and Rabalais, J.W., *Evaluation of Shooting Distance by AFM and FTIR/ATR Analysis of GSR.* Journal of Forensic Sciences, 2008. **53**(6): p. 1381-1386.DOI: https://doi.org/10.1111/j.1556-4029.2008.00854.x.
126. Sharma, S. and Lahiri, S., *A Preliminary Investigation into the use of FTIR Microscopy as a Probe for the Identification of Bullet Entrance Holes and the Distance of Firing.* Science & Justice, 2009. **49**(3): p. 197-204.DOI: https://doi.org/10.1016/j.scijus.2008.07.002.
127. Bueno, J., Sikirzhytski, V., and Lednev, I.K., *Attenuated Total Reflectance-FT-IR Spectroscopy for Gunshot Residue Analysis: Potential for Ammunition Determination.* Analytical Chemistry, 2013. **85**(15): p. 7287-7294.DOI: https://doi.org/10.1021/ac4011843.
128. Álvarez, Á. and Yáñez, J., *Screening of Gunshot Residue in Skin Using Attenuated Total Reflection Fourier Transform Infrared (ATR FT-IR) Hyperspectral Microscopy.* Applied Spectroscopy, 2020. **74**(4): p. 400-407.DOI: https://doi.org/10.1177/0003702819892930.
129. Fabbris, S., Profumo, A., Alberini, G., Bonomi, S., Milanese, C., Donghi, M., Amadasi, A., Patrini, M., Cucca, L., and Merli, D., *Interaction of Gunshot Residues (GSR) with Natural and Synthetic Textiles Having Different Structural Features.* Talanta, 2020. **2**: p. 100017.DOI: https://doi.org/10.1016/j.talo.2020.100017.
130. Latzel, S., Neimke, D., Schumacher, R., Barth, M., and Niewöhner, L., *Shooting Distance Determination by m-XRF - Examples on Spectra Interpretation and Range Estimation.* Forensic Science International, 2012. **223**(1-3): p. 273-278.DOI: https://doi.org/10.1016/j.forsciint.2012.10.001.
131. Janssen, M., Stamouli, A., and Knijnenberg, A. *Exploration of mXRF Analysis of Gunshot Residue from Cartridge Cases*. in *Scanning Microscopies 2015*. 2015. International Society for Optics and Photonics.

132. Langstraat, K., Knijnenberg, A., Edelman, G., Van De Merwe, L., Van Loon, A., Dik, J., and Van Asten, A., *Large Area Imaging of Forensic Evidence with MA-XRF.* Scientific Reports, 2017. **7**(1): p. 1-11.DOI: https://doi.org/10.1038/s41598-017-15468-5.
133. Gong, S.A., Homburger, N., and Huang, L., *Elemental Profiling of Total Gunshot Residue Using Total Reflection X-ray Fluorescence Spectrometry.* Journal of Forensic Sciences, 2022. **67**(3): p. 1198-1207.DOI: https://doi.org/10.1111/1556-4029.14988.
134. Margot, P., *Forensic Science on Trial - What is the Law of the Land?* Australian Journal of Forensic Sciences, 2011. **43**(2-3): p. 89-103.DOI: 10.1080/00450618.2011.555418.
135. Charles, S. and Jonckheere, A., *The Use and Understanding of Forensic Reports by Judicial Actors—The Field of Gunshot Residue Expertise as an Example.* Forensic Science International, 2022. **335**: p. 111312.DOI: https://doi.org/10.1016/j.forsciint.2022.111312.
136. Cardinetti, B., Ciampini, C., Abate, S., Marchetti, C., Ferrari, F., Di Tullio, D., D'onofrio, C., Orlando, G., Gravina, L., and Torresi, L., *A Proposal for Statistical Evaluation of the Detection of Gunshot Residues on a Suspect.* Scanning, 2006. **28**(3): p. 142-147.
137. Bozza, S., Taroni, F., and Biedermann, A., *Bayes Factors for Forensic Decision Analyses with R*. 1st ed. 2022. ed. Springer Texts in Statistics. 2022, Cham: Springer Nature.
138. Biedermann, A., Bozza, S., and Taroni, F., *Probabilistic Evidential Assessment of Gunshot Residue Particle Evidence (Part I): Likelihood Ratio Calculation and Case Pre-Assessment using Bayesian Networks.* Forensic Science International, 2009. **191**(1): p. 24-35.
139. Biedermann, A., Bozza, S., and Taroni, F., *Probabilistic Evidential Assessment of Gunshot Residue Particle Evidence (Part II): Bayesian Parameter Estimation for Experimental Count Data.* Forensic Science International, 2011. **206**(1): p. 103-110.DOI: https://doi.org/10.1016/j.forsciint.2010.07.009.
140. European Network of Forensic Science Institutes, *ENFSI Guideline for Evaluative Reporting in Forensic Science.* ENSFI, 2015.
141. Maitre, M., Kirkbride, K., Horder, M., Roux, C., and Beavis, A., *Current Perspectives in the Interpretation of Gunshot Residues in Forensic Science: A Review.* Forensic Science International, 2017. **270**: p. 1-11.DOI: https://doi.org/10.1016/j.forsciint.2016.09.003.
142. Romolo, F.S. and Margot, P., *Identification of Gunshot Residue: A Critical Review.* Forensic Science International, 2001. **119**(2): p. 195-211.DOI: https://doi.org/10.1016/S0379-0738(00)00428-X.
143. Feeney, W., Menking-Hoggatt, K., Arroyo, L., Curran, J., Bell, S., and Trejos, T., *Evaluation of Organic and Inorganic Gunshot Residues in Various Populations Using LC-MS/MS.* Forensic Chemistry, 2022. **27**: p. 100389.DOI: https://doi.org/10.1016/j.forc.2021.100389.
144. Menking-Hoggatt, K., Ott, C., Vander Pyl, C., Dalzell, K., Curran, J., Arroyo, L., and Trejos, T., *Prevalence and Probabilistic Assessment of Organic and Inorganic Gunshot Residue and Background Profiles using LIBS, Electrochemistry, and SEM-EDS.* Forensic Chemistry, 2022. **29**: p. 100429.DOI: https://doi.org/10.1016/j.forc.2022.100429.

145. Maitre, M., Horder, M., Kirkbride, K.P., Gassner, A.-L., Weyermann, C., Gupta, A., Beavis, A., and Roux, C., *An Application Example of the Likelihood Ratio Approach to the Evaluation of Organic Gunshot Residues using a Fictional Scenario and Recently Published Data.* Forensic Science International, 2022. **335**: p. 111267.DOI: https://doi.org/10.1016/j.forsciint.2022.111267.
146. Seyfang, K.E., Lucas, N., Redman, K.E., Popelka-Filcoff, R.S., Kobus, H.J., and Kirkbride, K.P., *Glass-Containing Gunshot Residues and Particles of Industrial and Occupational Origins: Considerations for Evaluating GSR Traces.* Forensic Science International, 2019. **298**: p. 284-297.DOI: https://doi.org/10.1016/j.forsciint.2019.03.010.
147. Lindsay, E., McVicar, M.J., Gerard, R.V., Randall, E.D., and Pearson, J., *Passive Exposure and Persistence of Gunshot Residue (GSR) on Bystanders to a Shooting: Comparison of Shooter and Bystander Exposure to GSR.* Canadian Society of Forensic Science Journal, 2011. **44**(3): p. 89-96.DOI: https://doi.org/10.1080/00085030.2011.10768144.
148. Tucker, W., Lucas, N., Seyfang, K.E., Kirkbride, K.P., and Popelka-Filcoff, R.S., *Gunshot Residue and Brakepads: Compositional and Morphological Considerations for Forensic Casework.* Forensic Science International, 2017. **270**: p. 76-82.DOI: https://doi.org/10.1016/j.forsciint.2016.11.024.
149. Berk, R.E., *Automated SEM/EDS Analysis of Airbag Residue. I: Particle Identification.* Journal of Forensic Sciences, 2009. **54**(1): p. 60-68.DOI: https://doi.org/10.1111/j.1556-4029.2008.00918.x.
150. Berk, R.E., *Automated SEM/EDS Analysis of Airbag Residue. II: Airbag Residue as a Source of Percussion Primer Residue Particles.* Journal of Forensic Sciences, 2009. **54**(1): p. 69-76.DOI: https://doi.org/10.1111/j.1556-4029.2008.00919.x.
151. Laflèche, D.J.N., Brière, S.J.J., Faragher, N.F., and Hearns, N.G.R., *Gunshot Residue and Airbags: Part I. Assessing the Risk of Deployed Automotive Airbags to Produce Particles Similar to Gunshot Residue.* Canadian Society of Forensic Science Journal, 2018. **51**(2): p. 48-57.DOI: https://doi.org/10.1080/00085030.2018.1463202.
152. Laflèche, D.J. and Hearns, N.G., *Gunshot Residue and Airbags: Part II. A Case Study.* Canadian Society of Forensic Science Journal, 2019. **52**(1): p. 26-32.DOI: https://doi.org/10.1080/00085030.2018.1543008.
153. Mosher, P., McVicar, M., Randall, E., and Sild, E., *Gunshot Residue-Similar Particles Produced by Fireworks.* Canadian Society of Forensic Science Journal, 1998. **31**(3): p. 157-168.DOI: https://doi.org/10.1080/00085030.1998.10757115.
154. Drzyzga, O., *Diphenylamine and Derivatives in the Environment: A Review.* Chemosphere, 2003. **53**(8): p. 809-818.DOI: https://doi.org/10.1016/S0045-6535(03)00613-1.
155. Brożek-Mucha, Z., *Chemical and Physical Characterisation of Welding Fume Particles for Distinguishing from Gunshot Residue.* Forensic Science International, 2015. **254**: p. 51-58.DOI: https://doi.org/10.1016/j.forsciint.2015.06.033.
156. Lucas, N., Brown, H., Cook, M., Redman, K., Condon, T., Wrobel, H., Kirkbride, K.P., and Kobus, H., *A Study into the Distribution of Gunshot Residue Particles in the Random Population.* Forensic Science International, 2016. **262**: p. 150-155.DOI: https://doi.org/10.1016/j.forsciint.2016.02.050.
157. Stamouli, A., Niewöhner, L., Larsson, M., Colson, B., Uhlig, S., Fojtasek, L., Machado, F., and Gunaratnam, L., *Survey of Gunshot Residue Prevalence on the*

Hands of Individuals from Various Population Groups In and Outside Europe. Forensic Chemistry, 2021. **23**: p. 100308.DOI: https://doi.org/10.1016/j.forc.2021.100308.

158. Blakey, L., Sharples, G.P., Chana, K., and Birkett, J.W., *Environmental Assessment of Gunshot Residue Particles in the Public Domain of the United Kingdom.* Journal of Forensic Sciences, 2023. **68**(4): p. 1107-1444.DOI: DOI: 10.1111/1556-4029.15267.
159. Fedick, P.W. and Bain, R.M., *Swab Touch Spray Mass Spectrometry for Rapid Analysis of Organic Gunshot Residue from Human Hand and Various Surfaces using Commercial and Fieldable Mass Spectrometry Systems.* Forensic Chemistry, 2017. **5**: p. 53-57.DOI: https://doi.org/10.1016/j.forc.2017.06.005.
160. Hearns, N.G.R., Laflèche, D.N., and Sandercock, M.L., *Preparation of a Ytterbium-tagged Gunshot Residue Standard for Quality Control in the Forensic Analysis of GSR.* Journal of Forensic Sciences, 2015. **60**(3): p. 737-742.DOI: https://doi.org/10.1111/1556-4029.12729.
161. Donghi, M., Orsenigo, S., Niewoehner, L., Barth, M., Fiocchi, C., and Pomi, A., *A New Ammunition for Forensic Needs: FIOCCHI-RIS.* Forensic Chemistry, 2019. **13**: p. 100159.DOI: https://doi.org/10.1016/j.forc.2019.100159.
162. Nunziata, F., Romolo, F.S., Burnett, B., Manna, L., Orsenigo, S., and Donghi, M., *Molybdenum in Gunshot Residue: Experimental Evidences and Detection Challenges in the Presence of Lead and Sulfur.* Microscopy and Microanalysis, 2021. **27**(4): p. 666-677.DOI: https://doi.org/10.1017/s1431927621000453.
163. Séguin, K., Falardeau, M., Mousseau, V., Ducharme, N., Cadola, L., and Crispino, F., *First Lessons Regarding the Data Analysis of Gunshot Residue Traces at Activity Level in TTADB.* Canadian Society of Forensic Science Journal, 2021. **54**(4): p. 196-209.DOI: https://doi.org/10.1080/00085030.2021.2007666.
164. French, J. and Morgan, R., *An Experimental Investigation of the Indirect Transfer and deposition of Gunshot Residue: Further Studies Carried out with SEM–EDX Analysis.* Forensic Science International, 2015. **247**: p. 14-17.DOI: https://doi.org/10.1016/j.forsciint.2014.10.023.
165. French, J., Morgan, R., and Davy, J., *The Secondary Transfer of Gunshot Residue: An Experimental Investigation Carried Out with SEM-EDX Analysis.* X-Ray Spectrometry, 2014. **43**(1): p. 56-61.DOI: https://doi.org/10.1002/xrs.2498.
166. Arndt, J., Bell, S., Crookshanks, L., Lovejoy, M., Oleska, C., Tulley, T., and Wolfe, D., *Preliminary Evaluation of the Persistence of Organic Gunshot Residue.* Forensic Science International, 2012. **222**(1): p. 137-145.DOI: https://doi.org/10.1016/j.forsciint.2012.05.011.
167. Lucas, N., Cook, M., Kirkbride, K.P., and Kobus, H., *Gunshot Residue Background on Police Officers: Considerations for Secondary Transfer in GSR Evidence Evaluation.* Forensic Science International, 2019. **297**: p. 293-301.DOI: https://doi.org/10.1016/j.forsciint.2019.02.017.
168. Rosengarten, H., Israelsohn, O., Sirota, N., and Mero, O., *Finding GSR Evidence on used Towels.* Forensic Science International, 2021. **328**: p. 111032.DOI: https://doi.org/10.1016/j.forsciint.2021.111032.
169. Aliste, M. and Chávez, L.G., *Analysis of Gunshot Residues as Trace in Nasal Mucus by GFAAS.* Forensic Science International, 2016. **261**: p. 14-18.DOI: https://doi.org/10.1016/j.forsciint.2016.01.034.

170. Jalanti, T., Henchoz, P., Gallusser, A., and Bonfanti, M.S., *The Persistence of Gunshot Residue on Shooters' Hands.* Science & Justice, 1999. **39**(1): p. 48-52.DOI: https://doi.org/10.1016/S1355-0306(99)72014-9.
171. Parmar, A., Patel, D., Hari, P., Babu, R., and Maity, P., *Efficacy Study of Non-Lanthanide Small Luminescent Molecules as Gunshot Residue Indicators.* Forensic Science International, 2022. **331**: p. 111169.DOI: https://doi.org/10.1016/j.forsciint.2021.111169.
172. Weber, I.T., Terra, I.A.A., Melo, A.J.G.D., Lucena, M.A.D.M., Wanderley, K.A., Paiva-Santos, C.D.O., Antônio, S.G., Nunes, L.A.O., Paz, F.A.A., Sá, G.F.D., Júnior, S.A., and Rodrigues, M.O., *Up-Conversion Properties of Lanthanide-Organic Frameworks and How to Track Ammunitions using these Materials.* RSC Advances, 2012. **2**(7): p. 3083-3087.DOI: https://doi.org/10.1039/c2ra01214f.
173. Lucena, M.M., De Sá, G., Rodrigues, M., Alves, S., Talhavini, M., and Weber, I., *$ZnAl_2O_4$-Based Luminescent Marker for Gunshot Residue Identification and Ammunition Traceability.* Analytical Methods, 2013. **5**(3): p. 705-709.DOI: https://doi.org/10.1039/c2ay25535a.
174. Weber, I., Melo, A., Lucena, M., Consoli, E., Rodrigues, M., de Sá, G., Maldaner, A., Talhavini, M., and Alves Jr, S., *Use of Luminescent Gunshot Residues Markers in Forensic Context.* Forensic Science International, 2014. **244**: p. 276-284.DOI: https://doi.org/10.1016/j.forsciint.2014.09.001.
175. Lucena, M.A.M., Rodrigues, M.O., Gatto, C.C., Talhavini, M., Maldaner, A.O., Alves Jr, S., and Weber, I.T., *Synthesis of [Dy(DPA)(HDPA)] and its Potential as Gunshot Residue Marker.* Journal of Luminescence, 2016. **170**: p. 697-700.DOI: https://doi.org/10.1016/j.jlumin.2015.04.010.
176. Lucena, M.A.M., Oliveira, M.F.L., Arouca, A.M., Talhavini, M., Ferreira, E.A., Alves, S., Veiga-Souza, F.H., and Weber, I.T., *Application of the Metal-Organic Framework [Eu(BTC)] as a Luminescent Marker for Gunshot Residues: A Synthesis, Characterization, and Toxicity Study.* ACS Applied Materials & Interfaces, 2017. **9**(5): p. 4684-4691.DOI: https://doi.org/10.1021/acsami.6b13474.
177. Arouca, A., Lucena, M., Rossiter, R., Talhavini, M., and Weber, I., *Use of Luminescent Gunshot Residues Markers in Forensic Context-Part II.* Forensic Science International, 2017. **281**: p. 161-170.DOI: https://doi.org/10.1016/j.forsciint.2017.09.022.
178. Lucena, M.A., Ordoñez, C., Weber, I.T., Torre, M., García-Ruiz, C., and López-López, M., *Investigation of the Use of Luminescent Markers as Gunshot Residue Indicators.* Forensic Science International, 2017. **280**: p. 95-102.DOI: https://org/10.1016/j.forsciint.2017.09.013.
179. Serwy, I.B., Wanderley, K.A., Lucena, M.A., Maldaner, A.O., Talhavini, M., Rodrigues, M.O., and Weber, I.T., *$[Ln_2(BDC)_3(H_2O)_4]_n$: A Low Cost Alternative for GSR Luminescent Marking.* Journal of Luminescence, 2018. **200**: p. 24-29.DOI: https://doi.org/10.1016/j.jlumin.2018.02.039.
180. Filho, E.V., de Sousa Filho, P.C., Serra, O.A., Weber, I.T., Lucena, M.A.M., and Luz, P., *New Luminescent Lanthanide-Based Coordination Compounds: Synthesis, Studies of Optical Properties and Application as Marker for Gunshot Residues.* Journal of Luminescence, 2018. **202**: p. 89-96.DOI: https://doi.org/10.1016/j.jlumin.2018.05.012.
181. Albino de Carvalho, M., Talhavini, M., Pimentel, M.F., Amigo, J.M., Pasquini, C., Junior, S.A., and Weber, I.T., *NIR Hyperspectral Images for Identification of*

Gunshot Residue from Tagged Ammunition. Analytical Methods, 2018. **10**(38): p. 4711-4717.DOI: https://doi.org/10.1039/C8AY01341A.

182. Lucena, M., Arouca, A., Talhavini, M., Alves-Júnior, S., and Weber, I., *Ammunition Encoding by Means of Co-Doped Luminescent Markers.* Microchemical Journal, 2019. **145**: p. 539-546.DOI: https://doi.org/10.1016/j.microc.2018.09.013.
183. Silva, M.A., de Campos, N.R., Ferreira, L.A., Flores, L.S., Júnior, J.C., dos Santos, G.L., Corrêa, C.C., dos Santos, T.C., Ronconi, C.M., and Colaço, M.V., *A New Photoluminescent Terbium(III) Coordination Network Constructed from 1, 2, 4, 5-Benzenetetracarboxylic Acid: Synthesis, Structural Characterization and Application as a Potential Marker for Gunshot Residues.* Inorganica Chimica Acta, 2019. **495**: p. 118967.DOI: https://doi.org/10.1016/j.ica.2019.118967.
184. Arouca, A.M., Lucena, M.A., Rossiter, R.J., Talhavini, M., and Weber, I.T., *Analysis of Luminescent Gunshot Residue (LGSR) on Different Types of Fabrics.* Journal of Forensic Sciences, 2019. **65**(1): p. 67-72.DOI: https://doi.org/10.1111/1556-4029.14143.
185. Carneiro, C.R., Silva, C.S., de Carvalho, M.A., Pimentel, M.F., Talhavini, M., and Weber, I.T., *Identification of Luminescent Markers for Gunshot Residues: Fluorescence, Raman Spectroscopy, and Chemometrics.* Analytical Chemistry, 2019. **91**(19): p. 12444-12452.DOI: https://doi.org/10.1021/acs.analchem.9b03079.
186. Júnior, J.C.A., dos Santos, G.L., Colaço, M.V., Barroso, R.C., Ferreira, F.F., dos Santos, M.V., de Campos, N.R., Marinho, M.V., Jesus, L.T., Freire, R.O., and Marques, L.F., *New EuIII Pyromellitic Metal-Organic Framework of Intense Red-Orange Luminescence and High Thermal Stability for Marking in Gunshot Residues.* The Journal of Physical Chemistry C, 2020. **124**(18): p. 9996-10006.DOI: https://doi.org/10.1021/acs.jpcc.0c01374.
187. Carneiro, C.R., Silva, C.S., Pimentel, M.F., Talhavini, M., and Weber, I.T., *Application of Luminescent Markers to Ammunition Encoding in Forensic Routine using a Video Spectral Comparator (VSC).* Microchemical Journal, 2020. **159**: p. 105362.DOI: https://doi.org/10.1016/j.microc.2020.105362.
188. Lucena, M.A.M., Câmara, S.S., Talhavini, M., and Weber, I.T., *Yttrium Orthovanadates Phosphors as Up-Conversion Luminescent Markers for Gunshot Residue Identification.* Journal of Luminescence, 2022. **250**: p. 119020.DOI: https://doi.org/10.1016/j.jlumin.2022.119020.
189. de Oliveira Silva, J.l.P., Colaço, M.V., De Souza, L.A., dos Santos, M.V., Pugina, R.S., and Marques, L.F., *Exploring the Intense Lanthanide Luminescence and High Thermal Stability in a New Mixed Eu^{3+}/Tb^{3+} Organic Framework Series for Marking in Gunshot Residues.* The Journal of Physical Chemistry C, 2022. **126**(38): p. 16568-16577.DOI: https://doi.org/10.1021/acs.jpcc.2c05594.
190. Serra, A.R.B., Casagrande, T.R., de Lima, J.F., de Oliveira, M.F., Júnior, S.A., de Oliveira Junior, M., and Serra, O.A., *Synthesis and Structural Characterization of an Amorphous and Photoluminescent Mixed Eu/Zr Coordination Compound, a Potential Marker for Gunshot Residues.* Sci, 2022. **4**(4): p. 43.DOI: https://doi.org/10.3390/sci4040043.
191. Gomes, E.M., De Oliveira Silva, J.P., Colaço, M.V., Cuin, A., Franco, D.F., Scarpari, S.L., De Souza, D.O., Ferreira, M.S., Freire, R.O., and Marques, L.F., *Two Highly Photoluminescent Eu^{3+} β-diketonates Complexes with ε-Caprolactam as Ancillary Ligands: From Synthesis to the First Example as Gunshot Residue Markers.* Optical

Materials, 2023. **137**: p. 113527.DOI: https://doi.org/10.1016/j.optmat.2023.113527.
192. Chedid, A.A., Azevedo, L.S., da Silva Galaço, A.R.B., Casagrande, T.R., Serra, O.A., and de Oliveira, M.F., *Voltammetric Analysis of Luminescent Markers in Gunshot Residues.* Journal of Forensic Sciences, 2023. **68**(3): p. 780-789.DOI: https://doi.org/10.1111/1556-4029.15236.
193. Harshey, A., Das, T., and Srivastava, A., *Analytical Contributions of Lanthanide Based Metal-Organic Frameworks as Luminescent Markers: Recent Trends in Gunshot Residue Analysis.* Microchemical Journal, 2020. **154**: p. 104597.DOI: https://doi.org/10.1016/j.microc.2020.104597.
194. Allendorf, M.D., Bauer, C.A., Bhakta, R.K., and Houk, R.J.T., *Luminescent Metal–Organic Frameworks.* Chemical Society Reviews, 2009. **38**(5): p. 1330-1352.DOI: 10.1039/B802352M.
195. Armelao, L., Quici, S., Barigelletti, F., Accorsi, G., Bottaro, G., Cavazzini, M., and Tondello, E., *Design of Luminescent Lanthanide Complexes: From Molecules to Highly Efficient Photo-Emitting Materials.* Coordination Chemistry Reviews, 2010. **254**(5-6): p. 487-505.DOI: https://doi.org/10.1016/j.ccr.2009.07.025.
196. Cui, Y., Yue, Y., Qian, G., and Chen, B., *Luminescent Functional Metal–Organic Frameworks.* Chemical Reviews, 2011. **112**(2): p. 1126-1162.DOI: https://doi.org/10.1021/cr200101d.
197. James, S.L., *Metal-Organic Frameworks.* Chemical Society Reviews, 2003. **32**(5): p. 276-288.DOI: https://doi.org/10.1039/B200393G.
198. Cook, T.R., Zheng, Y.-R., and Stang, P.J., *Metal–Organic Frameworks and Self-Assembled Supramolecular Coordination Complexes: Comparing and Contrasting the Design, Synthesis, and Functionality of Metal–Organic Materials.* Chemical Reviews, 2012. **113**(1): p. 734-777.DOI: https://doi.org/10.1021/cr3002824.
199. Furukawa, H., Cordova, K.E., O'Keeffe, M., and Yaghi, O.M., *The Chemistry and Applications of Metal-Organic Frameworks.* Science, 2013. **341**(6149): p. 1230444.DOI: https://doi.org/10.1126/science.1230444.
200. Zhu, Q.-L. and Xu, Q., *Metal–Organic Framework Composites.* Chemical Society Reviews, 2014. **43**(16): p. 5468-5512.DOI: https://doi.org/10.1039/C3CS60472A.
201. Guan, H.-Y., LeBlanc, R.J., Xie, S.-Y., and Yue, Y., *Recent Progress in the Syntheses of Mesoporous Metal–Organic Framework Materials.* Coordination Chemistry Reviews, 2018. **369**: p. 76-90.DOI: https://doi.org/10.1016/j.ccr.2018.05.001.
202. Pascanu, V., González Miera, G., Inge, A.K., and Martín-Matute, B.n., *Metal–Organic Frameworks as Catalysts for Organic Synthesis: A Critical Perspective.* Journal of the American Chemical Society, 2019. **141**(18): p. 7223-7234.DOI: https://doi.org/10.1021/jacs.9b00733.
203. Raptopoulou, C.P., *Metal-Organic Frameworks: Synthetic Methods and Potential Applications.* Materials, 2021. **14**(2): p. 310.DOI: https://doi.org/10.3390/ma14020310.
204. Stock, N. and Biswas, S., *Synthesis of Metal-Organic Frameworks (MOFs): Routes to Various MOF Topologies, Morphologies, and Composites.* Chemical Reviews, 2012. **112**(2): p. 933-969.DOI: https://doi.org/10.1021/cr200304e.
205. Liu, B., Vellingiri, K., Jo, S.-H., Kumar, P., Ok, Y.S., and Kim, K.-H., *Recent Advances in Controlled Modification of the Size and Morphology of Metal-Organic Frameworks.* Nano Research, 2018. **11**(9): p. 4441-4467.DOI: https://doi.org/10.1007/s12274-018-2039-3.

206. Li, Z., Zhu, G., Guo, X., Zhao, X., Jin, Z., and Qiu, S., *Synthesis, Structure, and Luminescent and Magnetic Properties of Novel Lanthanide Metal-Organic Frameworks with Zeolite-like Topology.* Inorganic chemistry, 2007. **46**(13): p. 5174-5178.DOI: https://doi.org/10.1021/ic061666i.
207. Wang, Y., Du, H., Xie, J., Gao, Q., and Zhou, J., *Study on White-Light-Emitting Materials of Lanthanide Metal-Organic Frameworks Based on Ligand of 1, 3, 5-Benzenetricarboxylate.* Integrated Ferroelectrics, 2018. **190**(1): p. 20-31.DOI: https://doi.org/10.1080/10584587.2018.1456115.
208. Li, L., Shen, S., Su, J., Ai, W., Bai, Y., and Liu, H., *Facile One-Step Solvothermal Synthesis of a Luminescent Europium Metal-Organic Framework for Rapid and Selective Sensing of Uranyl Ions.* Analytical and Bioanalytical Chemistry, 2019. **411**(18): p. 4213-4220.DOI: https://doi.org/10.1007/s00216-019-01875-2.
209. Pan, Y., Su, H.-Q., Zhou, E.-L., Yin, H.-Z., Shao, K.-Z., and Su, Z.-M., *A Stable Mixed Lanthanide Metal–Organic Framework for Highly Sensitive Thermometry.* Dalton Transactions, 2019. **48**(11): p. 3723-3729.DOI: https://doi.org/10.1039/c9dt00217k.
210. Zhang, P.-F., Yang, G.-P., Li, G.-P., Yang, F., Liu, W.-N., Li, J.-Y., and Wang, Y.-Y., *Series of Water-Stable Lanthanide Metal–Organic Frameworks Based on Carboxylic Acid Imidazolium Chloride: Tunable Luminescent Emission and Sensing.* Inorganic Chemistry, 2019. **58**(20): p. 13969-13978.DOI: https://di.org/10.1021/acs.inorgchem.9b01954.
211. Cheng, X., Hu, J., Li, J., and Zhang, M., *Tunable Emission and Selective Luminescence Sensing for Nitro-Pollutants and Metal Ions Based on Bifunctional Lanthanide Metal-Organic Frameworks.* Journal of Luminescence, 2020. **221**: p. 117100.DOI: https://doi.org/10.1016/j.jlumin.2020.117100.
212. Lu, W., Wei, Z., Gu, Z.-Y., Liu, T.-F., Park, J., Park, J., Tian, J., Zhang, M., Zhang, Q., and Gentle III, T., *Tuning the Structure and Function of Metal–Organic Frameworks via Linker Design.* Chemical Society Reviews, 2014. **43**(16): p. 5561-5593.DOI: https://doi.org/10.1039/C4CS00003J.
213. Sun, Y. and Zhou, H.-C., *Recent Progress in the Synthesis of Metal–Organic Frameworks.* Science and Technology of Advanced Materials, 2015. **16**(5): p. 054202.DOI: https://doi.org/10.1088/1468-6996/16/5/054202.
214. Peh, S.B. and Zhao, D., *Synthesis and Development of Metal–Organic Frameworks*, in *Nanoporous Materials for Molecule Separation and Conversion*. 2020, Elsevier. p. 3-43.
215. Melo, L.L., Castro Jr, G.P., and Gonçalves, S.M., *Substantial Intensification of the Quantum Yield of Samarium (III) Complexes by Mixing Ligands: Microwave-Assisted Synthesis and Luminescence Properties.* Inorganic Chemistry, 2019. **58**(5): p. 3265-3270.DOI: https://doi.org/10.1021/acs.inorgchem.8b03340.
216. Kwon, H.T., Vo, T.K., Kim, J.-H., Kim, W.-S., and Kim, J., *Microwave-Assisted Continuous Flow Synthesis of Mesoporous Metal-Organic Framework MIL-100 (Fe) and its Application to Cu (I)-Loaded Adsorbent for CO/CO_2 Separation.* Materials Chemistry and Physics, 2020. **253**: p. 123278.DOI: https://doi.org/10.1016/j.matchemphys.2020.123278.
217. Wu, R.-Z., Yang, X., Zhang, L.-W., and Zhou, P.-P., *Luminescent Lanthanide Metal–Organic Frameworks for Chemical Sensing and Toxic Anion Detection.* Dalton Transactions, 2017. **46**(30): p. 9859-9867.DOI: https://doi.org/10.1039/C7DT01790A.

218. Gharib, M., Safarifard, V., and Morsali, A., *Ultrasound Assisted Synthesis of Amide Functionalized Metal-Organic Framework for Nitroaromatic Sensing.* Ultrasonics Sonochemistry, 2018. **42**: p. 112-118.DOI: https://doi.org/10.1016/j.ultsonch.2017.11.009.
219. Varsha, M. and Nageswaran, G., *Direct Electrochemical Synthesis of Metal Organic Frameworks.* Journal of The Electrochemical Society, 2020. **167**(15): p. 155527.DOI: https://doi.org/10.1149/1945-7111/abc6c6.
220. Głowniak, S., Szczęśniak, B., Choma, J., and Jaroniec, M., *Mechanochemistry: Toward Green Synthesis of Metal–Organic Frameworks.* Materials Today, 2021. **46**: p. 109-124.DOI: https://doi.org/10.1016/j.mattod.2021.01.008.
221. Rubio-Martinez, M., Avci-Camur, C., Thornton, A.W., Imaz, I., Maspoch, D., and Hill, M.R., *New Synthetic Routes Towards MOF Production at Scale.* Chemical Society Reviews, 2017. **46**(11): p. 3453-3480.DOI: https://doi.org/10.1039/C7CS00109F.
222. Aguiar, L.W., da Silva, C.T.P., de Lima, H.H.C., Moises, M.P., and Rinaldi, A.W., *Evaluation of the Synthetic Methods for Preparing Metal Organic Frameworks with Transition Metals.* AIMS Materials Science, 2018. **5**(3): p. 467-478.DOI: https://doi.org/10.3934/matersci.2018.3.467.
223. Lee, Y.-R., Kim, J., and Ahn, W.-S., *Synthesis of Metal-Organic Frameworks: A Mini Review.* Korean Journal of Chemical Engineering, 2013. **30**(9): p. 1667-1680.DOI: https://doi.org/10.1007/s11814-013-0140-6.
224. Yuan, S., Feng, L., Wang, K., Pang, J., Bosch, M., Lollar, C., Sun, Y., Qin, J., Yang, X., and Zhang, P., *Stable Metal–Organic Frameworks: Design, Synthesis, and Applications.* Advanced Materials, 2018. **30**(37): p. 1704303.DOI: https://doi.org/10.1002/adma.201704303.
225. Müller-Buschbaum, K., *Luminescent MOFs and Frameworks*, in *Reference Module in Chemistry, Molecular Sciences and Chemical Engineering*. 2015, Elsevier.
226. Zhang, Y., Yuan, S., Day, G., Wang, X., Yang, X., and Zhou, H.-C., *Luminescent Sensors Based on Metal-Organic Frameworks.* Coordination Chemistry Reviews, 2018. **354**: p. 28-45.DOI: https://doi.org/10.1016/j.ccr.2017.06.007.
227. Müller-Buschbaum, K., Beuerle, F., and Feldmann, C., *MOF Based Luminescence Tuning and Chemical/Physical Sensing.* Microporous and Mesoporous Materials, 2015. **216**: p. 171-199.DOI: https://doi.org/10.1016/j.micromeso.2015.03.036.
228. Gonzalez, V., Vignati, D.A., Leyval, C., and Giamberini, L., *Environmental Fate and Ecotoxicity of Lanthanides: are they a Uniform Group Beyond Chemistry?* Environment International, 2014. **71**: p. 148-157.DOI: https://doi.org/10.1016/j.envint.2014.06.019.
229. Gwenzi, W., Mangori, L., Danha, C., Chaukura, N., Dunjana, N., and Sanganyado, E., *Sources, Behaviour, and Environmental and Human Health Risks of High-Technology Rare Earth Elements as Emerging Contaminants.* Science of the Total Environment, 2018. **636**: p. 299-313.DOI: https://doi.org/10.1016/j.scitotenv.2018.04.235.
230. Cui, Y., Zhang, J., Chen, B., and Qian, G., *Lanthanide Metal-Organic Frameworks for Luminescent Applications*, in *Handbook on the Physics and Chemistry of Rare Earths*. 2016, Elsevier. p. 243-268.
231. Calderone, P.J., Plonka, A.M., Banerjee, D., Nizami, Q.A., and Parise, J.B., *Lanthanide Metal-Organic Frameworks Based on a Thiophenedicarboxylate*

Linker: Characterization and Luminescence. Solid State Sciences, 2013. **15**: p. 36-41.DOI: https://doi.org/10.1016/j.solidstatesciences.2012.09.005.

232. Bao, G., Wen, S., Lin, G., Yuan, J., Lin, J., Wong, K.-L., Bünzli, J.-C.G., and Jin, D., *Learning from Lanthanide Complexes: The Development of Dye-Lanthanide Nanoparticles and their Biomedical Applications.* Coordination Chemistry Reviews, 2021. **429**: p. 213642.DOI: https://doi.org/10.1016/j.ccr.2020.213642.
233. Zaitoun, M. and Al-Tarawneh, S., *Effect of Varying Lanthanide Local Coordination Sphere on Luminescence Properties Illustrated by Selected Inorganic and Organic Rare Earth Complexes Synthesized in Sol–Gel Host Glasses.* Journal of Luminescence, 2011. **131**(8): p. 1795-1801.DOI: https://doi.org/10.1016/j.jlumin.2011.03.039.
234. Katkova, M.A. and Bochkarev, M.N., *New Trends in Design of Electroluminescent Rare Earth Metallo-Complexes for OLEDs.* Dalton Transactions, 2010. **39**(29): p. 6599-6612.DOI: https://doi.org/10.1039/C001152E.
235. Fordham, S., Wang, X., Bosch, M., and Zhou, H.-C., *Lanthanide Metal-Organic Frameworks: Syntheses, Properties, and Potential Applications*. Structure and Bonding. Vol. 163. 2014. 1-27.
236. Ma, L.N., Liu, Y., Li, Y.Z., Hu, Q.X., Hou, L., and Wang, Y.Y., *Three Lanthanide Metal-Organic Frameworks Based on an Ether-Decorated Polycarboxylic Acid Linker: Luminescence Modulation, CO_2 Capture and Conversion Properties.* Chemistry–An Asian Journal, 2020. **15**(1): p. 191-197.DOI: https://doi.org/10.1002/asia.201901506.
237. Heffern, M.C., Matosziuk, L.M., and Meade, T.J., *Lanthanide Probes for Bioresponsive Imaging.* Chemical Reviews, 2014. **114**(8): p. 4496-4539.DOI: https://doi.org/10.1021/cr400477t.
238. Junker, A.K.R., Hill, L.R., Thompson, A.L., Faulkner, S., and Sørensen, T.J., *Shining Light on the Antenna Chromophore in Lanthanide Based Dyes.* Dalton Transactions, 2018. **47**(14): p. 4794-4803.DOI: https://doi.org/10.1039/C7DT04788F.
239. Samanta, P., Let, S., Mandal, W., Dutta, S., and Ghosh, S.K., *Luminescent Metal–Organic Frameworks (LMOFs) as Potential Probes for the Recognition of Cationic Water Pollutants.* Inorganic Chemistry Frontiers, 2020. **7**(9): p. 1801-1821.DOI: https://doi.org/10.1039/d0qi00167h.
240. Brisdon, A.K., *UV-Visible Spectroscopy*, in *Inorganic Spectroscopic Methods.* . 1998, Oxford Science Publications. p. 70-73.
241. Yin, H.-Q. and Yin, X.-B., *Metal–Organic Frameworks with Multiple Luminescence Emissions: Designs and Applications.* Accounts of Chemical Research, 2020. **53**(2): p. 485-495.DOI: https://doi.org/10.1021/acs.accounts.9b00575.
242. Zhang, Y., Liu, S., Zhao, Z.-S., Wang, Z., Zhang, R., Liu, L., and Han, Z.-B., *Recent Progress in Lanthanide Metal–Organic Frameworks and their Derivatives in Catalytic Applications.* Inorganic Chemistry Frontiers, 2021. **8**(3): p. 590-619.DOI: https://doi.org/10.1039/d0qi01191f.
243. Li, X., Lu, S., Tu, D., Zheng, W., and Chen, X., *Luminescent Lanthanide Metal–Organic Framework Nanoprobes: From Fundamentals to Bioapplications.* Nanoscale, 2020. **12**(28): p. 15021-15035.DOI: https://doi.org/10.1039/d0nr03373a.
244. Li, H., Li, L., Lin, R.-B., Zhou, W., Zhang, Z., Xiang, S., and Chen, B., *Porous Metal-Organic Frameworks for Gas Storage and Separation: Status and Challenges.*

EnergyChem, 2019. **1**(1): p. 100006.DOI: https://doi.org/10.1016/j.enchem.2019.100006.

245. Collins, D.J. and Zhou, H.-C., *Hydrogen Storage in Metal–Organic Frameworks.* Journal of Materials Chemistry, 2007. **17**(30): p. 3154-3160.DOI: https://doi.org/10.1039/B702858J.
246. Yang, D. and Gates, B.C., *Catalysis by Metal Organic Frameworks: Perspective and Suggestions for Future Research.* ACS Catalysis, 2019. **9**(3): p. 1779-1798.DOI: https://doi.org/10.1021/acscatal.8b04515.
247. Zhao, J., Wei, F., Xu, W., and Han, X., *Enhanced Antibacterial Performance of Gelatin/Chitosan Film Containing Capsaicin Loaded MOFs for Food Packaging.* Applied Surface Science, 2020. **510**: p. 145418.DOI: https://doi.org/10.1016/j.apsusc.2020.145418.
248. Wang, H., Lashkari, E., Lim, H., Zheng, C., Emge, T.J., Gong, Q., Yam, K., and Li, J., *The Moisture-Triggered Controlled Release of a Natural Food Preservative from a Microporous Metal–Organic Framework.* Chemical Communications, 2016. **52**(10): p. 2129-2132.DOI: https://doi.org/10.1039/C5CC09634K.
249. Liu, C.-S., Sun, C.-X., Tian, J.-Y., Wang, Z.-W., Ji, H.-F., Song, Y.-P., Zhang, S., Zhang, Z.-H., He, L.-H., and Du, M., *Highly Stable Aluminum-Based Metal-Organic Frameworks as Biosensing Platforms for Assessment of Food Safety.* Biosensors and Bioelectronics, 2017. **91**: p. 804-810.DOI: https://doi.org/10.1016/j.bios.2017.01.059.
250. Horcajada, P., Chalati, T., Serre, C., Gillet, B., Sebrie, C., Baati, T., Eubank, J.F., Heurtaux, D., Clayette, P., Kreuz, C., Chang, J.-S., Hwang, Y.K., Marsaud, V., Bories, P.-N., Cynober, L., Gil, S., Férey, G., Couvreur, P., and Gref, R., *Porous Metal–Organic Framework Nanoscale Carriers as a Potential Platform for Drug Delivery and Imaging.* Nature Materials, 2009. **9**: p. 172.DOI: https://doi.org/10.1038/nmat2608.
251. Sun, C.Y., Qin, C., Wang, C.G., Su, Z.M., Wang, S., Wang, X.L., Yang, G.S., Shao, K.Z., Lan, Y.Q., and Wang, E.B., *Chiral Nanoporous Metal-Organic Frameworks with High Porosity as Materials for Drug Delivery.* Advanced Materials, 2011. **23**(47): p. 5629-5632.DOI: https://doi.org/10.1002/adma.201102538.
252. Chen, X., Tong, R., Shi, Z., Yang, B., Liu, H., Ding, S., Wang, X., Lei, Q., Wu, J., and Fang, W., *MOF Nanoparticles with Encapsulated Autophagy Inhibitor in Controlled Drug Delivery System for Antitumor.* ACS Applied Materials & Interfaces, 2018. **10**(3): p. 2328-2337.DOI: https://doi.org/10.1021/acsami.7b16522.
253. Gandara-Loe, J., Souza, B.E., Missyul, A., Giraldo, G., Tan, J.-C., and Silvestre-Albero, J., *MOF-Based Polymeric Nanocomposite Films as Potential Materials for Drug Delivery Devices in Ocular Therapeutics.* ACS Applied Materials & Interfaces, 2020. **12**(27): p. 30189-30197.DOI: https://doi.org/10.1021/acsami.0c07517.
254. Schnabel, J., Ettlinger, R., and Bunzen, H., *Zn-MOF-74 as pH-Responsive Drug-Delivery System of Arsenic Trioxide.* ChemNanoMat, 2020. **6**(8): p. 1229-1236.DOI: https://doi.org/10.1002/cnma.202000221.
255. Bécue, A. and Champod, C., *Fingermarks and Other Impressions - A Review (July 2013 - July 2016)*, in *18th International Forensic Science Managers Symposium*. 2016: Lyon (France).

256. Bécue, A., Eldridge, H., and Champod, C., *Interpol Review of Fingermarks and Other Body Impressions 2016–2019.* Forensic Science International: Synergy, 2020. **2**: p. 442-480.DOI: https://doi.org/10.1016/j.fsisyn.2020.01.013.
257. Bécue, A., *Emerging Fields in Fingermark (Meta) Detection - A Critical Review.* Analytical Methods, 2016. **8**(45): p. 7983-8003.DOI: https://doi.org/10.1039/C6AY02496C.
258. Chadwick, S., Moret, S., Jayashanka, N., Lennard, C., Spindler, X., and Roux, C., *Investigation of Some of the Factors Influencing Fingermark Detection.* Forensic Science International, 2018. **289**: p. 381-389.DOI: https://doi.org/10.1016/j.forsciint.2018.06.014.
259. Liang, K., Carbonell, C., Styles, M.J., Ricco, R., Cui, J., Richardson, J.J., Maspoch, D., Caruso, F., and Falcaro, P., *Biomimetic Replication of Microscopic Metal–Organic Framework Patterns using Printed Protein Patterns.* Advanced Materials, 2015. **27**(45): p. 7293-7298.DOI: https://doi.org/10.1002/adma.201503167.
260. Moret, S., Scott, E., Barone, A., Liang, K., Lennard, C., Roux, C., and Spindler, X., *Metal-Organic Frameworks for Fingermark Detection—A Feasibility Study.* Forensic Science International, 2018. **291**: p. 83-93.DOI: https://doi.org/10.1016/j.forsciint.2018.08.005.
261. de Jong, R. and de Puit, M., *Fluorescent Metal Organic Frameworks for the Visual Enhancement of Latent Fingermarks.* Forensic Science International, 2018. **291**: p. 12-16.DOI: https://doi.org/10.1016/j.forsciint.2018.07.033.
262. Hafner, M.R., Carraro, F., Brandner, L.A., Maniam, S., Grenci, G., Ljubojevic-Holzer, S., Bischof, H., Malli, R., Borisov, S.M., and Doonan, C., *Fatty Acids as Biomimetic Replication Agents for Luminescent Metal–Organic Framework Patterns.* Chemical Communications, 2020. **56**(84): p. 12733-12736.DOI: https://doi.org/10.1039/d0cc03876h.
263. Kumar, A., Sahoo, S.C., Mehta, S.K., Soni, P., Sharma, V., and Kataria, R., *A Luminescent Zn-MOF for the Detection of Explosives and Development of Fingerprints.* Analytical Methods, 2022. **14**(7): p. 700-707.DOI: https://doi.org/10.1039/d1ay01977e.
264. Lennard, C., *Fingermark Detection and Identification: Current Research Efforts.* Australian Journal of Forensic Sciences, 2020. **52**(2): p. 125-145.DOI: https://doi.org/10.1080/00450618.2018.1474948.
265. Truccolo, G., Boseley, R.E., Lewis, S.W., and Gee, W.J., *Chapter 313 - Forensic Applications of Rare Earths: Anticounterfeiting Materials and Latent Fingerprint Developers*, in *Handbook on the Physics and Chemistry of Rare Earths*. 2020. p. 45-117.
266. Hu, Z., Deibert, B.J., and Li, J., *Luminescent Metal–Organic Frameworks for Chemical Sensing and Explosive Detection.* Chemical Society Reviews, 2014. **43**(16): p. 5815-5840.DOI: https://doi.org/doi.org/10.1039/c4cs00010b.
267. Zhao, Y., Guan, Q.L., Bai, F.Y., Xing, Y.H., and Sun, L.X., *An Inorganic-Organic Hydrogen Cluster: Fluorescence Response of the High Efficient Detection of Fe^{3+}, OH^- and Nitro Explosives.* Journal of Molecular Structure, 2021. **1225**: p. 129115.DOI: https://doi.org/10.1016/j.molstruc.2020.129115.
268. To, K.C., Ben-Jaber, S., and Parkin, I.P., *Recent Developments in the Field of Explosive Trace Detection.* ACS Nano, 2020. **14**(9): p. 10804-10833.DOI: https://doi.org/10.1021/acsnano.0c01579.

269. Hall, N.J. and Wynne, C.D., *Odor Mixture Training Enhances Dogs' Olfactory Detection of Home-Made Explosive Precursors.* Heliyon, 2018. **4**(12): p. e00947.DOI: https://doi.org/10.1016/j.heliyon.2018.e00947.
270. Choi, S.-S. and Son, C.E., *Analytical Method for the Estimation of Transfer and Detection Efficiencies of Solid State Explosives using Ion Mobility Spectrometry and Smear Matrix.* Analytical Methods, 2017. **9**(17): p. 2505-2510.DOI: https://doi.org/10.1039/C7AY00529F.
271. Poliquit, B.Z., Burn, P.L., and Shaw, P.E., *Properties of PDMS-Divinylbenzene Based Pre-Concentrators for Nitroaromatic Vapors.* Journal of Materials Chemistry C, 2020. **8**(47): p. 16967-16973.DOI: https://doi.org/10.1039/d0tc03228j.
272. Moram, S.S.B., Shaik, A.K., Byram, C., Hamad, S., and Soma, V.R., *Instantaneous Trace Detection of Nitro-Explosives and Mixtures with Nanotextured Silicon Decorated with Ag–Au Alloy Nanoparticles using the SERS Technique.* Analytica Chimica Acta, 2020. **1101**: p. 157-168.DOI: https://doi.org/10.1016/j.aca.2019.12.026.
273. Wang, X., Qin, T., Qin, Y., Abdelrahman, A.H., Witte, R.S., and Xin, H., *Microwave-Induced Thermoacoustic Imaging for Embedded Explosives Detection in High-Water Content Medium.* IEEE Transactions on Antennas and Propagation, 2019. **67**(7): p. 4803-4810.DOI: https://doi.org/10.1109/TAP.2019.2908267.
274. Esrafili, L., Gharib, M., Morsali, A., and Retailleau, P., *Rational Morphology Control of Nano-Scale Amide Decorated Metal-Organic Frameworks by Ultrasonic Method: Capability to Selective and Sensitive Detection of Nitro Explosives.* Ultrasonics Sonochemistry, 2020: p. 105110.DOI: https://doi.org/10.1016/j.ultsonch.2020.105110.
275. Ju, P., Yang, H., Jiang, L., Li, M., Yu, Y., and Zhang, E., *A Novel High Sensitive Cd-MOF Fluorescent Probe for Acetone Vapor in Air and Picric Acid in Water: Synthesis, Structure and Sensing Properties.* Spectrochimica Acta Part A: Molecular and Biomolecular Spectroscopy, 2021. **246**: p. 118962.DOI: https://doi.org/10.1016/j.saa.2020.118962.
276. Jiang, B., Liu, W., Liu, S., and Liu, W., *Coumarin-Encapsulated MOF Luminescence Sensor for Detection of Picric Acid in Water Environment.* Dyes and Pigments, 2021. **184**: p. 108794.DOI: https://doi.org/10.1016/j.dyepig.2020.108794.
277. Song, J.H. and Kang, D.W., *Hazardous Nitroaromatic Explosives Detection by Emerging Porous Solid Sensors.* Coordination Chemistry Reviews, 2023. **492**: p. 215279.DOI: https://doi.org/10.1016/j.ccr.2023.215279.
278. Zeng, X.-S., Xu, H.-L., Xu, Y.-C., Li, X.-Q., Nie, Z.-Y., Gao, S.-Z., and Xiao, D.-R., *A Series of Porous Interpenetrating Metal–Organic Frameworks based on Fluorescent Ligands for Nitroaromatic Explosive Detection.* Inorganic Chemistry Frontiers, 2018.DOI: https://doi.org/10.1039/c8qi00123e.
279. Gole, B., Bar, A.K., and Mukherjee, P.S., *Fluorescent Metal–Organic Framework for Selective Sensing of Nitroaromatic Explosives.* Chemical Communications, 2011. **47**(44): p. 12137-12139.DOI: https://doi.org/10.1039/c1cc15594f.
280. Lan, A., Li, K., Wu, H., Olson, D.H., Emge, T.J., Ki, W., Hong, M., and Li, J., *A Luminescent Microporous Metal–Organic Framework for the Fast and Reversible Detection of High Explosives.* Angewandte Chemie, 2009. **121**(13): p. 2370-2374.DOI: https://doi.org/10.1002/anie.200804853.

281. Fu, H.-R., Yan, L.-B., Wu, N.-T., Ma, L.-F., and Zang, S.-Q., *Dual-Emission MOF ⊃ Dye Sensor for Ratiometric Fluorescence Recognition of RDX and Detection of a Broad Class of Nitro-Compounds.* Journal of Materials Chemistry A, 2018. **6**(19): p. 9183-9191.DOI: https://doi.org/10.1039/C8TA02857E.
282. Mukherjee, S., Desai, A.V., Manna, B., Inamdar, A.I., and Ghosh, S.K., *Exploitation of Guest Accessible Aliphatic Amine Functionality of a Metal–Organic Framework for Selective Detection of 2, 4, 6-Trinitrophenol (TNP) in Water.* Crystal Growth & Design, 2015. **15**(9): p. 4627-4634.DOI: https://doi.org/10.1021/acs.cgd.5b00902.
283. Abuzalat, O., Wong, D., Park, S.S., and Kim, S., *Highly Selective and Sensitive Fluorescent Zeolitic Imidazole Frameworks Sensor for Nitroaromatic Explosive Detection.* Nanoscale, 2020. **12**(25): p. 13523-13530.DOI: https://doi.org/10.1039/d0nr01653e.
284. Wang, C., Tian, L., Zhu, W., Wang, S., Wang, P., Liang, Y., Zhang, W., Zhao, H., and Li, G., *Dye@ Bio-MOF-1 Composite as a Dual-Emitting Platform for Enhanced Detection of a Wide Range of Explosive Molecules.* ACS Applied Materials & Interfaces, 2017. **9**(23): p. 20076-20085.DOI: https://doi.org/10.1021/acsami.7b04172.
285. Mukherjee, S., Ganguly, S., Chakraborty, A., Mandal, A., and Das, D., *Green Synthesis of Self Assembled Nanospherical Dysprosium MOFs: Selective and Efficient Detection of Picric Acid in Aqueous and Gas Phase.* ACS Sustainable Chemistry & Engineering, 2018. **7**(1): p. 819-830.DOI: https://doi.org/10.1021/acssuschemeng.8b04429.
286. Yang, L., Liu, Y.-L., Liu, C.-G., Ye, F., and Fu, Y., *A Luminescent Sensor Based on a New Cd-MOF for Nitro Explosives and Organophosphorus Pesticides Detection.* Inorganic Chemistry Communications, 2020. **122**: p. 108272.DOI: https://doi.org/10.1016/j.inoche.2020.108272.
287. Li, H., Chen, Q., Zhang, Z., Wang, Z., Gong, Z., and Fan, M., *Functionalized Fluorescent Zr-MOF Based on Photoinduced Electron Transfer for Highly Sensitive Detection of Nitroaromatic Explosives.* Dyes and Pigments, 2023. **210**: p. 111035.DOI: https://doi.org/10.1016/j.dyepig.2022.111035.
288. Sun, Q., Yang, K., Ma, W., Zhang, L., and Yuan, G., *A Highly Stable 8-Hydroxyquinolinate-Based Metal–Organic Framework as a Selective Fluorescence Sensor for Fe^{3+}, $Cr_2O_7^{2-}$ and Nitroaromatic Explosives.* Inorganic Chemistry Frontiers, 2020. **7**(22): p. 4387-4395.DOI: https://doi.org/10.1039/D0QI01032D.
289. Sun, X., Li, X., Yao, S., Krishna, R., Gu, J., Li, G., and Liu, Y., *A Multifunctional Double Walled Zirconium Metal–Organic Framework: High Performance for CO 2 Adsorption and Separation and Detecting Explosives in the Aqueous Phase.* Journal of Materials Chemistry A, 2020. **8**(33): p. 17106-17112.DOI: https://doi.org/10.1039/d0ta04778c.
290. Qiu, Z.-J., Fan, S.-T., Xing, C.-Y., Song, M.-M., Nie, Z.-J., Xu, L., Zhang, S.-X., Wang, L., Zhang, S., and Li, B.-J., *Facile Fabrication of an AIE-Active Metal–Organic Framework for Sensitive Detection of Explosives in Liquid and Solid Phases.* ACS Applied Materials & Interfaces, 2020.DOI: https://doi.org/10.1021/acsami.0c17165.
291. Devi, S., Shaswat, S., Kumar, V., Sachdev, A., Gopinath, P., and Tyagi, S., *Nitrogen-Doped Carbon Quantum Dots Conjugated Isoreticular Metal-Organic Framework-3 Particles Based Luminescent Probe for Selective Sensing of Trinitrotoluene*

Explosive. Microchimica Acta, 2020. **187**: p. 1-10.DOI: https://doi.org/10.1007/s00604-020-04496-0.

292. He, N., Gao, M., Shen, D., Li, H., Han, Z., and Zhao, P., *Rapid Visual Detection of Nitroaromatic Explosives using a Luminescent Europium-Organic Framework Material.* Forensic Science International, 2019. **297**: p. 1-7.DOI: https://doi.org/10.1016/j.forsciint.2019.01.004.
293. Nagarkar, S.S., Joarder, B., Chaudhari, A.K., Mukherjee, S., and Ghosh, S.K., *Highly Selective Detection of Nitro Explosives by a Luminescent Metal–Organic Framework.* Angewandte Chemie, 2013. **125**(10): p. 2953-2957.DOI: https://doi.org/10.1002/ange.201208885.
294. Mondal, P. and Rath, S.P., *Highly Selective and Sensitive Detection of Picric Acid Explosive by a Bisporphyrin Cleft: Synergistic Effects of Encapsulation, Efficient Electron Transfer, and Hydrogen Bonding.* European Journal of Inorganic Chemistry, 2015. **2015**(29): p. 4956-4964.DOI: https://doi.org/10.1002/ejic.201500645.
295. Majeed, S., Junaid, H.M., Waseem, M.T., Khan, Z.A., Khan, A.M., and Shahzad, S.A., *Mechanochromic and AIE Active Fluorescent Probes for Solution and Vapor Phase Detection of Picric Acid: Application of Logic Gate.* Journal of Photochemistry and Photobiology A: Chemistry, 2022. **432**: p. 114057.DOI: https://doi.org/10.1016/j.jphotochem.2022.114057.
296. Beatty, M.A., Selinger, A.J., Li, Y., and Hof, F., *Parallel Synthesis and Screening of Supramolecular Chemosensors that Achieve Fluorescent Turn-On Detection of Drugs in Saliva.* Journal of the American Chemical Society, 2019. **141**(42): p. 16763-16771.DOI: https://doi.org/10.1021/jacs.9b07073.
297. Du, X., Hao, H., Qin, A., and Tang, B.Z., *Highly Sensitive Chemosensor for Detection of Methamphetamine by the Combination of AIE Luminogen and Cucurbit [7] Uril.* Dyes and Pigments, 2020. **180**: p. 108413.DOI: https://doi.org/10.1016/j.dyepig.2020.108413.
298. Gill, A.D., Hickey, B.L., Zhong, W., and Hooley, R.J., *Selective Sensing of THC and Related Metabolites in Biofluids by Host: Guest Arrays.* Chemical Communications, 2020. **56**(31): p. 4352-4355.DOI: https://doi.org/10.1039/d0cc01489c.
299. Rosa-Gastaldo, D., Scopano, A., Zaramella, M., and Mancin, F., *Nanoscale Supramolecular Probes for the Naked-Eye Detection of Illicit Drugs.* ACS Applied Nano Materials, 2020. **3**(10): p. 9616-9621.DOI: https://doi.org/10.1021/acsanm.0c02370.
300. Clancy, L., Philp, M., Shimmon, R., and Fu, S., *Development and Validation of a Color Spot Test Method for the Presumptive Detection of 25-NBOMe Compounds.* Drug Testing and Analysis, 2020.DOI: https://doi.org/10.1002/dta.2905.
301. Chen, M., Burn, P.L., and Shaw, P.E., *Luminescence-Based Detection and Identification of Illicit Drugs.* Physical Chemistry Chemical Physics, 2023. **25**(19): p. 13244-13259.DOI: 10.1039/D3CP00524K.
302. Zhang, S., Yao, W., Fu, D., Zhang, C., and Zhao, H., *Fabrication of Magnetic Zinc Adeninate Metal–Organic Frameworks for the Extraction of Benzodiazepines from Urine and Wastewater.* Journal of Separation Science, 2018. **41**(8): p. 1864-1870.DOI: https://doi.org/10.1002/jssc.201701226.
303. Alhaddad, M. and Sheta, S.M., *Dual Naked-Eye and Optical Chemosensor for Morphine Detection in Biological Real Samples Based on Cr(III) Metal–Organic*

Framework Nanoparticles. ACS Omega, 2020. **5**(43): p. 28296-28304.DOI: https://doi.org/10.1021/acsomega.0c04249.

304. Guo, G., Wang, T., Ding, X., Wang, H., Wu, Q., Zhang, Z., Ding, S., Li, S., and Li, J., *Fluorescent Lanthanide Metal-Organic Framework for Rapid and Ultrasensitive Detection of Methcathinone in Human Urine.* Talanta, 2022. **249**: p. 123663.DOI: https://doi.org/10.1016/j.talanta.2022.123663.
305. Zhang, Y. and Yan, B., *A Novel Cucurbit [7] Uril Anchored Bis-Functionalized Metal-Organic Framework Hybrid and its Potential use in Fluorescent Analysis of Illegal Stimulants in Saliva.* Sensors and Actuators B: Chemical, 2020. **324**: p. 128656.DOI: https://doi.org/10.1016/j.snb.2020.128656.
306. Li, X., Sun, L., Xu, B., Dai, L., Xiao, Y., Ding, Y., Liu, Q., Meng, M., Xi, R., Guo, L., and Yin, Y., *MOF-Gold Core-Satellite Nanostructure Based SERS Platform for Fentanyl Detection in Multiple Complex Samples.* Sensors and Actuators B: Chemical, 2023. **385**: p. 133710.DOI: https://doi.org/10.1016/j.snb.2023.133710.
307. Liu, C.-S., Li, J., and Pang, H., *Metal-Organic Framework-Based Materials as an Emerging Platform for Advanced Electrochemical Sensing.* Coordination Chemistry Reviews, 2020. **410**: p. 213222.DOI: https://doi.org/10.1016/j.ccr.2020.213222.
308. Bilge, S., Dogan-Topal, B., Gürbüz, M.M., Yücel, A., Sınağ, A., and Ozkan, S.A., *Recent Advances in Electrochemical Sensing of Cocaine: A Review.* TrAC Trends in Analytical Chemistry, 2022. **157**: p. 116768.DOI: https://doi.org/10.1016/j.trac.2022.116768.
309. Su, F., Zhang, S., Ji, H., Zhao, H., Tian, J.-Y., Liu, C.-S., Zhang, Z., Fang, S., Zhu, X., and Du, M., *Two-Dimensional Zirconium-Based Metal–Organic Framework Nanosheet Composites Embedded with Au Nanoclusters: A Highly Sensitive Electrochemical Aptasensor toward Detecting Cocaine.* ACS Sensors, 2017. **2**(7): p. 998-1005.DOI: https://doi.org/10.1021/acssensors.7b00268.
310. Naghian, E., Marzi Khosrowshahi, E., Sohouli, E., Ahmadi, F., Rahimi-Nasrabadi, M., and Safarifard, V., *A New Electrochemical Sensor for the Detection of Fentanyl Lethal Drug by a Screen-Printed Carbon Electrode Modified with the Open-Ended Channels of Zn(ii)-MOF.* New Journal of Chemistry, 2020. **44**(22): p. 9271-9277.DOI: https://doi.org/10.1039/D0NJ01322F.
311. Fu, K., Zhang, R., He, J., Bai, H., and Zhang, G., *Sensitive Detection of Ketamine with an Electrochemical Sensor Based on UV-Induced Polymerized Molecularly Imprinted Membranes at Graphene and MOFs Modified Electrode.* Biosensors and Bioelectronics, 2019. **143**: p. 111636.DOI: https://doi.org/10.1016/j.bios.2019.111636.
312. Mousaabadi, K.Z., Ensafi, A.A., and Rezaei, B., *Simultaneous Determination of Some Opioid Drugs Using Cu-hemin MOF@MWCNTs as an Electrochemical Sensor.* Chemosphere, 2022. **303**: p. 135149.DOI: https://doi.org/10.1016/j.chemosphere.2022.135149.
313. Cao, Q., Jiang, D., Xu, F., Wen, J., Wang, W., Shiigi, H., and Chen, Z., *Au-Doped MOFs Catalyzed ElectrochemiluminEscence Platform Coupled with Target-Induced Self-Enrichment for Detection of Synthetic Cannabinoid RCS-4.* Microchimica Acta, 2022. **189**(9): p. 313.DOI: https://doi.org/10.1007/s00604-022-05397-0.

314. Suo, H., Zhu, Q., Zhang, X., Chen, B., Chen, J., and Wang, F., *High-Security Anti-Counterfeiting Through Upconversion Luminescence.* Materials Today Physics, 2021. **21**: p. 100520.DOI: https://doi.org/10.1016/j.mtphys.2021.100520.
315. Zhou, H., Han, J., Cuan, J., and Zhou, Y., *Responsive Luminescent MOF Materials for Advanced Anticounterfeiting.* Chemical Engineering Journal, 2022. **431**: p. 134170.DOI: https://doi.org/10.1016/j.cej.2021.134170.
316. Yiu, Y.C. and Chu, Z., *A Multilevel Optical Anticounterfeiting System Based on Color Space-Correlated Raman Spectroscopy of Diamond.* Advanced Photonics Research, 2023. **4**(4): p. 2200281.DOI: https://doi.org/10.1002/adpr.202200281.
317. Deneff, J.I., Butler, K.S., Rohwer, L.E., Pearce, C.J., Valdez, N.R., Rodriguez, M.A., Luk, T.S., and Sava Gallis, D.F., *Encoding Multilayer Complexity in Anti-Counterfeiting Heterometallic MOF-Based Optical Tags.* Angewandte Chemie International Edition, 2021. **60**(3): p. 1203-1211.DOI: https://doi.org/10.1002/ange.202013012.
318. Li, Z., Núñez, R., Light, M.E., Ruiz, E., Teixidor, F., Viñas, C., Ruiz-Molina, D., Roscini, C., and Planas, J.G., *Water-Stable Carborane-Based Eu^{3+}/Tb^{3+} Metal–Organic Frameworks for Tunable Time-Dependent Emission Color and Their Application in Anticounterfeiting Bar-Coding.* Chemistry of Materials, 2022. **34**(10): p. 4795-4808.DOI: https://doi.org/10.1021/acs.chemmater.2c00323.
319. Liu, P., Zhang, Y., Li, B., Han, L., and Xu, Y., *Trap Depth Engineering in MgGa2O4: Bi^{3+} for Muticolor Dynamic Anti-Counterfeiting, Encryption and Optical Temperature Sensing Applications.* Chemical Engineering Journal, 2022. **437**: p. 135389.DOI: https://doi.org/10.1016/j.cej.2022.135389.
320. Gao, M., Li, J., Lu, X., Li, R., Hong, C., Zhao, S., and Li, G., *Lanthanides-Based Invisible Multicolor Luminescent Hydrogels and Films for Anti-Counterfeiting.* Inorganica Chimica Acta, 2024. **560**: p. 121813.DOI: https://doi.org/10.1016/j.ica.2023.121813.
321. Gao, Z., Xu, B., Zhang, T., Liu, Z., Zhang, W., Sun, X., Liu, Y., Wang, X., Wang, Z., and Yan, Y., *Spatially Responsive Multicolor Lanthanide-MOF Heterostructures for Covert Photonic Barcodes.* Angewandte Chemie, 2020. **132**(43): p. 19222-19226.DOI: https://doi.org/10.1002/ange.202009295.
322. Gao, Z., Yang, S., Xu, B., Zhang, T., Chen, S., Zhang, W., Sun, X., Wang, Z., Wang, X., Meng, X., and Zhao, Y.S., *Laterally Engineering Lanthanide-MOFs Epitaxial Heterostructures for Spatially Resolved Planar 2D Photonic Barcoding.* Angewandte Chemie International Edition, 2021. **60**(46): p. 24519-24525.DOI: https://doi.org/10.1002/anie.202109336.
323. Yao, Y., Gao, Z., Lv, Y., Lin, X., Liu, Y., Du, Y., Hu, F., and Zhao, Y.S., *Heteroepitaxial Growth of Multiblock Ln-MOF Microrods for Photonic Barcodes.* Angewandte Chemie International Edition, 2019. **58**(39): p. 13803-13807.DOI: https://doi.org/10.1002/anie.201907433.
324. Liu, X.-T., Wang, K., Chang, Z., Zhang, Y.-H., Xu, J., Zhao, Y.S., and Bu, X.-H., *Engineering Donor–Acceptor Heterostructure Metal–Organic Framework Crystals for Photonic Logic Computation.* Angewandte Chemie International Edition, 2019. **58**(39): p. 13890-13896.DOI: https://doi.org/10.1002/anie.201906278.
325. Macrino, C.J., Silva, E.M., Cunha, V.R., Fonseca, V.R., Cunha Neto, Á., Araújo, J.R., Lacerda Jr, V., and Romão, W., *Synthesis, Characterization, and Application of Europium (III) Complexes as Luminescent Markers of Banknotes.* Journal of the

Brazilian Chemical Society, 2021. **32**: p. 1070-1081.DOI: https://doi.org/10.21577/0103-5053.20210010.

326. Kumar, P., Singh, S., and Gupta, B.K., *Future Prospects of Luminescent Nanomaterial Based Security Inks: from Synthesis to Anti-Counterfeiting Applications.* Nanoscale, 2016. **8**(30): p. 14297-14340.DOI: https://doi.org/10.1039/C5NR06965C.
327. Jones, P. and Nesbitt, R., *A Photoluminescence Technique for Detection of Gunshot Residue.* Journal of Forensic Science, 1975. **20**(2): p. 231-242.DOI: https://doi.org/10.1520/JFS10269J.
328. Nesbitt, R., Wessel, J., Wolten, G., and Jones, P., *Evaluation of a Photoluminescence Technique for the Detection of Gunshot Residue.* Journal of Forensic Science, 1977. **22**(2): p. 288-303.DOI: https://doi.org/10.1520/JFS10590J.
329. Gabriele, I., Race, M., Papirio, S., and Esposito, G., *Phytoremediation of Pyrene-Contaminated Soils: A Critical Review of The Key Factors Affecting the Fate of Pyrene.* Journal of Environmental Management, 2021. **293**: p. 112805.DOI: https://doi.org/10.1016/j.jenvman.2021.112805.
330. Martín-Rodríguez, R., Valiente, R., Polizzi, S., Bettinelli, M., Speghini, A., and Piccinelli, F., *Upconversion Luminescence in Nanocrystals of $Gd_3Ga_5O_{12}$ and $Y_3Al_5O_{12}$ doped with Tb^{3+}–Yb^{3+} and Eu^{3+}–Yb^{3+}.* The Journal of Physical Chemistry C, 2009. **113**(28): p. 12195-12200.DOI: https://doi.org/10.1021/jp901711g.
331. Masoomi, M.Y., Morsali, A., Dhakshinamoorthy, A., and Garcia, H., *Mixed-Metal MOFs: Unique Opportunities in Metal–Organic Framework (MOF) Functionality and Design.* Angewandte Chemie International Edition, 2019. **58**(43): p. 15188-15205.DOI: https://doi.org/10.1002/anie.201902229.
332. Abednatanzi, S., Derakhshandeh, P.G., Depauw, H., Coudert, F.-X., Vrielinck, H., Van Der Voort, P., and Leus, K., *Mixed-Metal Metal–Organic Frameworks.* Chemical Society Reviews, 2019. **48**(9): p. 2535-2565.DOI: https://doi.org/10.1039/C8CS00337H.
333. Cadman, L.K., Mahon, M.F., and Burrows, A.D., *The Effect of Metal Distribution on the Luminescence Properties of Mixed-Lanthanide Metal–Organic Frameworks.* Dalton Transactions, 2018. **47**(7): p. 2360-2367.DOI: https://doi.org/10.1039/C7DT04583B.
334. Xu, J., Liu, J., Li, Z., Wang, X., Xu, Y., Chen, S., and Wang, Z., *Optimized Synthesis of Zr (IV) Metal Organic Frameworks (MOFs-808) for Efficient Hydrogen Storage.* New Journal of Chemistry, 2019. **43**(10): p. 4092-4099.DOI: https://doi.org/10.1039/c8nj06362a.
335. Rodrigues, M.O., Brito-Silva, A.M., Alves Júnior, S., Simone, C.A.D., Araújo, A.A.S., Carvalho, P.H.V.d., Santos, S.C.G., Aragão, K.A.S., Freire, R.O., and Mesquita, M.E., *Structural and Spectroscopic Studies of the 2D Coordination Polymers,∞[Tb(DPA)(HDPA)] and ∞[Gd (DPA)(HDPA)].* Química Nova, 2009. **32**(2): p. 286-291.DOI: https://doi.org/10.1590/S0100-40422009000200004.
336. Fernandes, A., Jaud, J., Dexpert-Ghys, J., and Brouca-Cabarrecq, C., *Study of New Lanthanide Complexes of 2,6-Pyridinedicarboxylate: Synthesis, Crystal Structure of Ln(Hdipic)(dipic) with Ln=Eu, Gd, Tb, Dy, Ho, Er, Yb, Luminescence Properties of Eu(Hdipic)(dipic).* Polyhedron, 2001. **20**(18): p. 2385-2391.DOI: https://doi.org/10.1016/S0277-5387(01)00841-5.

337. Ratnayake, S.P., *Characterization Studies of Ceramic-Based Composites Related to Functionalized Filler-Matrix Interface*, in *Interfaces in Particle and Fibre Reinforced Composites*. 2020, Elsevier. p. 369-389.
338. Barrios, V.A.E., Méndez, J.R.R., Aguilar, N.V.P., Espinosa, G.A., and Rodríguez, J.L.D., *FTIR - An Essential Characterization Technique for Polymeric Materials.* Infrared Spectroscopy-Materials Science, Engineering and Technology, 2012: p. 195-214.DOI: https://doi.org/10.5772/36044.
339. Ali, S.M., Bonnier, F., Lambkin, H., Flynn, K., McDonagh, V., Healy, C., Lee, T., Lyng, F., and Byrne, H., *A Comparison of Raman, FTIR and ATR-FTIR Micro Spectroscopy for Imaging Human Skin Tissue Sections.* Analytical Methods, 2013. **5**(9): p. 2281-2291.DOI: https://doi.org/10.1039/C3AY40185E.
340. Silva, I.G.N., Cunha, C.S., Morais, A.F., Brito, H.F., and Mustafa, D., *Eu^{3+} or Sm^{3+}-Doped Terbium-Trimesic Acid MOFs: Highly Efficient Energy Transfer Anhydrous Luminophors.* Optical Materials, 2018. **84**: p. 123-129.DOI: https://doi.org/10.1016/j.optmat.2018.06.065.
341. Gršković, B., Zrnec, D., Popović, M., Petek, M.J., Primorac, D., and Mršić, G., *Effect of Ultraviolet C Radiation on Biological Samples.* Croatian Medical Journal, 2013. **54**(3): p. 263-271.DOI: https://doi.org/10.3325/cmj.2013.54.263.
342. Çubuk, M.C., *Utilisation of Ultraviolet Light for Detection and Enhancement of Latent Prints.* Z Zagadnien Nauk Sadowych, 2002. **51**: p. 150-154.
343. Arora, H. and Tosti, A., *Safety and Efficacy of Nail Products.* Cosmetics, 2017. **4**(3): p. 24.DOI: https://doi.org/10.3390/cosmetics4030024.
344. Markova, A. and Weinstock, M.A., *Risk of Skin Cancer Associated with the use of UV Nail Lamp.* The Journal of Investigative Dermatology, 2013. **133**(4): p. 1097.DOI: https://doi.org/10.1038/jid.2012.440.
345. Shipp, L.R., Warner, C.A., Rueggeberg, F.A., and Davis, L.S., *Further Investigation into the Risk of Skin Cancer Associated with the use of UV Nail Lamps.* JAMA Dermatology, 2014. **150**(7): p. 775-776.DOI: https://doi.org/10.1001/jamadermatol.2013.8740.
346. Manley, M., *Near-Infrared Spectroscopy and Hyperspectral Imaging: Non-Destructive Analysis of Biological Materials.* Chemical Society Reviews, 2014. **43**(24): p. 8200-8214.DOI: https://doi.org/10.1039/c4cs00062e.
347. Destefani, C.A., Motta, L.C., Costa, R.A., Macrino, C.J., Bassane, J.F.P., Filho, J.F.A., Silva, E.M., Greco, S.J., Carneiro, M.T.W.D., Endringer, D.C., and Romão, W., *Evaluation of Acute Toxicity of Europium–Organic Complex Applied as a Luminescent marker for the Visual Identification of Gunshot Residue.* Microchemical Journal, 2016. **124**: p. 195-200.DOI: https://doi.org/10.1016/j.microc.2015.08.021.
348. Gawande, M.B., Shelke, S.N., Zboril, R., and Varma, R.S., *Microwave-Assisted Chemistry: Synthetic Applications for Rapid Assembly of Nanomaterials and Organics.* Accounts of Chemical Research, 2014. **47**(4): p. 1338-1348.DOI: https://doi.org/10.1021/ar400309b.
349. Peh, S.B. and Zhao, D., *Synthesis and Development of Metal-Organic Frameworks*, in *Nanoporous Materials for Molecule Separation and Conversion*. 2020, Elsevier. p. 3-43.
350. Mottillo, C. and Friščić, T., *Advances in Solid-State Transformations of Coordination Bonds: From the Ball Mill to the Aging Chamber.* Molecules, 2017. **22**(1): p. 144.DOI: https://doi.org/10.3390/molecules22010144.

351. Remya, V.R. and Kurian, M., *Synthesis and Catalytic Applications of Metal-Organic Frameworks: A Review on Recent Literature.* International Nano Letters, 2019. **9**(1): p. 17-29.DOI: 10.1007/s40089-018-0255-1.
352. Klinowski, J., Paz, F.A.A., Silva, P., and Rocha, J., *Microwave-Assisted Synthesis of Metal-Organic Frameworks.* Dalton Transactions, 2011. **40**(2): p. 321-330.DOI: https://doi.org/10.1039/C0DT00708K.
353. Siddiqui, M.T.H., Chan, F.L., Nizamuddin, S., Baloch, H.A., Kundu, S., Czajka, M., Griffin, G., Tanksale, A., Shah, K., and Srinivasan, M., *Comparative Study of Microwave and Conventional Solvothermal Synthesis for Magnetic Carbon Nanocomposites and Bio-Oil from Rice Husk.* Journal of Environmental Chemical Engineering, 2019. **7**(4): p. 103266.DOI: https://doi.org/10.1016/j.jece.2019.103266.
354. Ryu, U., Jee, S., Rao, P.C., Shin, J., Ko, C., Yoon, M., Park, K.S., and Choi, K.M., *Recent Advances in Process Engineering and Upcoming Applications of Metal–Organic Frameworks.* Coordination Chemistry Reviews, 2021. **426**: p. 213544.DOI: https://doi.org/10.1016/j.ccr.2020.213544.
355. de la Hoz, A., Díaz-Ortiz, Á., and Moreno, A., *Microwaves in Organic Synthesis. Thermal and Non-Thermal Microwave Effects.* Chemical Society Reviews, 2005. **34**(2): p. 164-178.DOI: https://doi.org/10.1039/B411438H.
356. Seetharaj, R., Vandana, P.V., Arya, P., and Mathew, S., *Dependence of Solvents, pH, Molar Ratio and Temperature in Tuning Metal-Organic Framework Architecture.* Arabian Journal of Chemistry, 2019. **12**(3): p. 295-315.DOI: https://doi.org/10.1016/j.arabjc.2016.01.003.
357. Mendes, R.F., Rocha, J., and Almeida Paz, F.A., *Chapter 8 - Microwave Synthesis of Metal-Organic Frameworks*, in *Metal-Organic Frameworks for Biomedical Applications*, M. Mozafari, Editor. 2020, Woodhead Publishing. p. 159-176.
358. de la Hoz, A., Díaz-Ortiz, A., and Prieto, P., *Chapter 1 - Microwave-Assisted Green Organic Synthesis*, in *Alternative Energy Sources for Green Chemistry*. 2016, The Royal Society of Chemistry. p. 1-33.
359. Basu, S., *Formation of Gunshot Residues.* Journal of Forensic Science, 1982. **27**(1): p. 72-91.DOI: doi.org/10.1520/JFS11453J.
360. Flynn, J., Stoilovic, M., Lennard, C., Prior, I., and Kobus, H., *Evaluation of X-ray Microfluorescence Spectrometry for the Elemental Analysis of Firearm Discharge Residues.* Forensic Science International, 1998. **97**(1): p. 21-36.DOI: http://doi.org/10.1016/S0379-0738(98)00127-3.
361. Vogelsanger, B., Ossola, B., Schädeli, U., Antenen, D., and Ryf, K. *Ballistic Shelf Life of Propellants for Medium and Small Calibre Ammunition – Influence Of Deterrent Diffusion And Nitrocellulose Degradation*. 2001.
362. Klerk, W., *Assessment of Stability of Propellants and Safe Lifetimes.* Propellants, Explosives, Pyrotechnics, 2015. **40**: p. 388-393.DOI: https://doi.org/10.1002/prep.201500040.
363. Trache, D. and Tarchoun, A.F., *Analytical Methods for Stability Assessment of Nitrate Esters-Based Propellants.* Critical Reviews in Analytical Chemistry, 2019. **49**(5): p. 415-438.DOI: https://doi.org/10.1080/10408347.2018.1540921.
364. Chovancová, M., Očko, P., Pechová, A., and Lopuch, J., *Lifetime Prediction of Propellants According to NATO Standards.* Problemy Techniki Uzbrojenia, 2006. **35**.

365. Queensland Government. *Explosives: Hazards of Storing Propellant Powders*. 2016 13/04/2023]; Available from: https://www.qld.gov.au/emergency/safety/explosives-fireworks/explosives/hazards-ammunition.
366. Yan, W., Wang, L., Yangxiao, K., Fu, Z., and Wu, T., *Effects of Ligand and Guest Solvent Molecules on the Luminescence Properties of Tb:Eu-Codoped Indium-Based MOFs.* Dalton Transactions, 2016. **45**(11): p. 4518-4521.DOI: https://doi.org/10.1039/C5DT04844C.
367. Strasser, A. and Vogler, A., *Phosphorescence of Gadolinium(III) Chelates Under Ambient Conditions.* Inorganica Chimica Acta, 2004. **357**(8): p. 2345-2348.DOI: https://doi.org/10.1016/j.ica.2004.01.024.
368. Charles, R.G., Freiser, H., Friedel, R., Hilliard, L.E., and Johnston, W.D., *Infra-Red Absorption Spectra of Metal Chelates Derived from 8-Hydroxyquinoline, 2-Methyl-8-Hydroxyquinoline, and 4-Methyl-8-Hydroxyquinoline.* Spectrochimica Acta, 1956. **8**(1): p. 1-8.DOI: https://doi.org/10.1016/0371-1951(56)80018-0.
369. Stan, C.S., Peptu, C., Marcotte, N., Horlescu, P., and Sutiman, D., *Photoluminescent Properties of Novel Y(III), Sm(III), Eu(III), Gd(III) and Tb(III) Complexes with 2-(1H-1,2,4-Triazol-3-yl)Pyridine.* Inorganica Chimica Acta, 2015. **429**: p. 160-167.DOI: https://doi.org/10.1016/j.ica.2015.01.041.
370. Sigma-Aldrich, *Metal-Organic Framework (MOF) Constructor*. 2012.
371. Lin, Z.-J., Yang, Z., Liu, T.-F., Huang, Y.-B., and Cao, R., *Microwave-Assisted Synthesis of a Series of Lanthanide Metal-Organic Frameworks and Gas Sorption Properties.* Inorganic Chemistry, 2012. **51**(3): p. 1813-1820.DOI: https://doi.org/10.1021/ic202082w.
372. Dang, S., Song, S., Feng, J., and Zhang, H., *Microwave-Assisted Synthesis of Nanoscale Eu(BTC)(H_2O)·DMF with Tunable Luminescence.* Science China Chemistry, 2015. **58**(6): p. 973-978.DOI: https://doi.org/10.1007/s11426-014-5272-y.
373. Butova, V.V.e., Soldatov, M.A., Guda, A.A., Lomachenko, K.A., and Lamberti, C., *Metal-Organic Frameworks: Structure, Properties, Methods of Synthesis and Characterization.* Russian Chemical Reviews, 2016. **85**(3): p. 280.DOI: https://doi.org/10.1070/RCR4554.
374. Khan, H., Yerramilli, A.S., D'Oliveira, A., Alford, T.L., Boffito, D.C., and Patience, G.S., *Experimental Methods in Chemical Engineering: X-Ray Diffraction Spectroscopy—XRD.* The Canadian Journal of Chemical Engineering, 2020. **98**(6): p. 1255-1266.DOI: https://doi.org/10.1002/cjce.23747.
375. Inoue, M. and Hirasawa, I., *The Relationship Between Crystal Morphology and XRD Peak Intensity on $CaSO_4$·$2H_2O$.* Journal of Crystal Growth, 2013. **380**: p. 169-175.DOI: https://doi.org/10.1016/j.jcrysgro.2013.06.017.
376. Allendorf, M.D., Stavila, V., Witman, M., Brozek, C.K., and Hendon, C.H., *What Lies Beneath a Metal–Organic Framework Crystal Structure? New Design Principles From Unexpected Behaviors.* Journal of the American Chemical Society, 2021. **143**(18): p. 6705-6723.DOI: https://doi.org/10.1021/jacs.0c10777.
377. Hobday, C.L., Krause, S., Rogge, S.M., Evans, J.D., and Bunzen, H., *Perspectives on the Influence of Crystal Size and Morphology on the Properties of Porous Framework Materials.* Frontiers in Chemistry, 2021. **9**: p. 772059-772059.DOI: https://doi.org/10.3389/fchem.2021.772059.

378. Laurikenas, A., Beganskiene, A., and Kareiva, A., *On the Synthesis and Characterization of Lanthanide Metal-Organic Frameworks.* Ceramics, 2018. **1**(1): p. 54-64.DOI: https://doi.org/10.3390/ceramics1010006.
379. Abdelbaky, M.S., Amghouz, Z., García-Granda, S., and García, J.R., *Synthesis, Structures and Luminescence Properties of Metal-Organic Frameworks based on Lithium-Lanthanide and Terephthalate.* Polymers, 2016. **8**(3): p. 86.DOI: https://doi.org/10.3390/polym8030086.
380. Liu, Q., Wang, D.-M., Li, Y.-Y., Yan, M., Wei, Q., and Du, B., *Synthesis and Luminescent Properties of $Eu(TTA)_3{\cdot}3H_2O$ Nanocrystallines.* Luminescence, 2010. **25**(4): p. 307-310.DOI: https://doi.org/10.1002/bio.1150.
381. Wang, Y., Ma, D.Y., Jiang, Z.H., Zhang, Y.J., Yuan, H., Lv, Y.G., Liu, H., Zhu, Y.C., and Fang, W. *Synthesis, Characterization and Luminescent Properties of a Rare Earth Complex $Eu(TTA)_3(TPPO)_2$*. in *Advanced Materials Research*. 2012. Trans Tech Publ.
382. Gao, H.-L., Yi, L., Zhao, B., Zhao, X.-Q., Cheng, P., Liao, D.-Z., and Yan, S.-P., *Synthesis and Characterization of Metal-Organic Frameworks Based on 4-Hydroxypyridine-2,6-dicarboxylic Acid and Pyridine-2,6-dicarboxylic Acid Ligands.* Inorganic Chemistry, 2006. **45**(15): p. 5980-5988.DOI: 10.1021/ic060550j.
383. Zhou, L.-Q., Wang, F., Tang, Z.-W., Zhou, L.-R., and Sun, J.-T., *Synthesis and Spectroscopic Study of a Terbium(III) 2,6-Pyridinedicarboxylate Complex.* Spectroscopy Letters, 2010. **43**(2): p. 108-113.DOI: 10.1080/00387010903278317.
384. Xiang, L., Jingyan, W., Qingyuan, L., JIANG, S., ZHANG, T., and Shengfu, J., *Synthesis of Rare Earth Metal-Organic Frameworks (Ln-MOFs) and their Properties of Adsorption Desulfurization.* Journal of Rare Earths, 2014. **32**(2): p. 189-194.DOI: https://doi.org/10.1016/S1002-0721(14)60050-8.
385. Souza, E.R., Silva, I.G., Teotonio, E.E., Felinto, M.C., and Brito, H.F., *Optical Properties of Red, Green and Blue Emitting Rare Earth Benzenetricarboxylate Compounds.* Journal of Luminescence, 2010. **130**(2): p. 283-291.DOI: https://doi.org/10.1016/j.jlumin.2009.09.004.
386. Alammar, T., Hlova, I.Z., Gupta, S., Balema, V., Pecharsky, V.K., and Mudring, A.-V., *Luminescence Properties of Mechanochemically Synthesized Lanthanide Containing MIL-78 MOFs.* Dalton Transactions, 2018. **47**(22): p. 7594-7601.DOI: https://doi.org/10.1039/C7DT04771A.
387. Nozohour Yazdi, M., Yamini, Y., Asiabi, H., and Alizadeh, A., *A Metal-Organic Framework Prepared From Benzene-1,3,5-Tricarboxylic Acid and Copper(II), and Functionalized with Various Polysulfides as a Sorbent for Selective Sorption of Trace Amounts of Heavy Metal Ions.* Microchimica Acta, 2018. **185**(11): p. 525.DOI: 10.1007/s00604-018-3059-0.
388. Medina-Velazquez, D.Y., Caldiño, U., Morales-Ramirez, A., Reyes-Miranda, J., Lopez, R.E., Escudero, R., Ruiz-Guerrero, R., and Morales Perez, M.F., *Synthesis of Luminescent Terbium-Thenoyltriflouroacetone MOF Nanorods for Green Laser Application.* Optical Materials, 2019. **87**: p. 3-10.DOI: https://doi.org/10.1016/j.optmat.2018.08.021.
389. Nekoei, A.-R., Tayyari, S.F., Vakili, M., Holakoei, S., Hamidian, A.H., and Sammelson, R.E., *Conformation and Vibrational Spectra and Assignment of 2-Thenoyltrifluoroacetone.* Journal of Molecular Structure, 2009. **932**(1-3): p. 112-122.DOI: https://doi.org/10.1016/j.molstruc.2009.05.045.

390. Uzoukwu, B.A., *Some Metal Complexes of 1,3-Diketone: Syntheses, UV-Vis, IR, 1H, ^{13}C and ^{19}F NMR Spectral Studies of the Complexes of U(VI), Fe(III), V(V) and Ca(II) with 2-Thenoyltrifluoroacetone (HTTA).* Inorganica Chimica Acta, 1990. **176**(1): p. 143-148.DOI: https://doi.org/10.1016/S0020-1693(00)85105-1.
391. Murinzi, T.W., Hosten, E., and Watkins, G.M., *Synthesis and Characterization of a Cobalt-2,6-Pyridinedicarboxylate MOF with Potential Application in Electrochemical Sensing.* Polyhedron, 2017. **137**: p. 188-196.DOI: https://doi.org/10.1016/j.poly.2017.08.030.
392. Wang, L. and Chen, Y., *Lanthanide Doped Carbon Dots as a Fluorescence Chromaticity-Based pH Probe.* Microchimica Acta, 2018. **185**(10): p. 489.DOI: https://doi.org/10.1007/s00604-018-3027-8.
393. Świderski, G., Lewandowska, H., Świsłocka, R., Wojtulewski, S., Siergiejczyk, L., Wilczewska, A.Z., and Misztalewska, I., *Spectroscopic (IR, Raman, NMR), Thermal and Theoretical (DFT) Study of Alkali Metal Dipicolinates (2,6) and Quinolinates (2,3).* Arabian Journal of Chemistry, 2019. **12**(8): p. 4414-4426.DOI: https://doi.org/10.1016/j.arabjc.2016.06.011.
394. Venna, S.R., Jasinski, J.B., and Carreon, M.A., *Structural Evolution of Zeolitic Imidazolate Framework-8.* Journal of the American Chemical Society, 2010. **132**(51): p. 18030-18033.DOI: 10.1021/ja109268m.
395. Gustafsson, M., Bartoszewicz, A., Martín-Matute, B., Sun, J., Grins, J., Zhao, T., Li, Z., Zhu, G., and Zou, X., *A Family of Highly Stable Lanthanide Metal–Organic Frameworks: Structural Evolution and Catalytic Activity.* Chemistry of Materials, 2010. **22**(11): p. 3316-3322.DOI: https://doi.org/10.1021/cm100503q.
396. Haque, E., Khan, N.A., Park, J.H., and Jhung, S.H., *Synthesis of a Metal–Organic Framework Material, Iron Terephthalate, by Ultrasound, Microwave, and Conventional Electric Heating: A Kinetic Study.* Chemistry–A European Journal, 2010. **16**(3): p. 1046-1052.DOI: https://doi.org/10.1002/chem.200902382.
397. Usman, K.A.S., Maina, J.W., Seyedin, S., Conato, M.T., Payawan, L.M., Dumée, L.F., and Razal, J.M., *Downsizing Metal-Organic Frameworks by Bottom-Up and Top-Down Methods.* NPG Asia Materials, 2020. **12**(1): p. 58.DOI: https://doi.org/10.1038/s41427-020-00240-5.
398. Ahmadi, M., Ayyoubzadeh, S.M., Ghorbani-Bidkorbeh, F., Shahhosseini, S., Dadashzadeh, S., Asadian, E., Mosayebnia, M., and Siavashy, S., *An Investigation of Affecting Factors on MOF Characteristics for Biomedical Applications: A Systematic Review.* Heliyon, 2021. **7**(4): p. e06914.DOI: https://doi.org/10.1016/j.heliyon.2021.e06914.
399. Seoane, B., Castellanos, S., Dikhtiarenko, A., Kapteijn, F., and Gascon, J., *Multi-Scale Crystal Engineering of Metal Organic Frameworks.* Coordination Chemistry Reviews, 2016. **307**: p. 147-187.DOI: https://doi.org/10.1016/j.ccr.2015.06.008.
400. Ghosh, D. and Luwang, M.N., *One-Pot Synthesis of 2-Thenoyltrifluoroacetone Surface Functionalised SrF2:Eu^{3+} Nanoparticles: Trace Level Detection of Water.* RSC Advances, 2015. **5**(58): p. 47131-47139.DOI: https://doi.org/10.1039/C5RA08566G.
401. Jung, D.-W., Yang, D.-A., Kim, J., Kim, J., and Ahn, W.-S., *Facile Synthesis of MOF-177 by a Sonochemical Method Using 1-Methyl-2-Pyrrolidinone as a Solvent.* Dalton Transactions, 2010. **39**(11): p. 2883-2887.DOI: https://doi.org/10.1039/B925088C.

402. Ahnfeldt, T., Moellmer, J., Guillerm, V., Staudt, R., Serre, C., and Stock, N., *High-Throughput and Time-Resolved Energy-Dispersive X-Ray Diffraction (EDXRD) Study of the Formation of CAU-1-(OH) 2: Microwave and Conventional Heating.* Chemistry–A European Journal, 2011. **17**(23): p. 6462-6468.DOI: https://doi.org/10.1002/chem.201003708.
403. Chen, Y.-Y., Si, Y.-F., Kong, F.-T., Liu, Z.-g., and Li, J.-w., *Effects of Yttrium on Microstructures and Properties of Ti-17Al-27Nb Alloy.* Transactions of Nonferrous Metals Society of China, 2006. **16**(2): p. 316-320.DOI: https://doi.org/10.1016/S1003-6326(06)60054-X.
404. Srinivasan, R., Yogamalar, N.R., Elanchezhiyan, J., Joseyphus, R.J., and Bose, A.C., *Structural and Optical Properties of Europium Doped Yttrium Oxide Nanoparticles for Phosphor Applications.* Journal of Alloys and Compounds, 2010. **496**(1): p. 472-477.DOI: https://doi.org/10.1016/j.jallcom.2010.02.083.
405. Healy, C., Patil, K.M., Wilson, B.H., Hermanspahn, L., Harvey-Reid, N.C., Howard, B.I., Kleinjan, C., Kolien, J., Payet, F., and Telfer, S.G., *The Thermal Stability of Metal-Organic Frameworks.* Coordination Chemistry Reviews, 2020. **419**: p. 213388.DOI: https://doi.org/10.1016/j.ccr.2020.213388.
406. Angeloski, A., Gentle, A.R., Scott, J.A., Cortie, M.B., Hook, J.M., Westerhausen, M.T., Bhadbhade, M., Baker, A.T., and McDonagh, A.M., *From Lead(II) Dithiocarbamate Precursors to a Fast Response PbS Positive Temperature Coefficient Thermistor.* Inorganic Chemistry, 2018. **57**(4): p. 2132-2140.DOI: https://doi.org/10.1021/acs.inorgchem.7b03009.
407. Bala, P., Samantaray, B., and Srivastava, S., *Dehydration Transformation in Ca-montmorillonite.* Bulletin of Materials Science, 2000. **23**(1): p. 61-67.DOI: https://doi.org/10.1007/BF02708614.
408. Howarth, A.J., Liu, Y., Li, P., Li, Z., Wang, T.C., Hupp, J.T., and Farha, O.K., *Chemical, Thermal and Mechanical Stabilities of Metal–Organic Frameworks.* Nature Reviews Materials, 2016. **1**(3): p. 1-15.DOI: https://doi.org/10.1038/natrevmats.2015.18.
409. Jiang, H.-L., Tsumori, N., and Xu, Q., *A Series of (6,6)-Connected Porous Lanthanide−Organic Framework Enantiomers with High Thermostability and Exposed Metal Sites: Scalable Syntheses, Structures, and Sorption Properties.* Inorganic Chemistry, 2010. **49**(21): p. 10001-10006.DOI: https://doi.org/10.1021/ic101294s.
410. Fonseca, R.R.F., Gaspar, R.D.L., Raimundo, I.M., and Luz, P.P., *Photoluminescent Tb^{3+}-based Metal-Organic Framework as a Sensor for Detection of Methanol in Ethanol Fuel.* Journal of Rare Earths, 2019. **37**(3): p. 225-231.DOI: https://doi.org/10.1016/j.jre.2018.07.006.
411. Xianzhe, D., Nan, L., Yuyuan, W., and Zhenping, T., *Systematical Study on the Influencing Factors of Synchronous Thermal Analyses of Samples-Taking the Chalcanthite as an Example.* Frontiers in Chemistry, 2022. **10**: p. 863083.DOI: https://doi.org/10.3389/fchem.2022.863083.
412. Erickson, K.L. and Oelfke, J., *Effect of Oxygen Concentration on Thermal Decomposition of Organic Polymers*. 2007, Sandia National Lab.(SNL-NM), Albuquerque, NM (United States).
413. Chiang, W.-F., Fang, H.-Y., Wu, C.-H., Huang, C.-J., Chang, C.-Y., Chang, Y.-M., and Chen, C.-L., *The Effect of Oxygen on the Kinetics of the Thermal Degradation for*

Rice Straw. Journal of the Air & Waste Management Association, 2009. **59**(2): p. 148-154.DOI: https://doi.org/10.3155/1047-3289.59.2.148.

414. Lopez-Ruiz, L., Salas-Juárez, C.J., Garduño-Wilches, I., Beltran, H., Orozco-Valencia, U., López-Esquivel, R., Guzman-Olguin, J., Centeno-Alvarez, M., and Guzman-Mendoza, J., *Luminescent Analysis of [Eu_2DPA_3] MOF as High Purity Red-Emitting Phosphor with Thermal Stability.* Journal of Luminescence, 2023. **263**: p. 120020.DOI: https://doi.org/10.1016/j.jlumin.2023.120020.
415. Chen, B., Yang, Y., Zapata, F., Qian, G., Luo, Y., Zhang, J., and Lobkovsky, E.B., *Enhanced Near-Infrared−Luminescence in an Erbium Tetrafluoroterephthalate Framework.* Inorganic Chemistry, 2006. **45**(22): p. 8882-8886.DOI: https://doi.org/10.1021/ic060568u.
416. Martín-Ramos, P., Pereira, L., Coutinho, J., Koprowiak, F., Bolvin, H., Lavín, V., Martín, I., Martín-Gil, J., and Silva, M.R., *Structure, Luminescence and Magnetic Properties of an Erbium(III) β-diketonate Homodinuclear Complex.* New Journal of Chemistry, 2016. **40**(10): p. 8251-8261.DOI: https://doi.org/10.1039/C6NJ01598K.
417. Coban, M.B., Erkarslan, U., Oylumluoglu, G., Aygun, M., and Kara, H., *Hydrothermal Synthesis, Crystal Structure and Photoluminescent Properties; 3D Holmium(III) Coordination Polymer.* Inorganica Chimica Acta, 2016. **447**: p. 87-91.DOI: https://doi.org/10.1016/j.ica.2016.03.038.
418. Dang, S., Sun, L.-N., Song, S.-Y., Zhang, H.-J., Zheng, G.-L., Bi, Y.-F., Guo, H.-D., Guo, Z.-Y., and Feng, J., *Syntheses, Crystal Structures and Near-Infrared Luminescent Properties of Holmium (Ho) and Praseodymium (Pr) Ternary Complexes.* Inorganic Chemistry Communications, 2008. **11**(5): p. 531-534.DOI: https://doi.org/10.1016/j.inoche.2008.02.001.
419. Cao, W., Tang, Y., Cui, Y., and Qian, G., *Energy Transfer in Metal–Organic Frameworks and its Applications.* Small Structures, 2020. **1**(3): p. 2000019.DOI: https://doi.org/10.1002/sstr.202000019.
420. Zhao, B., Zhao, X.Q., Chen, Z., Shi, W., Cheng, P., Yan, S.P., and Liao, D.Z., *Structures and Near-Infrared Luminescence of Unique 4d–4f Heterometal-Organic Frameworks (HMOF).* CrystEngComm, 2008. **10**(9): p. 1144-1146.DOI: https://doi.org/10.1039/B807491G.
421. Dang, S., Yu, J., Yu, J., Wang, X., Sun, L., Feng, J., Fan, W., and Zhang, H., *Novel Holmium (Ho) and Praseodymium (Pr) Ternary Complexes with Fluorinated-Ligand and 4,5-Diazafluoren-9-One.* Materials Letters, 2011. **65**(11): p. 1642-1644.DOI: https://doi.org/10.1016/j.matlet.2011.02.043.
422. León-Luis, S.F., Rodríguez-Mendoza, U.R., Lalla, E., and Lavín, V., *Temperature Sensor Based on the Er^{3+} Green Upconverted Emission in a Fluorotellurite Glass.* Sensors and Actuators B: Chemical, 2011. **158**(1): p. 208-213.DOI: https://doi.org/10.1016/j.snb.2011.06.005.
423. Yu, P., Wen, X., Toh, Y.-R., and Tang, J., *Temperature-Dependent Fluorescence in Carbon Dots.* The Journal of Physical Chemistry C, 2012. **116**(48): p. 25552-25557.DOI: https://doi.org/10.1021/jp307308z.
424. Souza, E.R., Zulato, C.H.F., Mazali, I.O., and Sigoli, F.A., *Synthesis and Photoluminescent Properties of Lanthanides Acetoacetanilide Complexes.* Journal of Fluorescence, 2013. **23**(5): p. 939-946.DOI: https://doi.org/10.1007/s10895-013-1219-5.

425. Souza, E.R., Mazali, I.O., and Sigoli, F.A., *Structural Investigation and Photoluminescent Properties of Gadolinium(III), Europium(III) and Terbium(III) 3-Mercaptopropionate Complexes.* Journal of Fluorescence, 2014. **24**(1): p. 203-211.DOI: https://doi.org/10.1007/s10895-013-1288-5.
426. Wang, S., McGuirk, C.M., d'Aquino, A., Mason, J.A., and Mirkin, C.A., *Metal–Organic Framework Nanoparticles.* Advanced Materials, 2018. **30**(37): p. 1800202.DOI: https://doi.org/10.1002/adma.201800202.
427. Chen, C., Feng, X., Zhu, Q., Dong, R., Yang, R., Cheng, Y., and He, C., *Microwave-Assisted Rapid Synthesis of Well-Shaped MOF-74(Ni) for CO_2 Efficient Capture.* Inorganic Chemistry, 2019. **58**(4): p. 2717-2728.DOI: https://doi.org/10.1021/acs.inorgchem.8b03271.
428. Lv, X.-L., Yuan, S., Xie, L.-H., Darke, H.F., Chen, Y., He, T., Dong, C., Wang, B., Zhang, Y.-Z., and Li, J.-R., *Ligand Rigidification for Enhancing the Stability of Metal–Organic Frameworks.* Journal of the American Chemical Society, 2019. **141**(26): p. 10283-10293.DOI: https://doi.org/10.1021/jacs.9b02947.
429. Tan, K., Nijem, N., Gao, Y., Zuluaga, S., Li, J., Thonhauser, T., and Chabal, Y.J., *Water Interactions in Metal Organic Frameworks.* CrystEngComm, 2015. **17**(2): p. 247-260.DOI: 10.1039/C4CE01406E.
430. Li, Y. and Yang, R.T., *Gas Adsorption and Storage in Metal−Organic Framework MOF-177.* Langmuir, 2007. **23**(26): p. 12937-12944.DOI: https://doi.org/10.1021/la702466d.
431. Kökçam-Demir, Ü., Goldman, A., Esrafili, L., Gharib, M., Morsali, A., Weingart, O., and Janiak, C., *Coordinatively Unsaturated Metal Sites (Open Metal Sites) in Metal–Organic Frameworks: Design and Applications.* Chemical Society Reviews, 2020. **49**(9): p. 2751-2798.DOI: https://doi.org/10.1039/C9CS00609E.
432. Huang, Z., Zhao, F., Fan, L., Zhao, W., Chen, B., Chen, X., Zhou, S.-F., Xiao, J., and Zhan, G., *Improved Hydrolytic Robustness and Catalytic Performance of Flexible Lanthanide-Based Metal-Organic Frameworks: A Matter of Coordination Environments.* Materials & Design, 2020. **194**: p. 108881.DOI: https://doi.org/10.1016/j.matdes.2020.108881.
433. Liu, X., Wang, X., and Kapteijn, F., *Water and Metal–Organic Frameworks: From Interaction Toward Utilization.* Chemical Reviews, 2020. **120**(16): p. 8303-8377.DOI: https://doi.org/10.1021/acs.chemrev.9b00746.
434. Garg, A., Almáši, M., Saini, R., Paul, D.R., Sharma, A., Jain, A., and Jain, I.P., *A Highly Stable Terbium (III) Metal-Organic Framework MOF-76 (Tb) for Hydrogen Storage and Humidity Sensing.* Environmental Science and Pollution Research, 2022: p. 1-15.DOI: https://doi.org/10.1007/s11356-022-21290-y.
435. Singh, M.P., Dhumal, N.R., Kim, H.J., Kiefer, J., and Anderson, J.A., *Influence of Water on the Chemistry and Structure of the Metal–Organic Framework Cu3(btc)2.* The Journal of Physical Chemistry C, 2016. **120**(31): p. 17323-17333.DOI: https://10.1021/acs.jpcc.6b02906.
436. Ghosh, S.K. and Bharadwaj, P.K., *Self-Assembly of Lanthanide Helicate Coordination Polymers into 3D Metal-Organic Framework Structures.* Inorganic chemistry, 2004. **43**(7): p. 2293-2298.DOI: https://doi.org/10.1021/ic034982v.
437. Zhu, T., Ikarashi, K., Ishigaki, T., Uematsu, K., Toda, K., Okawa, H., and Sato, M., *Structure and Luminescence of Sodium and Lanthanide (III) Coordination Polymers with Pyridine-2, 6-Dicarboxylic Acid.* Inorganica Chimica Acta, 2009. **362**(10): p. 3407-3414.DOI: https://doi.org/10.1016/j.ica.2009.01.036.

438. Wang, T. and Li, H., *A Simple and Green Strategy for Preparing Luminescent Tb3+ Complex-Based Nanocomposite with Stable Luminescence in Water.* Materials Research Bulletin, 2017. **93**: p. 28-34.DOI: https://doi.org/10.1016/j.materresbull.2017.04.034.
439. Gao, J., Zhao, G., and Kang, J., *The Application of Trimesic Acid to the Determination of Terbium by Spectrofluorimetry.* Talanta, 1995. **42**(10): p. 1497-1503.DOI: https://doi.org/10.1016/0039-9140(95)01601-7.
440. Jurkowski, W., Heilmann, M., Becker, A.M., Buchholz, R., and Brück, T.B., *Terbium Excitation Spectroscopy as a Detection Method for Chromatographic Separation of Lanthanide-Binding Biomolecules.* ACS Omega, 2020. **5**(42): p. 27050-27056.DOI: https://doi.org/10.1021/acsomega.0c02135.
441. Liu, B., Vikrant, K., Kim, K.-H., Kumar, V., and Kailasa, S.K., *Critical Role of Water Stability in Metal–Organic Frameworks and Advanced Modification Strategies for the Extension of their Applicability.* Environmental Science: Nano, 2020. **7**(5): p. 1319-1347.DOI: https://doi.org/10.1039/C9EN01321K.
442. Lu, T.-Q., Cheng, L.-T., Wang, X.-T., Chen, C., Zheng, J., Lu, D.-F., and Zheng, X.-Y., *Lanthanide Metal–Organic Frameworks with High Chemical Stability as Multifunctional Materials: Cryogenic Magnetic Cooler and Luminescent Probe.* Crystal Growth & Design, 2022. **22**(8): p. 4917-4925.DOI: https://doi.org/10.1021/acs.cgd.2c00426.
443. Song, T.-Q., Yuan, K., Qiao, W.-Z., Shi, Y., Dong, J., Gao, H.-L., Yang, X.-P., Cui, J.-Z., and Zhao, B., *Water Stable [Tb_4] Cluster-Based Metal–Organic Framework as Sensitive and Recyclable Luminescence Sensor of Quercetin.* Analytical Chemistry, 2019. **91**(4): p. 2595-2599.DOI: https://doi.org/10.1021/acs.analchem.8b05281.
444. Dreyfus, P., Lessing, B., de Sousa Nascimento, M., and Purcena, J.C., *Small Arms in Brazil: Production, Trade, and Holdings*. 2010: Switzerland.
445. Lucena, M.A.M., Oliveira, M.F.L., Arouca, A.M., Talhavini, M., Ferreira, E.A., Alves, S., Veiga-Souza, F.H., and Weber, I.T., *Application of the Metal–Organic Framework [Eu(BTC)] as a Luminescent Marker for Gunshot Residues: A Synthesis, Characterization, and Toxicity Study.* ACS Applied Materials & Interfaces, 2017. **9**(5): p. 4684-4691.DOI: 10.1021/acsami.6b13474.
446. Inc, G., *Safe Action Pistols (G17-G44): Instructions for Use*. 2020. p. 27-32.
447. Bolton, M., *Firearms & Toolmark Examiner, Australian Federal Police*. 2023, Personal Communication.
448. Burnett, B.R. and Nunziata, F., *Divergent Gunshot Residues and Characterization of the Memory Effect in a. 22 Caliber Revolver and Pistol.* Egyptian Journal of Forensic Sciences, 2023. **13**(1): p. 1-20.DOI: https://doi.org/10.1186/s41935-023-00326-5.
449. Wallace, J. and McQuillan, J., *Discharge Residues from Cartridge-Operated Industrial Tools.* Journal of the Forensic Science Society, 1984. **24**(5): p. 495-508.DOI: https://doi.org/10.1016/S0015-7368(84)72329-2.
450. Winchester Ammunition, *Centrefire Loaded Rounds - Material Safety Data Sheet*. 2014. p. 1-7.
451. Winchester Ammunition, *Bullets – Jacket Lead Core - Material Safety Data Sheet*. 2013. p. 1-5.
452. Carneiro, C.R., Lucena, M.A., Santos-Silva, C., and Weber, I.T., *Nontoxic Ammunition: Challenges and Perspectives for GSR Identification.* Wiley

Interdisciplinary Reviews: Forensic Science, 2023. **5**(3): p. e1477.DOI: https://doi.org/10.1002/wfs2.1477.

453. Gascho, D., Zoelch, N., Deininger-Czermak, E., Tappero, C., Richter, H., Thali, M.J., and Schaerli, S., *In Situ Identification of Action 4, SECA and QD-PEP Bullets from Special Police Ammunitions by Computed Ttomography.* Medicine, Science and the Law, 2020. **60**(3): p. 188-195.DOI: https://doi.org/10.1177/0025802420911555.
454. North Atlantic Treaty Organisation, *AEP-97 Multi-Calibre Manial of Proof and Inspection (M-CMOPI) for NATO Small Arms Ammunition.* NATO Standard, 2020: p. 258.
455. Waszczuk, J., *Firearms & Toolmark Examiner, Australian Federal Police*. 2023, Personal Communication.
456. Matys, M., Piotrowski, K., Kukulski, B., Binek, W., and Sobolewska, M. *Analysis of the Noise Generated by Variable Types of Firearms*. in *Euronoise*. 2018. Crete, Greece.
457. Heard, B.J., *Forensic Ballistics in Court Interpretation and Presentation of Firearms Evidence*. 2013, Chichester, England: Wiley-Blackwell.
458. Mattijssen, E.J.A.T. and Kerkhoff, W., *Bullet Trajectory Reconstruction – Methods, Accuracy and Precision.* Forensic Science International, 2016. **262**: p. 204-211.DOI: https://doi.org/10.1016/j.forsciint.2016.03.039.
459. Krishna, S. and Ahuja, P., *A Chronological Study of Gunshot Residue (GSR) Detection Techniques: A Narrative Review.* Egyptian Journal of Forensic Sciences, 2023. **13**(1): p. 51.DOI: https://doi.org/10.1186/s41935-023-00369-8.
460. Simas, V., Schram, B., Canetti, E.F., Maupin, D., and Orr, R., *Factors Influencing Marksmanship in Police Officers: A Narrative Review.* International Journal of Environmental Research and Public Health, 2022. **19**(21): p. 14236.DOI: https://doi.org/10.3390/ijerph192114236.
461. Ellis, M.B. and Miller, C.A., *Efforts to Ban Lead Ammunition: A Comparison between Europe and the United States.* Wildlife Society Bulletin, 2023. **47**(2): p. e1449.DOI: https://doi.org/10.1002/wsb.1449.